
Cassini observations of the ring current in
Saturn's magnetosphere

Thesis submitted for the degree of
Doctor of Philosophy
at the University of Leicester

by

Stephanie Kellett

Radio and Space Plasma Physics Group
Department of Physics and Astronomy
University of Leicester

January 2011

Abstract

Cassini observations of the ring current in Saturn's magnetosphere

Stephanie Kellett

In this thesis we have employed plasma and magnetic field data from the Cassini spacecraft in order to better understand Saturn's ring current region. Three data studies are presented along with a derivation of the general expression for the field-perpendicular current density in terms of the plasma bulk parameters.

In the first data study an essentially direct determination of the equatorial current sheet thickness was made using data from six north-south Cassini orbits. The dayside data indicated the presence of an equatorial current disk with a near constant half-thickness of $\sim 1.5 R_S$. More variable conditions were found on the nightside. The data examined also provided evidence of a northward displacement of the current layer from the equatorial plane.

Next, the nature of the ring current in Saturn's dayside magnetosphere was investigated. The total azimuthal current density was found to rise from small values near $\sim 6 R_S$, peak at $\sim 100 \text{ pA m}^{-2}$ near $\sim 8 R_S$, and then reduce to values below $\sim 25 \text{ pA m}^{-2}$ at distances beyond $\sim 15 R_S$, up to the $20 R_S$ limit of our study. The overall total current density profile was found to be similar to that produced by the pressure gradient current, but augmented in strength by factors of ~ 1.5 - 2.0 by the difference between the inertia and pressure anisotropy currents. Comparison of the current density profiles deduced from plasma data with those obtained from current disk modelling of the magnetic field perturbations showed good agreement with the gross features.

Finally, both the local time dependency and temporal variability of Saturn's ring current was explored using data obtained from eleven near-equatorial Cassini orbits. In general, the plasma parameters, azimuthal current, and related magnetic perturbation fields were found to exhibit only modest variations with local time and from pass-to-pass over the interval of this study.

Declarations

The research undertaken during the course of this doctoral programme has led to the submission and publication of the following scientific papers:

Kellett, S., E.J. Bunce, A.J. Coates, and S.W.H. Cowley (2009), Thickness of Saturn's ring current determined from north-south Cassini passes through the current layer, *J. Geophys. Res.*, *114*, A04209, doi:10.1029/2008JA013942.

Kellett, S., C.S. Arridge, E.J. Bunce, A.J. Coates, S.W.H. Cowley, M.K. Dougherty, A.M. Persoon, N. Sergis, and R.J. Wilson (2010), Nature of the ring current in Saturn's dayside magnetosphere, *J. Geophys. Res.*, *115*, A08201, doi:10.1029/2009JA015146.

Kellett, S., C.S. Arridge, E.J. Bunce, A.J. Coates, S.W.H. Cowley, M.K. Dougherty, A.M. Persoon, N. Sergis, and R.J. Wilson (2010), Saturn's ring current: Local time dependence and temporal variability, *J. Geophys. Res.*, *116*, A05220, doi:10.1029/2010JA016216.

Acknowledgements

First and foremost I'd like to thank my supervisor, Stan Cowley, who has the amazing ability to explain anything to anyone. I am very grateful for his guidance, support and encouragement over the last few years. I would also like to thank the other members of my thesis committee, Emma Bunce and Derek Raine, who have given their time and support when I have needed it. I also acknowledge STFC for funding my PhD.

A massive thanks to everyone in the Radio and Space Plasma Physics group who has helped me, be-friended me, and laughed with (or at) me over the past few years. It's been an absolute privilege to work with everyone and there's no way I'd have completed this thesis without you all. Special thanks go to my office mates past and present - Sarah Badman, Suzie Imber and Elizabeth Davey. Your entertaining tales, cake baking skills, and the chocolate drawer really kept me going! Thanks also to Hannah Vickers for being completely crazy and persuading me to do the Great North Run in our final year!

I would also like to thank everyone at LUKC for providing an outlet and bashing me every week - training certainly made me forget about thesis writing for a while! Outside of work there are my wonderful undergrad friends Jay, Verity and Claire who have encouraged me, listened to my rants about data not doing what it should, and been the source of much entertainment! Thanks also to my family for their love and support - I am incredibly lucky to have you and don't expect you to read any further than this page!

Finally, my biggest thanks goes to Piyal for always reminding me not to focus on the 2 bad bricks, but to see the 998 good bricks as well. For your positivity, support and encouragement I am eternally grateful.

For Mum, in loving memory

The most wasted day of all is that on which we have not laughed.

Sebastien R.N. Chamfort (1741 – 1794)

List of Contents

Chapter 1 - Introduction to solar-planetary physics	1
1.1 Introduction	1
1.2 The Sun and the solar wind	1-2
1.2.1 The solar wind	2-3
1.3 Solar and interplanetary magnetic fields	3
1.3.1 Frozen-in flow	4-7
1.4 Effects of solar wind propagation	7-8
1.4.1 Corotating Interaction Regions (CIRs)	8
1.5 Planetary magnetospheres	9-10
1.5.1 Reconnection	10-11
1.5.2 The Dungey cycle	11-12
1.5.3 Effects of planetary rotation	12
1.5.4 Combined effect of solar wind-driven convection and corotation	13-14
1.6 The ring current	14-15
Chapter 2 - The Saturnian magnetosphere	16
2.1 Introduction	16
2.1.1 Previous fly-bys	16-17
2.2 Saturn's magnetic field	17
2.2.1 Magnetic field models	17-18
2.3 Saturn's magnetosphere	18
2.3.1 The inner magnetosphere	18-19
2.3.2 The middle and outer magnetosphere	19-20
2.4 Magnetospheric dynamics	20-21
2.5 Saturn's aurora	21
2.6 Saturn kilometric radiation	21-22
2.7 Periodicities in Saturn's magnetosphere	22-23
2.8 Saturn's ring current region	23-26

Chapter 3 - Instrumentation	27
3.1 Introduction	27
3.2 The Cassini orbiter and its mission	27-29
3.3 The Cassini magnetometer	29-30
3.3.1 The fluxgate magnetometer	30-31
3.4 The Cassini Plasma Spectrometer	31-32
3.4.1 The Electron Spectrometer (ELS)	32-33
3.4.2 The Ion Mass Spectrometer (IMS)	33-34
3.5 The Cassini Magnetospheric Imaging Instrument	34
3.5.1 The Charge Energy Mass Spectrometer (CHEMS)	34-35
3.5.2 The Low Energy Magnetospheric Measurements System (LEMMS)	35-36
3.6 The Cassini Radio and Plasma Wave Science Investigation	37-39
Chapter 4 - Thickness of Saturn's ring current determined from north-south Cassini passes through the current layer	40
4.1 Introduction	40-41
4.2 Modelling Saturn's ring current	41-43
4.3 North-south Cassini passes through the ring current layer	43-44
4.4 Cassini observations on north-south passes through the ring current	44
4.4.1 Recognising the current layer in magnetic field data	44-47
4.4.2 Dayside passes	47-51
4.4.3 Nightside passes	51-53
4.4.4 Overview of current sheet thickness and offset results	54-56
4.5 Summary	56-58
Chapter 5 - Derivation of the azimuthal current density from plasma bulk parameters	59
5.1 Introduction	59
5.2 Basic theory	59-61
5.3 Inertia current density	62-63
5.4 Pressure gradient current density	63-67

5.5	Pressure anisotropy current density	67-71
5.6	Azimuthal current density	71
Chapter 6 - Nature of the ring current in Saturn's dayside magnetosphere		72
6.1	Introduction	72
6.2	Plasma current density	73-75
6.3	Plasma parameter profiles	75-80
6.4	Current density profiles	80-83
6.5	Summary and Discussion	83-85
Chapter 7 - Local time dependency and temporal variability of Saturn's ring current		86
7.1	Introduction	86
7.2	Data set and methodology	86
7.2.1	Data coverage	86-87
7.2.2	Plasma properties and data sources	87-89
7.2.3	Plasma parameter profiles	89-90
7.2.4	Current density profiles	90-93
7.2.5	Comparison with field modelling results	93-94
7.3	Results	94
7.3.1	Local time dependence	94-99
7.3.2	Pass-to-pass temporal variability	99-102
7.3.3	Overall mean profiles	102-104
7.4	Summary and Discussion	104-108
Chapter 8 - Summary and Future Work		109
8.1	Introduction	109
8.2	Summary	109-113
8.3	Future Work	113-114
References		115

Chapter 1

Introduction to solar-planetary physics

1.1 - Introduction

Solar-planetary physics is concerned with the large and small scale interactions between the Sun and the environments of all solar system bodies. This thesis focuses on the magnetic and plasma environment of Saturn, the sixth planet away from the Sun. This first chapter provides an introduction to the Sun, solar wind, and the fundamental plasma physics required to understand the interaction between the Sun and magnetised planets. Chapter 2 then focuses on Saturn's magnetic and plasma environment with a particular focus on the ring current region. In Chapter 3 we discuss the Cassini orbiter and the instruments employed to obtain the data presented in this thesis. In Chapter 4 we present a study to determine the thickness of Saturn's ring current using data obtained from north-south Cassini passes through the current layer. A derivation of the azimuthal current density in terms of plasma parameters is presented in Chapter 5, which is then used in the data-based studies of Chapters 6 and 7. Chapter 6 addresses the nature of the ring current in Saturn's dayside magnetosphere using azimuthal current density profiles derived from plasma and magnetic field data. This study is then extended in Chapter 7 to consider a wider range of orbits in order to explore the local time dependence and temporal variability of Saturn's ring current. Finally, Chapter 8 summarises the main findings of these studies and provides suggestions for future work.

1.2 – The Sun and the solar wind

The Sun is a yellow dwarf star of spectral type G2V. It is our nearest star and lies a distance of $\sim 1.5 \times 10^8$ km (1 AU – Astronomical Unit) from the Earth and $\sim 1.4 \times 10^9$ km (~ 9.5 AU) from Saturn. The Sun is a massive ball of gas composed of approximately 90% hydrogen, 10% helium, and 0.1% heavier elements [*Priest, 1995*], and is held together and compressed by its own gravitational attraction. Figure 1.1 shows the solar interior and atmosphere. The radius of the Sun (the distance from its centre to the bottom of its atmosphere) is $\sim 6.96 \times 10^5$ km. The Sun's core extends radially to one quarter of the total radius and here the temperature and pressure are so high, $\sim 1.5 \times 10^7$ K

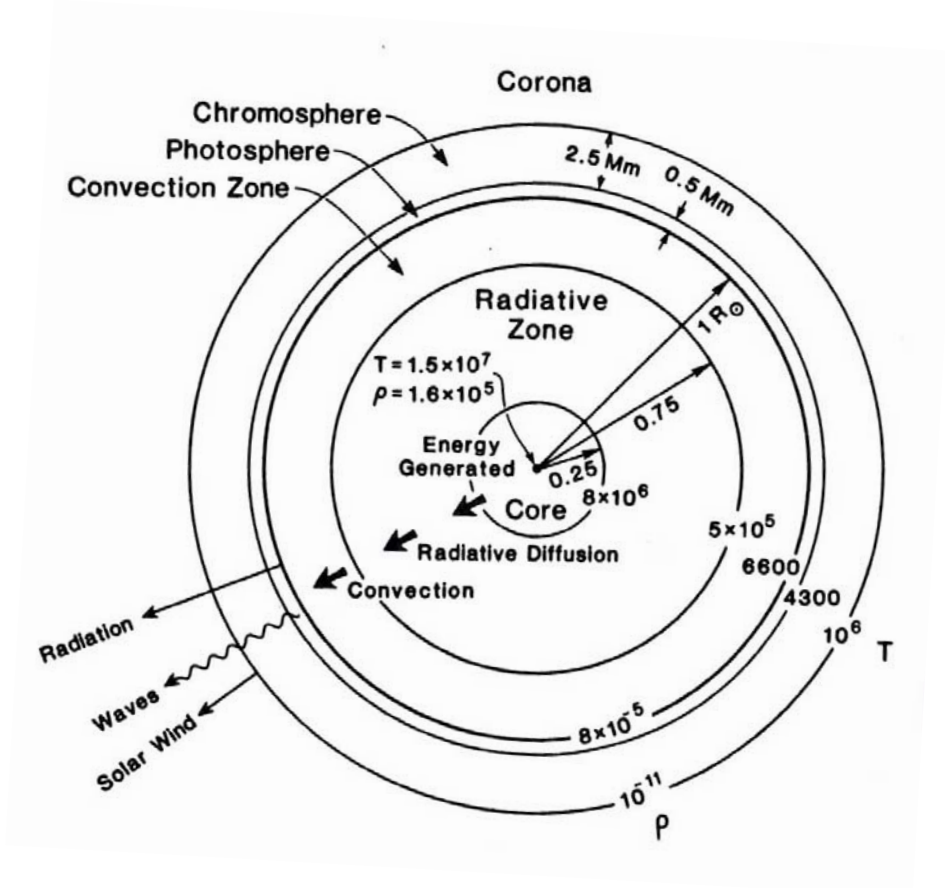


Figure 1.1. Cross section of the Sun showing the overall structure of the solar interior (the core, the radiative zone, and the convection zone) and the solar atmosphere (the photosphere, chromosphere, and corona). [From *Priest*, 1995.]

and $\sim 10^{16}$ Pa respectively, that nuclear fusion reactions take place. Hydrogen nuclei combine to produce helium nuclei, and energy is released in the form of photons, which then radiate outwards. These nuclear reactions are the source of the Sun's energy. A thick radiative zone surrounds the core. Here, thermal radiation transfers the intense heat of the core outward. The density and temperature decrease rapidly outside the core such that the outer layer of the Sun's interior is a turbulent convection zone, with an average temperature of $\sim 5 \times 10^5$ K.

The Sun's atmosphere lies above the convection zone, and is comprised of three layers. The bottom layer, the photosphere, is ~ 500 km thick and is at a temperature of ~ 6600 K. This layer emits most of the Sun's visible light. The photosphere is covered with a granular pattern outlining the convection cells beneath. Figure 1.2 shows the granulation pattern and a sunspot, which appear as dark patches on the photosphere. Sunspots mark regions of intense magnetic activity, which inhibit convection resulting in a region of reduced temperature at the surface, making it appear dark against the hotter background. The number of sunspots varies over time, with sunspot maxima (or minima) occurring approximately every 11 years. This process is termed the solar cycle and will be discussed below. Above the photosphere lies the chromosphere. This layer is $\sim 2.5 \times 10^3$ km thick and here the temperature drops to ~ 4300 K. The temperature then increases to reach $\sim 10^6$ K at the base of the corona, the outermost region of the Sun's atmosphere. This is a high enough temperature to strip atoms of their electrons and form ions, thus producing a charge-neutral plasma. The corona extends away from the Sun in all directions forming the solar wind, a low density plasma that fills the solar system. The existence of a persistent solar wind was first proposed by Biermann in 1951 by studying the anti-sunward direction of comet tails.

1.2.1 – The solar wind

The heliosphere is the region of space controlled by the Sun and bounded by the local interstellar medium (LISM) at a distance of ~ 110 - 160 AU. If we assume that the Sun's atmosphere is in hydrostatic equilibrium and apply the equation of force balance, we find that the pressure of the solar plasma at large radial distances from the Sun falls off to a limiting value of $\sim 2 \times 10^{-5}$ N m⁻². If the pressure in the LISM were greater than this

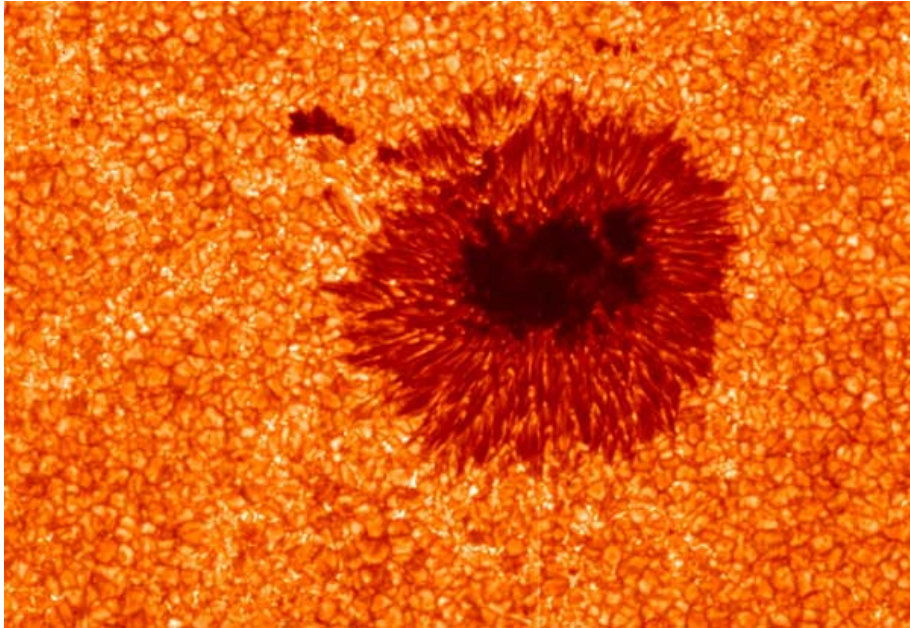


Figure 1.2. Image of a sunspot and solar granulation obtained from the Hinode spacecraft. [Courtesy of NASA.]

limiting pressure, the Sun's atmosphere would be confined by the LISM and reach hydrostatic equilibrium. However, using density and temperature estimates for the LISM of 3 cm^{-3} and $3 \times 10^3 \text{ K}$ respectively, we obtain a pressure of $\sim 10^{-13} \text{ Nm}^{-2}$ for the LISM. This is clearly much lower than the limiting hydrostatic pressure of the solar plasma and so the solar atmosphere does not reach hydrostatic equilibrium. Instead, there is a continuous outflow of coronal plasma at a rate of $\sim 10^9 \text{ kg}$ per second [Priest, 1995], i.e. the solar wind. The solar wind is composed mainly of protons and electrons, with a small amount of helium ions, and trace amounts of heavier ions. Table 1.1 summarises some typical properties of the solar wind at the orbital distances of the Earth and Saturn. Values at the Earth are taken from Hundhausen [1995], except for the solar wind dynamic pressure, which is calculated using $P_{sw} = \rho V^2$ where ρ is the mass density and V is the solar wind speed. Values are then extrapolated to Saturn under the assumption that solar wind density falls off as r^{-2} , where r is distance from the Sun.

The solar wind not only varies with the 27-day rotation of the Sun, but also in response to irregular, violent eruptions in the corona, e.g. flares, and coronal mass ejections (CMEs) - massive bursts of solar wind released from the Sun's corona.

1.3. Solar and interplanetary magnetic fields

The Sun has an 11-year activity cycle, which can be tracked by measuring the number of sunspots visible on the Sun's surface. At solar minimum (the start of the cycle) the sunspot number is low and the solar magnetic field is approximately dipolar. Approaching solar maximum, the sunspot number increases and the magnetic field becomes disordered. After 11 years, the sunspot number again reaches a minimum and the magnetic field is ordered again, but with the opposite polarity. The cycle begins again and it takes another 11 years for the Sun's magnetic field to return to its original polarity. The monthly sunspot numbers for the last five solar cycles are shown in Figure 1.3. The times of the Pioneer-11, Voyager-1 and -2 spacecraft fly-bys of Saturn are marked by the vertical black arrows. The studies presented in this thesis use data obtained from the Cassini mission, which arrived at Saturn in 2004, and is currently still in orbit. The Cassini orbital tour from 2004-2010 is indicated on the figure by the horizontal black line.

Solar wind properties	Earth	Saturn
Distance from the Sun (AU)	1	9.6
Solar wind speed (km s ⁻¹)	450	450
Solar wind proton density (cm ⁻³)	6.6	0.07
Solar wind electron density (cm ⁻³)	7.1	0.08
Solar wind dynamic pressure (nPa)	2.2	0.02
Average IMF magnitude (nT)	7	0.7

Table 1.1. Typical solar wind properties at the Earth and Saturn. Values at the Earth are taken from *Hundhausen* [1995], and then extrapolated to Saturn under the assumption that solar wind properties fall off as r^{-2} , where r is distance from the Sun.

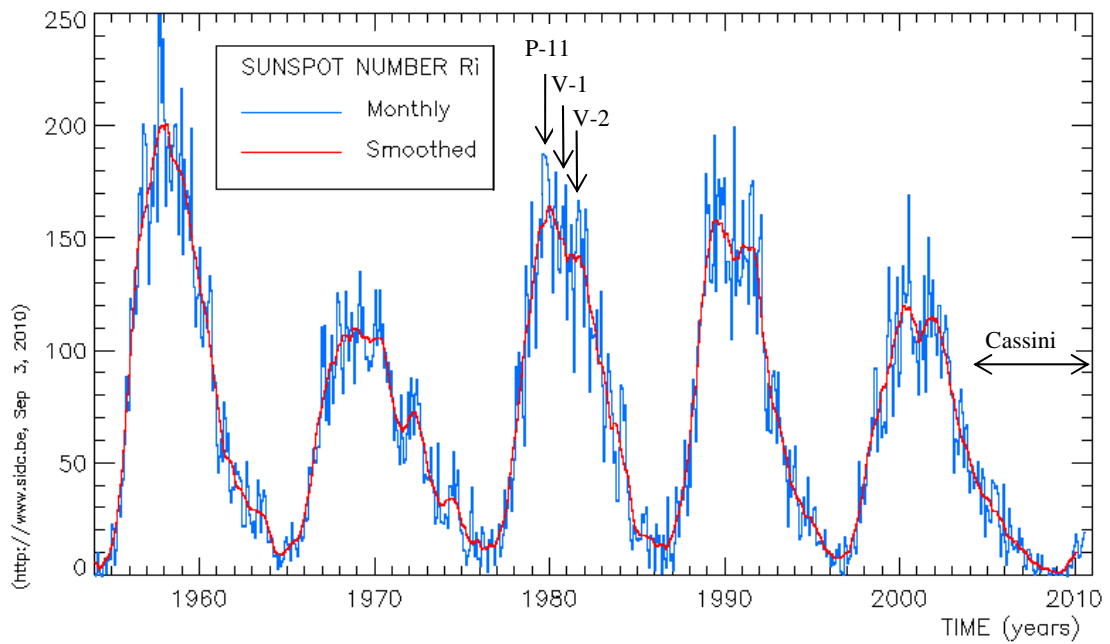


Figure 1.3. The monthly (blue) and monthly smoothed (red) sunspot numbers for the last five solar cycles. The Pioneer-11, Voyager-1 and -2 flybys of Saturn are marked by the vertical black arrows. The Cassini orbital tour from 2004-2010 is indicated by the horizontal black line. [Adapted from an image courtesy of Solar Influences Data Analysis Center.]

1.3.1 – Frozen-in Flow

The solar wind travels at supersonic speeds and carries with it a remnant of the Sun's magnetic field, called the interplanetary magnetic field (IMF), i.e. the field is frozen-in to the plasma. In order to understand the transport of field lines and plasma we must derive an expression for the 'motion' of the magnetic field.

First we consider the motion of a single particle in a magnetic field of strength \mathbf{B} . The force acting on the particle is given by

$$\mathbf{F} = q\mathbf{v} \wedge \mathbf{B} , \quad (1.1)$$

where q and \mathbf{v} are the charge and velocity of the particle respectively. This force (called the Lorentz force) always acts in a direction perpendicular to \mathbf{v} and \mathbf{B} . The resultant motion of the particle is a gyration around the field line, as well as a drift along the field line. For a particle of mass m , and charge q , in a magnetic field of strength B , the angular frequency of the circular motion (known as the gyrofrequency or cyclotron frequency) is given by

$$\Omega = \frac{qB}{m} , \quad (1.2)$$

with a radius of gyration (called the gyroradius or Larmor radius) given by

$$r_L = \frac{v_{\perp}}{\Omega} = \frac{mv_{\perp}}{qB} , \quad (1.3)$$

where v_{\perp} is the particle's velocity perpendicular to the field. The radius of this circular motion thus depends on the particle's energy, while the sense depends on the charge, with electrons moving in a right-handed direction about the field line, while ions move in a left-handed direction. So the charged particle will gyrate around the magnetic field according to the perpendicular component of its velocity and drift parallel to the field according to its initial parallel velocity, resulting in a helical motion of the particle along the magnetic field line. If there is an electric field (\mathbf{E}) present that is perpendicular to \mathbf{B} , then the charged particle will experience an $\mathbf{E} \wedge \mathbf{B}$ drift (in a direction perpendicular to both \mathbf{E} and \mathbf{B}) as well. This drift velocity is given by

$$\mathbf{v}_d = \frac{\mathbf{E} \wedge \mathbf{B}}{B^2} . \quad (1.4)$$

The presence of an electric field acts to accelerate the particle during half of its gyratory orbit and decelerate it during the other half of its orbit. The result is a distorted circle

(with a larger radius of curvature during half the orbit, and a smaller radius of curvature in the remaining half of the orbit) and a drift of the particle in a direction perpendicular to \mathbf{E} and \mathbf{B} . Since the $\mathbf{E} \wedge \mathbf{B}$ drift velocity is independent of m and q , the drift is in the same direction for both electrons and ions, and so the $\mathbf{E} \wedge \mathbf{B}$ drift does not generate a current in a charge-neutral plasma.

Alfvén's frozen-in theorem states that particles and a field are 'frozen-in' if the particles on a field line experience these motions (gyratory, a drift parallel to the field, and an $\mathbf{E} \times \mathbf{B}$ drift) only. If the particle gyrocentres lie on a particular field line at some initial time, then as the particles move, their gyrocentres remain on the same field line as each other for all other times. Whether the plasma is best regarded as frozen to the magnetic field, or the magnetic field to the plasma, depends on the relative energies of the field and particles ($\frac{B^2}{2\mu_0}$ and $\frac{1}{2}\rho v^2$ respectively). If the plasma energy dominates, it can be regarded as carrying the field with it. If the field energy dominates, we think instead of the field lines moving, carrying the plasma. Either approach is in any case entirely equivalent.

We can determine if the plasma and field are frozen in as follows. Firstly we must consider a simplified form of Ohm's law for a plasma with a finite conductivity σ ,

$$\mathbf{E} + \mathbf{v} \wedge \mathbf{B} = \frac{\mathbf{j}}{\sigma}, \quad (1.5)$$

where \mathbf{j} is the current density. Re-arranging and substituting into Faraday's law, $\text{curl}\mathbf{E} = -\frac{\partial\mathbf{B}}{\partial t}$, yields

$$\frac{\partial\mathbf{B}}{\partial t} = \nabla \wedge \left(\mathbf{v} \wedge \mathbf{B} - \frac{\mathbf{j}}{\sigma} \right).$$

We can substitute for \mathbf{j} using Ampère's law, $\text{curl}\mathbf{B} = \mu_0\mathbf{j}$, where we neglect the displacement current (a valid approximation when the plasma speed is much less than the speed of light). This gives

$$\frac{\partial\mathbf{B}}{\partial t} = \nabla \wedge (\mathbf{v} \wedge \mathbf{B}) - \frac{\nabla \wedge (\nabla \wedge \mathbf{B})}{\mu_0\sigma}.$$

Using the vector identity $\nabla^2 \mathbf{A} = \nabla(\nabla \cdot \mathbf{A}) - \nabla \wedge (\nabla \wedge \mathbf{A})$ we have

$$\frac{\partial \mathbf{B}}{\partial t} = \nabla \wedge (\mathbf{v} \wedge \mathbf{B}) + \frac{\nabla^2 \mathbf{B}}{\mu_0 \sigma} - \frac{\nabla(\nabla \cdot \mathbf{B})}{\mu_0 \sigma} .$$

Since $\nabla \cdot \mathbf{B} = 0$ (no magnetic monopoles) we then have

$$\frac{\partial \mathbf{B}}{\partial t} = \nabla \wedge (\mathbf{v} \wedge \mathbf{B}) + \frac{\nabla^2 \mathbf{B}}{\mu_0 \sigma} , \quad (1.6)$$

which is the induction equation and describes the ‘motion’ of the magnetic field. The first term on the right hand side is the convective transport term, which represents how the field and plasma move together under the action of the $\mathbf{E} \wedge \mathbf{B}$ drift. The second term is the diffusion term. Equation (1.6) can be re-written in approximate dimensional form as

$$\frac{B}{\tau} = \frac{vB}{L} + \frac{B}{L^2 \mu_0 \sigma} ,$$

where B is the average magnetic field strength, τ is the characteristic time of magnetic field variations, v is the average plasma velocity, and L is the characteristic scale length. The ratio of the convective transport and diffusion terms is known as the magnetic Reynolds number, R_m , and is given by

$$R_m = \mu_0 \sigma v L . \quad (1.7)$$

If L and σ are large, as in the solar wind, then $R_m \gg 1$ ($R_m \sim 7 \times 10^{16}$ in the solar wind [Baumjohann and Treumann, 1997]) and the transport term dominates (i.e. the field and plasma are frozen together). When $R_m \ll 1$ the diffusion term dominates and the frozen-in approximation breaks down. Thus, the field can diffuse through the plasma and reconnection can occur, as will be discussed below.

In terms of individual particle drifts, the frozen-in approximation breaks down if the particles experience other motions, for example due to a gradient in the magnetic field strength, or a curvature of the magnetic field lines. If there is a change in the magnetic field strength across the field (in the direction perpendicular to \mathbf{B}) on a distance scale comparable with the gyroradius, then a drift velocity is produced. As the particle gyrates, it will experience a stronger field on one side of its orbit than the other. This causes its gyroradius to be increased where the field has smaller values and decreased where the field has larger values, resulting in a drift of the particle in a direction perpendicular to the magnetic field and its gradient. This is the gradient drift, the drift velocity of which is given by

$$\mathbf{V}_{\nabla B} = \frac{mv_{\perp}^2}{qB^2} \frac{(\mathbf{B} \wedge \nabla B)}{B}, \quad (1.8)$$

A curvature of the magnetic field lines will cause the particles to experience a centrifugal acceleration as they move along the field. This gives rise to the curvature drift, the drift velocity of which is given by

$$\mathbf{V}_{curv} = \frac{mv_{\parallel}^2}{qB^2} \frac{\mathbf{R}_C \wedge \mathbf{B}}{R_C^2} \quad (1.9)$$

where \mathbf{R}_C is the local radius of curvature.

Both the gradient and curvature drift velocities are dependent on the charge of the particle, meaning that ions and electrons will move in opposite directions, therefore generating a current. At the Earth, electrons drift eastwards and protons drift westwards, resulting in an azimuthal current known as the ring current. Since the gradient and curvature drift velocities are also proportional to particle energy, the higher energy particles will experience stronger gradient and curvature drifts than the $\mathbf{E} \wedge \mathbf{B}$ drift and so the frozen-in approximation is more likely to break down.

1.4 – Effects of solar wind propagation

The solar wind and the frozen-in IMF propagate away from the Sun and into interplanetary space. While the outflow of plasma is near-purely radial, the foot of each field line remains frozen to the surface of the rotating Sun. This combination of radial plasma outflow and solar rotation causes the field lines to become wound into a spiral, known as the Parker spiral (since it was first described by Parker in 1958). Figure 1.4 shows this effect for a typical solar wind speed of 400 km s^{-1} .

Around solar minimum the Sun's magnetic field is approximately dipolar and aligned with the spin axis, so the radial component of the field is oppositely directed in each hemisphere (e.g. away from the Sun in the northern hemisphere and towards the Sun in the southern hemisphere). This gives rise to a thin current sheet, called the heliospheric current sheet (HCS) located across the equatorial plane. When the Sun's dipole axis is then tilted with respect to its spin axis (the angle of tilt generally decreases with decreasing solar activity) the HCS undulates in and out of the ecliptic plane as the

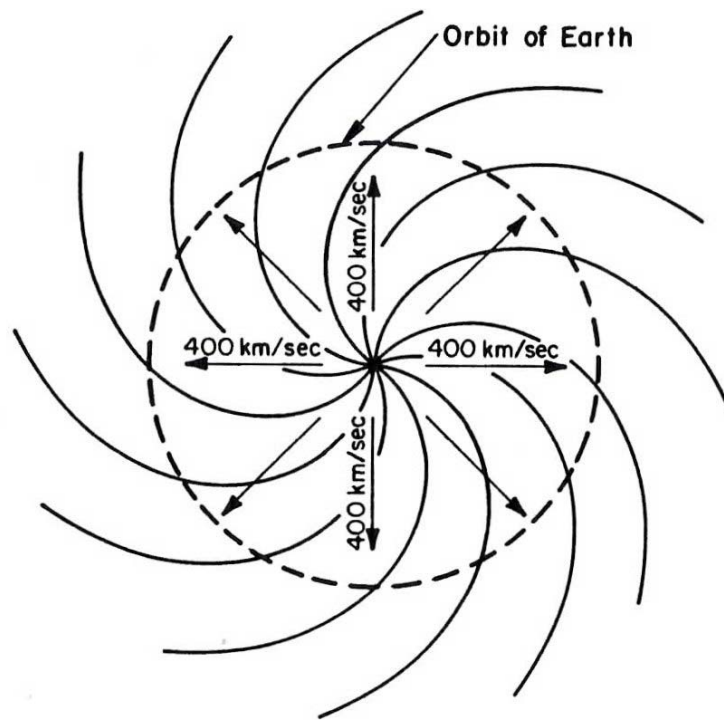


Figure 1.4. The Parker spiral configuration for a solar wind speed of 400 km s^{-1} . The solid black lines show the magnetic field lines, which become more tightly wound as heliocentric distance increases. [From *Hundhausen*, 1995.]

Sun rotates [Gosling and Pizzo, 1999]. An artist's impression of the HCS is shown in Figure 1.5. Around solar maximum the Sun's magnetic field is more disordered and so the structures of both the Parker spiral and the HCS are more complex.

1.4.1 – Corotating Interaction Regions (CIRs)

The solar wind is composed of fast and slow regions of flow, which originate from different regions on the Sun. The slow solar wind has a velocity of $\sim 400 \text{ km s}^{-1}$, while the fast solar wind has a velocity of $\sim 750 \text{ km s}^{-1}$. If we assume the Sun has a dipolar magnetic field, then near the magnetic equator the magnetic field is strong and in the north-south direction (i.e. approximately parallel to the Sun's surface). Here, the coronal plasma is trapped on closed field lines, forming dense bright arcades. Further away from the Sun the field weakens sufficiently for the plasma pressure to force the field loops open, resulting in a dense, slow solar wind that streams away from the Sun. Near the poles of the Sun, the magnetic field is more radial and the plasma escapes more easily from funnel-like regions of open field lines, called coronal holes, to form the tenuous, fast solar wind [Gosling and Pizzo, 1999]. Around solar minimum the emission of the slow solar wind occurs mainly around the equator, however, by the time of solar maximum the poles are also emitting a slow solar wind. Since both fast and slow solar wind can flow from similar magnetic latitudes, it is possible to have both fast and slow solar winds propagating into any one radial direction at differing times. When a region of fast solar wind follows a region of slow solar wind, the fast solar wind catches up and runs into the slow solar wind forming a compression region as the flow speed increases. The field strength and plasma density are also increased in these regions. Rarefaction regions, in which the field strength and plasma density are reduced, form when slow solar wind follows fast solar wind and the flow speed decreases. At Saturn the solar wind dynamic pressure is $\sim 0.01 \text{ nPa}$ during rarefactions and $\sim 0.1 \text{ nPa}$ during compressions, with corresponding variations of the IMF strength from $\sim 0.1 \text{ nT}$ during rarefactions to $\sim 1 \text{ nT}$ during compressions [Mitchell *et al.*, 2009b]. Although the solar wind plasma moves radially outward, the compression and rarefaction regions approximately corotate with the Sun, and are therefore called corotating interaction regions (CIRs). The pattern of interaction that develops in the solar equatorial plane is illustrated in Figure 1.6 where the spirals represent magnetic field lines.

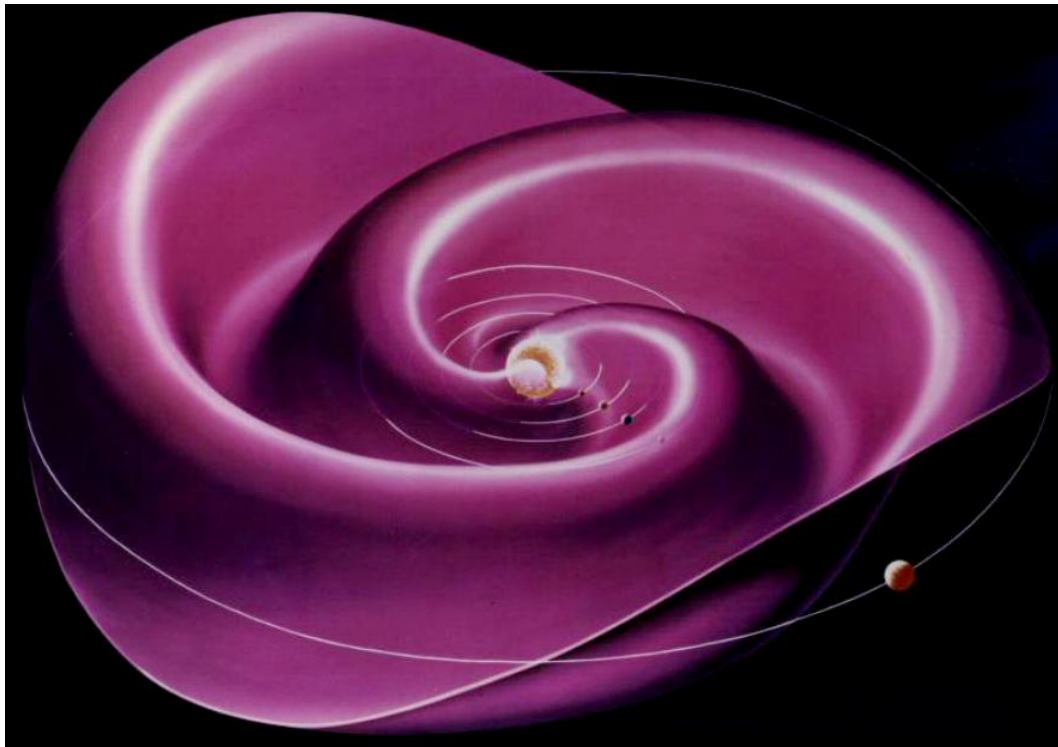


Figure 1.5. An artist's impression of the heliospheric current sheet configuration in interplanetary space. [Courtesy NASA.]

1.5 - Planetary magnetospheres

We now consider the interaction of the solar wind and IMF with a magnetised body such as a planet. A magnetosphere is a magnetic cavity in the solar wind which contains and is controlled by the planet's internally-generated magnetic field. Within our solar system there are six planets (Mercury, Earth, Jupiter, Saturn, Uranus, and Neptune) and one moon (Ganymede) that are known to possess intrinsic magnetic fields. Although the physical mechanism that shapes the magnetosphere is the same for all planets, planetary magnetospheres can be different depending on the magnetic moment of the planet, its rotation rate, plasma sources and sinks, and the local solar wind properties depending on distance from the Sun. The relative sizes of the planetary magnetospheres are shown in Figure 1.7, and some noteworthy planetary parameters for the Earth and Saturn are given in Table 1.2. Saturn has the second largest magnetosphere in the solar system, which will be discussed in more detail in Chapter 2. Chapman and Ferraro first introduced the concept of a closed magnetosphere in 1931 by application of the frozen-in condition to the solar wind-planetary field interaction. According to Alfvén's frozen-in theorem, the solar wind plasma is frozen to the IMF and the planetary plasma is frozen to the planetary field. Therefore, when the solar wind encounters a magnetosphere the plasma populations and their associated magnetic fields cannot mix. As a consequence of Ampère's law a thin current sheet, called the magnetopause, forms at the boundary between the two. A closed magnetosphere is formed, as shown in Figure 1.8. The solar wind is then deflected around the magnetosphere. Since the solar wind is supersonic, a bow shock is formed upstream of the magnetosphere, shown by the black dashed line in Figure 1.8. Across the shock, solar wind plasma is slowed, compressed and heated, forming a turbulent region of plasma, called the magnetosheath, between the bow shock and the magnetopause.

The pressure of the impinging solar wind compresses the magnetosphere on the dayside until pressure balance is achieved between the internal (planetary) and external (solar wind) pressures. Using a simple analysis we can calculate the distance at which this pressure balance is achieved, i.e. the magnetopause stand-off distance at the

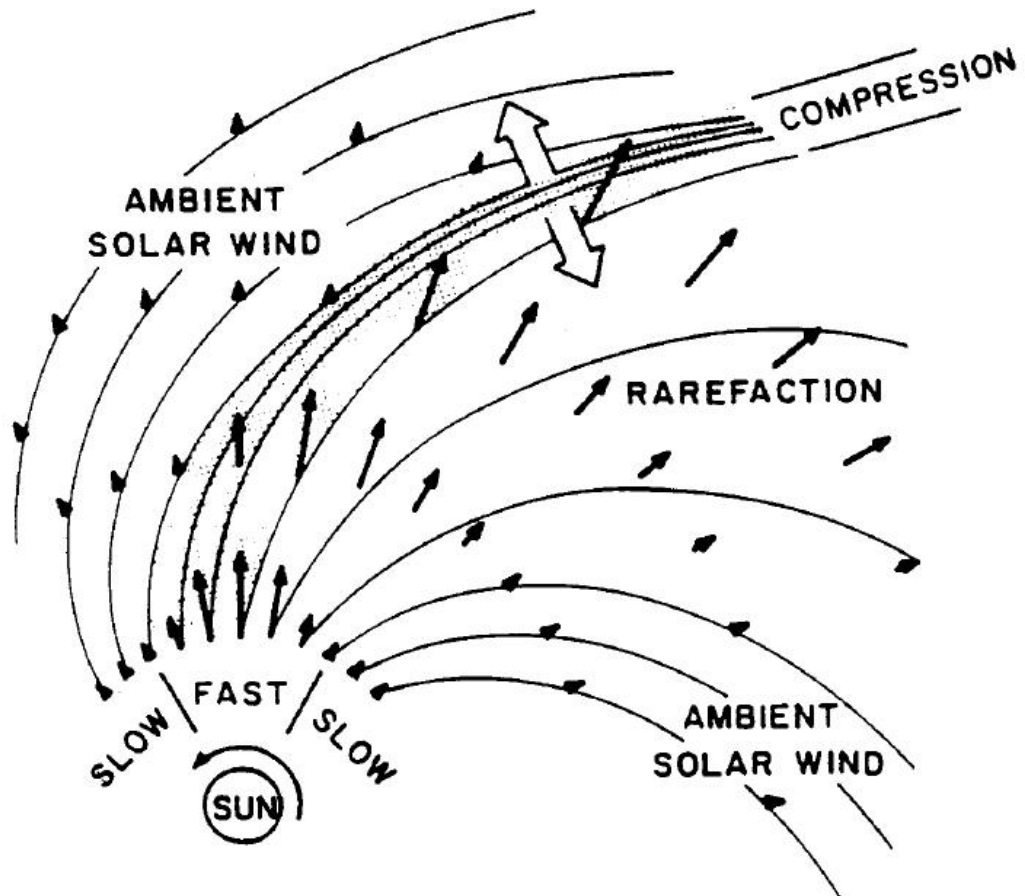


Figure 1.6. A schematic illustrating the evolution of a corotating interaction region in the solar equatorial plane. The solid black lines represent magnetic field lines, while the black arrows show the radial outflow of the solar wind plasma. [From *Gosling and Pizzo, 1999.*]

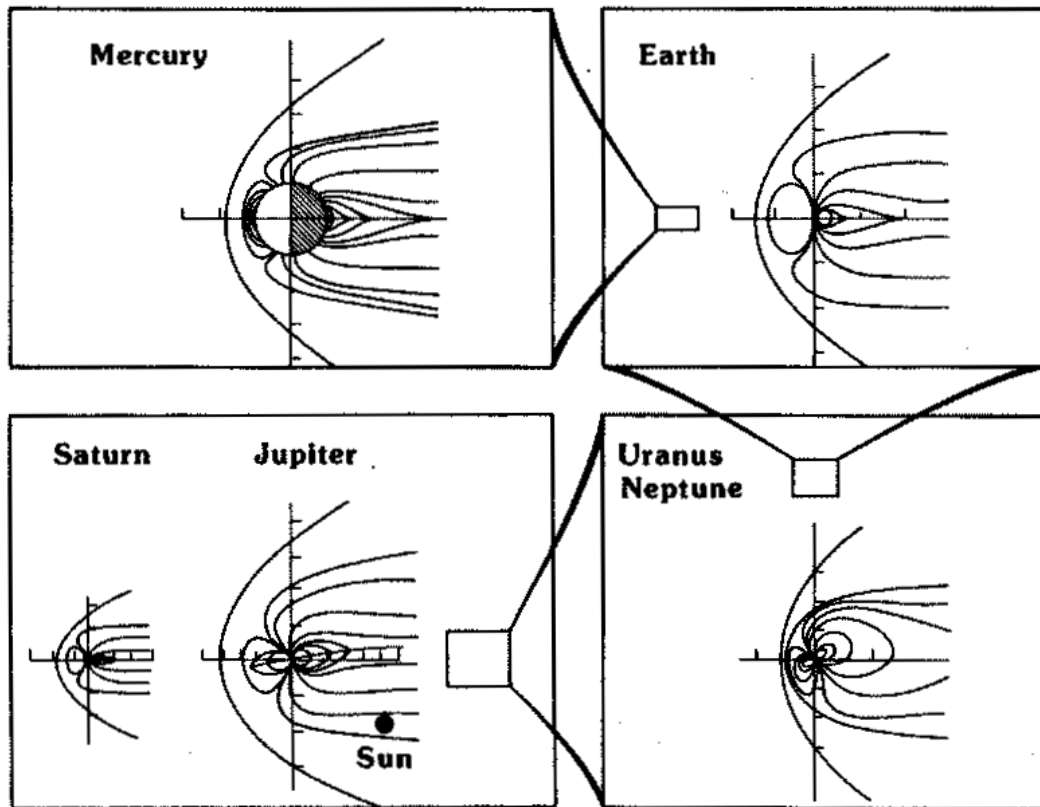


Figure 1.7. Comparison of the sizes of planetary magnetospheres in our solar system.
 [From *Russell and Walker*, 1995.]

Planetary parameters	Earth	Saturn
Mean radius (km)	6371 ⁽¹⁾	58232 ⁽¹⁾
Equatorial radius (km)	6378	60268 ⁽²⁾
Polar radius (km)	6357	54364 ⁽²⁾
Rotation period (hr)	24	10.59 ⁽³⁾ *
Dipole tilt (°)	10.5	< 1 ⁽⁴⁾
Equatorial surface field strength (nT)	31000	21100 ⁽⁵⁾
Magnetopause stand-off distance (R_{planet})	$\sim 10 R_{\text{E}}$ ⁽⁶⁾	$\sim 22 R_{\text{S}}$ ⁽⁷⁾
Bow shock stand-off distance (R_{planet})	$\sim 15 R_{\text{E}}$ ⁽⁸⁾	$\sim 25\text{-}30 R_{\text{S}}$ ^(9, 10)

Table 1.2. Planetary parameters for the Earth and Saturn.

(1) NASA

(2) *Trauger et al.* [1998]

(3) *Anderson and Schubert* [2007]

(4) *Smith et al.* [1980]

(5) *Dougherty et al.* [2005]

(6) *Sibeck et al.* [1991]

(7) *Arridge et al.* [2006]

(8) *Peredo et al.* [1995]

(9) *Achilleos et al.* [2006]

(10) *Masters et al.* [2008]

* It should be noted that Saturn's rotation rate is variable; different rotation rates depending on latitude and multiple rotation periods have been assigned to various regions.

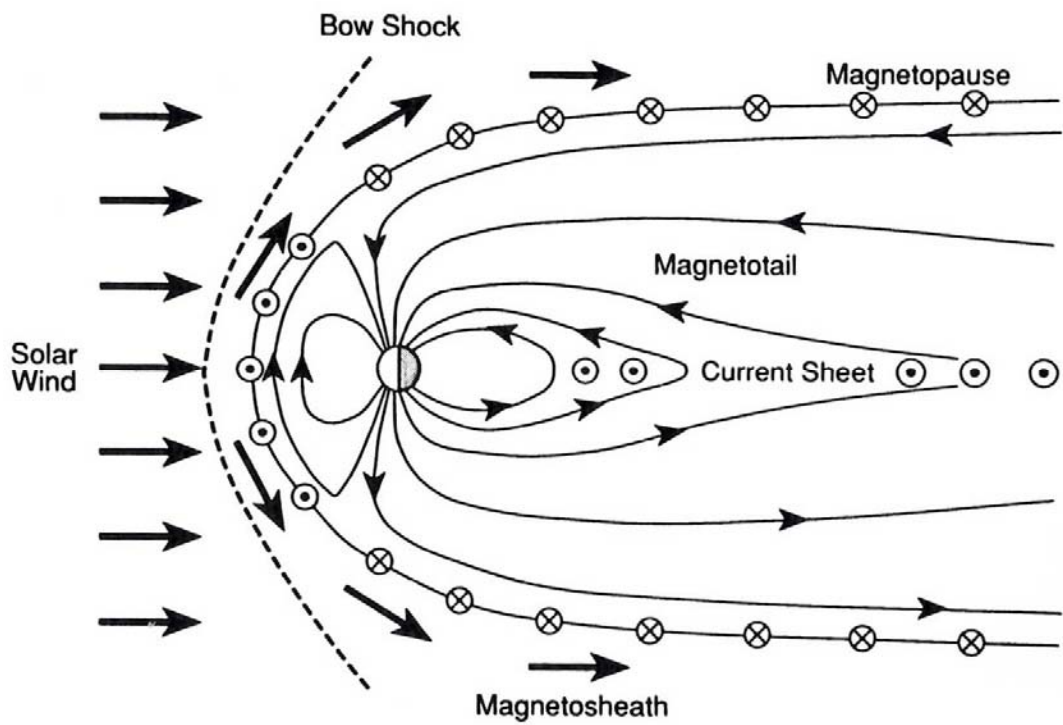


Figure 1.8. A schematic of a closed magnetosphere in the noon-midnight meridian for the case of the Earth. The solar wind impinges on the left (thick black arrows) and is deflected by the bow shock (black dashed line), forming the magnetosheath. The planetary magnetic field lines are shown by the thin solid black lines, and the IMF is directed southwards. The directions of the magnetopause and magnetotail currents are represented by the circled dots (duskward) and crosses (dawnward). [From *Hughes*, 1995.]

subsolar point $\left(\frac{R_{MP}}{R_p}\right)$, where R_{MP} is the magnetopause stand-off distance and R_p is the planetary radius.

The total solar wind pressure is dominated by the dynamic pressure (while the thermal and magnetic pressures make minor contributions) given by

$$P_{SW} = 2\rho V^2. \quad (1.10)$$

The pressure of the planetary magnetic field at the magnetopause is given by

$$P_{MP} = \frac{B_{MP}^2}{2\mu_0},$$

where the field strength at the magnetopause, $B_{MP} = 2B_{dipole} = 2B_{eq}\left(\frac{R_p}{R_{MP}}\right)^3$.

Therefore,

$$P_{MP} = \frac{2B_{eq}^2}{\mu_0}\left(\frac{R_p}{R_{MP}}\right)^6. \quad (1.11)$$

Pressure balance occurs when $P_{SW} = P_{MP}$, so combining equations (1.10) and (1.11) gives

$$\frac{R_{MP}}{R_p} = \left(\frac{B_{eq}^2}{\mu_0\rho V^2}\right)^{1/6}. \quad (1.12)$$

Using equation (1.12) and values for the Earth and Saturn obtained from Tables 1.1 and 1.2, we obtain $R_{MP} \sim 8.4 R_E$ and $\sim 16 R_S$ for the Earth and Saturn respectively. In reality, a full analysis would include the effects of the magnetospheric plasma and internal plasma currents, which both act to push the boundary further out.

On the nightside, the magnetosphere extends into a long magnetotail where the field lines are stretched out by processes described in the following sections.

1.5.1 – Reconnection

A direct consequence of the frozen-in approximation is that thin current sheets form at the boundary between different plasma and field regions, e.g. the magnetopause, as mentioned above. Ampère's law requires a current to flow at these boundaries since

there are large gradients in both strength and direction between the interplanetary and planetary magnetic fields. A similar current sheet is formed in the magnetotail between the northern and southern tail lobes. These current sheets are shown in Figure 1.8. Their direction at the magnetopause depends on the orientation of the planetary field and the IMF and are indicated by the circled dots (outward, towards dusk) and crosses (inward, towards dawn).

We now consider the magnetopause current sheet, shown by the grey shaded region in Figure 1.9a. In regions where the IMF has a component anti-parallel to the planet's field, the current sheet has a short scale length in one direction (i.e. its width), which leads to a small magnetic Reynolds number, and therefore to a potential break down of the frozen-in approximation. The diffusion term dominates in the induction equation (equation 1.6) and the magnetic field lines diffuse into the current sheet (Figure 1.9b). Magnetic reconnection can then occur. The magnetic field lines 'break' and then 'reconnect' with each other. These newly reconnected field lines are highly kinked, and will be subject to a magnetic tension force that acts to straighten them out. This action accelerates the field lines away from the reconnection site, allowing more field lines to diffuse into the current sheet and undergo reconnection (Figure 1.9c). The reconnection process that occurs at the magnetopause is the starting point of a cyclical flow within the magnetosphere (called the Dungey cycle) which is discussed below.

1.5.2 – The Dungey cycle

Figure 1.10 shows the Dungey cycle, a solar wind-driven magnetospheric convection process that is present at both the Earth and Saturn. The numbered lines in Figure 1.10 show the succession of configurations planetary field line 1 assumes after reconnection at the dayside magnetopause with IMF field line 1'. Reconnection at the magnetopause produces planetary field lines that are 'open', meaning they are connected to the planet at one end while the other end is in the solar wind. Solar wind plasma can now enter the magnetosphere, thus enabling the transfer of mass, momentum, and energy from the solar wind to the planetary magnetosphere. The newly opened field line is then transported anti-sunward by the solar wind flow (lines 2-5), forming an extended magnetotail. On the nightside of the planet, the field line sinks towards the centre of the magnetotail, and reconnection occurs in the tail current sheet (line 6). Without this

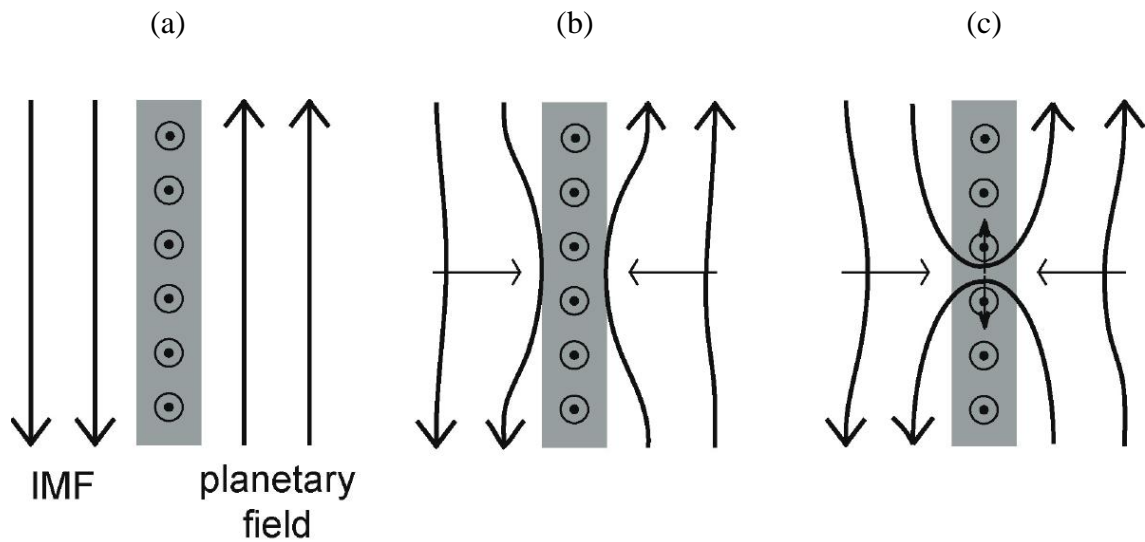


Figure 1.9. A schematic showing the reconnection process between oppositely directed IMF and planetary magnetic field lines. (a) The current sheet between the two fields is represented by the grey shaded region. (b) As the frozen-in approximation breaks down, the fields are able to diffuse into the current sheet. (c) The field lines break and reconnect with each other. They then accelerate away from the reconnection region. [Courtesy of S.V. Badman, ISAS/JAXA.]

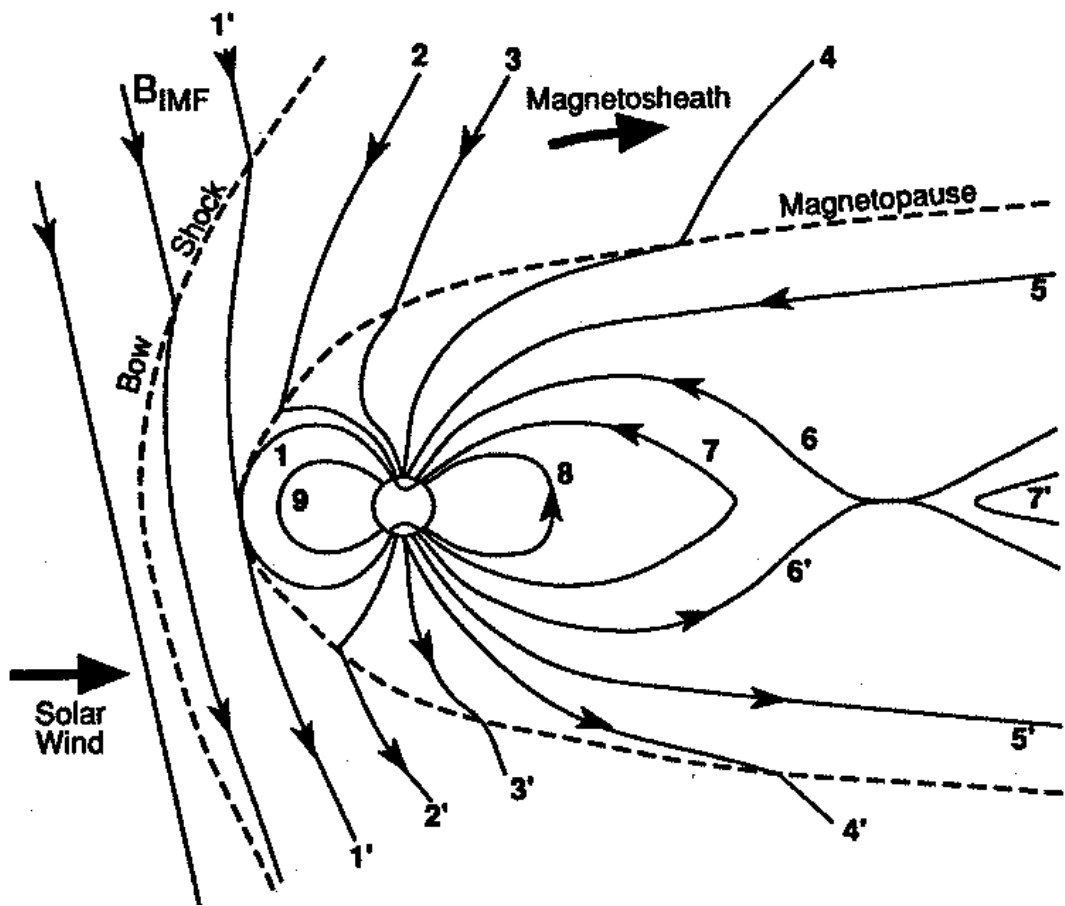


Figure 1.10. A schematic of the open magnetosphere for the case of the Earth. The solar wind flow is from left to right and is represented by the thick black arrows. The thin solid black lines show the interplanetary (IMF) and planetary magnetic field lines. The numbered field lines show the changing configuration of a planetary magnetic field line (labelled 1) following reconnection at the dayside magnetopause with an IMF field line (labelled 1'). [From *Hughes*, 1995.]

second reconnection point the entire planetary magnetic field would become connected to the interplanetary magnetic field. The newly closed field line then flows towards the planet (lines 7 and 8), and convects around either the dawn or dusk side of the planet back to the dayside (line 9), thus completing its cycle.

Although the Dungey cycle is the dominant magnetospheric driving mechanism at the Earth, the fast rotation of the outer planets, such as Saturn, along with the pressure exerted by internal sources, can cause internal processes to dominate the magnetospheric circulation.

1.5.3 – Effects of planetary rotation

As a planet rotates, the magnetic field and plasma inside the magnetosphere will rotate around with it, provided there are no other forces acting. This corotation is a consequence of collisions between ions and neutrals in the ionised upper atmosphere (ionosphere). These collisions impart momentum to the ions and are so frequent that, in the lower ionosphere at least, the ions are essentially forced to move with the atmosphere. Since the magnetic field is frozen in to the ions in the atmosphere, it will also corotate with the planet. The magnetospheric plasma above the atmosphere is in turn frozen to the magnetic field and so this also corotates. The result is a transfer of angular momentum up the magnetic field into the magnetospheric plasma, causing it to rotate with the planet. At larger radial distances ($>4 R_S$ at Saturn), the magnetospheric plasma diffuses outwards (due to centrifugal forces) and slows to ensure that angular momentum is conserved. As a result, the frozen-in field lines are stretched radially outwards, more on the nightside than the dayside since the dayside magnetosphere is constrained by the pressure of the impinging solar wind. Compared to the case of the Earth, the rapid rotation of the outer planets has a strong influence on their magnetospheric dynamics. The presence of mass sources inside the magnetosphere (e.g. Saturn's rings and icy moons), however, can affect the extent to which the magnetic field (and plasma) corotate.

1.5.4 – Combined effect of solar wind-driven convection and corotation

Given that the flow in the magnetosphere is influenced both by the solar wind interaction and by planetary rotation, it is important to assess which effect is the most important. Here we combine simple models of these flows to determine whether a planetary magnetosphere is dominated by solar wind-driven flows or by corotation with the planet. First we consider the solar wind-driven convection (i.e. the Dungey cycle). In the equatorial plane, the Dungey cycle flow is directed from the magnetotail towards the dayside (in the X direction). The magnetic field \mathbf{B} points in the Z direction e.g. for the case of the Earth (up and out of the equatorial plane, along the magnetic axis), so the electric field \mathbf{E} associated with this flow is in the Y direction (from dawn to dusk). If we assume the simple case where \mathbf{E} is constant in the equatorial plane such that $|\mathbf{E}| = E_0$ then we can write $\mathbf{E}_{conv} = E_0 \hat{\mathbf{y}}$.

Thus,

$$\mathbf{V}_{conv} = \frac{\mathbf{E}_{conv} \wedge \mathbf{B}}{B^2} = \frac{E_0}{B} \hat{\mathbf{y}} \wedge \hat{\mathbf{z}} = \frac{E_0}{B} \hat{\mathbf{x}}$$

where $\mathbf{B} = B_{eq} \left(\frac{R_p}{r} \right)^3 \hat{\mathbf{z}}$.

We thus have

$$\mathbf{V}_{conv} = \frac{E_0}{B_{eq}} \left(\frac{r}{R_p} \right)^3 \hat{\mathbf{x}},$$

where the flow is directed towards the Sun.

We now consider the corotation flow. If the plasma and field rotate exactly with the angular velocity of the planet ω_p , then everywhere in the equatorial plane the corotation velocity can be expressed as

$$\mathbf{V}_{corot} = r \omega_p \hat{\boldsymbol{\phi}},$$

where r is the radial distance and $\hat{\boldsymbol{\phi}}$ is the azimuthal unit vector in the direction of planetary rotation.

We can now vectorially combine the convection and corotation velocities to determine the total flow. Since $|\mathbf{V}_{corot}| \propto r$ and $|\mathbf{V}_{conv}| \propto r^3$ we can see that corotation dominates at small radial distances and convection at larger radial distances. On the

dawn meridian the corotation and convection flows are in the same direction. However, on the dusk meridian the flows are oppositely directed. Here there will be a point where $V = 0$, i.e. a stagnation point, at a radius R_{SP} . For $r < R_{SP}$ the corotation flow dominates, and for $r > R_{SP}$ the convection flow dominates.

Equating the expressions for the convection and corotation velocities it is possible to determine R_{SP} .

$$|V_{conv}| = |V_{corot}|$$

$$\frac{E_0}{B_{eq}} \left(\frac{R_{SP}}{R_p} \right)^3 = R_{SP} \omega_p$$

Thus,

$$\frac{R_{SP}}{R_p} = \left(\frac{\omega_p B_{eq} R_p}{E_0} \right)^{1/2}.$$

Comparing R_{SP} with the distance to the magnetopause R_{MP} allows us to determine the relative importance of corotation and convection for a given planet's magnetosphere.

For the Earth we have $\omega_p = 7.27 \times 10^{-5} \text{ rad s}^{-1}$, $B_{eq} = 31000 \text{ nT}$, $R_p = 6371 \text{ km}$, and $E_0 = 2 \times 10^{-4} \text{ V m}^{-1}$, which gives $R_{SP} \approx 8.5 R_E$, compared with $R_{MP} \approx 10 R_E$. Thus in the Earth's magnetosphere the main flow is dominated by the convection flow (the Dungey cycle), with a modestly sized core of corotating flow. For Saturn we have $\omega_p = 1.65 \times 10^{-4} \text{ rad s}^{-1}$, $B_{eq} = 21100 \text{ nT}$, $R_p = 60268 \text{ km}$, and $E_0 = 2 \times 10^{-5} \text{ V m}^{-1}$, which gives $R_{SP} \approx 100 R_S$, compared with $R_{MP} \approx 20 R_S$. Thus in Saturn's magnetosphere, the stagnation point would lie outside the magnetopause, indicating that corotation dominates at Saturn.

1.6 – The ring current

The ring current is an electric current caused by charged particles trapped in a planet's magnetosphere. Along with their gyromotion around and periodic bouncing motion along field lines, charged particles trapped in a magnetosphere are also subject to drift motions due to the gradient and curvature of the magnetic field (as discussed in Section 1.3.1). The combined effect of this gradient and curvature drift is an azimuthal drift of particles, which is oppositely directed for ions and electrons. For the case of the Earth,

ions move westward and electrons move eastward, which results in a net westward current around the Earth, known as the ring current.

The ring current at Earth produces a southward perturbation field, which acts to decrease the strength of Earth's northward planetary field close to the planet. Although the ring current is always present at Earth, it intensifies during a magnetic storm and can therefore substantially alter the overall magnetic configuration of the magnetosphere. The ring current at Saturn is discussed further in Section 2.8.

Chapter 2

The Saturnian magnetosphere

2.1 - Introduction

In this chapter we now focus on the Saturnian magnetosphere and review our understanding of its structure and dynamics, with a particular focus on the ring current region. Surrounded by a magnificent system of rings and many moons, Saturn is one of the most awe-inspiring sights in the solar system. Figure 2.1 shows Saturn's ring structure and the relative positions of some of its moons. Saturn is the sixth planet from the Sun, orbiting at a distance of 9.5 AU, and has an orbital period of ~ 29.5 years. Saturn is the second largest planet in the solar system (after Jupiter) with a mass ~ 95 times that of the Earth. It is composed of $\sim 75\%$ hydrogen, $\sim 25\%$ helium, with traces of other heavier elements, and has an average density of 687 kg m^{-3} . Saturn's interior is believed to be similar to that of Jupiter, with a rocky core, a liquid metallic hydrogen layer and a molecular hydrogen layer (see Figure 2.2). The rapid planetary rotation rate (~ 10.59 h) generates a centrifugal force that causes the equatorial regions of the planet to bulge outwards and the poles to flatten. Saturn's equatorial diameter is $\sim 10\%$ larger than its pole-to-pole diameter (see Table 1.2). Throughout this thesis we use a planetary radius of 60268 km, herein referred to as $1 R_S$, the equatorial radius at a pressure of 1 bar. Saturn's rapid rotation rate combined with its liquid metallic hydrogen layer, generates a very large planetary magnetic field, the properties of which will be discussed in more detail in Section 2.2. Because there is a tilt of $\sim 27^\circ$ between Saturn's rotational and orbital planes, Saturn experiences seasons. The data used in this thesis were obtained during the prime phase of the Cassini mission, under conditions of southern hemisphere summer (northern hemisphere winter).

2.1.1 – Previous fly-bys

Previous to the Cassini-Huygens mission the Saturnian system had been visited by three spacecraft. Pioneer-11, Voyager-1, and Voyager-2 made fly-bys of the planet in September 1979, November 1980, and August 1981 respectively. The trajectories of these spacecraft are shown in Figure 2.3 in a view projected onto Saturn's equatorial

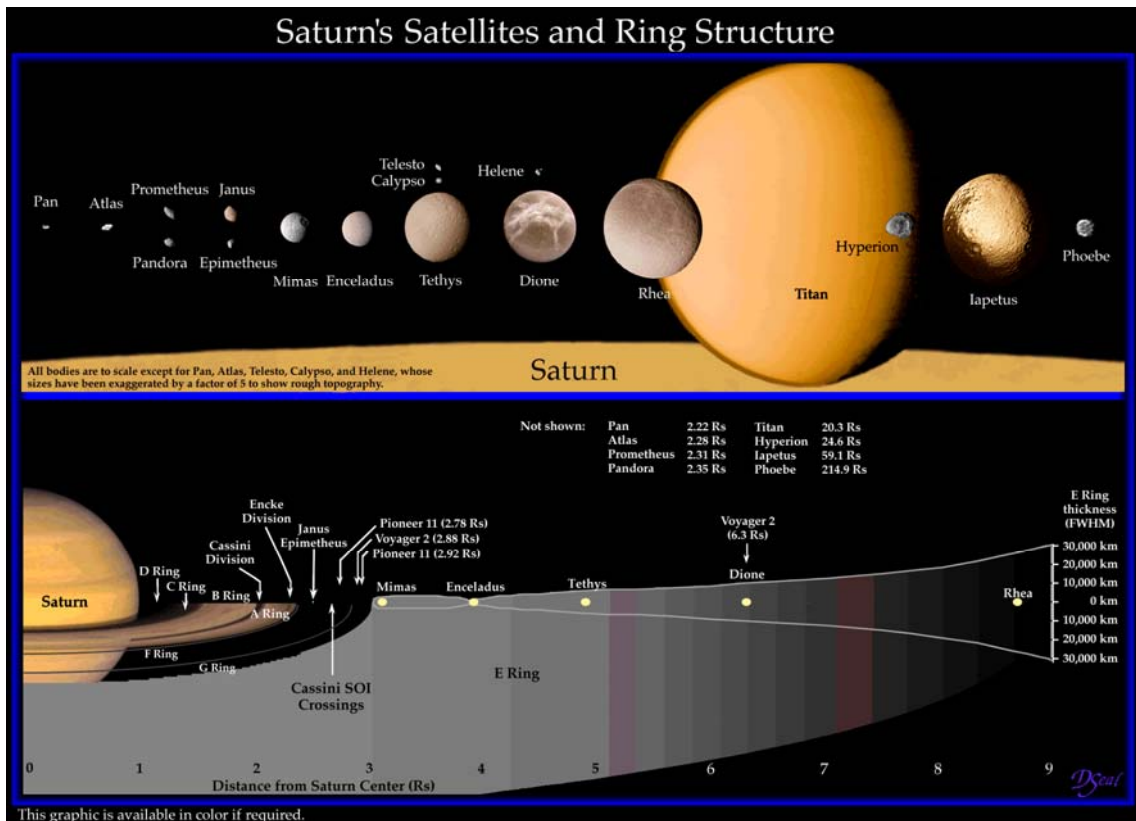


Figure 2.1. Saturn's ring structure and the relative positions of some of its moons
 [Courtesy of NASA/JPL.]

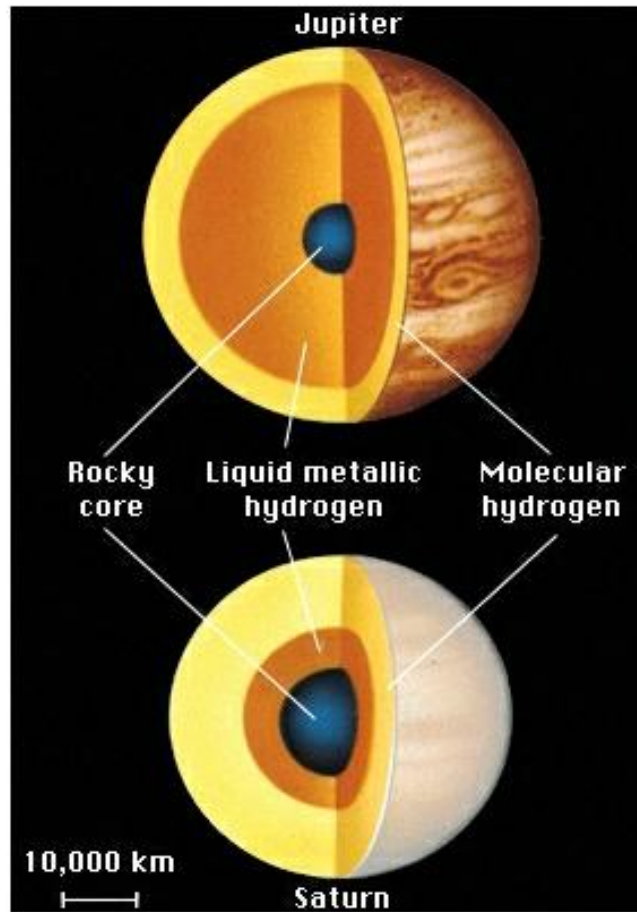


Figure 2.2. The interior structures of Jupiter and Saturn. [Courtesy of the European Southern Observatory.]

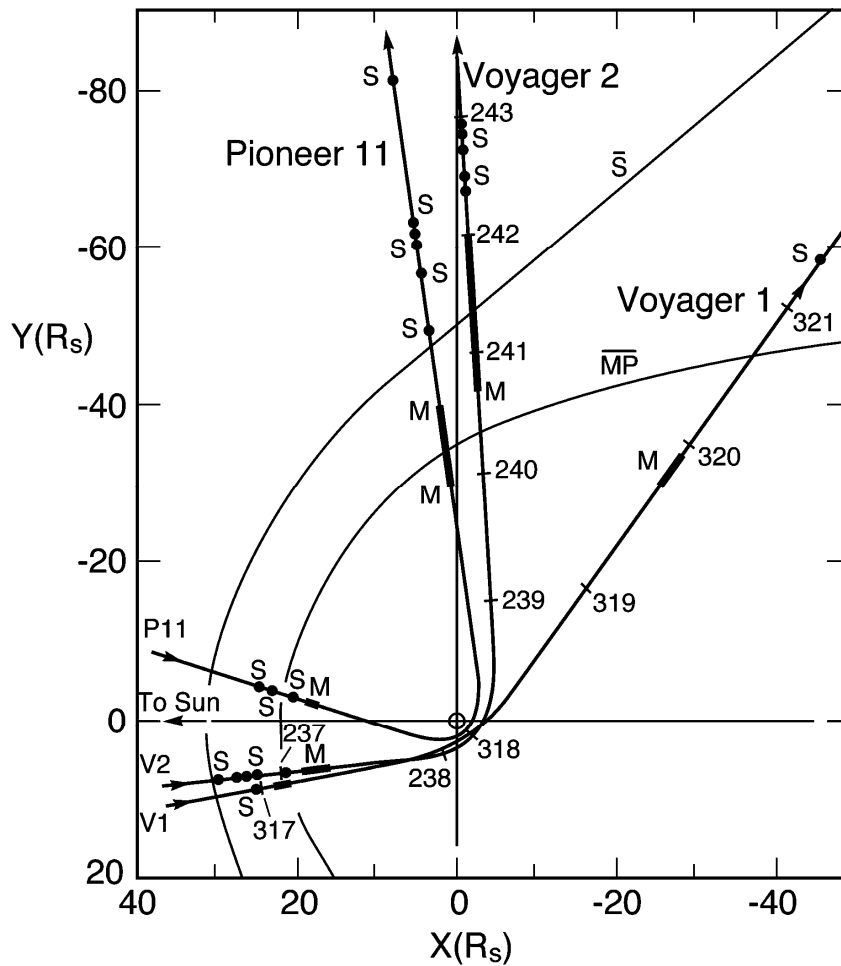


Figure 2.3. Trajectories of the Pioneer-11, Voyager-1 and Voyager-2 fly-bys of Saturn projected onto the equatorial plane. The coordinate system employed is such that X points along the Saturn-Sun line, Z is along Saturn's spin axis, and Y completes the right-handed set. Observed bow shock and magnetopause crossings are labelled S and M respectively. [From *Dougherty et al.*, 2004.]

Multipole term	Z3⁽¹⁾	SPV⁽²⁾	Cassini-SOI⁽³⁾	Burton et al.⁽⁴⁾
g_{10}	21248	21225	21084	21162
g_{20}	1613	1566	1544	1514
g_{30}	2683	2332	2150	2283

Table 2.1. Multipole terms for several models of Saturn’s intrinsic magnetic field.

(1) Z3 zonal harmonic model [*Connerney et al.*, 1982]

(2) Saturn-Pioneer-Voyager (SPV) model [*Davis and Smith*, 1990]

(3) Cassini-SOI model [*Dougherty et al.*, 2005]

(4) Most recent Cassini model of *Burton et al.* [2009]

plane. All three spacecraft entered Saturn's magnetosphere close to the noon meridian. Pioneer-11 and Voyager-2 exited nearly along the dawn meridian while Voyager-1 exited further down the tail. Although these three fly-bys of the planet only covered a limited range of local times and radial distance they still provided a useful data set for early studies of Saturn's magnetosphere. Since its arrival at Saturn in 2004, the Cassini spacecraft has significantly enhanced our knowledge of the Saturnian system by providing data over a wide range of local times, latitudes and radial distances. Cassini's ongoing orbital tour will be discussed in more detail in Chapter 3.

2.2 - Saturn's magnetic field

Saturn's intrinsic magnetic field was first detected in September 1979 by the instruments onboard the Pioneer-11 spacecraft [Acuña and Ness, 1980; Smith *et al.*, 1980]. Measurements from the three fly-bys of Pioneer-11, Voyager-1, and Voyager-2 revealed that the planetary field is primarily that of a dipole, with a magnetic moment of $\sim 21000 \text{ nT } R_S^3$ ($\sim 0.21 R_S^3 \text{ G}$) [Acuña and Ness, 1980; Smith *et al.*, 1980; Ness *et al.*, 1981, 1982]. However, the magnetometer observations from all three spacecraft also revealed quadrupole and octupole terms. Cassini observations have confirmed that the quadrupole term is equivalent to a displacement of the dipole axis by $\sim 0.037 R_S$ northward of the spin equator [Dougherty *et al.*, 2005]. The polarity of the Saturnian dipole is opposite to that of the Earth, so the field lines point southwards at the equator, i.e. magnetic north is located in the northern hemisphere, and magnetic south in the southern hemisphere. Saturn's magnetic field shows a remarkable symmetry about the spin axis of the planet with there being less than 0.1° tilt between the dipole and spin axes [Burton *et al.*, 2010]. This is a unique feature within our solar system since the other magnetised planets have significant tilts between their dipole and spin axes, e.g. the Earth has an 11.5° tilt.

2.2.1 – Magnetic field models

Several models of Saturn's intrinsic magnetic field have been developed based upon magnetic field data obtained close to periapsis. These include the Z3 zonal harmonic model [Connerney *et al.*, 1982], derived from Voyager-1 and -2 magnetometer observations, the Saturn-Pioneer-Voyager (SPV) model [Davis and Smith, 1990], which

is based on all available pre-Cassini data, and the Cassini-SOI model [Dougherty *et al.*, 2005], which uses magnetometer data obtained during Cassini's Saturn orbital insertion. In this thesis we employ the Cassini-SOI model, which is axially symmetric about Saturn's spin axis and employs dipole, quadrupole and octupole terms. The corresponding coefficients are listed in Table 2.1 along with those for the Z3 and SPV models. More recently, Burton *et al.* [2009] have derived a model of Saturn's intrinsic magnetic field using data obtained from forty-five Cassini periapsis passes spanning the interval from July 2004 to June 2007. The coefficients corresponding to this model are also shown in Table 2.1. Although we have employed the Cassini-SOI model in this thesis it should be noted that none of the results presented would be substantially altered if we had employed any of the other available models.

2.3 - Saturn's magnetosphere

Saturn's magnetosphere is the region dominated and controlled by Saturn's magnetic field. A schematic of Saturn's magnetosphere is shown in Figure 2.4. Its global configuration and dynamics are shaped not only by interactions with the solar wind and the planetary atmosphere, but also by interactions with internal plasma sources such as the planetary rings and satellites. These interactions and its unique plasma environment make it one of the most interesting planetary plasma environments in the solar system.

The Pioneer-11 and Voyager fly-by data, together with a much larger field and particle data set provided more recently by the Cassini orbiter [e.g. Dougherty *et al.*, 2005; Krimigis *et al.*, 2005; Young *et al.*, 2005; Bunce *et al.*, 2007; Schippers *et al.*, 2008; André *et al.*, 2008; Sergis *et al.*, 2009] have yielded a picture of the principal features of Saturn's magnetosphere that is sketched in Figure 2.5. This figure shows a cut through the noon-midnight meridian with the solar wind blowing from right to left, and represents the southern summer conditions that prevailed during the prime phase of the Cassini mission (2004-2008) considered in this thesis.

2.3.1 – The inner magnetosphere

Saturn's inner magnetosphere is the region within $\sim 6 R_S$, which is dominated by the strong near-dipolar magnetic field. In this region the field strength is greatest and close

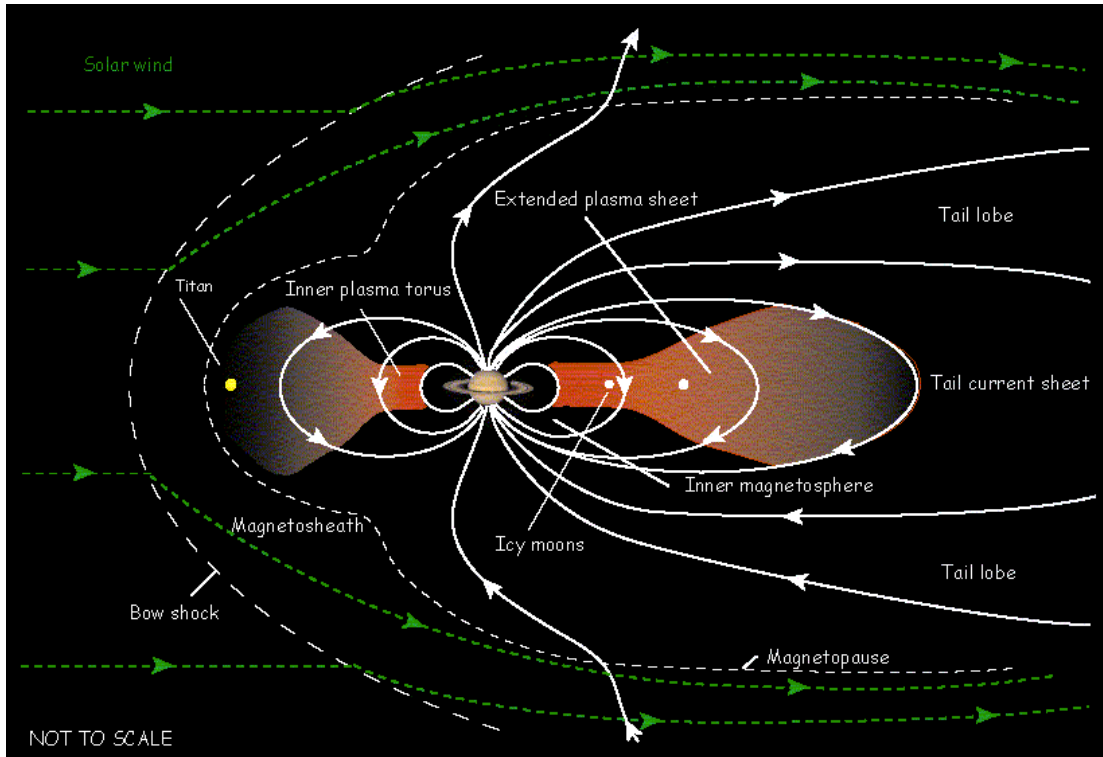


Figure 2.4. Schematic of Saturn's magnetosphere showing the planetary magnetic field lines, plasma regimes and the relative locations of some of the moons. [Courtesy of Dr. Emma Bunce, University of Leicester.]

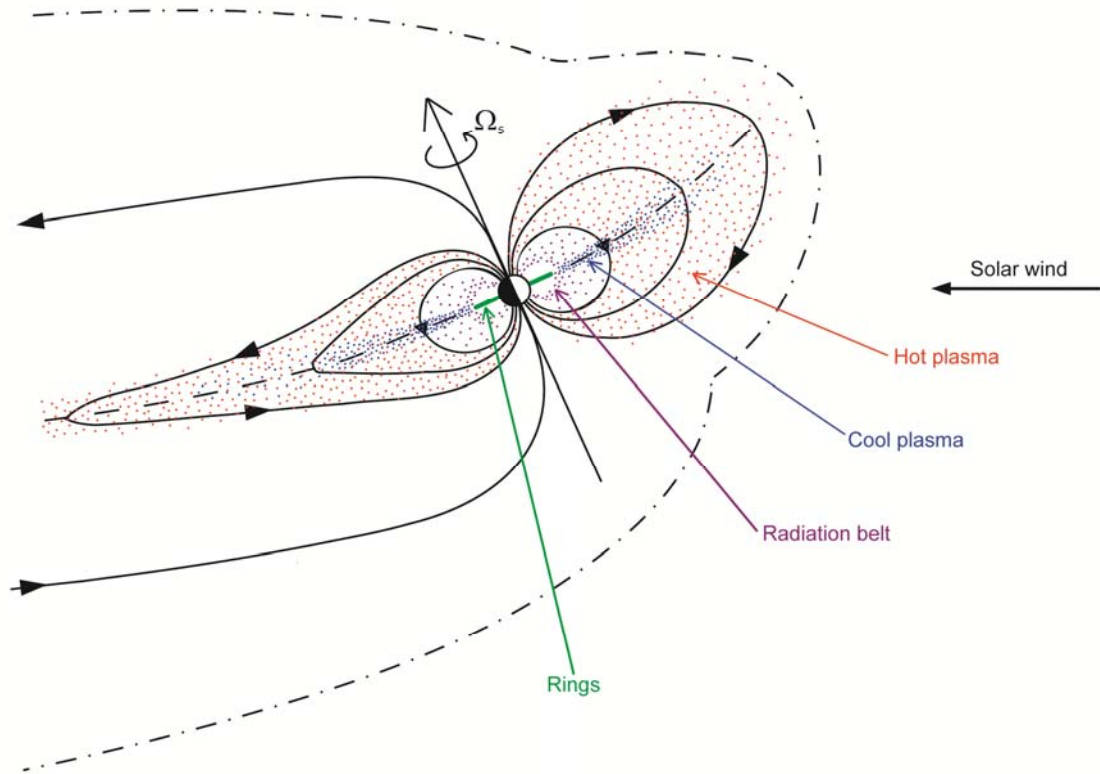


Figure 2.5. Sketch of the principal features of Saturn’s magnetosphere in the noon-midnight meridian plane for southern summer conditions, with the solar wind blowing from right to left as indicated. The outer black dot-dashed line indicates the magnetopause, extending typically to $\sim 20\text{-}25 R_S$ in the sub-solar region, depending on the dynamic pressure of the solar wind [Arridge *et al.*, 2006; Kanani *et al.*, 2010], while the interior solid black lines show magnetic field lines. The blue dotted region represents cool (~ 1 eV to a few hundreds of eV) water-group plasma which is centrifugally confined near the equatorial plane by the rotation of the plasma with the planet about the tilted spin axis. This plasma is evolved from moon sources in the inner magnetosphere and is transported radially outwards. The red dotted region represents warm and hot ($\sim \text{keV}$ to several tens of keV) plasma which is transported inwards from the outer regions to a relatively sharp inner boundary at $\sim 7 R_S$ as shown, and is more uniformly distributed along the field lines. The purple dotted region represents the inner radiation belt of high-energy particles that extends inside the boundary of the hot plasma, and is limited in the inner region by Saturn’s main ring system extending to $\sim 3 R_S$ in the equatorial plane, represented by the green lines on either side of the planet. The diagram also shows the observed displacement of the magnetic equator (dashed line; where the radial field component switches sign) northward of the spin equator in the outer magnetospheric regions on both the day and night sides of the planet, due to the solar wind flow under southern summer conditions.

to the planet the field lines corotate with the planet (due to ion-neutral collisions in the upper atmosphere). Corotation starts to break down just inside Enceladus's orbit at $\sim 3\text{-}4 R_S$ as shown by *Wilson et al.* [2009]. The plasma in the inner magnetosphere is dominated by the cool (~ 1 eV to a few tens of eV) water-group plasma (i.e. O^+ , OH^+ , H_2O^+ , and H_3O^+), which is represented by the blue dotted region in Figure 2.5. This plasma is evolved from moon sources in the inner magnetosphere (principally Enceladus) and is transported radially outwards.

Enceladus is a small (radius ~ 250 km) cryovolcanically active moon that orbits Saturn at a distance of $3.95 R_S$ and is the source of most of the water group plasma in Saturn's magnetosphere. Additional sources of water group plasma are Saturn's rings and other icy moons. Magnetic field and plasma data from the Cassini spacecraft identified an atmospheric plume of water vapour and water ice grains particles near Enceladus's south pole (see Figure 2.6) as the dominant source of water group molecules for Saturn's magnetosphere [*Dougherty et al.*, 2005; *Tokar et al.*, 2006]. The large number of micron-sized water ice grains that are ejected are the primary source of Saturn's tenuous, extended E-ring [*Porco et al.*, 2006]. The plume originates from the region of surface cracks named 'tiger stripes' (see Figure 2.7) discovered near the moon's south pole [*Porco et al.*, 2006]. The gas is typically released at a rate of $\sim 200 \text{ kg s}^{-1}$ but has been observed to be as high as $\sim 1600 \text{ kg s}^{-1}$ [*Saur et al.*, 2008 and references therein]. This forms a neutral water cloud between $\sim 2\text{-}10 R_S$ [*Jurac et al.*, 2002], the density of which peaks at Enceladus's orbital distance [*Jurac and Richardson*, 2005]. This neutral gas is eventually ionised predominantly by charge exchange and hot electron impact and picked up by the magnetic field, adding to the corotating magnetospheric plasma [*Pontius and Hill*, 2006].

2.3.2 – The middle and outer magnetosphere

At radial distances beyond $\sim 6 R_S$ the magnetic field becomes stretched and departs from the dipolar configuration it exhibits in the inner magnetosphere [*Bunce et al.*, 2008; *Carbary et al.*, 2010 and references therein]. In this region lies the extended plasma sheet that covers radial distances from ~ 7 to $\sim 15 R_S$ [*Sittler et al.*, 1983]. The extended plasma sheet is a variable region containing a mixture of cold and hot plasma populations and is the primary contributor to the equatorial ring current. The equatorial

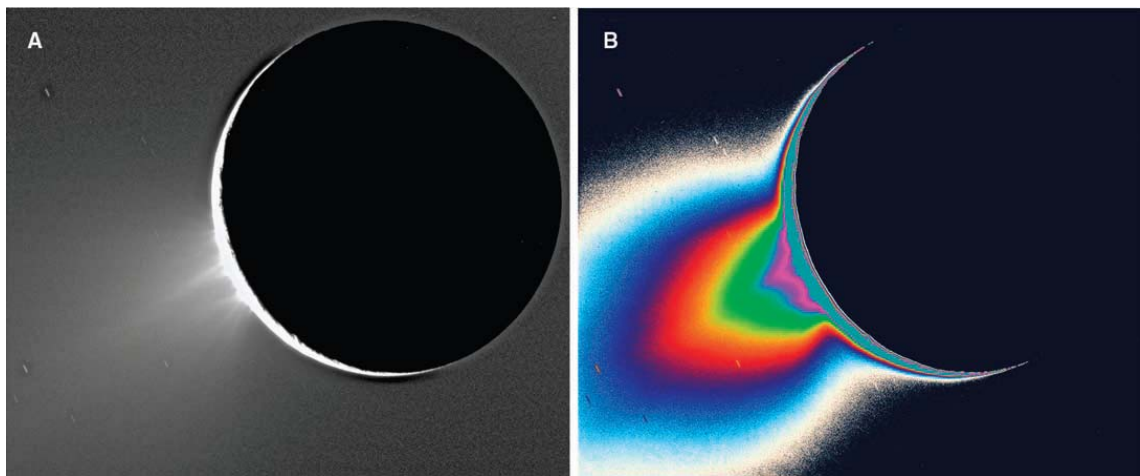


Figure 2.6. (A) Cassini image of Enceladus's atmospheric plume in which individual jets can be distinguished. The south pole is pointing towards the lower left. (B) A light level colour-coded version of (A) which enhances the visibility of the fainter components of the plume and highlights their enormous extent. [From *Porco et al.*, 2006.]

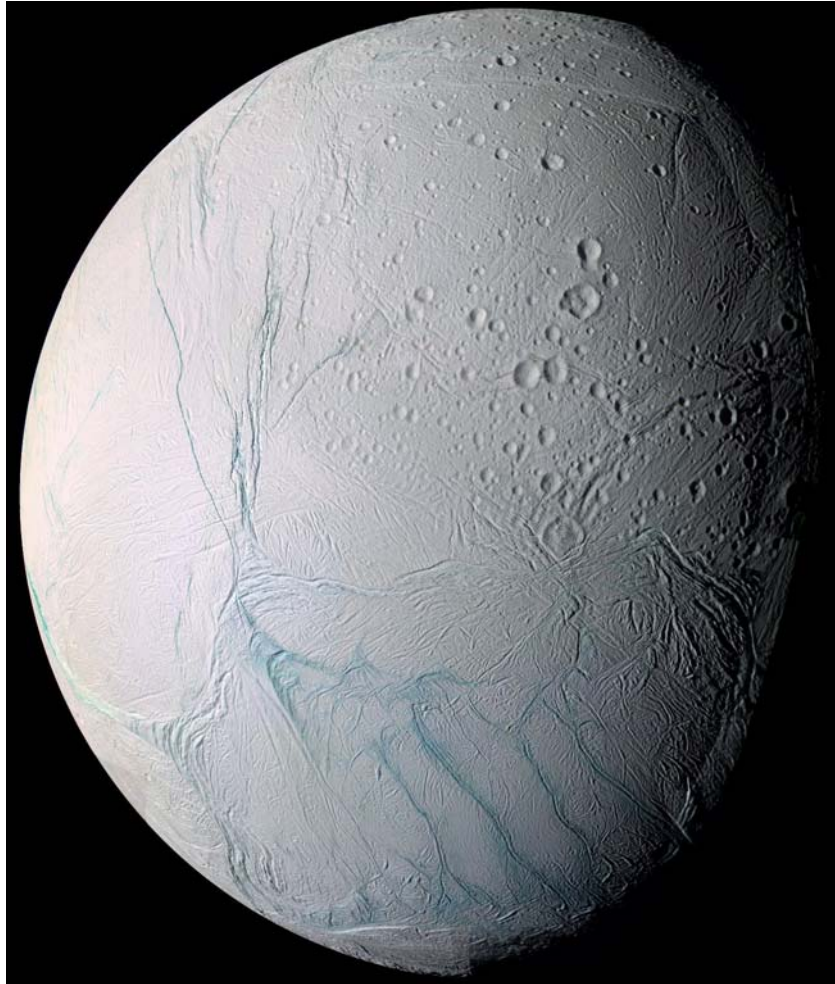


Figure 2.7. An enhanced colour image of Enceladus, based on data from the Cassini spacecraft, clearly showing the ‘tiger stripes’ in the southern polar region. [Courtesy of NASA.]

ring current at Saturn is similar in form to the ring current that flows westward around the Earth, which is generated by the relative drift of ions and electrons in opposite directions around the planet. Saturn's ring current is represented in Figure 2.5 by the distension of the equatorial field lines outward from the planet, and extends approximately from the inner boundary of the warm/hot plasma region (red dots) to within a few R_S of the magnetopause on the dayside, while merging into the central tail plasma sheet on the nightside. Significant empirical features of Saturn's ring current not represented in Figure 2.5 include the fact that Cassini energetic neutral atom imaging of the hot plasma component reveals a rather dynamic medium with periodic enhancements near the planetary period (~ 10.8 h) and rotating longitudinal asymmetries [Krimigis *et al.*, 2007; Carbary *et al.*, 2008a,b]. The ring current will be discussed further in Section 2.8.

It is noteworthy that because the internal planetary field is highly aligned with the spin axis at Saturn, to better than $\sim 0.1^\circ$ [Burton *et al.*, 2010], these equatorial field and plasma structures do not oscillate significantly north-south at the planetary period as they do, for example, at Jupiter. Instead, as indicated in Figure 2.5 by the dashed line, Cassini field data have shown that the magnetic equator (where the radial field component switches sign) is usually displaced northward of the spin equator in the outer magnetospheric regions on both the day and night sides of the planet [Cowley *et al.*, 2006; Arridge *et al.*, 2008b]. Both of these effects are presumed to be due to the tilt of the spin axis relative to the solar wind flow. The nightside offset, but not the dayside offset, has also been verified in Cassini particle data [Carbary *et al.*, 2008c; Sergis *et al.*, 2009].

2.4 – Magnetospheric dynamics

The plasma dynamics of a planetary magnetosphere depend on the nature of the plasma sources and sinks and the transport mechanisms which are responsible for the movement of plasma between the two. As previously discussed in Section 1.5, the flows in Saturn's magnetosphere are dominated by the effects of planetary rotation. In the regions close to the planet, the magnetic field and plasma corotate with the planet due to collisions between ions and neutrals in the Saturn's ionosphere while at larger

radial distances the plasma flows may also be driven by the interaction with the solar wind [e.g. *Cowley et al.*, 2004].

The transport of plasma from the inner to the outer parts of the magnetosphere is thought to occur via the interchange instability mechanism, which is driven by centrifugal forces exerted by the plasma on the magnetic field. Through this process cold, dense plasma from the inner magnetosphere moves outward and is replaced by hotter, more tenuous plasma moving inward from the outer magnetosphere [*Hill et al.*, 2005; *Chen and Hill*, 2008; *André et al.*, 2008 and references therein; *Rymer et al.*, 2009]. The plasma is eventually removed from the magnetosphere either in the form of plasmoids formed when the magnetic field reconnects in the magnetotail or is lost down the planetary field lines into the ionosphere (*Grodent et al.*, 2010).

2.5 - Saturn's aurora

Saturn, like the Earth and Jupiter, has aurorae, which are generated when energetic particles interact with gas (atomic and molecular hydrogen for Saturn) in the upper atmosphere. In general, Saturn's aurorae take the form of bright continuous ovals surrounding the poles of the planet and have been observed in visible, infrared (IR) and ultraviolet (UV) wavelengths. The first unambiguous detections of Saturn's aurora were made by the two Voyager spacecraft during their fly-bys in 1980 and 1981 [*Broadfoot et al.*, 1981]. Subsequent observations have been made using instruments onboard the Hubble Space Telescope (HST) [e.g., *Trauger et al.*, 1998; *Clarke et al.*, 2005, 2009; *Grodent et al.*, 2005, 2010; *Nichols et al.*, 2009, 2010]. Composite images of Saturn's southern hemisphere aurorae obtained by the HST during January 2004 are shown in Figure 2.8. A joint Cassini-HST campaign in January 2004 showed that Saturn's UV aurora respond strongly to a solar wind CIR compression. The aurorae became more intense and were located closer to the poles with the increase in solar wind pressure [*Clarke et al.*, 2005; *Crary et al.*, 2005].

2.6 - Saturn kilometric radiation

Saturn kilometric radiation (SKR) is an intense radio emission spanning the frequency range from 100 kHz to 1300 kHz that originates from the auroral regions in the northern

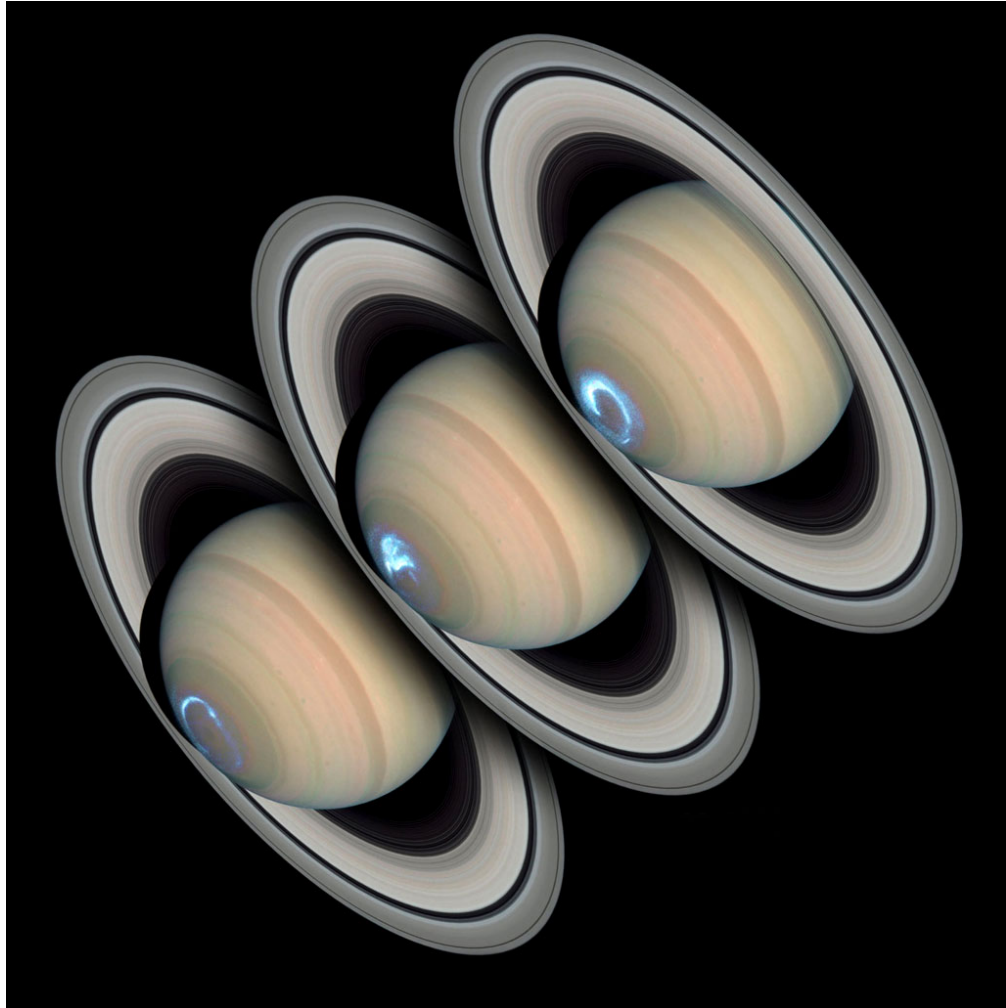


Figure 2.8. Composite images of Saturn's southern hemisphere aurorae obtained by the HST during on 24th, 26th and 28th January 2004. Each of the three images combines ultraviolet images of the auroral emissions with visible wavelength images of the planet and rings. [Courtesy of NASA.]

and southern hemispheres. The SKR is thought to be generated by the cyclotron maser instability [e.g. *Wu and Lee, 1979*] of precipitating electrons moving along magnetic field lines in the auroral regions of Saturn. The charged particles responsible for the SKR are controlled by Saturn's magnetic field and so the modulation of the SKR provides a link to the planet's interior. Traditionally, periodicities in the radio emissions of a planet are therefore used to estimate the internal rotation rate of the giant planets (i.e. the planetary rotation rate) [*Zarka et al., 2007*]. However, this is not possible for Saturn as the period of the SKR has been found to vary on the timescale of years. The periodicity in the SKR was measured to be 10 h 39 min 24 ± 7 s by the Voyager-1 and -2 fly-bys in 1980 and 1981, and this was adopted as Saturn's rotation period. However, subsequent Ulysses and Cassini measurements have revealed that the period of the SKR modulation varies by the order of 1% on time scales of a year to several years [e.g. *Galopeau and Lecacheux, 2000; Gurnett et al., 2005*]. Recent measurements made by Cassini have also revealed that the SKR has different periods in the northern and southern hemispheres, ~ 10.6 h in the northern hemisphere and ~ 10.8 h in the southern hemisphere [*Kurth et al., 2008; Gurnett et al., 2009*], and so it is not possible that the SKR modulation can represent Saturn's rotation period exactly. At the time of writing, it is still not clear what the physical mechanism for this is. Although the SKR cannot be used to determine the planetary rotation period, the variation in the period of the SKR modulation has led to the creation of a variable period longitude system. This system can be used to organise magnetospheric phenomena such as variations in the external magnetic field, the plasma density in the inner magnetosphere, and enhanced intensities of energetic ions [*Kurth et al., 2007, 2008*].

2.7 – Periodicities in Saturn's magnetosphere

Oscillations (termed magnetospheric period oscillations) related to the SKR modulation have been found to be ubiquitous throughout the magnetosphere in *in situ* data. Oscillations have been observed in the magnetic field [*Giampieri et al., 2006*], plasma particles [*Carbary et al., 2007, 2008a; Gurnett et al., 2007*], the position of the magnetopause and the bow shock [*Clarke et al., 2006, 2010*], the position of Saturn's southern auroral oval [*Nichols et al., 2008*], and other magnetospheric phenomena.

The modulation of the SKR has been found to be independent of the position of the observer and so is described as being ‘strobe like’. However, the oscillations in other magnetospheric phenomena are not strobe like, but rotate around the planet at the magnetospheric period [Andrews *et al.*, 2010]. These oscillations also propagate radially, resulting in phase fronts that spiral outward from the planet [Andrews *et al.*, 2008, 2010 and references therein]. Brandt *et al.* [2010] have suggested that the periodic magnetic field perturbations observed at Saturn are caused by the asymmetric plasma pressure of energetic (>2 keV) particles that are periodically injected and subsequently drift around Saturn (i.e. a rotating partial ring current), but this model has difficulty in explaining the differing periods in the northern and southern hemispheres. There is still much to be learned about the periodicities in Saturn’s magnetosphere and this is currently a ‘hot topic’ for research. As far as the work presented in this thesis is concerned, oscillations in the ring current region are left for future study since here we will investigate the overall averaged properties.

2.8 - Saturn’s ring current region

The presence of an eastward-flowing ring current in Saturn’s middle magnetosphere was first inferred from the Pioneer-11 magnetic field data [Smith *et al.*, 1980], and further studied using magnetic field and plasma particle data from the Voyager fly-bys [Ness *et al.*, 1981, 1982; Connerney *et al.*, 1981b; Krimigis *et al.*, 1983; Richardson and Sittler, 1990; Richardson, 1995]. The ring current produces a northward perturbation field at the inner edge of the ring current region, which acts to oppose the planetary field (which is directed southwards at the equator) and a southward perturbation field at the outer edge, which enhances the planetary field. The ring current also acts to radially distend the equatorial magnetic field lines outward from the planet due to the increased radial fields that occur, which are in opposite directions above and below the equatorial plane (see Figure 2.9). These magnetic perturbations were found to be well modelled using a simple, axi-symmetric current disk, whose parameters are the cylindrical radii of its inner and outer edges (R_1 and R_2), its half-thickness (D), and a parameter describing the current density in the disk ($\mu_0 I_0$), assumed to fall inversely as the cylindrical radial distance from the magnetic axis [Connerney *et al.*, 1983; Bunce and Cowley, 2003; Giampieri and Dougherty, 2004]. This model was based on one already introduced for use at Jupiter [Connerney *et al.*, 1981a]. The current density within the disk is then

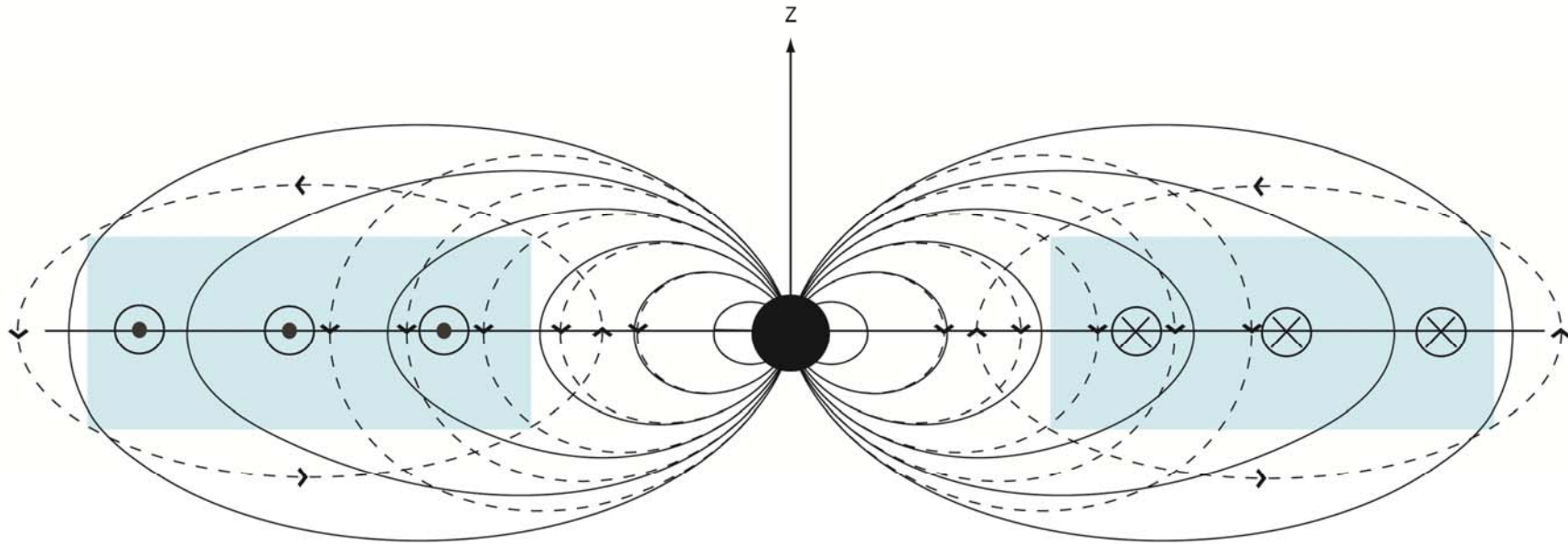


Figure 2.9. Sketch of the magnetic field configuration in the magnetic meridian plane for Saturn's ring current region with the planet at the centre. The model ring current region is shown by the blue box with associated dashed black lines representing the magnetic field of the ring current alone. Similar (near-dipolar) dashed black lines show the field lines corresponding to the internal planetary field alone while the solid black lines show how these field lines are distended outward by the ring current. [Adapted from *Bunce et al.*, 2008.]

taken to be given by $j_\phi = I_0/\rho$ where ρ is the perpendicular distance from the magnetic/spin axis. Fits to the magnetic field data obtained on the Pioneer-11 and Voyager fly-bys revealed a ring current with a radial extent between ~ 8 and $\sim 16 R_S$, a half-thickness of $\sim 3 R_S$, and a total current of ~ 10 MA. More recently, the same model, here termed the CAN (Connerney, Acuña, and Ness) model has been applied to the more extensive data set obtained by the Cassini spacecraft.

Bunce et al. [2007] studied magnetic field data from a set of near-equatorial Cassini orbits and showed that the ring current is significantly influenced by the size of the magnetosphere as initially suggested by *Alexeev et al.* [2006]. The inner edge of the ring current region remains essentially fixed at $\sim 6.5 R_S$ as the magnetosphere increases in size. However, the outer edge of the region increases from $\sim 15 R_S$ to $22 R_S$ along with a slight increase of the average current density parameter from ~ 45 to 55 nT as the magnetosphere expands. Thus, the strength and radial extent of the current increases as the magnetosphere expands outward due to decreasing solar wind dynamic pressure. This ring current strengthening leads to the formation of an equatorial ‘magnetodisc’ configuration at all local times for weak solar wind dynamic pressures. A ‘magnetodisc’ forms when the magnetic field becomes more and more stretched near the rotational equator, forming a thin, stretched disk of magnetic flux. During compressed conditions the magnetosphere assumes a more ‘quasi-dipolar’ (not that different from a dipole field) configuration on the dayside [*Bunce et al.*, 2008; *Arridge et al.* 2008a].

An area of considerable uncertainty, and of significant interest in this thesis, relates to the north-south structure of the ring current at Saturn, and its relation to the distribution of cool and hot plasma sketched in Figure 2.5. Determinations of the overall thickness of Saturn’s ring current from magnetic field measurements have to date only been obtained from data from the oblique fly-bys of the Pioneer and Voyager spacecraft, yielding values for the half-thickness on either side of the equator of between ~ 1.5 and $\sim 3 R_S$ [*Connerney et al.*, 1981b; *Bunce and Cowley*, 2003; *Giampieri and Dougherty*, 2004]. In Chapter 4 we present data from six Cassini orbits which cut north-south through Saturn’s equatorial plane at almost fixed radial distance within the ring current region. These data allow for the first time an essentially direct study of the

equatorial current sheet thickness, its offset from the equator, and an initial examination of its relation to the distribution of plasma about the equatorial plane.

Physically, the plasma currents that form the ring current are due to one or more of three possible effects, namely the spatial gradient of the perpendicular plasma pressure, the anisotropy of the plasma pressures parallel and perpendicular (P_{\parallel} and P_{\perp} respectively) to the field lines in the presence of field curvature, and the inertia of the flowing (near-corotating) plasma. The ring current at Earth is dominantly due to the first of these effects [e.g., *Wolf*, 1983], while at Jupiter all three components contribute, with the anisotropy effect being dominant within the nightside middle magnetosphere [*Caudal*, 1986; *Paranicas et al.*, 1991]. We note here, however, that the pressure anisotropy at Jupiter is $P_{\parallel} > P_{\perp}$, opposite to the case for Saturn, and thus is described by different physics. At Saturn, however, examination of plasma and magnetic field data from the Voyager fly-bys did not provide a fully conclusive result on the nature of the current. *McNutt* [1983, 1984] suggested the importance of the inertia current in the outer ring current region during the Voyager-1 fly-by, while *Mauk et al.* [1985] suggested that pressure gradient currents may be dominant within the more central regions, supported by early findings from the Cassini spacecraft [*Arridge et al.*, 2007; *Bunce et al.*, 2007]. However, Cassini has subsequently provided a much more extensive magnetic field and plasma bulk parameter data set [e.g., *Sergis et al.*, 2007, 2009; *Lewis et al.*, 2008; *Schippers et al.*, 2008; *Wilson et al.*, 2008; *McAndrews et al.*, 2009; *Persoon et al.*, 2009; *Thomsen et al.*, 2010] from which the contributions of these plasma currents to the total ring current can be estimated. *Sergis et al.* [2010] have combined density and pressure values from a number of near-equatorial passes to investigate average conditions over the radial range 6-15 R_S . They show that the inertia current density, though partially offset by westward directed anisotropy currents, is larger than the pressure gradient current density in the inner part of that radial range, and vice-versa in the outer part, with approximate equality at distances of ~ 9 -10 R_S . Related results have also been derived by *Achilleos et al.* [2010a], who have developed a self-consistent axi-symmetric model of force balance in Saturn's ring current region, though in this case the model suggests a resumption of dominant inertia currents in the outer region (at radial distances beyond $\sim 12 R_S$), in line with the results of *Arridge et al.* [2007]. Using a slightly improved version of this model (employing a more accurate

representation of the cold equatorial ion temperature over 10-25 R_S), *Achilleos et al.* [2010b] show that Saturn's magnetic field can be significantly modified by internal changes in the hot plasma pressure.

In Chapter 6 we employ magnetic field and plasma particle data from two near-equatorial Cassini passes to investigate the nature of the ring current in Saturn's dayside magnetosphere in a manner which is complementary to that of *Sergis et al.* [2010] and *Achilleos et al.* [2010a, b]. We then extend this study in Chapter 7 to consider data from a wider range of near-equatorial passes to explore the local time (LT) dependency and temporal variability of Saturn's ring current.

Chapter 3

Instrumentation

3.1 - Introduction

In the following chapters of this thesis we present and interpret data from a variety of instruments onboard the Cassini orbiter. The study described in Chapter 4 uses data obtained from the fluxgate magnetometer (FGM) and the electron spectrometer (CAPS/ELS). In addition to these data sets, the studies presented in Chapters 6 and 7 also use data from the ion mass spectrometer (CAPS/IMS), the Magnetospheric Imaging Instrument (MIMI) and the Radio and Plasma Wave Science (RPWS) investigation. In this chapter we provide an overview of the Cassini-Huygens mission followed by a description of the working principles of these instruments.

3.2 - The Cassini orbiter and its mission

The Cassini-Huygens mission is a joint endeavour of the National Aeronautics and Space Administration (NASA), the European Space Agency (ESA), and the Italian space agency Agenzia Spaziale Italiana (ASI) to thoroughly explore the Saturnian system. Mission objectives include making measurements of the planetary magnetosphere, and studies of the interactions of Saturn with the solar wind, of Titan with its environments, and of the icy satellites within the magnetosphere. Previous to the Cassini-Huygens mission, only three spacecraft had investigated the environment of Saturn: Pioneer-11, Voyager-1 and Voyager-2, which completed fly-bys in 1979, 1980 and 1981 respectively.

Cassini-Huygens is one of the largest and most ambitious interplanetary spacecraft ever built (see Figure 3.1). It measures 6.7 m high by 4 m wide and carries a total of 18 science instruments; 12 on the Cassini orbiter and 6 on the Huygens probe. The main orbiter consists of several sections stacked on top of each other, topped with a 4 m diameter high-gain antenna used for communications with Earth. Cassini also has two smaller low-gain antennae located at the very top of the high-gain antenna and towards the bottom of the spacecraft, which would be used for communications in the



Figure 3.1. The Huygens probe (gold dome) being mounted onto the Cassini spacecraft.
[Courtesy of NASA/JPL.]

event of a power failure or other such emergency situation. Most of the science instruments on the orbiter are carried by the fields and particles pallet and the remote sensing pallet, which are both situated about half way up the main stack. Figure 3.2 shows the Cassini spacecraft (with the Huygens probe still attached) with some of its science instruments labelled. Those that provided data used in this thesis are described in more detail in the following sections. Cassini is powered by three radioisotope thermoelectric generators (RTGs) and these are also labelled in Figure 3.2. Since Cassini is a three-axis stabilised spacecraft (i.e. thrusters and reaction wheels are used to maintain spacecraft attitude by transferring angular momentum between the wheels and the spacecraft) it is usually necessary to turn the entire spacecraft to orient the science instruments in the correct observing direction.

Cassini-Huygens was launched in October 1997 and travelled for seven years before achieving Saturn Orbit Insertion (SOI) in July 2004. During its journey to Saturn the spacecraft made four gravity-assist swing-by manoeuvres including two at Venus (April 1998 and June 1999), one at the Earth (August 1999) and one at Jupiter (December 2000). Figure 3.3 shows the interplanetary trajectory the spacecraft followed. After its arrival at Saturn the spacecraft began its initial four-year orbital tour of the Saturnian system. The Huygens probe was released from the spacecraft in December 2004, leaving the Cassini orbiter to continue its tour of Saturn. In January 2005, the Huygens probe entered the atmosphere of Titan and descended via parachute to the moon's surface. During its descent, the Huygens probe carried out detailed in situ measurements of the physical properties, the chemical composition and the dynamics of Titan's atmosphere. Data from the Huygens probe is not used in this thesis, so for a detailed description of the instruments see *Lebreton et al.* [2002].

Cassini completed its initial four-year mission in June 2008 and its first extended mission, called the Cassini Equinox Mission, in September 2010. It is now undertaking the Cassini Solstice Mission (named for the Saturnian summer solstice, occurring in May 2017), which ends in September 2017. This long term observation program allows the combining of measurements taken over many orbits of Saturn (over 130 to date), resulting in a detailed description of the physical processes which occur within Saturn's magnetosphere, and their variation with time (allowing the separation of temporal and spatial features). Cassini arrived just after Saturn's northern winter

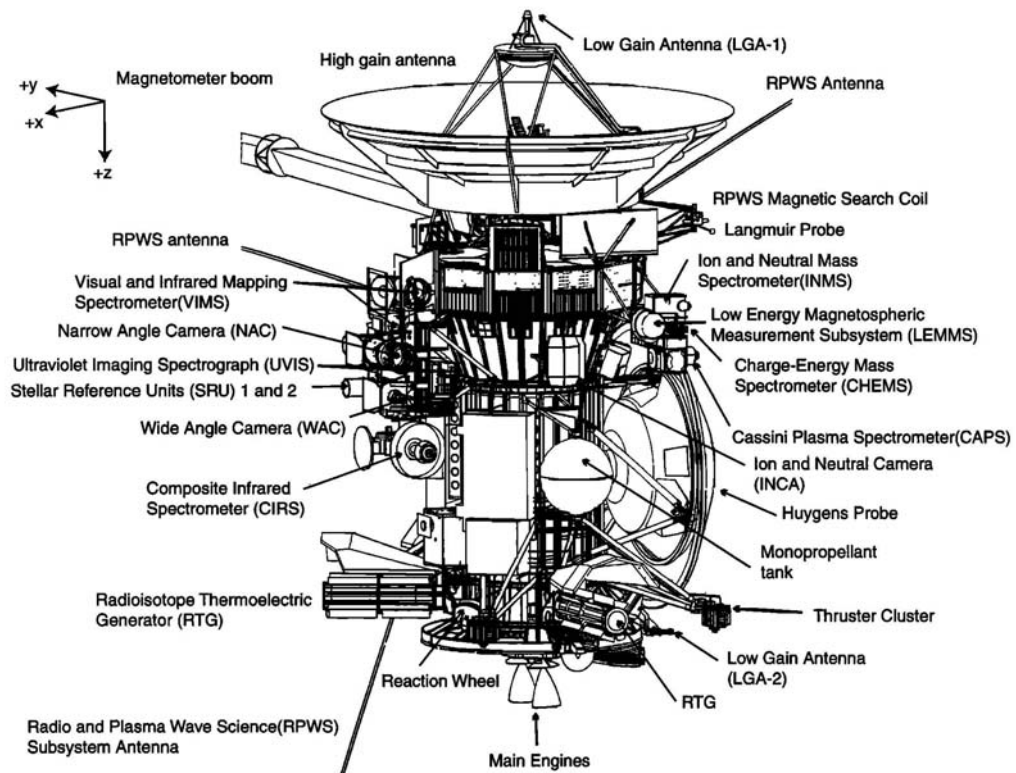


Figure 3.2. Diagram of the Cassini spacecraft showing science instruments and some of the engineering subsystems. [From *Burton et al.*, 2001.]

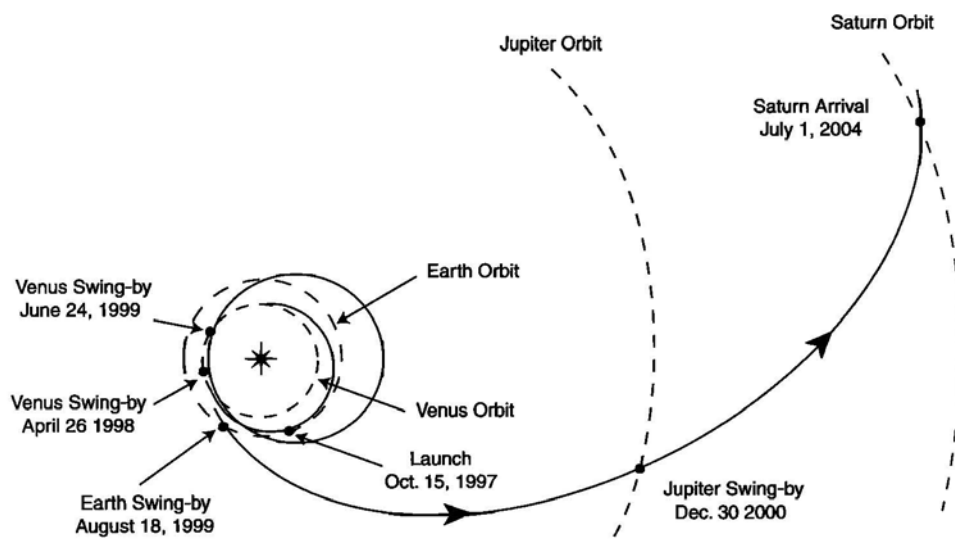


Figure 3.3. Cassini-Huygens interplanetary trajectory, showing all planetary encounters from launch in October 1997 to Saturn arrival in July 2004. [From *Burton et al.*, 2001.]

solstice, and will continue to orbit until a few months past northern summer solstice (May 2017) enabling seasonal and other long term changes within the system to be studied.

3.3 - The Cassini magnetometer

The Cassini dual technique magnetometer (MAG) [Dougherty *et al.*, 2004] is a direct-sensing instrument that measures the strength and direction of the magnetic field in the vicinity of the spacecraft. MAG addresses the nature of Saturn's internal field, its magnetosphere and its interaction with the solar wind, along with investigating the interactions of the moons with their plasma environment.

MAG consists of a flux gate magnetometer (FGM), a helium magnetometer capable of operating in both vector and scalar mode (V/SHM), a data processing unit, three power supplies, and the associated electronics. Figure 3.4 shows the location of the FGM and V/SHM magnetometers onboard Cassini. The FGM is located halfway along the 11 m magnetometer boom, with the V/SHM located at the end of the boom so that the magnetometers are distanced from the spacecraft and any associated field. A more detailed explanation of the MAG instrument and its scientific objectives can be found in Dougherty *et al.* [2004] while Ness *et al.* [1970] provide a full description of the working principles of generic FGM and VHM magnetometers since here we will only describe the key operating features.

In order to meet the science aims mentioned briefly above, MAG must provide measurements with high sensitivity over a wide dynamic range, from less than 1 nT in the solar wind to several thousand nT during Saturn fly-bys. Table 3.1 details the dynamic range and resolution of the magnetometer sensors. In its normal mode of operation MAG switches automatically between these ranges. The combination of two magnetometers not only improves the in-flight calibration process and measurement of the residual spacecraft field, but also fulfils the redundancy requirements for a long duration space mission.

The V/SHM makes both vector and scalar measurements of the ambient magnetic field and works on the response of an optically pumped metastable helium

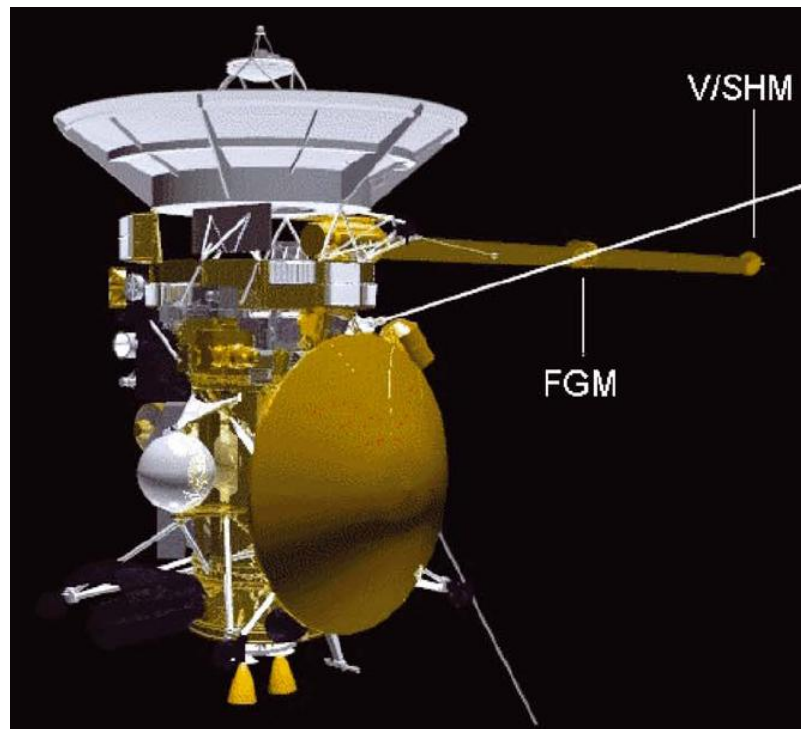


Figure 3.4. The location of the FGM and V/SHM magnetometers onboard Cassini.
[From *Dougherty et al.*, 2004.]

Sensor	Dynamic range	Resolution
FGM	± 40 nT	4.9 pT
	± 400 nT	48.4 pT
	± 10000 nT	1.2 nT
	± 44000 nT	5.4 nT
VHM	± 32 nT	3.9 pT
	± 256 nT	31.2 pT
SHM	256-16384 nT	36 pT

Table 3.1. Dynamic range and resolution of the magnetometer sensors. [From *Dougherty et al.*, 2004.]

population (contained in a glass cell) to external magnetic fields. Helium in an absorption cell is excited to produce a metastable population. Infra-red radiation then passes through a circular polariser and the absorption cell, into an infra-red detector. The ambient magnetic field is measured by sensing its effect on the Zeeman splitting that occurs in the optically pumped helium. The V/SHM failed in November 2004 after performing well during the early part of the mission. The studies presented in Chapters 4, 6 and 7 of this thesis require data from later orbits so we use magnetic field data exclusively from the FGM, of which the key operating features are described below.

3.3.1 – The fluxgate magnetometer (FGM)

The FGM measures the strength and direction of the ambient magnetic field using three orthogonal sensors, which produce an output voltage proportional to the value of the component of the magnetic field along their axes. Figure 3.5 is a photograph of the FGM with its case removed, together with its associated electronics. The normal sampling rate of the FGM is 32 vectors s^{-1} , but the data presented in this thesis is averaged to 1 min resolution.

The FGM is composed of three single-axis fluxgate sensors mounted orthogonally on a glass-ceramic block. Ceramic is chosen for its low thermal expansion coefficient, which minimises misalignments between the sensors due to temperature changes. Each fluxgate sensor consists of a drive coil wrapped around a highly magnetically permeable ring core, which is completely enclosed in a rectangular sense winding. A schematic diagram is shown in Figure 3.6 where H_{ext} represents the component of the external magnetic field along the sensor's axis of sensitivity. It is helpful to think of the ring core as two separate half cores (represented by the blue and green in the figure). A 15.625 kHz square wave is applied through the drive coil, which drives the ring core into a cycle of magnetic saturation (i.e. magnetised, unmagnetised, inversely magnetised, unmagnetised, magnetised etc.). As the current flows through the drive winding, one half core will be magnetised in one direction, while the other is magnetised in the opposite direction. In the absence of an external field (i.e. $H_{\text{ext}} = 0$) the two half cores go into and come out of saturation at the same time. The fields generated exactly cancel out due to them having the same strength but opposite orientation, giving no net change of flux in the sense winding and hence no induced

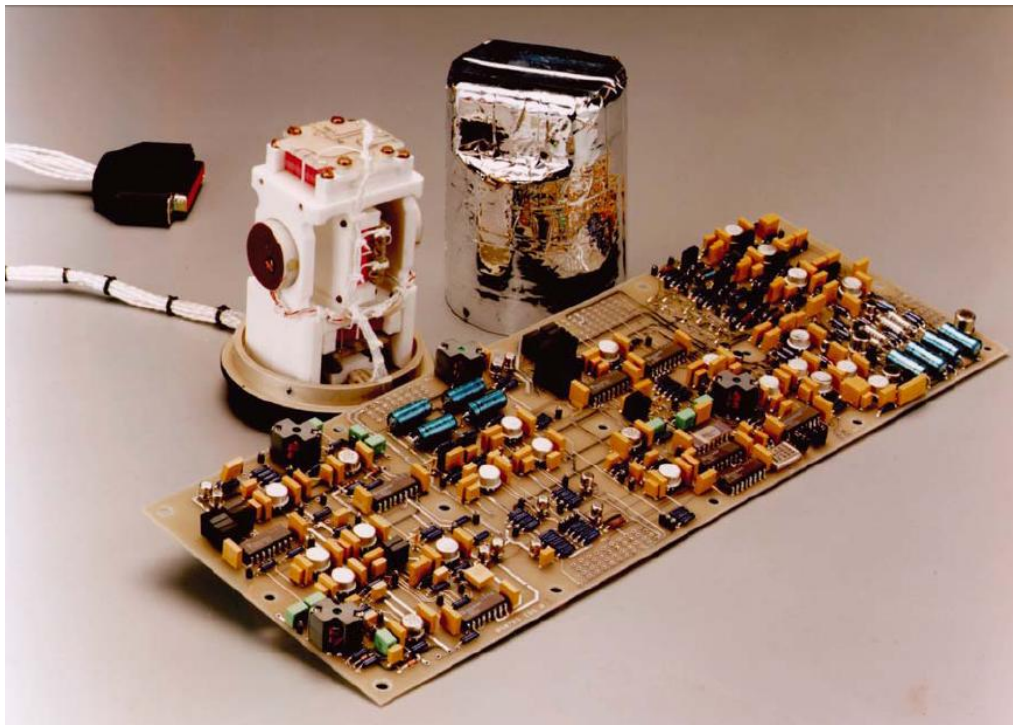


Figure 3.5. Photograph of the FGM with its case removed, and the associated electronics. [From *Dougherty et al.*, 2004.]

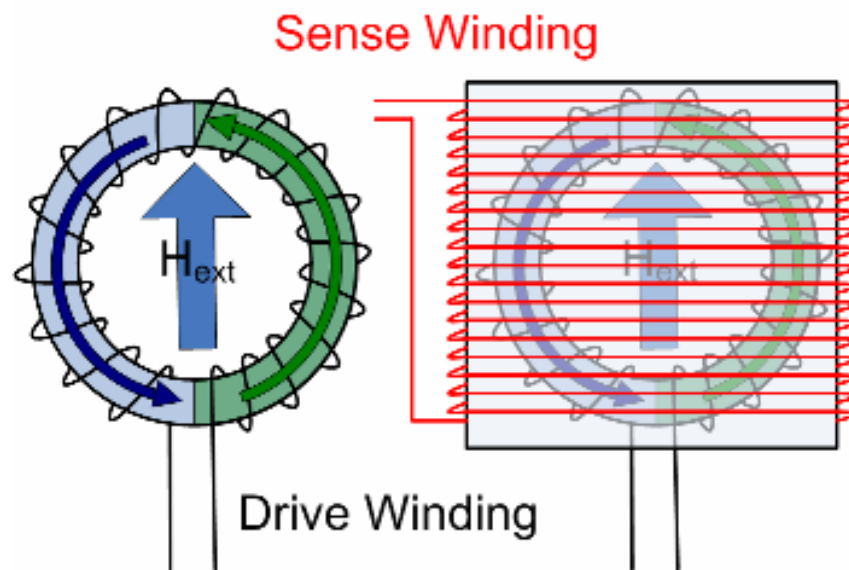


Figure 3.6. Schematic diagram of a single-axis fluxgate sensor. The drive coil is shown in black and the sense winding in red, while H_{ext} represents the component of the external magnetic field along the sensor's axis of sensitivity. [Courtesy of Imperial College London.]

voltage. When there is an external field, the half core generating a field in the opposite direction of the external field (the green half core in Figure 3.6) has its field weakened by the external field and thus comes out of saturation sooner than the half core generating a field in the same direction as the external field (the blue half core in Figure 3.6) which has its field strengthened by the external field. The fields no longer exactly cancel out and the changing flux within the coil induces a voltage in the sense winding with an amplitude proportional to the strength of the external field in the direction of the sensor's axis of sensitivity.

3.4 - The Cassini Plasma Spectrometer

The Cassini Plasma Spectrometer (CAPS) [Young *et al.*, 2004] makes comprehensive measurements of a variety of plasma phenomena found in Saturn's magnetosphere by measuring the flux of ions as a function of mass per charge, and the flux of ions and electrons as a function of energy per charge and angle of arrival relative to the instrument. The CAPS instrument consists of three sensors: the electron spectrometer (ELS), the ion beam spectrometer (IBS), and the ion mass spectrometer (IMS), along with a data processing unit (DPU), high-voltage power supply and an actuator. Figure 3.7 is a photograph of the CAPS instrument with the location of the three sensors highlighted, while Figure 3.8 shows a schematic of the Cassini spacecraft with the three CAPS sensors enlarged. The fields of view of all three sensors are shown, which are co-planar in order to obtain compatible electron and ion measurements. Spacecraft coordinates are also indicated. CAPS is mounted on a motor driven actuator (labelled ACT in Figure 3.8), which can rotate the instrument by $\pm 104^\circ$ in azimuth (in the spacecraft x - y plane). Surrounding spacecraft structures obstruct parts of the field of view and for that reason the useful range of motion is restricted to -80° to $+104^\circ$ in azimuth. The DPU manages the processing of all CAPS data and controls sensor and actuator motor functions.

Figure 3.9 is a simplified overview of the CAPS instrument layout and particle optics. All three sensors have in common that they are based on charged particle motion in electrostatic fields. After entering the sensors through wedge-shaped fields-of-view, particle trajectories are dispersed by electric fields and then measured using electron-multiplier detectors [Young *et al.*, 2004]. The IBS is a hemispherical electrostatic

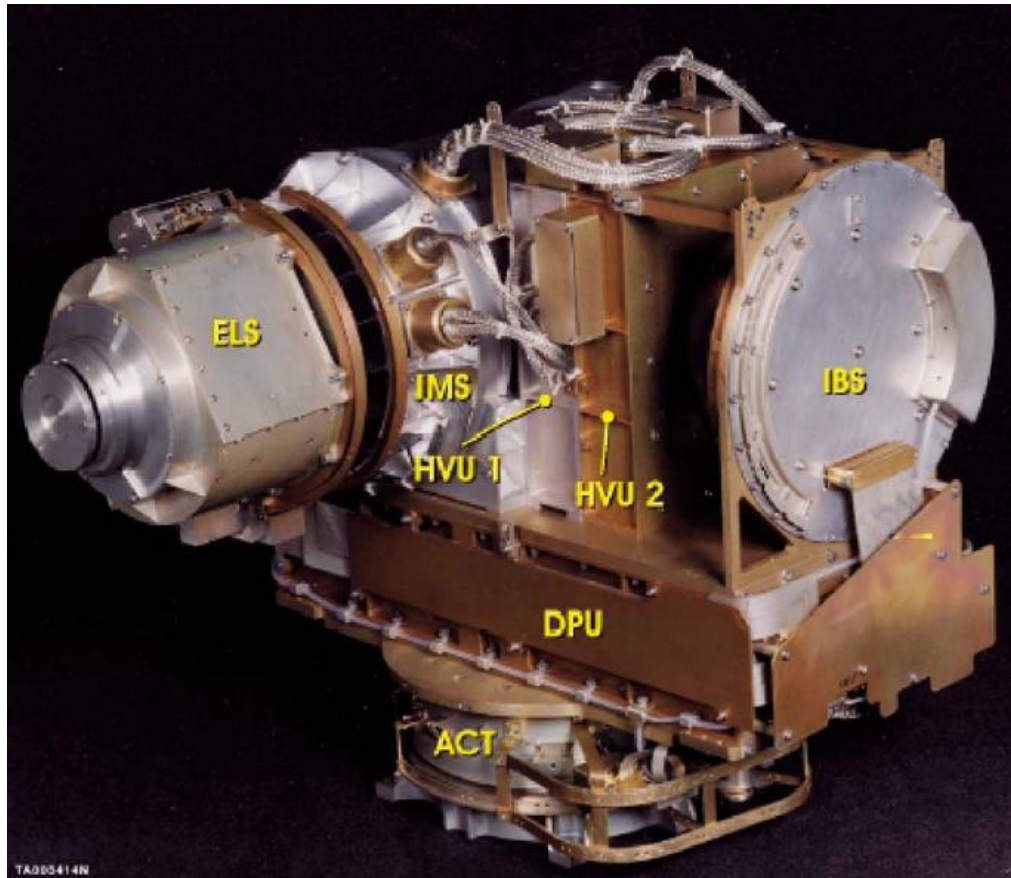


Figure 3.7. Photograph of the CAPS flight model prior to delivery to the Cassini spacecraft. [From *Young et al.*, 2004.]

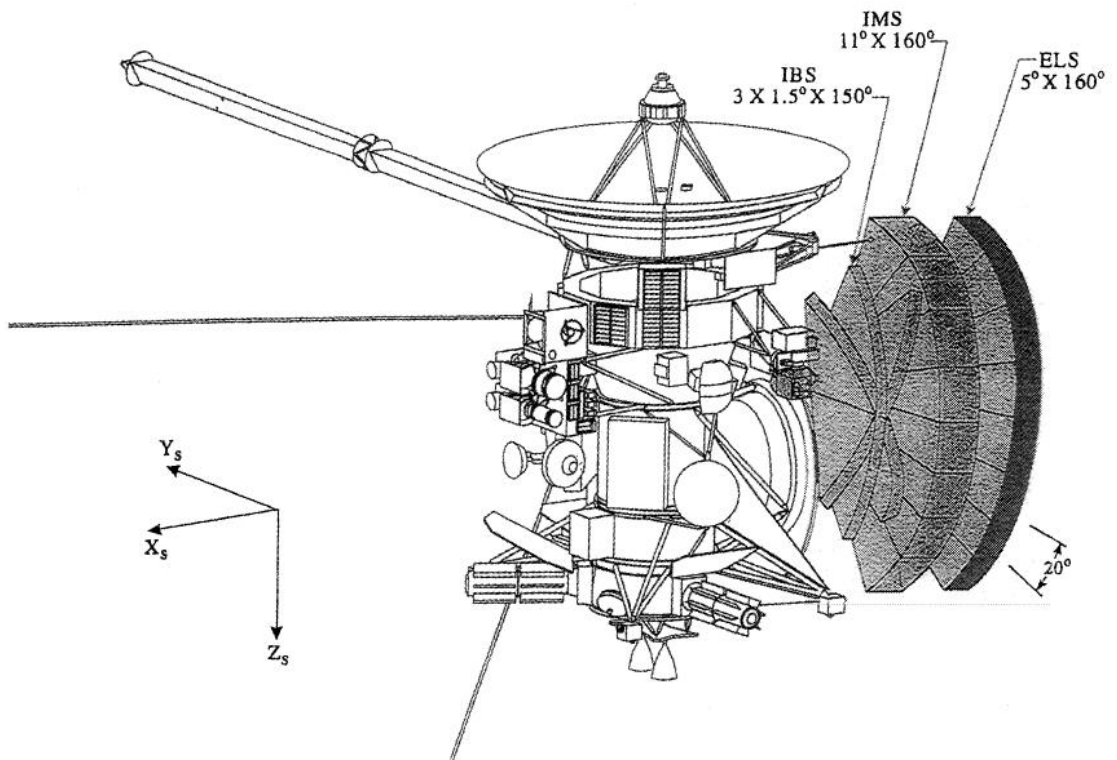


Figure 3.8. Schematic showing the CAPS fields of view and Cassini spacecraft coordinates. [From Rymer *et al.*, 2001.]

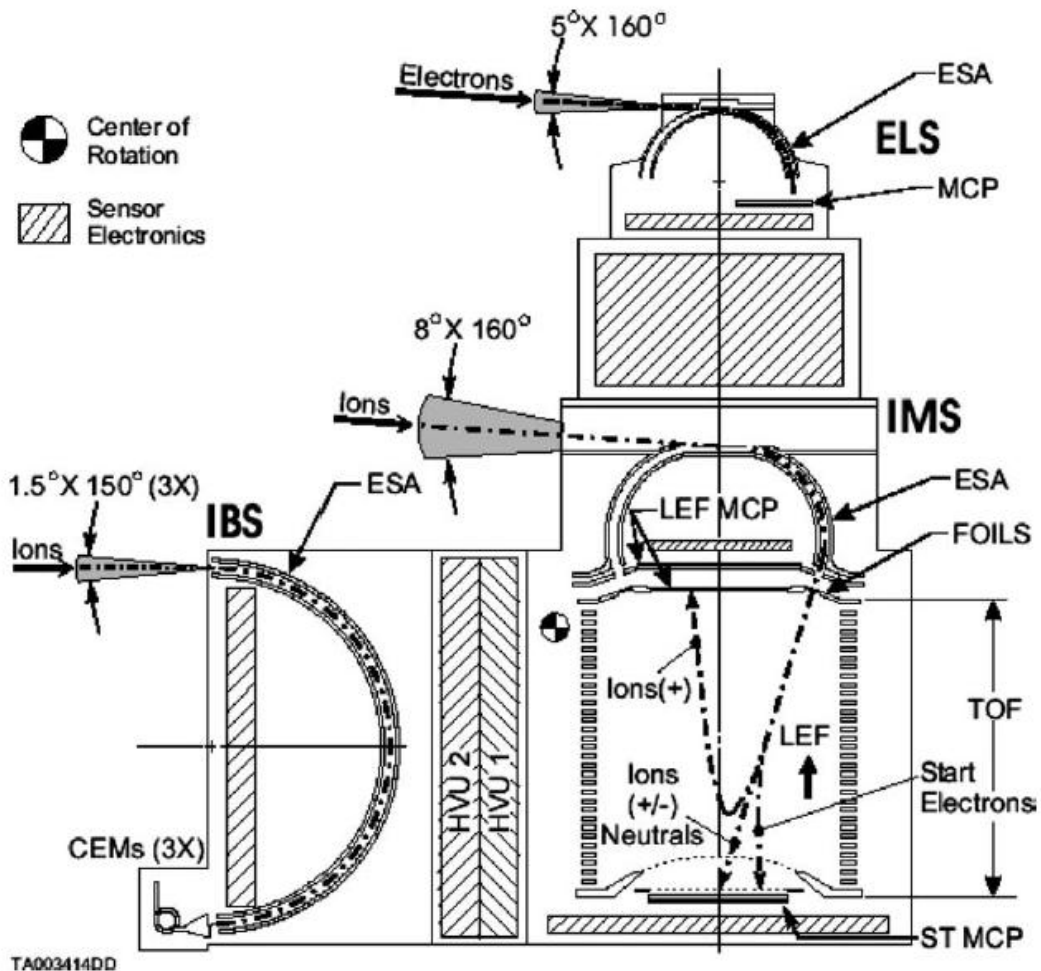


Figure 3.9. Optical layout, fields of view and key sensor elements of CAPS shown in the x - y (azimuthal) plane of the spacecraft. Cross hatched areas indicate sensor electronics subsystems while heavy dashed lines suggest the general shape of particle trajectories. [From *Young et al.*, 2004.]

analyser which measures the flux of positively charged atomic and molecular ions as a function of energy per charge and angle of arrival at the instrument over the energy range ~ 1 eV to ~ 50 keV. In this thesis we use data from the ELS and IMS sensors of the CAPS instrument, which are described in more detail below. The ELS instrument is mounted on top of the IMS instrument and so their fields of view are almost identical.

3.4.1 - The Electron Spectrometer (ELS)

The ELS measures the flux of electrons as a function of energy per charge and angle of arrival over the energy range from ~ 0.6 eV to ~ 26 keV. To minimise contamination by spacecraft photoelectrons, the ELS is mounted as far from nearby spacecraft surfaces as possible.

The ELS is a hemispherical top-hat electrostatic analyser, which is shown at the top of Figure 3.9. Electrons enter the sensor via a baffled collimator, which creates a parallel beam of particles. They then pass into the narrow gap between a pair of concentric hemispherical electrostatic analyser plates, which are blackened to reduce photoelectrons. A potential difference is maintained between the inner and outer plates (the outer plate is grounded while the inner is set to a positive voltage), such that only electrons with energies and angles within a range determined by this potential will have trajectories that allow them to pass through the analyser without being stopped by hitting a wall. Electrons of different energies are made to pass through the analyser by varying the potential. Electrons that successfully pass through the analyser then impact on an arc of micro-channel plates (MCPs). This generates a cascade of secondary electrons, which are collected by an arc of eight $20^\circ \times 5^\circ$ anodes, providing a full field of view of $160^\circ \times 5^\circ$ which can be swept in azimuth by the actuator. The electron direction of arrival is determined from the position at which it strikes the MCPs, which is recognised by the anode positioned behind the MCPs. An energy spectrum is obtained by changing the potential on the analyser plates, which changes the narrow band of electron energies that can traverse the region between the analyser plates. In normal operation, the analyser sweeps through a 64 level logarithmic energy spectrum from ~ 26 keV (bin 1) to ~ 0.6 eV (bin 63) in 2 seconds. The 64th energy level is a “fly-back” step to change the voltage from the lowest to the highest energy. During this time, no readings are taken [Lewis *et al.*, 2008].

In Chapter 4 we display plasma electron spectrograms over the energy range 0.6 – 26 keV using 1 min averaged data from anode 5 (chosen since its field of view is not obstructed by surrounding spacecraft structures for any actuator angle). For the studies presented in Chapters 6 and 7 we employ electron density and temperature measurements at 1 minute resolution obtained by integrating the particle distribution over three-dimensional velocity space. The methodology is described in Section 3 of *Lewis et al.* [2008].

3.4.2 - The Ion Mass Spectrometer (IMS)

The IMS measures the flux of positively charged atomic and molecular ions as a function of energy per charge, mass per charge (allowing different species to be distinguished) and angle of arrival at the instrument, over the energy range ~1 eV to ~50 keV. The IMS combines a toroidal top-hat electrostatic analyser with a linear electric field time-of-flight (TOF) mass spectrometer.

The toroidal analyser works in the same way as the hemispheric electrostatic analyser on the ELS sensor, as described in Section 3.4.1, although here the IMS field of view is $160^\circ \times 12^\circ$ which is divided into eight $20^\circ \times 12^\circ$ anodes. An energy spectrum is again obtained by stepping the analyser potential through a set of 64 logarithmically spaced values covering the range from ~1 eV up to ~50 keV in 4 seconds. Only ions with a particular energy and direction of arrival pass through the electrostatic analyser, at which point they pass into the TOF analyser. Ions that successfully pass through the electrostatic analyser are accelerated by an approximately -15 kV potential into one of the eight thin carbon foils, which are arranged in an arc at the entrance to the TOF analyser. As ions exit the foil they eject secondary electrons, which are detected by the start MCP. This is used as the TOF start signal and also determines the direction of arrival of the ion with respect to the IMS aperture. The TOF spectrometer is a cylindrical chamber bounded by linear electric field (LEF) rings, which focus positively charged particles. MCPs are located at the end of these rings, which when triggered provide the TOF stop signal. Anodes under the start and LEF MCPs collect the electrons emitted from the MCPs and pass the signals through amplifiers and a time-to-digital converter, which measures the time interval between the triggering of the start and stop MCPs.

In this thesis we employ ion density, temperature and velocity measurements obtained from forward modelling of IMS data. The forward modelling technique assumes the two major ion species are the water group, W^+ (mass of 17 AMU) and protons, H^+ (mass of 1 AMU). The two species are modelled by separate anisotropic Maxwellian distributions which have the same bulk flow velocity. This gives 9 free parameters to obtain the best fit, namely the density, n , and the parallel and perpendicular temperatures, T_{\parallel} and T_{\perp} for each species, along with the velocity in cylindrical coordinates V_{ρ} , V_{ϕ} , and V_z . A detailed explanation of the forward modelling technique can be found in *Wilson et al.* [2008].

3.5 - The Cassini Magnetospheric Imaging Instrument

The Magnetospheric Imaging Instrument (MIMI) [*Krimigis et al.*, 2004] is a neutral and charged particle detection system on the Cassini orbiter. MIMI is designed to make in situ measurements of the composition, charge state, and energy distribution of energetic ions (~ 7 keV to > 8 MeV per charge) and electrons (15 keV to > 11 MeV), and perform remote sensing of Saturn's magnetosphere by imaging energetic neutral atoms (ENAs), created when magnetospheric energetic ($E > 7$ keV) ions capture electrons from the ambient neutral gas and undergo charge exchange. This combination of in situ measurements and global imaging is used to study the overall configuration and dynamics of Saturn's magnetosphere. MIMI consists of one set of electronics serving three detector heads, which perform a broad variety of measurements; namely the Charge Energy Mass Spectrometer (CHEMS), the Low Energy Magnetospheric Measurements System (LEMMS), and the Ion and Neutral Camera (INCA). Figure 3.2 shows the location of the CHEMS, LEMMS and INCA sensors onboard Cassini. A more comprehensive review of MIMI can be found in *Krimigis et al.* [2004], such that here we will focus only on the main operating principles of the CHEMS and LEMMS detectors since data from INCA is not used in this thesis.

3.5.1 - The Charge Energy Mass Spectrometer (CHEMS)

CHEMS measures energetic ion fluxes, energy spectra, and ion composition over the range ~ 3 to 236 keV per charge. CHEMS is located on the particles and fields

instrument pallet and consists of an electrostatic analyser, three time-of-flight (TOF) telescopes, and the associated electronics. The three TOF telescopes are independent, each one covering 53° in latitude and 4° in azimuth (as shown in Figure 3.10), such that the total field of view is $\sim 160^\circ \times 4^\circ$. When the spacecraft rolls about its z -axis, CHEMS covers most of the unit sphere, allowing 3-D particle distribution functions to be measured.

A schematic diagram of CHEMS is shown in Figure 3.11. Ions with the correct energy per charge pass through the electrostatic analyser and the thin carbon foil at the entrance of the TOF telescope. As the ion exits the foil, secondary electrons are emitted, which are then deflected by electric fields inside the telescope. The start signal for the TOF analysis is generated by the secondary electrons striking one of the three start MCPs. The ion then strikes one of the three silicon solid-state detectors at the far end of the TOF telescope. The secondary electrons generated by this collision are detected by one of the three stop MCPs, providing the stop signal for the TOF analysis. The various detector signals are then sent to the MIMI main electronics unit for further processing.

3.5.2 - The Low Energy Magnetospheric Measurements System (LEMMS)

LEMMS is a double-ended telescope with a low energy and high energy end which measures energetic ion and electron fluxes. Ions with energies in the range 0.03 - 18 MeV and electrons in the range 0.015 - 0.884 MeV are measured by the low energy end of LEMMS, while high energy electrons (0.1 - 5 MeV) and ions (1.6 - 160 MeV) are measured by the high energy end [Krimigis *et al.*, 2004]. The low and high energy ends have oppositely-directed 15° and 30° conical fields of view respectively, and contain eleven silicon semiconductor detectors. The whole assembly is shielded by a platinum cover to avoid particles penetrating through the sides of the instrument. LEMMS is mounted on a rotating platform, with its spin axis parallel to the spacecraft y -axis, such that when rotating, the LEMMS telescopes sweep through 360° in the spacecraft x - z plane. 3-D particle distributions can only be obtained if the spacecraft itself is rotating about the z -axis. The rotating mechanism of LEMMS failed in the early stages of the mission (day 32/2005) such that its field of view has been fixed

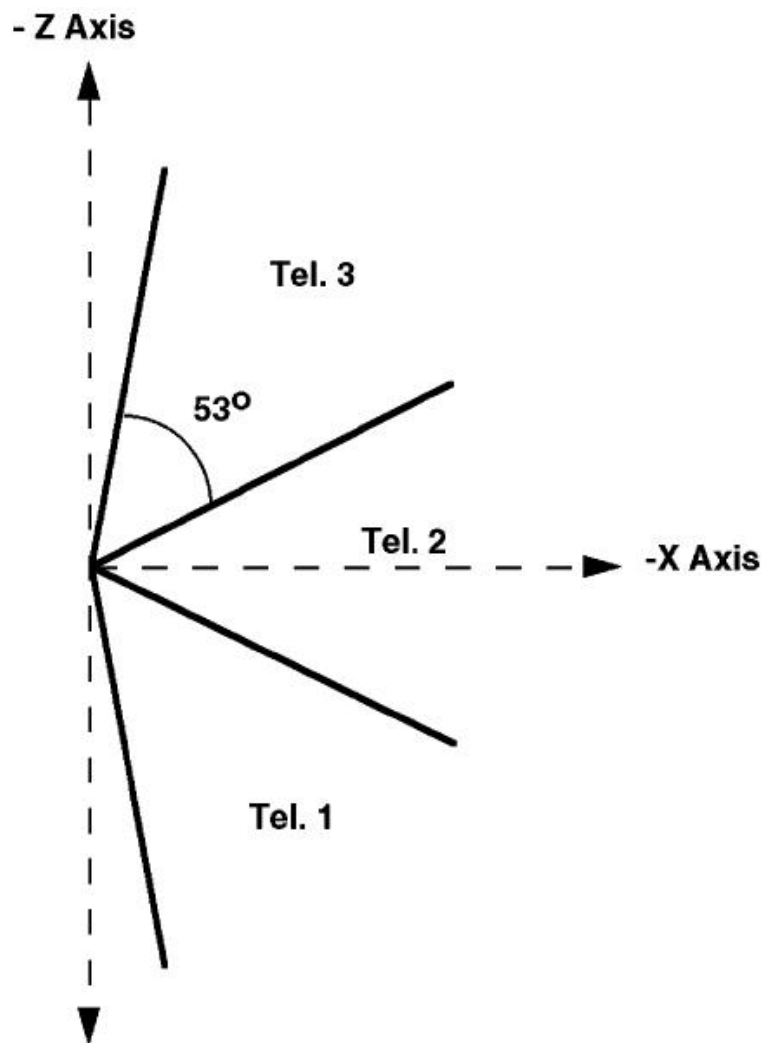


Figure 3.10. CHEMS telescopes fields of view relative to the spacecraft axes. [From *Krimigis et al.*, 2004.]

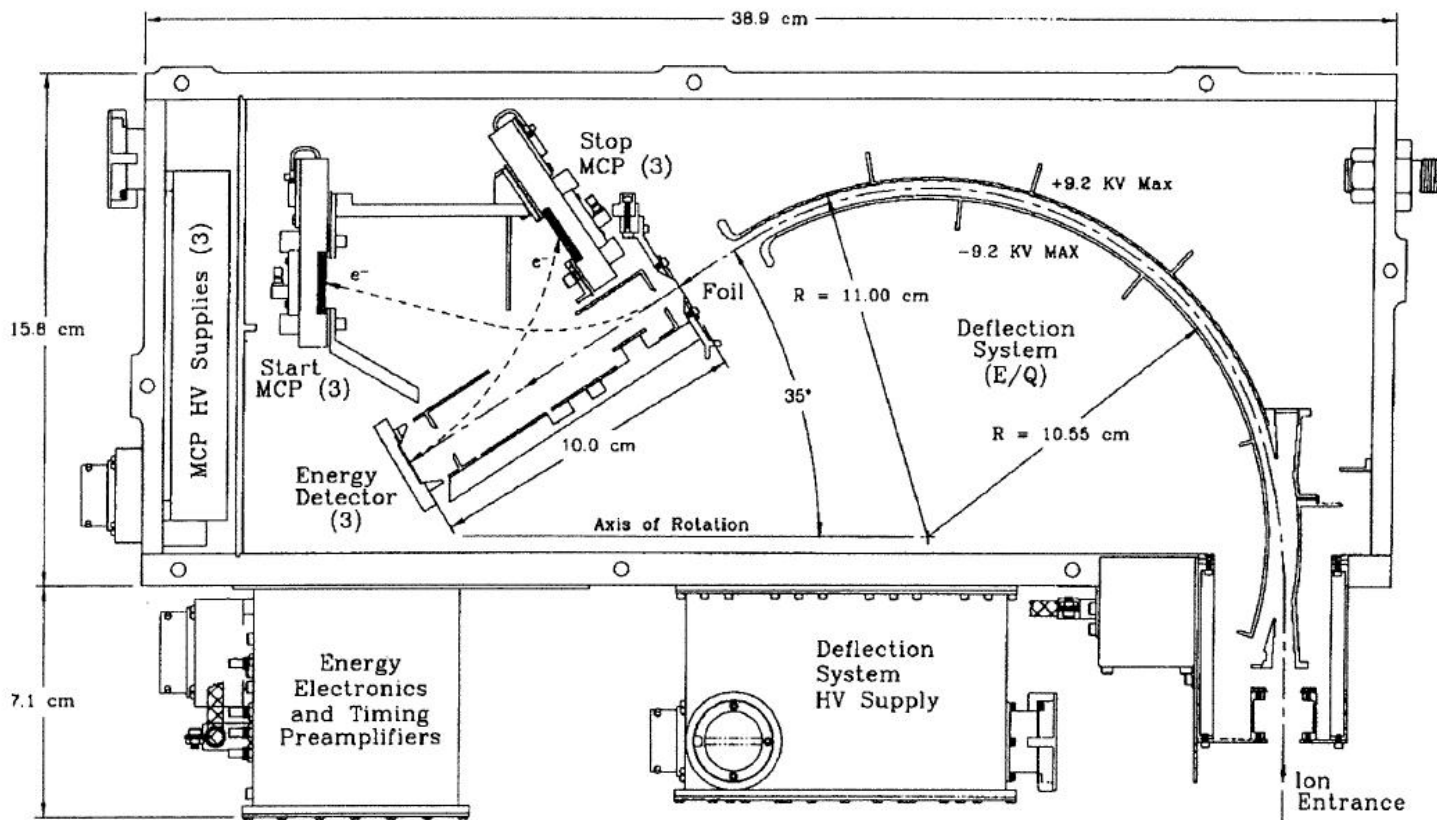


Figure 3.11. CHEMS mechanical configuration. [From *Krimigis et al.*, 2004.]

since then. It therefore samples varying pitch angles throughout an orbit depending on the spacecraft orientation. The overall configuration of LEMMS and the positions of all eleven detectors are shown in Figure 3.12. The position of the detectors inside the assembly determines the species and energy of the incident particle.

The low energy end of LEMMS is designed to measure low energy ions ($E \geq 30$ keV) and electrons (15 keV – 1 MeV). Ions and electrons enter the low energy end through a collimator. An internal permanent magnet produces an inhomogeneous magnetic field, which separates the incident ions and electrons. Figure 3.13 illustrates sample particle trajectories in the low energy end of LEMMS. Low energy electrons (up to 884 keV) are deflected by the magnetic field and impact on electron detectors E (E1 and E2) and F (F1 and F2) depending on their incident energy. Low energy ions are less affected by the magnetic field and impact on low energy ion detectors A and B (B is not shown in Figure 3.13) after following straighter trajectories. The high energy end measures high energy ions (1.5 - 160 MeV/charge) and electrons (0.1 – 5 MeV) using 5 detectors (D1, D2, D3a, D3b, and D4) using the same method as the low energy end. There is a gold absorber (labelled C in Figure 3.12) between detectors B and D4 to stop particles from the low energy end entering the high energy end if they penetrate detectors A or B. There is also a 25 mm aluminium foil in front of detector D1 to suppress incoming light and prevent low energy ions from entering the high energy end.

The time resolution for charged particle measurements using CHEMS and LEMMS can be < 0.1 s. However, in this thesis we employ 5 minute averaged density and pressure data for all particles with $E < 3$ keV, derived from CHEMS and LEMMS measurements. All of the LEMMS channels are utilised but we only use data from CHEMS telescope 2 since this is nearly aligned with the LEMMS telescope. Measurements from these two instruments can therefore be directly compared and form a continuous data set. For the common LEMMS and CHEMS energy range (24 - 236 keV), CHEMS measurements are used because they are practically free from light contamination and, since CHEMS measures H^+ and O^+ separately, the individual pressures can be compared if desired.

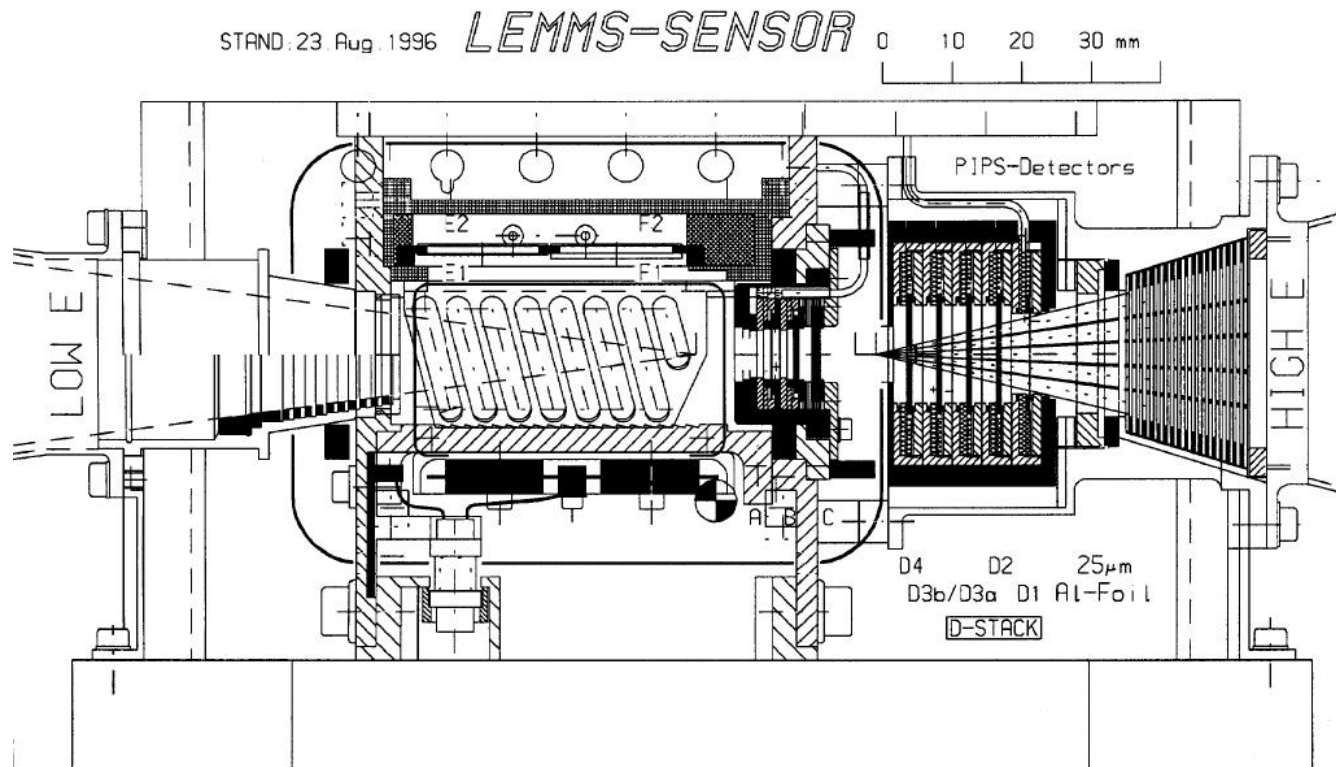


Figure 3.12. Configuration of the LEMMS detector head. Low energy particles entering the low energy end (LOW E) are measured with detectors E1, E2, F1, and F2 for electrons and A and B for ions. Particles with higher energies enter the high energy end (HIGH E) and are detected in a stack of detectors; D1, D2, D3a, D3b, and D4. [From *Krimigis et al.*, 2004.]

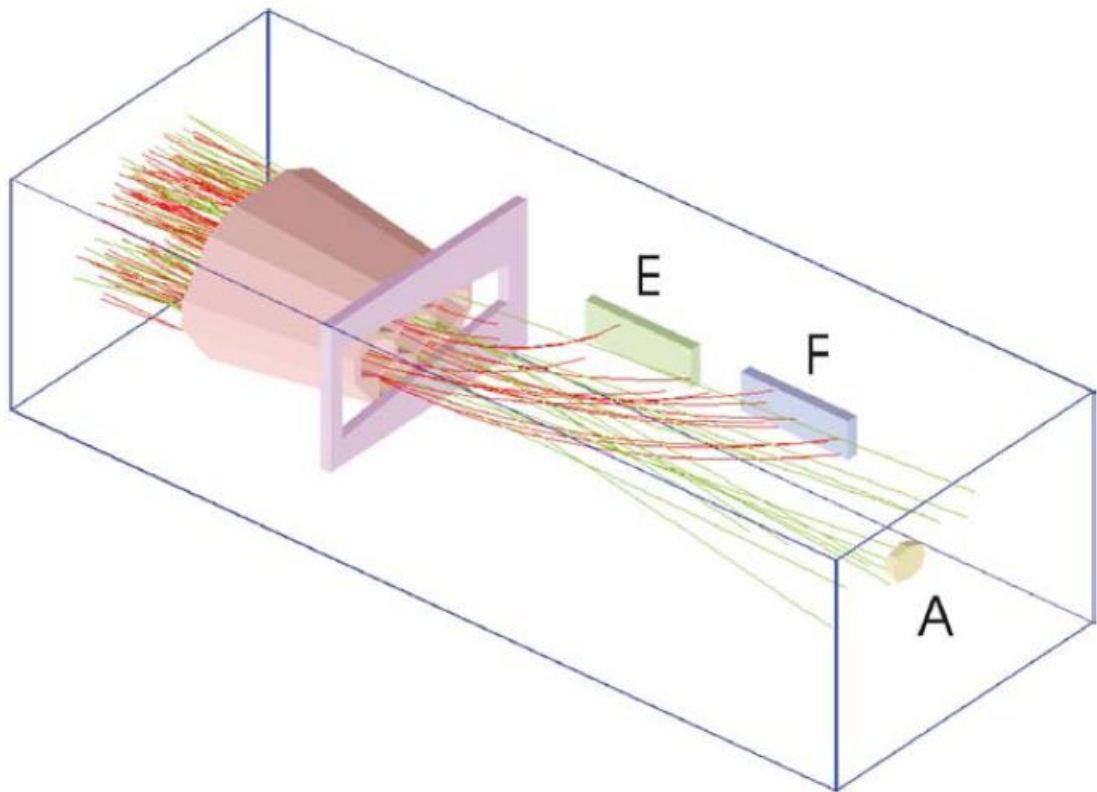


Figure 3.13. Particle trajectories in the LEMMS low energy end (from a simulation).
 [From *Krimigis et al.*, 2004.]

3.6 - The Cassini Radio and Plasma Wave Science Investigation

The Cassini Radio and Plasma Wave Science (RPWS) investigation [Gurnett *et al.*, 2004] is designed to study radio emissions, plasma waves, thermal plasma, and dust at Saturn. It does this by measuring the electric and magnetic fields, along with the electron density and temperature in the vicinity of the spacecraft. The RPWS instrument also measures the flux of dust and makes estimates of the mass of dust particles from the signature of impacts with the spacecraft. The RPWS instrumentation consists of three orthogonal magnetic antennas, three nearly-orthogonal electric antennas, a Langmuir probe, five receivers and the associated electronics.

The Langmuir probe is a positively charged metallic sphere, which is used to measure the electron density and temperature. A bias voltage is applied to the probe and the electrons in the surrounding plasma generate a current, which is measured as a function of the voltage. This current-voltage relation is then used to derive the electron density and temperature of the surrounding plasma. The RPWS magnetic antennas are used to detect the magnetic component of electromagnetic waves over the frequency range 1 Hz to 12 kHz while the electric field antennas are used to detect electric fields over the frequency range 1 Hz to 16 MHz. The use of three antennas allows RPWS to perform both direction-finding and polarisation measurements. The RPWS hardware is mounted in several locations on the Cassini orbiter as shown in Figure 3.14. The magnetic antennas are mounted on a short boom just under the high gain antenna; each aligned with the x , y and z axes of the spacecraft. The Langmuir probe is located at the end of a ~ 1 m boom that extends outwards from the magnetic antennas. The positions of the three electric antennas, labelled E_U , E_V and E_W are also shown. Each electric antenna is 10 m long and 2.86 cm in diameter and it should be noted that the E_U and E_V antennas can be used together as a dipole antenna (E_X), aligned along the x -axis.

A simple block diagram of the RPWS instrument is shown in Figure 3.15 with the three electric, three magnetic and Langmuir probe sensors shown on the left hand side. The data processing unit (DPU), which controls all instrument functions and handles all communications with the Cassini orbiter, is shown on the right. Signals from the RPWS antennas are processed by five on-board receivers, which are shown in the middle block of Figure 3.15. The high frequency receiver (HFR) provides

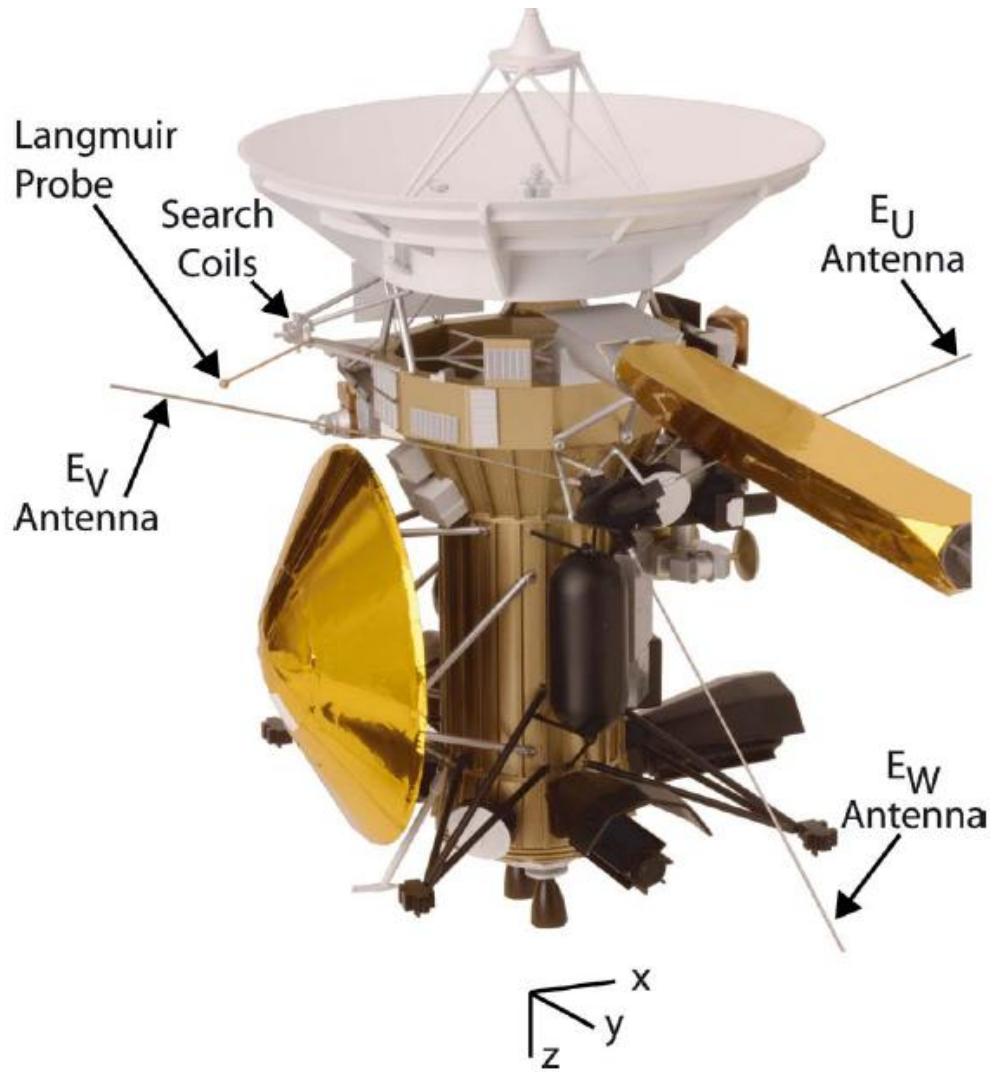


Figure 3.14. The Cassini spacecraft showing the locations of the RPWS sensors. [From Gurnett *et al.*, 2004.]

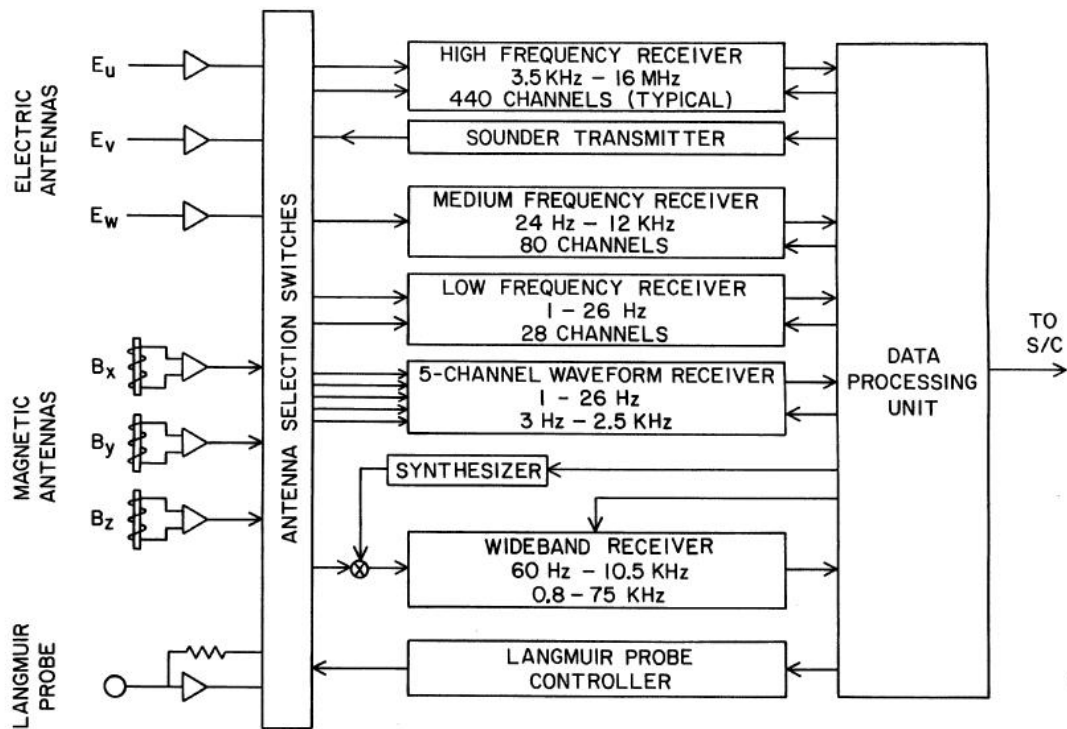


Figure 3.15. A functional block diagram of the RPWS instrument. [From Gurnett *et al.*, 2004.]

simultaneous auto- and cross-correlation intensity measurements from two selected antennas (the E_W antenna and any of the E_X , E_U or E_V antennas) over the frequency range 3.5 kHz to 16 MHz. Typically, the two inputs of the HFR switches between the three monopole antennas so that direction of arrival measurements can be made. The medium frequency receiver (MFR) provides intensity measurements over the frequency range 24 Hz to 12 kHz for a single antenna. In order to provide information about the electric and magnetic components of plasma waves, this receiver usually operates in a mode that toggles between the E_X electric dipole antenna and the B_X magnetic antenna. The low frequency receiver (LFR) also usually operates between the E_X and B_X antennas to provide intensity measurements over a frequency range of 1 to 26 Hz. The five channel waveform receiver (WFR) collects waveform measurements from up to five sensors simultaneously (e.g. two electric and three magnetic antennas) over short intervals. It operates over a frequency range of 1 Hz to 2.5 kHz in two bands; 1 to 26 Hz, or 3 Hz to 2.5 kHz. The wideband receiver provides near-continuous wideband electric and magnetic field waveform measurements over a frequency band of 60 Hz to 10.5 kHz or 800 Hz to 75 kHz using a single sensor (e.g. E_U , E_V , E_X , E_W , B_X , or the Langmuir probe). The RPWS instrument is quite complex and depending on its mode of operation the various receivers perform spectral analysis to provide intensity measurements over specific frequency bands and at a certain resolution. In this thesis we use total electron density measurements at 8-16 second resolution obtained from RPWS measurements of the upper hybrid resonance frequency (f_{UH}) using the HFR. An example frequency-time spectrogram showing an f_{UH} emission band is shown in Figure 3.16. Automatic data processing routines are used to track f_{UH} and compute the corresponding electron density as described below.

The upper hybrid frequency is given by $\omega_{UH} = (\omega_p^2 + \omega_c^2)^{1/2}$ where ω_p is the electron plasma angular frequency $\left[\omega_p = \left(\frac{n_e e^2}{\epsilon_0 m_e} \right)^{1/2} \right]$, and ω_c is the electron cyclotron angular frequency $\left[\omega_c = \frac{eB}{m_e} \right]$. Combining these expressions and using $f = \frac{\omega}{2\pi}$ we obtain the electron density, n_e (in cm^{-3}), $n_e = \frac{(f_{UH}^2 - f_C^2)}{(8980)^2}$. The electron cyclotron

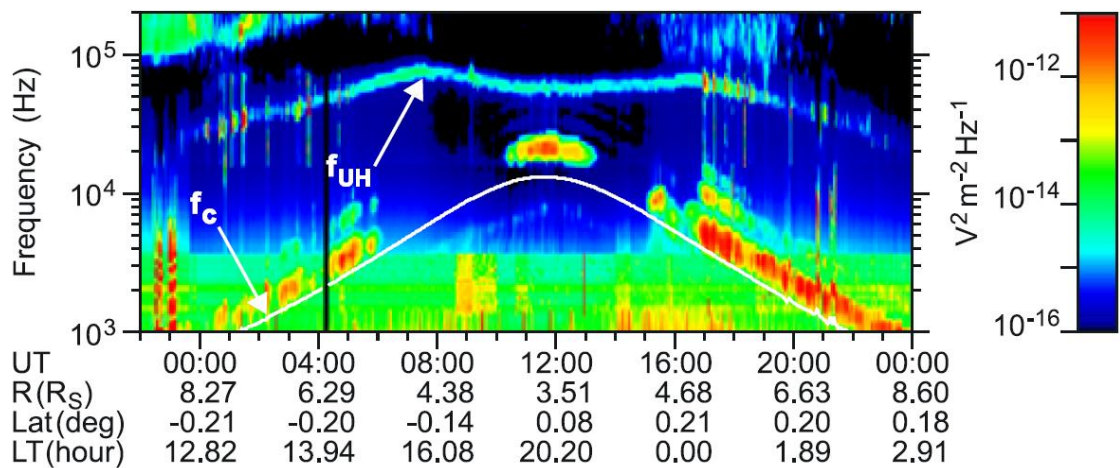


Figure 3.16. A frequency-time spectrogram showing electric field intensities detected by the Cassini RPWS during the pass through Saturn's inner magnetosphere on March 8-10, 2005. The narrowband emission marked f_{UH} is at the upper hybrid frequency. The white line marked f_c is the electron cyclotron frequency, derived from measurements of the magnetic field. [From *Persoon et al.*, 2005.]

frequency, f_C , is shown by the white line in Figure 3.16 and is computed from magnetic field measurements using $f_C = 28B$ where B is the magnitude of the magnetic field in nT, and f_C is in Hz.

Chapter 4

Thickness of Saturn's ring current determined from north-south Cassini passes through the current layer

4.1 – Introduction

As discussed in Section 2.8, direct determinations of the thickness of Saturn's ring current from magnetic field measurements have to date only been obtained from Pioneer-11 and Voyager data, yielding values for the half-thickness on either side of the equator of between ~ 1.5 and $\sim 3 R_S$ [Connerney *et al.*, 1981b; Bunce and Cowley, 2003; Giampieri and Dougherty, 2004]. However, these thickness estimates only provide overall values due to the oblique nature of the fly-by trajectories (see further discussion in Section 4.2 below), and in principle could also have been systematically affected by the seasonal offset of the current sheet from the spin equator also discussed in Section 2.8. The latter offsets were probably small, however, $\sim 0.1 R_S$ or less, during at least the Pioneer-11 and Voyager-1 fly-bys, due to the near-equinoctial conditions then prevailing [e.g., Arridge *et al.*, 2008b]. Thickness determinations could not be made from the data obtained from the initial phase of the Cassini mission, since the spacecraft orbit was near-equatorial for the first 28 revolutions ('Revs') about the planet, spanning the interval from Saturn orbit insertion (SOI) in July 2004 to August 2006. These data were ideal for studying the radial extent of the ring current, but in their modelling of the equatorial field perturbations Bunce *et al.* [2007] employed an assumed fixed value of the ring current half-thickness of $2.5 R_S$, based on the earlier fly-by results cited above.

Subsequent to this initial interval, however, the orbit of Cassini was tilted out of Saturn's equatorial plane, leading to a 'high latitude' mission phase extending from September 2006 to May 2007 (Revs 29 to 44). During this phase the spacecraft cut significantly north-south through the equatorial plane, allowing direct study of the current sheet thickness and its relation to the distributions of cool and warm plasma. However, many of these trajectories crossed the equatorial plane too close to the planet to pass directly through the ring current region near periapsis, while all of them were too distant at apoapsis, then being located either in the magnetosheath/solar wind or in the magnetotail. However, on six orbits, unique within this first 'high latitude' phase,

the spacecraft passed north-south through the equatorial plane at almost fixed radial distance within the ring current region, thus allowing a direct study of the north-south structure. Three of these passes occurred in the post-noon sector and three post-midnight, each at radial distances of ~ 9 , ~ 12 and $\sim 15 R_S$.

In this chapter we present the magnetic field and plasma electron data from these orbits, determine the thickness and offset of the current layer that was present, model the magnetic perturbations observed, and make an initial comparison with the plasma electron populations. We begin by describing the magnetic field modelling technique employed. The trajectory of Cassini through the ring current region on the six unique orbits is discussed and compared to the fly-by trajectories of Pioneer-11 and Voyagers-1 and -2 in Section 4.3. The results are presented in Section 4.4, along with a comparison of the offsets of the ring current layer from the equatorial plane obtained from this study with those derived from the *Arridge et al.* [2008b] model. The chapter then concludes with a summary in Section 4.5.

4.2 – Modelling Saturn’s ring current

In this chapter we employ a slightly augmented form of the CAN model to assess the magnetic field perturbations observed. We recall from Section 2.8 that in this model the current is taken to flow in an equatorially-centred cylindrically-symmetric disk whose axis of symmetry is the planet’s spin and magnetic axis. It is therefore convenient to employ cylindrical ρ - z coordinates, where ρ is the perpendicular distance from the axis of symmetry, and z is the distance along the axis from the equatorial plane, positive northward. The current disk is defined by an inner cylindrical radius R_1 , an outer cylindrical radius R_2 , and a half-thickness D . Within the disk the azimuthal current density is taken to be

$$j_\varphi(\rho) = \frac{I_0}{\rho} \quad , \quad (4.1)$$

where I_0 (with units of $A\ m^{-1}$) is a constant defining the magnitude of the current. Outside the disk the current density is zero.

It is evident that accurate determination of ring current parameters R_1 and R_2 requires magnetic data spanning the radial range of the current disk, while

determination of half-thickness D requires significant spacecraft motion north-south through the current layer. Figure 4.1 shows the trajectories of the pre-Cassini fly-bys in ρ - z coordinates, where the red line shows the trajectory of Pioneer-11, while the green and blue lines show the trajectories of Voyager-1 and -2, respectively. The inbound passes of all these spacecraft were in the noon sector, while the outbound passes were in the dawn to post-midnight sector. It can be seen that each of these trajectories spanned a significant radial range, combined with some north-south motion in the near-equatorial region. The regions occupied by the ring current inferred from these fly-by data using the above model are shown by the dashed line boxes in Figure 4.1. The green box shows the current region inferred by *Connerney et al.* [1983] using both Voyager data sets, with inner and outer radii of 8.0 and 15.5 R_S , a half-thickness of 3.0 R_S , and a current parameter given by $\mu_0 I_0 \approx 60.4$ nT. The red box similarly shows the current region inferred from Pioneer-11 data by *Bunce and Cowley* [2003] when the magnetosphere was more compressed by the solar wind than during the Voyager fly-bys. This current disk has inner and outer radii of 6.5 and 12.5 R_S , a half-thickness of 2.0 R_S , and a current parameter $\mu_0 I_0 \approx 76.5$ nT. The total magnetic moment associated with these current disks integrates to 21% of the planetary dipole moment for the Pioneer-11 data, and 38% of the planetary moment for the Voyager data. While these values were derived from overall fits to the magnetic field data, *Giampieri and Dougherty* [2004] made separate fits to the inbound and outbound data in each case, noting the differing local times of these passes. The inner radii were found to lie between ~ 6 and 8 R_S in all cases, as above, while the outer radii lay in the range ~ 12 to ~ 15 R_S for the inbound passes, also as above, and at larger distances of ~ 18 R_S for the outbound passes. The half-thickness ranged between 1.5 and 3.1 R_S on the inbound passes, and 2.4 to 2.8 R_S on the outbound passes. However, it can be seen from Figure 4.1 that these thickness estimates represent overall values for the current disk due to the simultaneous motion of the spacecraft in both ρ and z .

The black dashed box in Figure 4.1 shows a typical ring current disk cross-section determined by *Bunce et al.* [2007] from Cassini data obtained during the initial near-equatorial phase of the mission. This study analysed only the north-south (B_z) magnetic component data, from which the radial extent of the ring current could be determined, together with the total current integrated in thickness through the layer proportional to

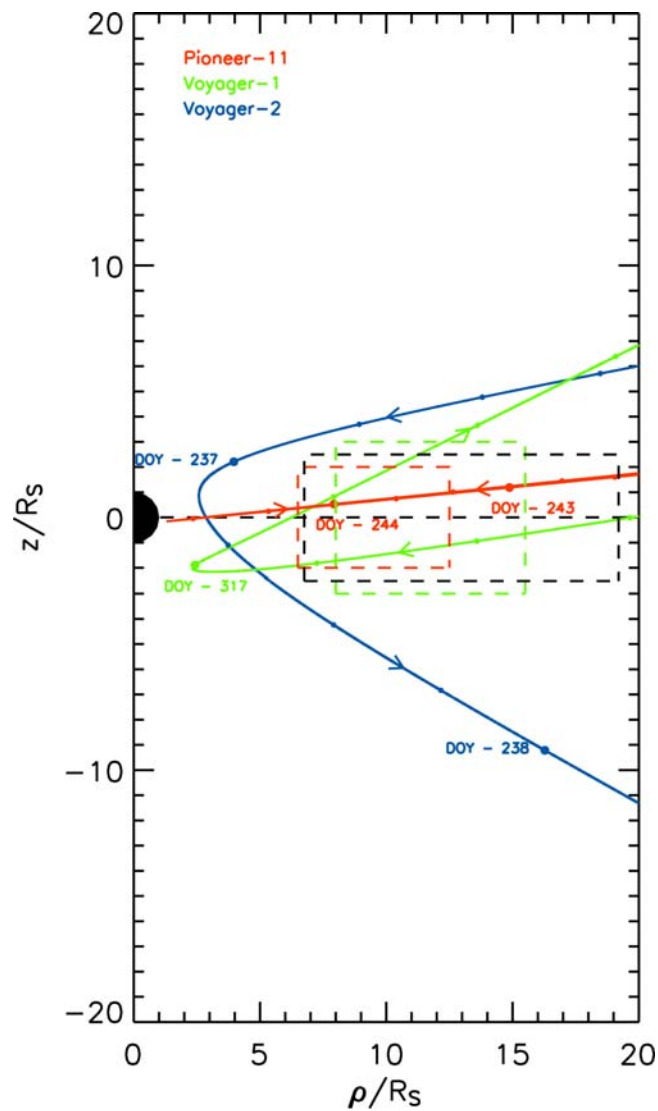


Figure 4.1. The trajectories of Pioneer-11, Voyager-1, and Voyager-2 relative to Saturn, in cylindrical coordinates. The horizontal axis shows the cylindrical radial distance from the planet’s spin (and magnetic) axis ρ , in R_s , while the vertical axis shows the distance from the equatorial plane z , also in R_s . The Pioneer-11 trajectory is shown in red, Voyager-1 in green, and Voyager-2 in blue. The large circles on each trajectory show day boundaries as indicated by the ‘day of year’ (DOY) numbers, while the smaller circles are 6 h markers. The dashed line boxes show the ring current region inferred from Pioneer-11 (red), Voyager (green), and Cassini (black) data.

$\mu_0 I_0 D$, but not the half-thickness D itself. For definiteness, a constant half-thickness of $2.5 R_S$ was thus assumed, as indicated above, on the basis of the previous fly-by results. Following an initial suggestion by *Alexeev et al.* [2006] based on the fly-by data and Cassini SOI modelling results, *Bunce et al.* [2007] showed that while the current sheet inner radius R_1 is nearly constant at $\sim 7 R_S$, the outer radius R_2 is strongly modulated by the size of the magnetosphere determined by the solar wind dynamic pressure, varying typically in the range between 15 and $21 R_S$ for strongly compressed and strongly expanded magnetospheres, respectively. The current region shown in Figure 4.1 corresponds to a sub-solar magnetopause distance of $22.6 R_S$, which is the median value in the Cassini magnetopause study reported by *Arridge et al.* [2006], associated with a solar wind dynamic pressure of 0.026 nPa. This current disk then has inner and outer radii of 6.75 and $19.2 R_S$, respectively. *Bunce et al.* [2007] showed that the current parameter $\mu_0 I_0$ also modestly increases with the system size. Overall, their study indicates that the magnetic moment of the ring current increases from $\sim 20\%$ of the planetary magnetic moment for highly compressed conditions (as for Pioneer-11) to $\sim 60\%$ of the planetary moment for highly expanded conditions.

4.3 – North-south Cassini passes through the ring current layer

In Figures 4.2 and 4.3 we show the trajectory of the Cassini spacecraft for the six unique orbits during the high-latitude mission phase in which the spacecraft passed essentially north-south through the ring current layer. Figure 4.2 shows the trajectories in a Cartesian coordinate system in which z points along the planet’s spin and magnetic axis, the x - z plane contains the Sun, and y completes the right-hand system. The panels of the figure show the trajectory as coloured solid lines projected into the equatorial x - y plane (top), the noon-midnight x - z plane (middle), and the dawn-dusk y - z plane (bottom). The dashed line in the top and middle panels also shows for reference the *Arridge et al.* [2006] model magnetopause position computed for the median sub-solar magnetopause distance of $22.6 R_S$ mentioned above. The panels in Figure 4.2a show the trajectories which passed through the ring current on the dayside, namely Revs 35 (red), 36 (green), and 37 (blue), while the panels in Figure 4.2b similarly show the trajectories that passed through the ring current on the nightside, namely Revs 40 (blue), 41 (green), and 42 (red). Large black dots on the trajectories are day markers, while small black dots indicate six hour intervals. Some day markers are labelled by the day

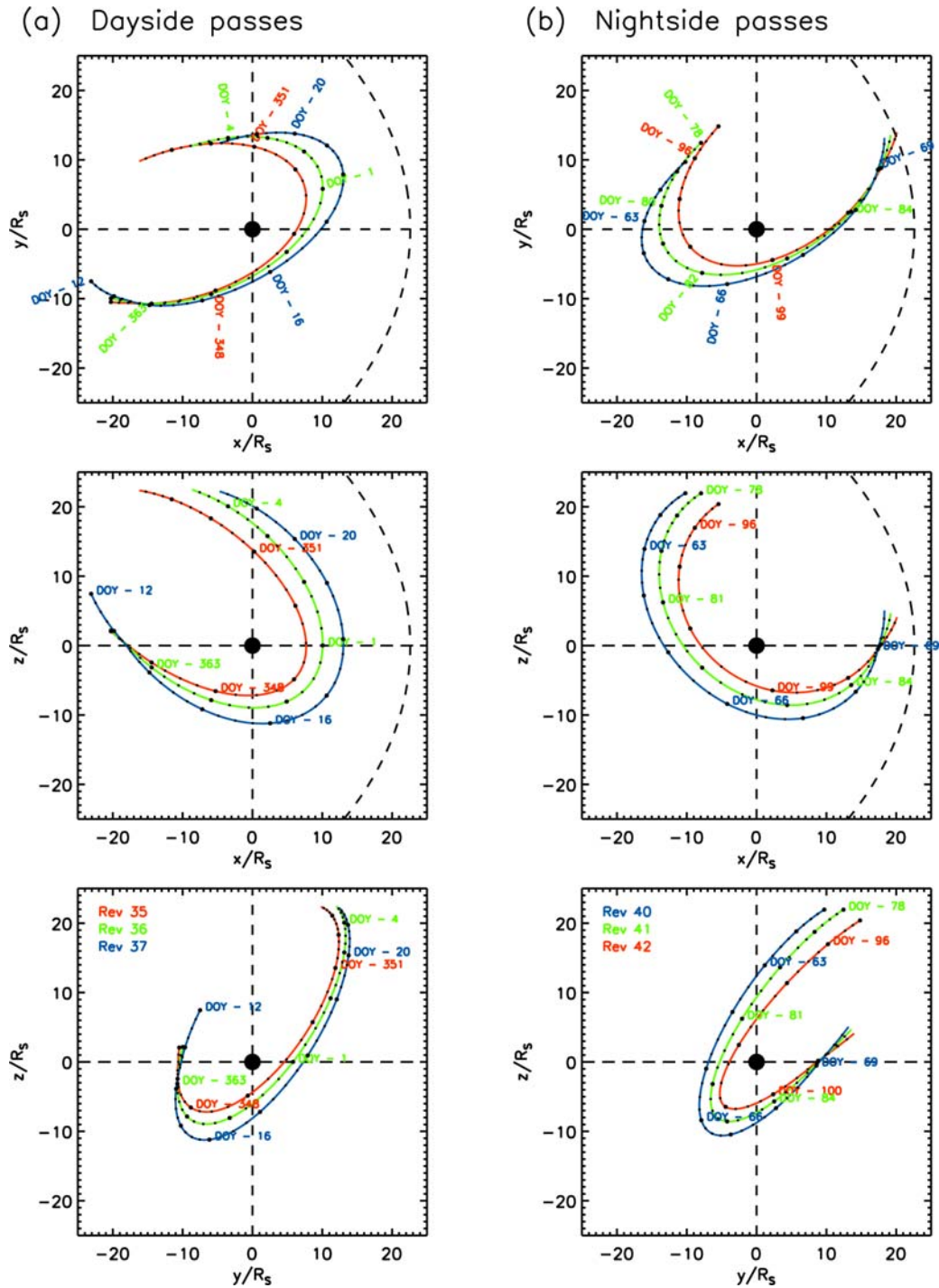


Figure 4.2. Cassini trajectories through the ring current region for each pass examined in this chapter. The coordinate system employed is such that z points along the planet's spin axis, the x - z plane contains the Sun, and y completes the right-hand system. The left-hand panels show the trajectories of the dayside passes, Rev 35 in red, Rev 36 in green, and Rev 37 in blue, while the right-hand panels similarly show the trajectories of the nightside passes, Rev 40 in blue, Rev 41 in green, and Rev 42 in red.

of year (DOY) number in the colour corresponding to the trajectory. These refer to the DOY in 2006 for Rev 35, and in 2007 for Revs 37-42, while Rev 36 spanned the year boundary. Figure 4.2a shows that on Revs 35-37 the spacecraft passed from south to north across the equatorial ring current in the post-noon sector. The equatorial crossings were at a radial distance of $8.8 R_S$ and a local time 14.1 h for Rev 35, $12.0 R_S$ and 14.2 h for Rev 36, and $15.0 R_S$ and 14.1 h for Rev 37 (the local times quoted here are in decimal hours). Figure 4.2b similarly shows that on Revs 40-42 the spacecraft passed from north to south across the ring current in the post-midnight sector. These equatorial crossings were at $15.3 R_S$ and 1.7 h for Rev 40, $12.0 R_S$ and 1.7 h for Rev 41, and $9.1 R_S$ and 1.4 h for Rev 42.

Figure 4.3 shows these trajectories in cylindrical ρ - z coordinates, using a similar format in which the dayside ring current passes are shown on the left and the nightside passes on the right. The black dashed box again indicates the ring current region inferred from Cassini data by *Bunce et al.* [2007] for the median magnetopause position, as in Figure 4.1. Comparison with the corresponding plot for the fly-by trajectories in Figure 4.1 (plotted on the same scale) highlights the very different ring current coverage provided by these Cassini orbits, which for the first time allow direct exploration of the north-south structure of the ring current layer at almost constant distance from the magnetic axis. Of course, these passes do not then provide detailed information on the simultaneous radial structure of the ring current then prevailing, but this uncertainty is ameliorated by the information obtained from the previous studies cited above on typical parameter values and their variability.

4.4 – Cassini observations on north-south passes through the ring current

4.4.1. Recognising the Current Layer in Magnetic Field Data

We begin our discussion of the Cassini observations by outlining how we recognise the current layer in magnetic field data. We imagine an annular disk, such as those depicted in the cross sections in Figures 4.1 and 4.3, carrying an azimuthal current of approximately uniform density across its width and consider the anticipated variation of the field components. First, from $\text{div } \mathbf{B} = 0$, the axial component B_z is not expected to vary greatly across the width of the current sheet and in the region immediately outside

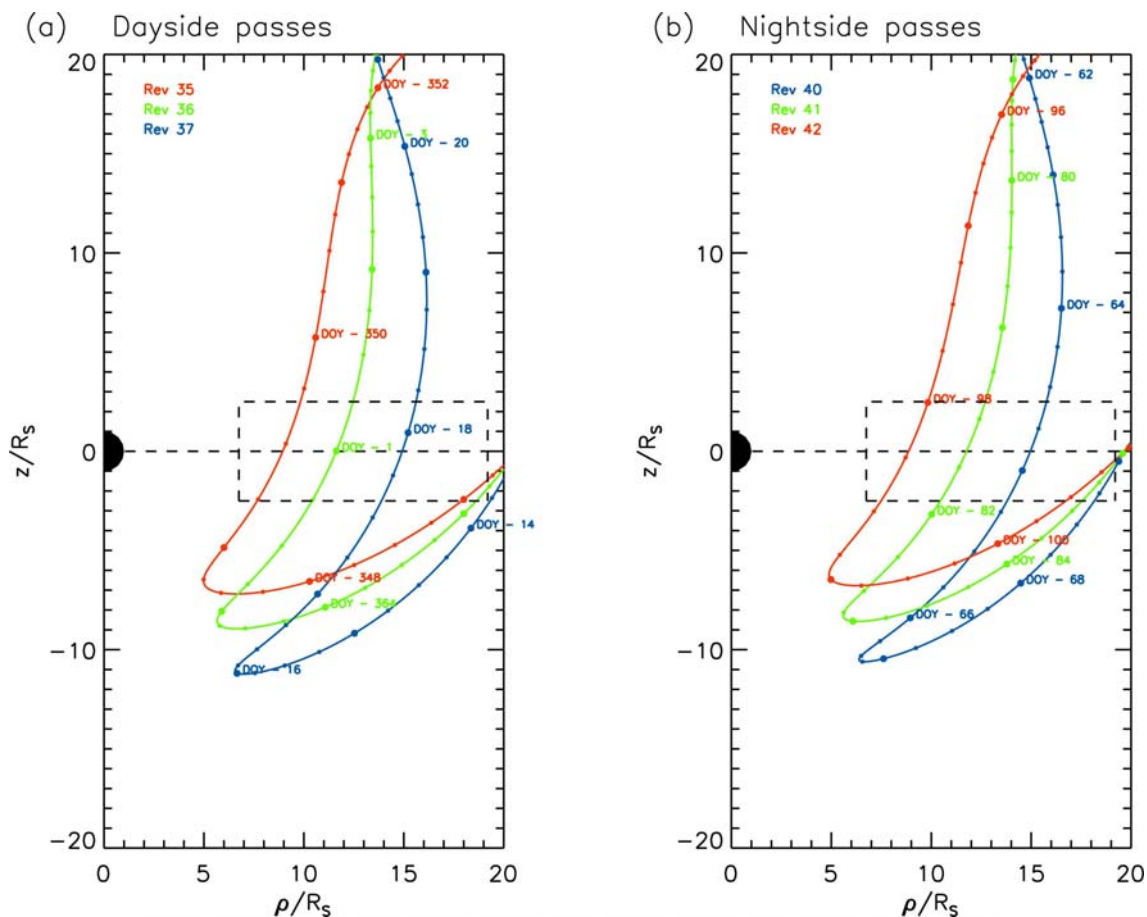


Figure 4.3. Cassini spacecraft trajectories are shown relative to Saturn in cylindrical ρ - z coordinates for each pass examined in this chapter. The left-hand panel shows the dayside passes, Rev 35 in red, Rev 36 in green, and Rev 37 in blue, while the right-hand panel shows the nightside passes, Rev 40 in blue, Rev 41 in green, and Rev 42 in red, in a similar format to Figure 4.1. The black dashed box shows the ring current region inferred from Cassini data.

the current layer, such that it does not provide clear constraints on the thickness of the layer. Second, however, the radial component B_ρ should vary approximately linearly with z within the current layer, while declining slowly with distance outside due to the finite size of the current disk. The north-south boundaries of the current layer, and hence its thickness, should thus be evident in the B_ρ component data, where an approximately linear growth with z within the layer gives way to a slow decay in magnitude beyond. This is the primary current sheet position diagnostic employed here.

In addition, however, we also seek to show to what extent the field perturbations can be modelled by the technique outlined in Section 4.2, thus lending support, or otherwise, to the identification of the location of the annular current disk by the above simple means. We recall from the previous section that while the data on the chosen passes should provide detailed information on the position and thickness of the current layer in the north-south direction, the coverage in radius is insufficient to provide accurate positions for the inner and outer radii of the current disk. In this case we simply use fixed values in the modelling, based on the ‘median’ model of *Bunce et al.* [2007] described in Section 4.2 above. Thus we use $R_1 = 6.75 R_S$ and $R_2 = 19.2 R_S$ throughout, corresponding to a median subsolar magnetopause distance of $22.6 R_S$. We note that predictions of the magnetopause distances for these passes based on the *Arridge et al.* [2006] model combined with the results of *Zieger and Hansen* [2008], in which solar wind conditions at Earth have been propagated to Saturn’s orbit using a magnetohydrodynamic (MHD) code, indicate that all these passes occurred under uncompressed conditions with a typical magnetopause distance of $\sim 25 R_S$, in approximate conformity with this choice. The half-thickness D in the disk model is then determined from the behaviour of the B_ρ field with z as outlined in the above discussion, while the current strength parameter $\mu_0 I_0$ is varied to give the best overall fit.

One issue with this procedure concerns the position of the north-south boundaries of the current layer determined from the B_ρ data, since as will be shown below, these imply the presence of small displacements of the centre of the current layer principally northward of the planet’s equator, particularly at larger radial distances, in approximate conformity with the results of *Arridge et al.* [2008b]. For simplicity we have then

displaced the whole current disk along the z axis, typically by a few tenths of an R_S , so that the north-south position of the model current layer agrees with that of the dominant currents that are local to the crossing. While this procedure thus takes account of the local displacement of the current layer from the equatorial plane, it does not take account of the tilting of the layer associated with the varying displacement with radial distance. However, the results of *Arridge et al.* [2008b] indicate that in the middle magnetosphere region examined here these tilt angles are typically only a few degrees (as confirmed by our results). The investigation of *Arridge et al.* [2008b] has shown that this tilt produces only minor effects on the model field profiles for highly inclined cuts through the current layer. A more intensive approach to the variable offset issue is therefore not justified for present purposes, though this effect must be included in data modelling for oblique passes through the current layer in which the offset may vary considerably while the spacecraft is in contact with the current layer [*Arridge et al.*, 2008b]. In view of the additional parallel uncertainties concerning, for example, the variability of the current sheet thickness and strength with radius and local time, a simple approach to determine the extent to which these data can be fitted by our simple model seems a reasonable initial step.

In addition to the current disk, we also include in the modelling a simple description of the fringing field of the magnetopause and tail current system, representing the curl-free field in the middle magnetosphere that results from the magnetopause surface currents and the central tail current sheet. This field was introduced by *Bunce et al.* [2007] in their modelling of the Cassini equatorial B_z data, and was found to improve the fit to these data while not greatly influencing the choice of ring current parameters, the additional field being typically $\sim 10\%$ of the peak perturbation field due to the ring current itself. Using the same Cartesian system as introduced above in relation to Figure 4.2, a linear dependence of B_z on x and approximate independence of y was assumed on the basis of prior magnetospheric magnetic modelling results [*Alexeev and Feldstein*, 2001; *Alexeev and Belenkaya*, 2005]. The field varies from a few nT negative near the subsolar magnetopause (due to the compressive effect of the solar wind dynamic pressure), to a few nT positive at similar distances on the nightside (due to the effect of the tail current system). The same model is adopted here, such that within distances of several R_S of the equatorial plane we have

$$B_z(x) = ax + b \quad . \quad (4.2)$$

Just one typical set of parameters is employed in the fits to all the passes, given by $a = -0.1 \text{ nT R}_S^{-1}$ and $b = 2.0 \text{ nT}$. This field is such that $B_z = -0.26 \text{ nT}$ near the subsolar magnetopause at $x = 22.6 \text{ R}_S$ (the median value as above), while $B_z = 4.26 \text{ nT}$ at similar distances in the tail, in overall conformity with the results of *Bunce et al.* [2007]. In addition, however, we now also introduce a related $B_x(z)$ field which ensures that the fringing field within the middle magnetosphere region is curl-free. This is simply

$$B_x(z) = az \quad , \quad (4.3)$$

where the arbitrary constant term has been taken to be zero by symmetry. This field thus contributes to B_ρ in a way that depends on the azimuth of the point in question (i.e. on local time). For a negative, on the nightside it enhances the B_ρ reversal across the equator produced by the ring current, while on the dayside it reduces the B_ρ reversal.

In addition to the field data, in the following sections we also display plasma electron spectrograms over the energy range 0.6 eV-26 keV, obtained by the electron spectrometer of the Cassini Plasma Spectrometer (CAPS/ELS) investigation [*Young et al.*, 2004]. These data will be used to provide an initial indication of the location of the current layer inferred from the magnetic field measurements relative to the distribution of magnetospheric plasma about the equator. Discussions of the electron populations observed on near-equatorial passes through the magnetosphere on other Cassini orbits may be found in *Young et al.* [2005], *Schippers et al.* [2008], *André et al.* [2008], and *Lewis et al.* [2008].

4.4.2. Dayside Passes

In Figure 4.4 we show results for the three passes through the dayside ring current layer, on Revs 35-37, shown in Figures 4.4a-c, respectively. Each panel shows two days of data centred near the equatorial plane crossing, which span north-south distances of $\sim 10 \text{ R}_S$ on either side as seen in Figures 4.2 and 4.3. The top panel of each plot shows an electron spectrogram, colour-coded according to the scale on the right, the scale being maintained constant throughout the plots shown here. The second and third panels then show the residual radial and axial fields determined from the spacecraft

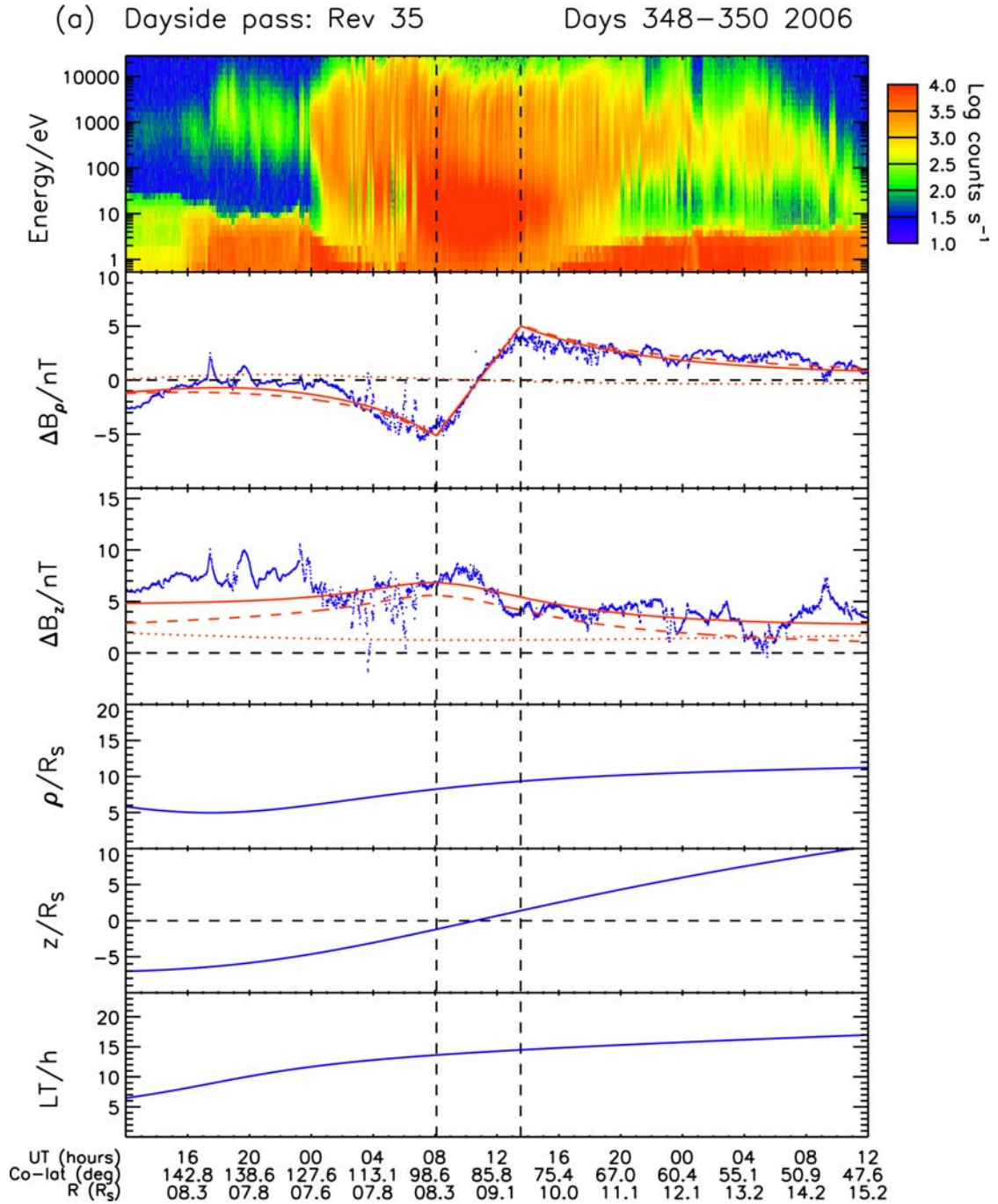


Figure 4.4a. Plot showing Cassini electron, magnetic field, and position data for Rev 35, a dayside passes through the ring current region. The top panel of the plot shows an electron spectrogram colour-coded according to the scale on the right. The second and third panels show the cylindrical radial and axial residual magnetic field components, ΔB_ρ and ΔB_z (in nT). The two vertical black dashed lines show the north-south boundaries of the current layer determined from the behaviour of the ΔB_ρ data. The fourth to sixth panels show spacecraft position data.

(b) Dayside pass: Rev 36

Days 365 2006-001 2007

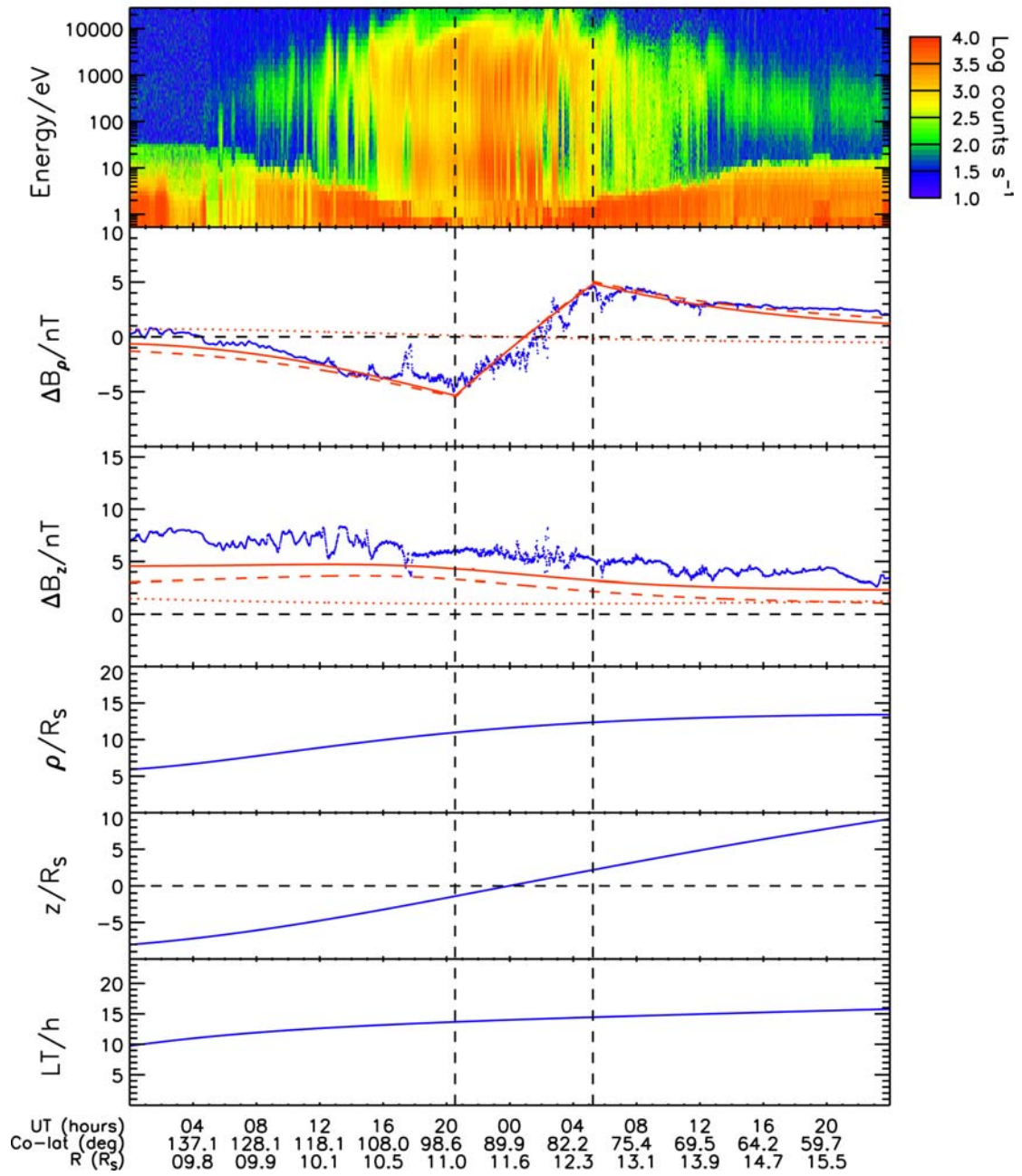


Figure 4.4b. As for Figure 4.4a except for Rev 36.

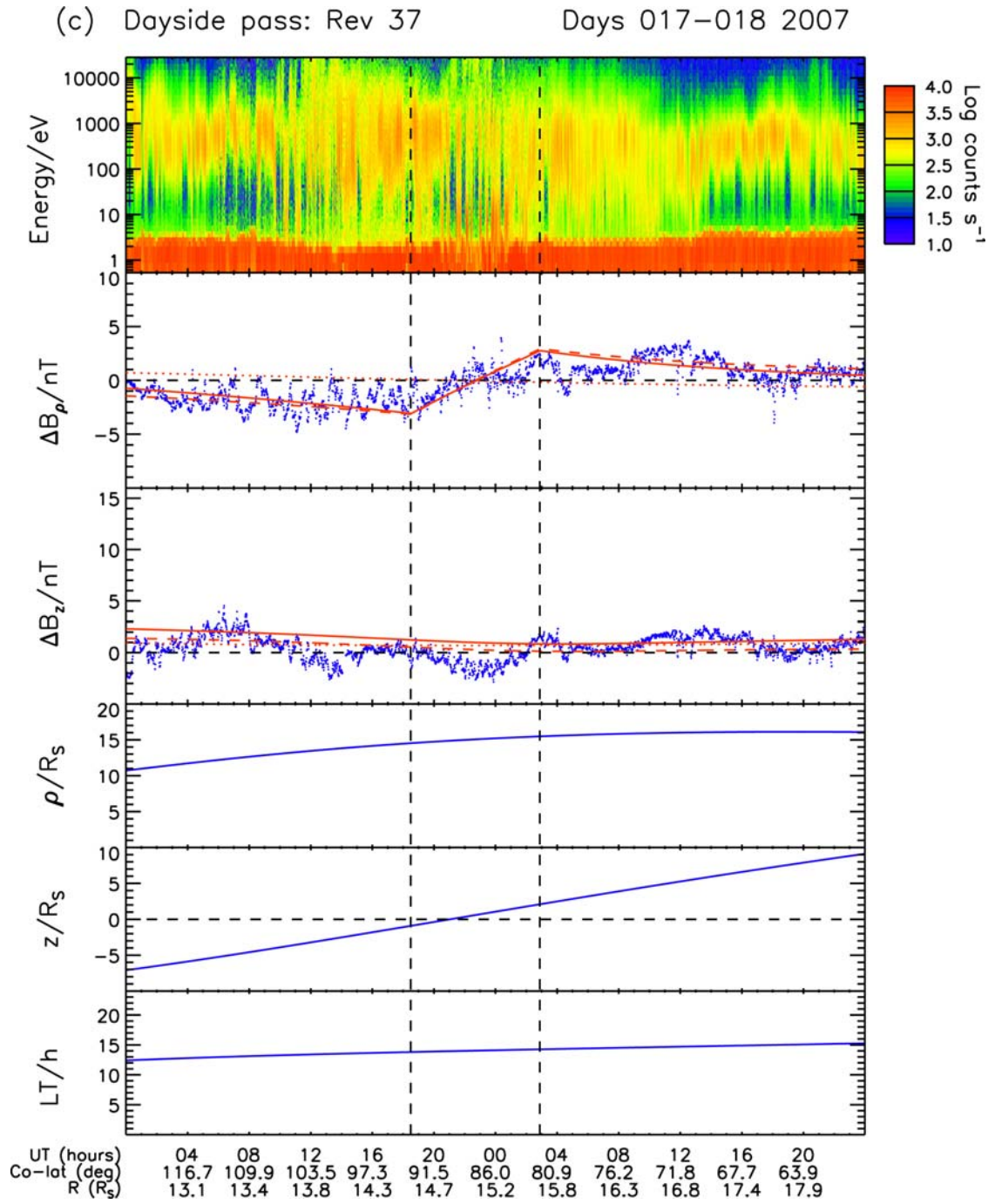


Figure 4.4c. As for Figure 4.4a except for Rev 37.

measurements, ΔB_ρ and ΔB_z , respectively, from which the ‘Cassini SOI’ internal field model of *Dougherty et al.* [2005] has been subtracted. These panels also show the fitted model field values, where the red dashed lines show the field due to the model ring current, the red dotted lines the fringing field of the magnetopause-tail current system, and the red solid lines the sum of these two. The two vertical black dashed lines show the north-south boundaries of the current layer determined from the behaviour of the ΔB_ρ data as will be discussed below. The fourth to sixth panels show spacecraft position data in cylindrical coordinates, specifically ρ and z in R_S , together with the local time in hours, while time and position data in spherical coordinates (the co-latitude angle from the north polar axis in degrees and the radial distance from the planet in R_S) are given at the foot of each panel.

We first examine Figure 4.4a showing results for Rev 35, corresponding to the innermost of the dayside passes, with a crossing of the equatorial plane at a radial distance of $8.9 R_S$ in the inner part of the ring current. Examination of the second panel shows a near-linear increase of ΔB_ρ with z centred near the equatorial crossing, followed by clearly-defined extrema and slower declines in field magnitude on either side. As discussed above, the extrema in ΔB_ρ represent the key signatures of the north-south current sheet boundary locations, marked by the vertical black dashed lines in the panel. We also note the anticipated near-constancy of the axial field ΔB_z shown in the third panel, though with considerable short-scale variability superposed. Denoting the z positions of the southern and northern boundaries of the current layer by z_1 and z_2 respectively, we find in this case that $z_1 = -1.2 R_S$ and $z_2 = 1.4 R_S$, thus giving a half-thickness $D = (z_2 - z_1)/2 = 1.3 R_S$, and an offset of the current sheet centre north of the equatorial plane of $\Delta z = (z_2 + z_1)/2 = 0.1 R_S$. The uncorrelated uncertainties in z_1 and z_2 , due mainly to the short-scale variability in the field data, yield uncertainties of about $\pm 0.2 R_S$ in both D and Δz (being given by $\pm \sqrt{\Delta z_1^2 + \Delta z_2^2}$). The uncertainties in these quantities for all the Revs considered here are of approximately the same magnitude. In the present case this implies an uncertainty in the half-thickness of about $\pm 15\%$, while the offset is consistent with zero. The position, half-thickness, and offset values are recorded for this and all the other crossings studied here in Table 4.1, together with further details such as the cylindrical radial distance of the north-south

Table 4.1. List of current sheet boundary crossing times and positions together with fitted current system parameters

Rev number	Current sheet crossing interval (DOY)	ρ_1 (R _S)	ρ_2 (R _S)	LT_1 (dec hr)	LT_2 (dec hr)	z_1 (R _S)	z_2 (R _S)	D (R _S)	Δz (R _S)	$\mu_0 I_0$ (nT)	k_{RC}	ΔB_ρ RMS deviation (nT)	ΔB_z RMS deviation (nT)
Dayside passes													
35	08:05 UT 349 – 13:34 UT 349	8.3	9.4	13.6	14.5	-1.2 ± 0.3	1.4 ± 0.3	1.3 ± 0.2	0.1 ± 0.2	48 ± 4	0.24	0.8	1.8
36	20:35 UT 365 – 05:18 UT 001	11.0	12.4	13.7	14.5	-1.4 ± 0.3	2.2 ± 0.3	1.8 ± 0.2	0.4 ± 0.2	44 ± 4	0.30	0.9	2.0
37	18:32 UT 017 – 02:54 UT 018	14.5	15.5	13.8	14.3	-0.9 ± 0.3	2.1 ± 0.3	1.5 ± 0.2	0.6 ± 0.2	37 ± 4	0.21	1.2	1.5
Nightside passes													
40	17:55 UT 064 – 20:08 UT 064	15.1	15.4	1.8	1.7	0.3 ± 0.2	1.1 ± 0.2	0.4 ± 0.15	0.7 ± 0.15	338 ± 26	0.52	1.0	1.0
41	10:15 UT 081 – 22:47 UT 081	10.3	12.7	2.5	1.3	-2.8 ± 0.4	2.2 ± 0.4	2.5 ± 0.3	-0.3 ± 0.3	49 ± 4	0.47	0.7	1.2
42	03:12 UT 098 – 05:26 UT 098	8.9	9.3	1.8	1.5	-0.2 ± 0.2	0.8 ± 0.2	0.5 ± 0.15	0.3 ± 0.15	156 ± 12	0.30	2.9	2.6

boundary positions (ρ_1 and ρ_2), and the corresponding local times (LT_1 and LT_2). In this case, for example, the southern boundary was observed at $\rho_1 = 8.3 R_S$ and the northern at $\rho_2 = 9.4 R_S$, thus spanning a radial range of only $1.1 R_S$, while in local time the southern boundary was observed at 13.6 h and the northern at 14.5 h, thus spanning a range of only 0.9 h.

We now discuss the model fit to the Rev 35 data shown by the red lines in the second and third panels of Figure 4.4a. Since we are using a fixed model of the magnetopause-tail fringing field as described above, together with fixed median values of the inner and outer radii of the ring current disk (6.75 and $19.2 R_S$, respectively), and with the half-thickness and offset of the disk being defined by the ΔB_ρ data as shown by the vertical dashed lines in Figure 4.4a, only one ‘free’ model parameter remains, i.e. the current parameter $\mu_0 I_0$. This has been determined by visual inspection of the data combined with consideration of the RMS deviation of the data points from the model for each field component. In Figure 4.4a our best fit model has $\mu_0 I_0 = 48$ nT, with an estimated uncertainty of about ± 4 nT. The corresponding ring current magnetic moment as a fraction of the planetary dipole moment (again using the ‘Cassini SOI’ model) can be used as a global measure of the ring current strength, and has a value in this case of $k_{RC} = 0.24$. These parameters are also recorded in Table 4.1, together with the root mean squared (RMS) deviation per point of the two field components over the two days of data shown in the figure. In Figure 4.4a these values are 0.8 nT for ΔB_ρ and 1.8 nT for ΔB_z , which are relatively modest compared with overall field magnitudes peaking at ~ 5 nT. Despite the caveats noted in Section 4.4.1, these results show that the overall field perturbations are described reasonably well by the simple current disk plus fringing field model employed here.

We now briefly compare the Rev 35 magnetic field data with the simultaneous electron data shown in the top panel of Figure 4.4a. This shows that the current sheet identified in the field data corresponds only to the central layer of the electron distribution observed by the spacecraft in its passage across the equatorial magnetosphere. In fact it corresponds to the region where the fluxes of low energy electrons, of order ~ 10 eV, are at their most intense during the crossing, while also in the presence of large fluxes of higher-energy electrons, from a few 100 eV to several

keV. (Note that the intense fluxes observed below ~ 10 eV away from the centre-plane crossing are mainly spacecraft photoelectrons.) These electron properties correspond to the inner part of the middle magnetosphere region in which significant populations of both cool and warm/hot electrons co-exist (see Figure 2.5), as described previously by *Young et al.* [2005], *Schippers et al.* [2008], *André et al.* [2008], and *Lewis et al.* [2008]. Outside the current sheet the electron fluxes generally decline with increasing distance from the equator, reducing particularly steeply with $|z|$ at the lower energies, such that the warm component centred near ~ 1 keV dominates beyond $|z| \sim 4 R_S$. The continued presence of these electron populations beyond the current layer indicates that the layer is overlain by field lines that pass through the equatorial plane at larger radial distances where the electron fluxes are generally reduced (Figure 2.5).

In Figure 4.4b we similarly show results for Rev 36, the dayside pass at intermediate radial distances, in which the equatorial plane was crossed at $11.9 R_S$, near the centre of the ring current under typical conditions. As for Rev 35, the signatures of the current sheet are again evident in the ΔB_ρ data, with a near-linear rise occurring across the equatorial plane and weaker falls in strength at larger distances, while ΔB_z again shows slowly-varying positive values. In this case the current sheet boundaries (dashed black vertical lines) are estimated to be located at z values of -1.4 and $2.2 R_S$, with a consequent half-thickness of $D = 1.8 R_S$, a little wider than that for Rev 35, and an offset of $\Delta z = 0.4 R_S$ (Table 4.1). The uncertainties in these quantities are again estimated to be about $\pm 0.2 R_S$, so the northward offset is now significant. A comparison with expectations based on the *Arridge et al.* [2008b] model will be presented in Section 4.4.4 below. The best fit field model now has $\mu_0 I_0 = 44$ nT (with an uncertainty of $\sim \pm 4$ nT), similar to that for Rev 35, with $k_{RC} = 0.30$ (Table 4.1). This model again gives a good overall description of the data, though the model ΔB_z field is consistently smaller than the data by ~ 2 nT, perhaps indicating the presence of a larger magnetopause-tail fringing field due for example to stronger tail currents in this case. Comparison with the electron data in the top panel of Figure 4.4b shows that the current sheet again corresponds to the central part of the equatorial electron distribution containing both low ~ 10 eV and higher ~ 100 eV to ~ 10 keV energy electrons, though the fluxes particularly at low energies are smaller than for Rev 35 as may have been expected due to the larger radial distance of the pass. The equatorial current sheet is

thus again surrounded by a layer of cool and hot electrons of diminishing intensity with increasing distance from the equator.

The final dayside pass occurred on Rev 37 shown in Figure 4.4c, in which the equatorial plane was crossed at $15.0 R_S$, typically corresponding to the outer part of the ring current. In this case the residual field data are smaller in amplitude and ‘noisier’ than for the previous dayside passes. Despite this, a current sheet pattern is still evident in the ΔB_ρ data, with negative values in the southern hemisphere reversing to positive values in the northern hemisphere across the equatorial plane. The ΔB_z values are small, and vary quasi-periodically about a near-zero mean. In this case we estimate the boundaries of the current sheet to lie at z values of -0.9 and $2.1 R_S$ respectively, such that $D = 1.5 R_S$ and $\Delta z = 0.6 R_S$. The half-thickness D is comparable to those determined on Revs 35 and 36, implying relatively steady values on the dayside, albeit on the basis of only three examples. The offset Δz is again significant compared with the estimated uncertainties, and somewhat larger than the value for Rev 36. The best fit model shown in Figure 4.4c has a current parameter $\mu_0 I_0 = 37$ nT, a slightly smaller value than for Revs 35 and 36 but not by a large factor, with a corresponding magnetic moment parameter $k_{RC} = 0.21$ (Table 4.1). The overall fit is reasonable within the scatter of the data, with comparable RMS deviations per point in each component of ~ 1.5 nT. Comparing the field data with the electron data in the upper panel of Figure 4.4c again shows that the current sheet is embedded within a layer of hot plasma that has a much wider north-south extent on the field lines of the more distant dayside magnetosphere (Figure 2.5). The relative lack of low-energy electrons near the equatorial plane compared with those observed in Figures 4.4a and 4.4b is in conformity with previous discussions of the variations of electron properties with radial distances, for example by *Young et al.* [2005], *Schippers et al.* [2008], *André et al.* [2008], and *Lewis et al.* [2008].

4.4.3. Nightside Passes

Results for the nightside passes are shown in Figure 4.5 in the same format as Figure 4.4, but are now presented in reverse order of time, so we again discuss from the inner to the outer passes in radial distance, and compare these with the observations at

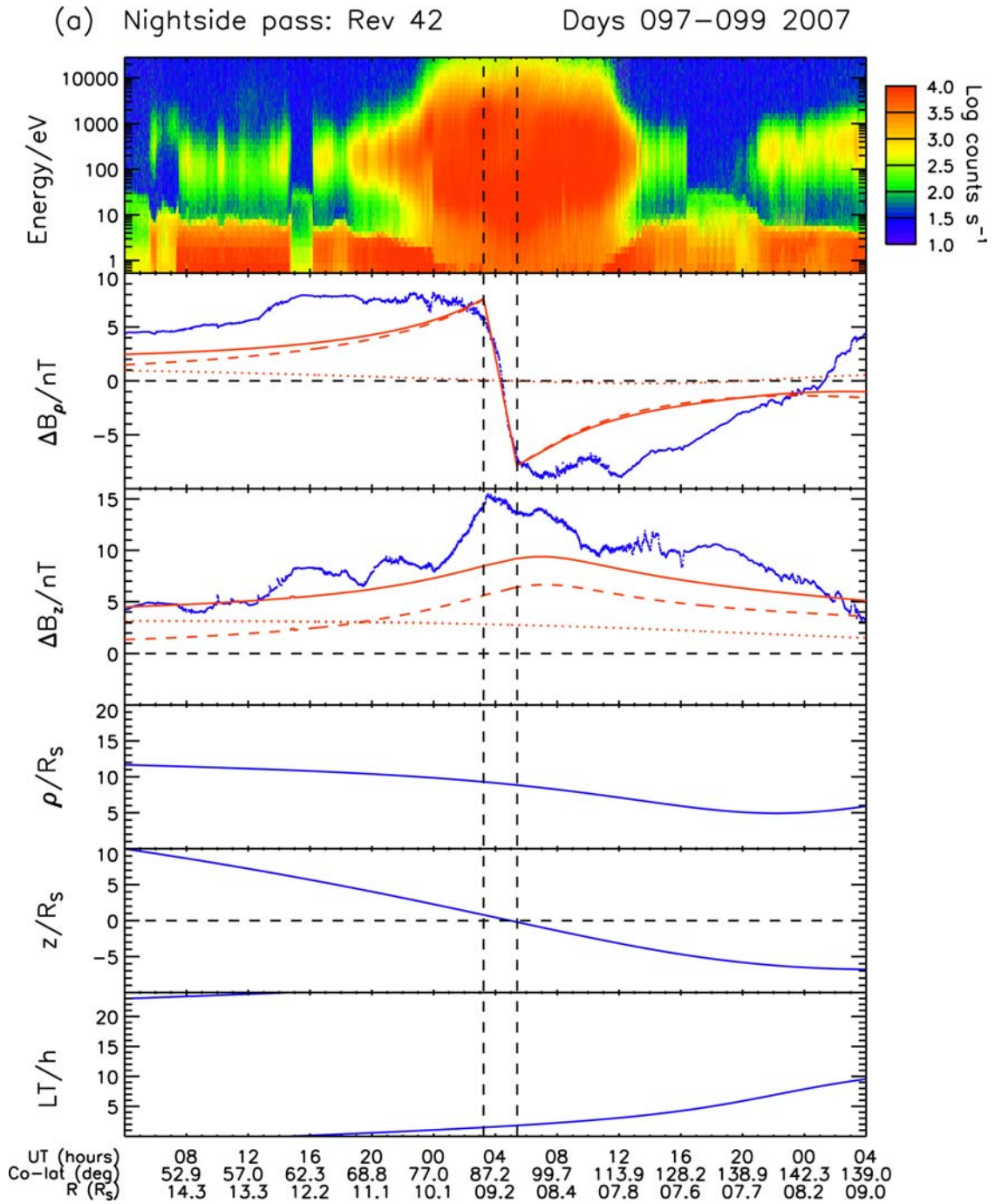


Figure 4.5a. Plot showing Cassini electron, magnetic field, and position data for Rev 42, a nightside pass through the ring current region. The format is the same as for Figure 4.4a.

(b) Nightside pass: Rev 41

Days 080–082 2007

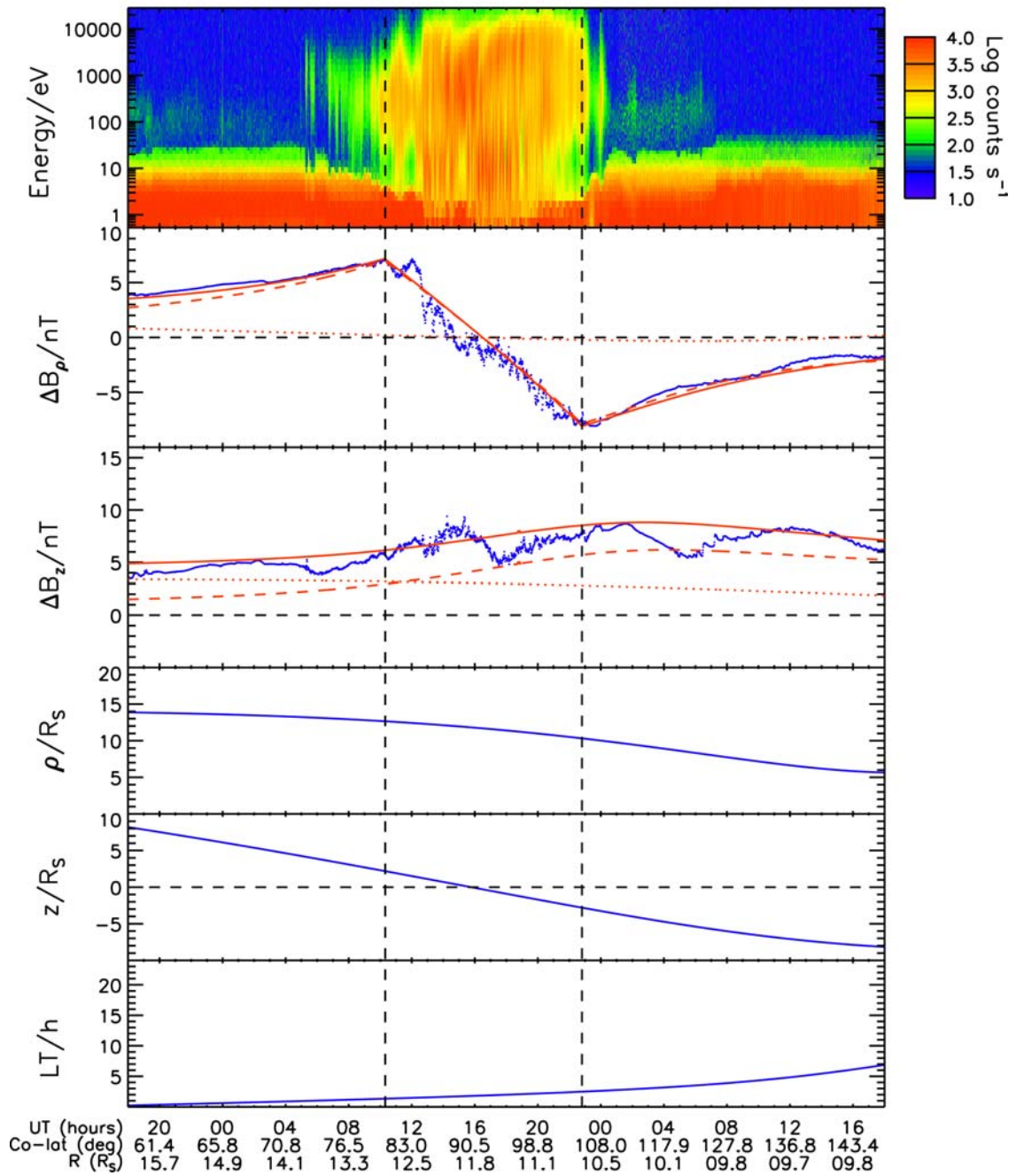


Figure 4.5b. As for Figure 4.5a except for Rev 41.

(c) Nightside pass: Rev 40

Days 063–065 2007

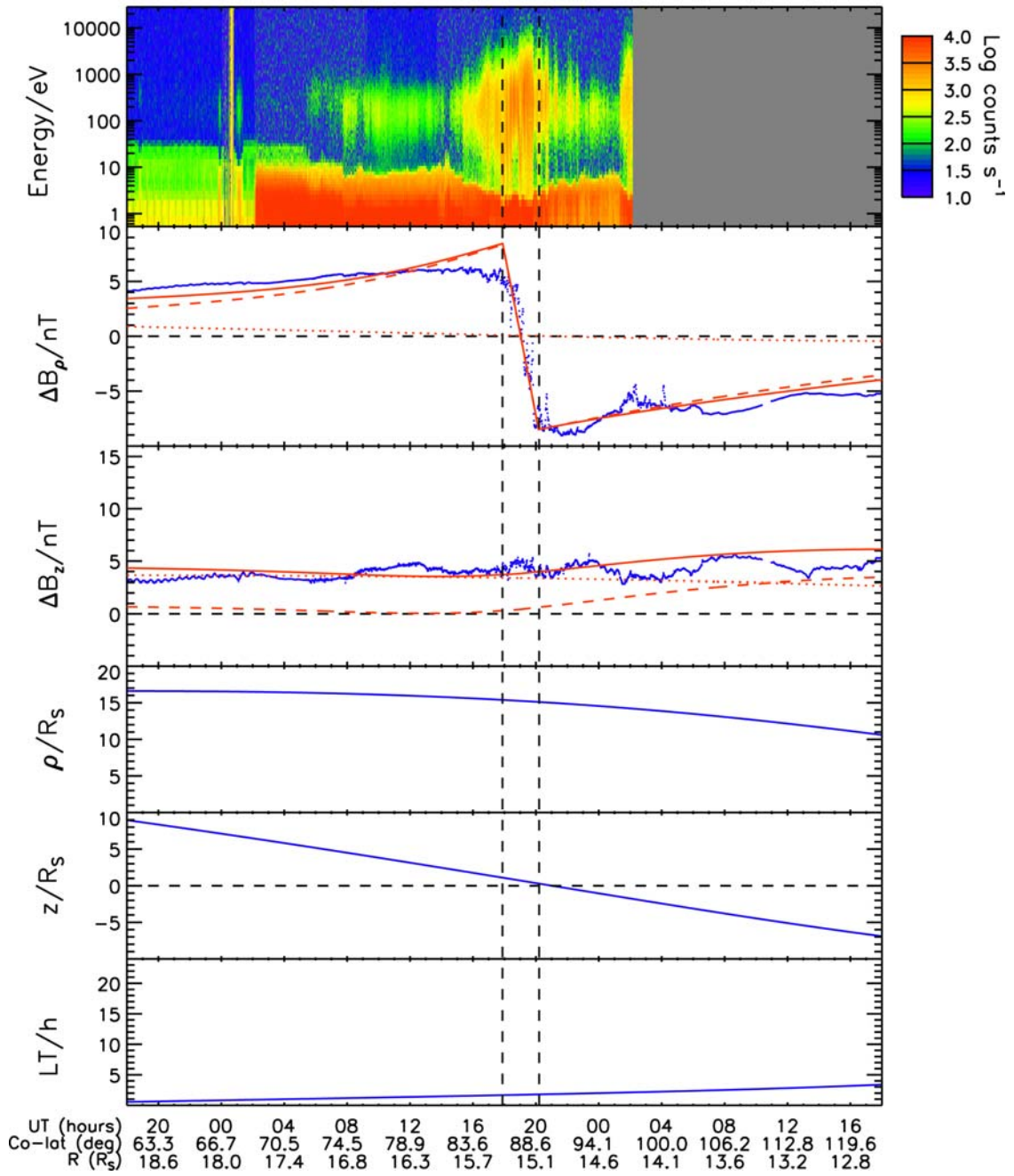


Figure 4.5c. As for Figure 4.5a except for Rev 40.

similar distances on the dayside. In Figure 4.5a we thus show results for Rev 42, for which the equatorial crossing was at a radial distance of $9.1 R_S$, similar to that for Rev 35 shown in Figure 4.4a. In this case, however, the residual field profiles do not completely follow expectations based on the discussion in Section 4.4.1, or those found on the dayside shown in Figure 4.4. The ΔB_ρ values show a very sharp fall on passing from north to south across the equatorial region essentially as before, but now exhibit extended intervals of large near-constant values outside this region before falling slowly in magnitude at larger distances, roughly for $|z| \geq 5 R_S$. The reversal in sign of ΔB_ρ to positive values at the end of the interval shown is found from examination of an extended data interval to be a few-hour transient feature of uncertain origin. The model field shown in Figure 4.5a has been chosen to fit the rapid near-equatorial variation in ΔB_ρ indicative of an equatorial current sheet, as before, and has model parameters $z_1 = -0.2 R_S$ and $z_2 = 0.8 R_S$ (vertical black dashed lines), indicative of a very small half-thickness $D = 0.5 R_S$ and a comparable offset $\Delta z = 0.3 R_S$, and $\mu_0 I_0 = 156 \text{ nT}$. However, it can be seen that this ‘best fit’ model does not fit the data very well overall (the RMS deviations per point now being $\sim 3.0 \text{ nT}$ in each component), particularly the sustained large ΔB_ρ values away from the equatorial region. These features are suggestive of the presence of additional currents flowing in a broader layer about the equatorial plane, presumably extending to larger distances from the planet, within which the intense thin current layer modelled above is embedded at its centre. Examination of the electron data in the top panel of Figure 4.5a certainly shows that this thin current sheet lies at the centre of a much broader region of intense fluxes covering the full energy range from a few eV to above 10 keV, that extends to distances of $\sim 2\text{-}3 R_S$ on either side of the equatorial plane.

Results from the more central nightside ring current pass on Rev 41 are shown in Figure 4.5b, with an equatorial crossing at $12.0 R_S$. In this case the residual field data now more resembles the dayside data, in conformity with simple expectations, with a near-linear variation of ΔB_ρ across the equatorial plane, and slower decreases in magnitude on either side. The boundaries of the current sheet shown by the vertical black dashed lines are estimated to lie at z values of -2.8 and $2.2 R_S$, thus yielding $D = 2.5 R_S$ and $\Delta z = -0.3 R_S$. The half-thickness is rather larger than those determined on the dayside, while the modest offset (with an uncertainty of about $\pm 0.3 R_S$) indicates

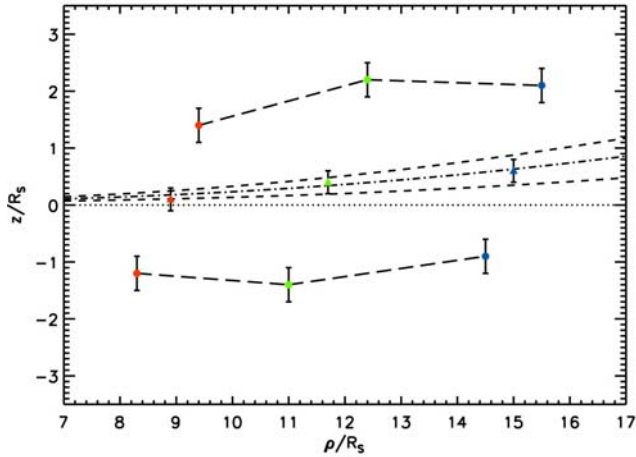
a current sheet displacement south of the equatorial plane. The best fit model with $\mu_0 I_0 = 49$ nT, leading to $k_{RC} = 0.47$, is seen to give an excellent fit to the data, with RMS values of ~ 0.7 and ~ 1.2 nT for ΔB_ρ and ΔB_z respectively (Table 4.1). Comparison with the electron data shown in the top panel of Figure 4.5b shows that, rather unlike the corresponding dayside data, the inferred nightside current sheet now encompasses essentially the whole of the hot equatorial electron region, although modest layers containing weaker warm electron fluxes extend on either side. The electrons in these external layers have energies between ~ 100 eV and a few keV north of the current layer, but are of lower energy, centred near ~ 100 eV, south of the current layer.

In Figure 4.5c we finally show results for Rev 40, the outermost nightside pass with an equatorial crossing at $15.3 R_S$. Here the nature of the data is essentially similar to that for Rev 41 in Figure 4.5b, except that the current layer is much thinner. In this case the lower and upper boundaries of the current layer are estimated to lie at $z_1 = 0.3 R_S$ and $z_2 = 1.1 R_S$, giving $D = 0.4 R_S$ and $\Delta z = 0.7 R_S$. The current layer observed on this pass is therefore the narrowest of all those examined here, and has the largest northward offset, though the latter is similar to that derived from the outermost dayside crossing at a similar radial distance. The ‘best-fit’ model with $\mu_0 I_0 = 338$ nT (and $k_{RC} = 0.52$) gives a good overall fit to the data, with RMS residuals per point of ~ 1 nT in each component (Table 4.1). Comparison with the electron data shows similar results to Rev 41, in that the current layer corresponds to the majority of the observed equatorial warm electron layer. This is very unlike its dayside counterpart in Figure 4.4c, though again surrounding layers containing weak fluxes of warm electrons are present, with energies extending to a few hundred eV. We note that there also appears to be a secondary partial entry into the hot plasma region and current layer just before the electron data gap starting at ~ 02 UT on day 65, which provides evidence of some current sheet motion at these distances in this case. We note, however, that evidence for large-scale wavy or flapping motions of the current layer are absent in the other examples presented, in agreement with the results presented in prior ring current studies [e.g., *Bunce et al.*, 2007].

4.4.4. Overview of Current Sheet Thickness and Offset Results

We now briefly overview the results derived above for the half-thickness of the ring current layer D , and the offset from the centre plane Δz , and compare the latter with the offset for the same epoch derived from the *Arridge et al.* [2008b] model. Results are shown in Figures 4.6a and 4.6b for the dayside and nightside passes, respectively. Considering the dayside results first, the upper panel in Figure 4.6a shows the positions of the northern and southern boundaries of the dayside current sheet in a ρ - z plot, where the lower boundary z_1 for each Rev is plotted as a solid circle at corresponding cylindrical radius ρ_1 , etc., as given in Table 4.1. The values determined from Revs 35, 36, and 37 are shown by the red, green, and blue symbols respectively, and are joined by the long-dashed lines under the (rather uncertain) assumption that they indicate spatial variations with distance from the planet in the absence of significant temporal variation. The offset values, Δz , are then shown in the upper panel by the similarly colour-coded triangles, plotted at the mean ρ position of the current sheet crossing. These indicate a steady increase in offset from values indistinguishable from zero in the inner ring current at $\sim 9 R_S$ to $\sim 0.6 R_S$ in the outer region at $\sim 15 R_S$. The implied tilt angle of the current sheet relative to the equatorial plane is $\sim 5^\circ$, in accordance with the discussion in Section 4.4.1. The black curves show model offsets obtained from equation (1) of *Arridge et al.* [2008b] using various ‘hinging’ distances R_H . The hinging distance is the characteristic distance from the planet where the current sheet no longer lies in the magnetic dipole equator [*Arridge et al.*, 2008b]. In the *Arridge et al.* [2008b] model, the current sheet warping is gradual and so the hinging distance is a characteristic distance at which this warping starts to occur. Here, we evaluate equation (1) of *Arridge et al.* [2008b] for a fixed solar latitude angle of 14.5° . This angle is directly appropriate for the epoch of Rev 35, but varies by only $\sim 0.5^\circ$ over the interval of the dayside passes examined here. The model values shown in the figure also include a small constant northward displacement of $0.037 R_S$ resulting from the internal planetary quadrupole field, as also employed in the analysis of *Arridge et al.* [2008b]. The lower short-dashed curve in Figure 4.6a shows the model offset for the ‘optimal hinging distance’ of $R_H = 29 R_S$, determined by *Arridge et al.* [2008b] from an analysis based on separating regions of positive and negative radial field observed on a large number of spacecraft orbits. This model somewhat underestimates the offsets in the

(a) Dayside passes



(b) Nightside passes

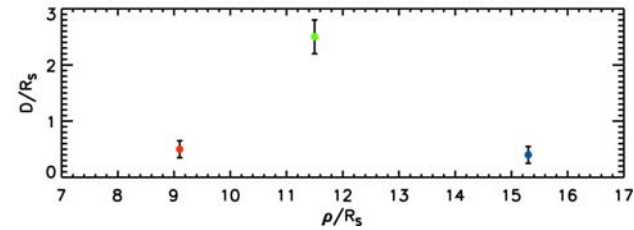
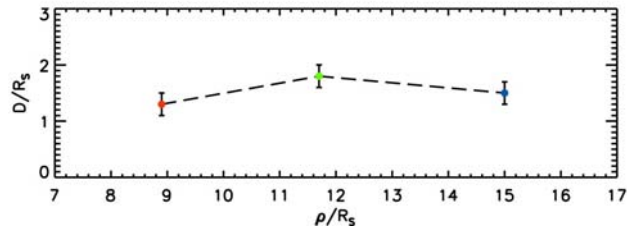
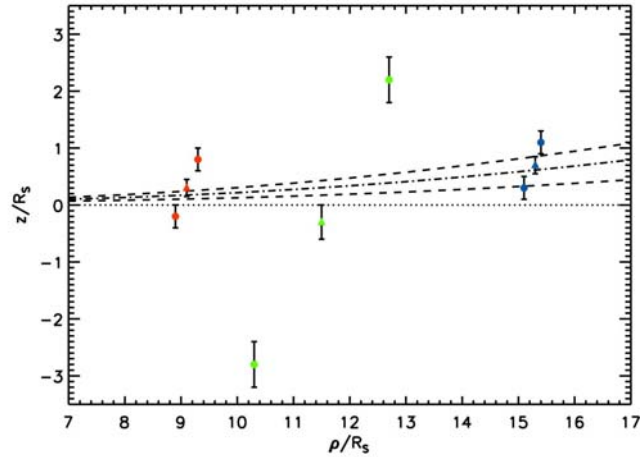


Figure 4.6. Plots summarising results for the positions of the upper and lower boundaries of the equatorial current sheet in the ring current region, together with the variation of the half-thickness D , for (a) the dayside passes, and (b) the nightside passes. The upper panels in each case show the boundary positions in cylindrical ρ - z coordinates, indicated by the red, green, and blue circles for Revs 35, 36, and 37 in Figure 4.6a, and similarly for Revs 42, 41, and 40 in Figure 4.6b. The similarly coloured triangles represent the ‘offset’ values, Δz , plotted at the mean ρ position of the current sheet crossing. The short-dashed curves show the model current sheet centre of the *Arridge et al.* [2008b] model for ‘hinging’ distances R_H of 16 (top) and 29 R_S (bottom), while the dot-dash curve shows the best fit model for our dayside data with $R_H = 20 R_S$. The lower panels show the similarly colour-coded values of the current sheet half-thickness D , plotted versus cylindrical radial distance ρ (R_S).

outer region obtained here by approximately a factor of two. The upper short-dashed curve then corresponds to $R_H = 16 R_S$, derived by *Arridge et al.* [2008b] from modelling magnetic field data from an individual Cassini pass. This model somewhat over-estimates the offsets found here, such that the two values of R_H obtained by *Arridge et al.* [2008b] using differing techniques bracket our data in Figure 4.6a. The best-fit (minimum RMS deviation) model for our dayside offsets occurs for $R_H = 20 R_S$, shown by the black dot-dashed line in Figure 4.6a, which is seen to give a reasonable account of our values. The lower panel of Figure 4.6a shows the corresponding values of the half-thickness D , similarly plotted at the mean ρ position of the current sheet crossing. This shows that the half-thickness is relatively constant over the range of distances covered by these passes, between ~ 1.3 and $\sim 1.8 R_S$, with a mean value of $1.5 R_S$, which we note is rather less than the typical half-thicknesses of $\sim 2-3 R_S$ derived from previous fly-by data discussed in Sections 4.1 and 4.2.

In Figure 4.6b we show corresponding results for the nightside passes in a similar format, in which the data for Revs 40, 41, and 42 are shown by the blue, green, and red symbols respectively. Now, however, we have not joined the much more variable data points by dashed lines so as not to suggest a potentially spurious strongly-varying spatial structure. We note in particular that the innermost (red) values derived from Rev 42 correspond to a thin current layer embedded at the centre of a much broader current and plasma region (the latter having a half-thickness of $\sim 2-3 R_S$), which presumably extends to larger radial distances, such as that observed on Rev 41 (green points). The subsequent thinning to much smaller values observed on Rev 40 (blue points) is suggestive of a rapid narrowing of the current layer towards a thin plasma sheet layer extending into the tail. However, the presence of significant temporal variability in the nightside parameters cannot be ruled out. We also note from our discussion of Figure 4.5c that there is some evidence for current sheet motion at these distances that could affect our thickness estimate. Considering the offset values shown by the triangles in the upper panel of Figure 4.6b, we see rather variable results, the value reversing sense to become unexpectedly south of the equator for the middle pass of the three. Due to this variability we have not attempted a separate fit of the *Arridge et al.* [2008b] model to these data, the model curves shown in Figure 4.6b being for the same ‘hinging’ distances of 16, 20, and $29 R_S$ as shown in Figure 4.6a, but now

evaluated for a solar latitude of 13.4° . This latitude is appropriate specifically to Rev 40, but again varies by only $\sim 0.5^\circ$ over the interval covered by these nightside passes. Focusing on the offset derived for the most distant pass as perhaps the best determined here, we note that the model values derived for hinging distances of 16 and $29 R_S$ again bracket this data point, with that for the ‘optimal hinging distance’ of $R_H = 29 R_S$ again being too small by a factor of about two. The model for a hinging distance of $20 R_S$, however, again agrees quite well. The lower panel of Figure 4.6b again demonstrates the very great variability of current sheet thickness results obtained from the nightside data, from thin layers of $\sim 0.5 R_S$ half-thickness observed in the inner and outer regions, to a layer of $\sim 2.5 R_S$ half-thickness observed in the central ring current region.

4.5 - Summary

In this chapter we have investigated magnetic field and plasma electron data from six Cassini orbits during which, unique within the mission to date, the spacecraft passed almost directly north-south through the equatorial plane within the ring current region of the middle magnetosphere. Three of these passes took place in the post-noon sector (~ 14 h LT) and three in the post-midnight sector (~ 02 h LT), each at radial distances of ~ 9 , ~ 12 and $\sim 15 R_S$. These distances compare with the usual radial extent of the ring current region between ~ 7 and $\sim 18 R_S$ as determined from equatorial magnetic profiles [Bunce *et al.*, 2007], such that the current sheet crossings correspond to the inner, middle, and outer regions of the ring current region respectively. Field and particle data from these orbits thus allow for the first time an investigation of the north-south structure of the ring current at almost fixed radius and local time, permitting in particular direct determinations of the thickness of the equatorial current layer and its offset from the equator, and an initial examination of the relation of the current layer to the distribution of plasma about the equatorial plane. Previous half-thickness estimates of typically $\sim 2-3 R_S$ have been made from data obtained on the highly oblique ring current passes during the fly-by missions of Pioneer-11 and Voyager-1 and -2 [Connerney *et al.*, 1981b, 1983; Bunce and Cowley, 2003; Giampieri and Dougherty, 2004].

Considering first the dayside data, all three passes indicate the presence of a current disk lying near the equatorial plane with a half-thickness of $\sim 1.5 R_S$, somewhat less than the $\sim 2-3 R_S$ values derived from the fly-by data. The current density in the disk appears approximately uniform across the layer width, certainly for the inner and central passes, producing a near-linear variation of the residual B_ρ field during the current sheet crossings. The overall residual fields are well-modelled by a *Connerney et al.* [1983] current disk with a lesser contribution from the magnetopause-tail fringing field. In the inner ring current, the current layer is centred near the planet's equatorial plane, but is displaced by $\sim 0.6 R_S$ north of the equatorial plane in the outer region. While confirmatory of the northward dayside current sheet offsets reported previously by *Cowley et al.* [2006] and *Arridge et al.* [2008b], this displacement is approximately twice that expected on the basis of the *Arridge et al.* [2008b] model using the 'optimal hinging distance' of $29 R_S$, but is in good accord with a model with a hinging distance of $\sim 20 R_S$. Comparison of the magnetic field data with simultaneously measured electron spectrograms reveals that the current layer is located inside a significantly broader equatorial layer of dayside plasma. The main current layer is located in the region containing the most intense fluxes of low-energy (~ 10 eV) electrons, which decline significantly in intensity outside the layer, while the warm/hot fluxes extend to much greater distances away from the equatorial plane. This finding is in agreement with the results of *Sergis et al.* [2009], who show that hot ion fluxes (~ 10 keV and above) extend broadly in latitude about the equator on the dayside, compared with the rather narrow current layer of $\sim 1.5 R_S$ half-thickness found here. One possible interpretation of this result is that the inertia current of centrifugally confined cool corotating plasma may be dominant in the central region, since the pressure-gradient current of a near-isotropic hot plasma is expected to be more broadly distributed along the field lines containing the plasma. However, such localised current layers can also be produced by other effects such as pressure anisotropy of the hot plasma population (specifically for parallel pressures that exceed the perpendicular pressure), as has been observed and modelled for the Earth's tail plasma sheet [e.g., *Sitnov et al.*, 2006, and references therein]. These important issues will therefore be investigated in Chapters 6 and 7.

The nightside ring current data show a greater variety of behaviours than the dayside data. The innermost pass at $\sim 9 R_S$ provides evidence for the presence of a thin

current layer of half-thickness $\sim 0.5 R_S$ embedded at the centre of a much broader layer of current and plasma extending several R_S from the equatorial plane, to which the above comments also apply. The plasma electrons in the layer extend broadly in energy over the range from a few eV to ≥ 10 keV. The pass through the central ring current at $\sim 12 R_S$ provides the widest current sheet example in our study with a half-thickness of $\sim 2.5 R_S$. In this case, the current sheet corresponds essentially to the whole of the north-south extent of the equatorial electron population, again extending over the full energy range given above, with only weak fluxes of low-energy particles extending in layers outside. This finding is again in agreement with the results of *Sergis et al.* [2009], who show that in the nightside ring current region (inside $15 R_S$) the hot ion pressure has a half-width at half maximum of $\sim 2.5 R_S$. These findings may suggest a more important role for hot plasma currents related to pressure gradients in this case, though again, these issues require future detailed study. The outer nightside ring current crossing at $\sim 15 R_S$ has a similar structure, with the current sheet again corresponding to almost the whole of the equatorial hot electron layer. However, in this case the current layer is the thinnest of all those observed in this study, with a half-thickness of only $0.4 R_S$. This suggests that the thicker ring current observed in the central region thins rapidly to smaller values on moving towards the tail plasma sheet, though we cannot rule out the possibility of significant temporal variations. The outer nightside data also provide evidence of a northward displacement of the current layer from the equatorial plane, which is again in reasonable agreement with the *Arridge et al.* [2008b] model and with the results derived from particle data by *Carbary et al.* [2008c] and *Sergis et al.* [2009]. Overall, the results found here provide significant impetus to future studies of the physical origins of the ring current in Saturn’s magnetosphere, and its relationship to the complex plasma populations contained within.

Chapter 5

Derivation of the azimuthal current density from plasma bulk parameters

5.1 - Introduction

For the studies presented in Chapters 6 and 7 of this thesis we use Cassini plasma and magnetic field data to calculate azimuthal current density profiles so that we may investigate the nature of Saturn's ring current. In this chapter we will therefore derive the general expression for the field-perpendicular current density in terms of the plasma bulk parameters before modifying it to suit the particular circumstances required for the studies presented in this thesis.

5.2 – Basic theory

There are two basic approaches to deriving the general expression for the field-perpendicular current density in terms of the plasma bulk parameters. The first is to integrate the single-particle drifts (inertia, ∇B and curvature) over the particle distribution functions (PDFs) to find the drift current density, and then add the magnetisation current density $j_M = \text{curl } \mathbf{M}$ (where \mathbf{M} is the magnetisation, i.e. the magnetic dipole moment per unit volume) to find the total current density. The second is to work from the momentum equation, which is the most succinct approach. We emphasise, however, that the two are entirely equivalent and lead to the same results.

The momentum equation is

$$\rho_m \frac{d\mathbf{V}}{dt} = \mathbf{j} \wedge \mathbf{B} - \text{div} \mathbf{P} \quad (5.1)$$

where ρ_m is the mass density, \mathbf{V} the plasma bulk velocity ($\mathbf{E} \wedge \mathbf{B}$ drift plus V_{\parallel} in general), \mathbf{j} the current density, \mathbf{B} the magnetic field, and \mathbf{P} the plasma pressure tensor (summed over all species). Taking the cross product of equation (5.1) with \mathbf{B} we get

$$\rho_m \mathbf{B} \wedge \frac{d\mathbf{V}}{dt} = \mathbf{B} \wedge (\mathbf{j} \wedge \mathbf{B}) - \mathbf{B} \wedge \text{div} \mathbf{P} .$$

The $\mathbf{B} \wedge (\mathbf{j} \wedge \mathbf{B})$ term can be simplified using $\mathbf{a} \wedge (\mathbf{b} \wedge \mathbf{c}) = \mathbf{b}(\mathbf{a} \cdot \mathbf{c}) - \mathbf{c}(\mathbf{a} \cdot \mathbf{b})$ to give the following

$$\mathbf{B} \wedge (\mathbf{j} \wedge \mathbf{B}) = \mathbf{j}B^2 - \mathbf{B}(\mathbf{j} \cdot \mathbf{B})$$

and since $\mathbf{j} \cdot \mathbf{B}$ is equal to $j_{\parallel} B$, we have

$$\mathbf{B} \wedge (\mathbf{j} \wedge \mathbf{B}) = \mathbf{j}B^2 - j_{\parallel} B^2 \hat{\mathbf{b}} = B^2 (\mathbf{j} - j_{\parallel} \hat{\mathbf{b}})$$

where $\hat{\mathbf{b}} = \frac{\mathbf{B}}{B}$ is the unit vector along \mathbf{B} . This can then be written as

$$\mathbf{B} \wedge (\mathbf{j} \wedge \mathbf{B}) = B^2 \mathbf{j}_{\perp}$$

where \mathbf{j}_{\perp} is the component of \mathbf{j} perpendicular to \mathbf{B} (i.e. the component we wish to calculate). Substituting back into equation (5.1) and re-arranging yields

$$\mathbf{j}_{\perp} = \frac{\mathbf{B}}{B^2} \wedge \left(\rho_m \frac{d\mathbf{V}}{dt} + \text{div} \mathbf{P} \right), \quad (5.2)$$

where the first term is the inertia current density and the second the pressure-related current density.

We now assume that the PDFs are gyrotropic about the field direction (valid for field spatial scales much larger than the particle gyroradii), so that the pressure tensor (\mathbf{P}) is also gyrotropic, and can be written as

$$\mathbf{P} = P_{\perp} \mathbf{1} + (P_{\parallel} - P_{\perp}) \frac{\mathbf{B}\mathbf{B}}{B^2} \quad (5.3)$$

where $\mathbf{1}$ is the 3×3 unit matrix, and the 3×3 dyadic matrix $\mathbf{B}\mathbf{B}$ is such that $(\mathbf{B}\mathbf{B})_{ij} = B_i B_j$. Thus in a coordinate system aligned with \mathbf{B} such that $\mathbf{B} = (0, 0, B)$, the pressure tensor is diagonal

$$\mathbf{P} = \begin{bmatrix} P_{\perp} & 0 & 0 \\ 0 & P_{\perp} & 0 \\ 0 & 0 & P_{\parallel} \end{bmatrix},$$

where P_{\perp} is the pressure perpendicular to \mathbf{B} and P_{\parallel} is the pressure parallel to \mathbf{B} .

Equation (5.3) can be re-written as $P_{ij} = P_{\perp} \delta_{ij} + (P_{\parallel} - P_{\perp}) \frac{B_i B_j}{B^2}$ where $\delta_{ij} = 1$ if $i = j$ and

$\delta_{ij} = 0$ if $i \neq j$. Taking the divergence of \mathbf{P} gives the following (using the summation convention for repeated suffixes)

$$\begin{aligned}
(\operatorname{div} \mathbf{P})_j &= \frac{\partial}{\partial x_i} P_{ij} = \frac{\partial}{\partial x_i} P_{\perp} \delta_{ij} + \frac{\partial}{\partial x_i} \left[(P_{\parallel} - P_{\perp}) \frac{B_i B_j}{B^2} \right] = \frac{\partial P_{\perp}}{\partial x_j} + \frac{\partial}{\partial x_i} \left[\left(\frac{P_{\parallel} - P_{\perp}}{B} \right) B_i \frac{B_j}{B} \right] \\
&= \frac{\partial P_{\perp}}{\partial x_j} + \left(\frac{P_{\parallel} - P_{\perp}}{B} \right) \frac{\partial}{\partial x_i} \left(B_i \frac{B_j}{B} \right) + \frac{B_i B_j}{B} \frac{\partial}{\partial x_i} \left(\frac{P_{\parallel} - P_{\perp}}{B} \right) \\
&= \frac{\partial P_{\perp}}{\partial x_j} + \left(\frac{P_{\parallel} - P_{\perp}}{B} \right) \left[B_i \frac{\partial}{\partial x_i} \left(\frac{B_j}{B} \right) + \frac{B_j}{B} \frac{\partial B_i}{\partial x_i} \right] + \frac{B_j}{B} B_i \frac{\partial}{\partial x_i} \left(\frac{P_{\parallel} - P_{\perp}}{B} \right),
\end{aligned}$$

which can be written as a vector equation,

$$\operatorname{div} \mathbf{P} = \nabla P_{\perp} + \left(\frac{P_{\parallel} - P_{\perp}}{B} \right) \left[(\mathbf{B} \cdot \nabla) \hat{\mathbf{b}} + \hat{\mathbf{b}} \operatorname{div} \mathbf{B} \right] + \hat{\mathbf{b}} (\mathbf{B} \cdot \nabla) \left(\frac{P_{\parallel} - P_{\perp}}{B} \right).$$

However, $\operatorname{div} \mathbf{B} = 0$, so we have

$$\operatorname{div} \mathbf{P} = \nabla P_{\perp} + (P_{\parallel} - P_{\perp}) (\hat{\mathbf{b}} \cdot \nabla) \hat{\mathbf{b}} + \hat{\mathbf{b}} \left[(\mathbf{B} \cdot \nabla) \left(\frac{P_{\parallel} - P_{\perp}}{B} \right) \right].$$

Substituting into equation (5.2) and remembering $\hat{\mathbf{b}} = \frac{\mathbf{B}}{B}$ gives the general expression for the field-perpendicular current density

$$\mathbf{j}_{\perp} = \frac{\hat{\mathbf{b}}}{B} \wedge \left[\rho_m \frac{d\mathbf{V}}{dt} + \nabla P_{\perp} + (P_{\parallel} - P_{\perp}) (\hat{\mathbf{b}} \cdot \nabla) \hat{\mathbf{b}} \right], \quad (5.4)$$

where we note that the last term in the expression for $\operatorname{div} \mathbf{P}$ drops out (since it is parallel to the magnetic field, \mathbf{B}). The terms on the right hand side of equation (5.4) are in turn the inertia current density, the pressure gradient current density, and the pressure anisotropy current density. We will now examine each term in turn.

5.3 Inertia current density

In this and the following sections we assume approximate axi-symmetry $\left(\text{i.e. } \frac{\partial}{\partial \varphi} = 0 \right)$, at least locally, for all quantities. We allow, however, the magnetic field to have a steady azimuthal component B_φ (generally small), associated e.g. with the sweepback of sub-corotating field lines, as well as poloidal components B_r and B_θ . We concentrate on the dominant azimuthal component of the current $j_{\perp\varphi}$, and do not consider the smaller radial and co-latitudinal currents implied by the presence of B_φ .

In the inertia current term we assume that the plasma is rotating azimuthally with bulk speed V_φ at radius r and co-latitude θ , so that

$$\frac{dV}{dt} = -\frac{V_\varphi^2}{\rho} \hat{\rho}, \quad (5.5a)$$

where ρ is the cylindrical radial distance from the axis, and $\hat{\rho}$ is the corresponding outward unit vector. In terms of spherical polar coordinates we have $\rho = r \sin\theta$, and $\hat{\rho} = \hat{r} \sin\theta + \hat{\theta} \cos\theta$.

Thus,

$$\frac{dV}{dt} = -\frac{V_\varphi^2}{r \sin\theta} (\hat{r} \sin\theta + \hat{\theta} \cos\theta). \quad (5.5b)$$

Substituting into the inertia current density term of equation (5.4), with unit vector $\hat{\mathbf{b}} = (b_r, b_\theta, b_\varphi)$ we find

$$\begin{aligned} \mathbf{j}_\perp &= \frac{1}{B} \left[\rho_m \hat{\mathbf{b}} \wedge \left(-\frac{V_\varphi^2}{r \sin\theta} (\hat{r} \sin\theta + \hat{\theta} \cos\theta) \right) \right] \\ &= \frac{1}{B} \frac{V_\varphi^2 \rho_m}{r \sin\theta} \left(-\hat{\mathbf{b}} \wedge \hat{r} \sin\theta - \hat{\mathbf{b}} \wedge \hat{\theta} \cos\theta \right), \end{aligned}$$

where

$$-\hat{\mathbf{b}} \wedge \hat{r} = \begin{vmatrix} \hat{r} & \hat{\theta} & \hat{\phi} \\ 1 & 0 & 0 \\ b_r & b_\theta & b_\varphi \end{vmatrix} = -b_\varphi \hat{\theta} + b_\theta \hat{\phi}, \quad \text{and} \quad -\hat{\mathbf{b}} \wedge \hat{\theta} = \begin{vmatrix} \hat{r} & \hat{\theta} & \hat{\phi} \\ 0 & 1 & 0 \\ b_r & b_\theta & b_\varphi \end{vmatrix} = b_\varphi \hat{r} - b_r \hat{\phi}.$$

Taking the azimuthal components we obtain the azimuthal component of the inertia current density

$$j_{\perp\phi i} = \frac{\rho_m V_\phi^2}{Br \sin\theta} (b_\theta \sin\theta - b_r \cos\theta) \quad (5.6a)$$

where B is total field strength, $b_\theta = \frac{B_\theta}{B}$, and $b_r = \frac{B_r}{B}$.

It is also possible to express the plasma rotation in terms of an angular velocity, Ω , where $V_\phi = \rho\Omega = r \sin\theta \Omega$. Substituting this into equation (5.6a) gives instead

$$j_{\perp\phi i} = \frac{\rho_m r \sin\theta \Omega^2}{B} (b_\theta \sin\theta - b_r \cos\theta) . \quad (5.6b)$$

We also note that for near-equatorial data we can ignore the second term in the bracket since the first term is very large compared with the second (since $\cos\theta \approx 0$ and $|b_r| \ll |b_\theta|$), in which case equations (5.6a) and (5.6b) can be simplified to

$$j_{\perp\phi i} \approx \frac{\rho_m V_\phi^2 b_\theta}{Br} = \frac{\rho_m r \sin\theta \Omega^2 b_\theta}{B} \quad (5.7)$$

where $\sin\theta \approx 1$.

5.4 Pressure gradient current density

We now examine the pressure gradient current density. With the assumptions detailed above, the perpendicular pressure gradient in spherical polar coordinates is given by

$$\nabla P_\perp = \frac{\partial P_\perp}{\partial r} \hat{\mathbf{r}} + \frac{1}{r} \frac{\partial P_\perp}{\partial \theta} \hat{\boldsymbol{\theta}} . \quad (5.8)$$

Combining the pressure gradient current density term in equation (5.4) with equation (5.8) gives

$$\mathbf{j}_{\perp P} = \frac{1}{B} [\hat{\mathbf{b}} \wedge \nabla P_\perp] = \frac{1}{B} \left[\frac{\mathbf{B}}{B} \wedge \nabla P_\perp \right] = \frac{\mathbf{B}}{B^2} \wedge \nabla P_\perp = \frac{1}{B^2} \left(B_r \frac{1}{r} \frac{\partial P_\perp}{\partial \theta} - B_\theta \frac{\partial P_\perp}{\partial r} \right) \hat{\boldsymbol{\phi}} ,$$

which gives the azimuthal component of the pressure gradient current density (in spherical polar coordinates) as

$$j_{\perp\phi P} = \frac{1}{B} \left[\frac{b_r}{r} \frac{\partial P_\perp}{\partial \theta} - b_\theta \frac{\partial P_\perp}{\partial r} \right] . \quad (5.9)$$

Now for simplicity we assume that the spacecraft is exactly on the spin equator, so that the measured gradient is $\frac{\partial P_{\perp}}{\partial r}$. If we are also exactly on the magnetic equator where

$b_r = 0$ and $\frac{\partial P_{\perp}}{\partial \theta} = 0$ then clearly the first term can be ignored. In general, however, this

is not exactly the case because (a) the quadrupole term in the internal planetary field is equivalent to a displacement of the dipole axis by $\sim 0.04 R_S$ northward of the spin equator, and (b) the solar wind dynamic pressure component along the spin axis in non-equinoctial conditions causes the magnetic equator to be ‘pushed’ away from the spin equator at all local times, as described by the *Arridge et al.* [2008b] “bowl” model, though the effect is rather small out to $\sim 20 R_S$.

To estimate the first term containing measured b_r but unmeasured $\frac{\partial P_{\perp}}{\partial \theta}$, we can

estimate the latter by considering how P_{\perp} varies along field lines. For example, if the pressure is isotropic, then its value is constant along a field line, so $\mathbf{B} \cdot \nabla P = 0$ or

$b_r \frac{\partial P}{\partial r} + \frac{b_{\theta}}{r} \frac{\partial P}{\partial \theta} = 0$, thus providing an estimate of $\frac{\partial P}{\partial \theta}$ given \mathbf{B} and $\frac{\partial P}{\partial r}$. In the inner

region, however, we have to consider anisotropic pressure, which varies with B along the field line in a manner depending on the details of the PDF. However, as a first

approximation it is reasonable to assume a bi-Maxwellian PDF $f = f_0 e^{-\frac{mv_{\parallel}^2}{2kT_{\parallel}}} e^{-\frac{mv_{\perp}^2}{2kT_{\perp}}}$.

For this PDF we have

$$n = \int_{AVS} f d^3v = \int_{-\infty}^{\infty} f 2\pi v_{\perp} dv_{\perp} dv_{\parallel} = 2\pi f_0 \int_{-\infty}^{\infty} dv_{\parallel} e^{-\frac{mv_{\parallel}^2}{2kT_{\parallel}}} \int_0^{\infty} dv_{\perp} v_{\perp} e^{-\frac{mv_{\perp}^2}{2kT_{\perp}}} = f_0 \left(\frac{2\pi kT_{\parallel}}{m} \right)^{1/2} \left(\frac{2\pi kT_{\perp}}{m} \right)$$

$$P_{\parallel} = m \int_{AVS} f v_{\parallel}^2 d^3v = m \int_{-\infty}^{\infty} f v_{\parallel}^2 2\pi v_{\perp} dv_{\perp} dv_{\parallel} = 2\pi m f_0 \int_{-\infty}^{\infty} dv_{\parallel} v_{\parallel}^2 e^{-\frac{mv_{\parallel}^2}{2kT_{\parallel}}} \int_0^{\infty} dv_{\perp} v_{\perp} e^{-\frac{mv_{\perp}^2}{2kT_{\perp}}} = nkT_{\parallel}$$

$$P_{\perp} = \frac{m}{2} \int_{AVS} f v_{\perp}^2 d^3v = \frac{m}{2} \int_{-\infty}^{\infty} f v_{\perp}^2 2\pi v_{\perp} dv_{\perp} dv_{\parallel} = \frac{2\pi m f_0}{2} \int_{-\infty}^{\infty} dv_{\parallel} e^{-\frac{mv_{\parallel}^2}{2kT_{\parallel}}} \int_0^{\infty} dv_{\perp} v_{\perp}^3 e^{-\frac{mv_{\perp}^2}{2kT_{\perp}}} = nkT_{\perp}.$$

If this is the PDF where the field strength is B on a field line, then the PDF where the field strength is B' (where $B' > B$) is given as

$$f = f_0 e^{-\frac{m}{2kT_{\parallel}}\left(v^2 - \frac{v_{\perp}^2}{B'}\right)} e^{-\frac{m}{2kT_{\perp}}\left(\frac{v_{\perp}^2}{B'}\right)} = f_0 e^{-\frac{mv_{\parallel}^2}{2kT_{\parallel}}} e^{-\frac{mv_{\perp}^2}{2k}\left(\frac{1}{T_{\parallel}}\left(1 - \frac{B}{B'}\right) + \frac{1}{T_{\perp}B'}\right)},$$

where we have $v_{\perp}^2 = \frac{v_{\perp}^2}{B'} B_0$ and $v_{\parallel}^2 = v^2 - \frac{v_{\perp}^2}{B'} B_0$ from conservation of particle magnetic moment and energy. This PDF is another bi-Maxwellian with parallel temperature $T'_{\parallel} = T_{\parallel}$ and perpendicular temperature T'_{\perp} given by

$$\frac{1}{T'_{\perp}} = \frac{1}{T_{\parallel}}\left(1 - \frac{B}{B'}\right) + \frac{1}{T_{\perp}}\frac{B}{B'} = \frac{1}{T_{\parallel}} + \frac{B}{B'}\left(\frac{1}{T_{\perp}} - \frac{1}{T_{\parallel}}\right).$$

From the above results we then have

$$n' = f_0 \left(\frac{2\pi k T'_{\parallel}}{m}\right)^{1/2} \left(\frac{2\pi k T'_{\perp}}{m}\right),$$

and since $T'_{\parallel} = T_{\parallel}$, we have

$$\frac{n'}{n} = \frac{T'_{\perp}}{T_{\perp}} = \frac{1}{T_{\perp}/T'_{\perp}} = \frac{1}{\left(\frac{T_{\perp}}{T_{\parallel}} + \frac{B}{B'}\left(1 - \frac{T_{\perp}}{T_{\parallel}}\right)\right)}.$$

Similarly $\frac{P'_{\parallel}}{P_{\parallel}} = \frac{n' T'_{\parallel}}{n T_{\parallel}} = \frac{n'}{n}$ since $T'_{\parallel} = T_{\parallel}$. We also have $\frac{P'_{\perp}}{P_{\perp}} = \frac{n' T'_{\perp}}{n T_{\perp}} = \left(\frac{T'_{\perp}}{T_{\perp}}\right)^2$.

Therefore if the perpendicular pressure is P_{\perp} at B , then the perpendicular pressure at B' on the same field line is P'_{\perp} given by

$$\frac{P'_{\perp}}{P_{\perp}} = \frac{1}{\left(\frac{T_{\perp}}{T_{\parallel}} + \left(1 - \frac{T_{\perp}}{T_{\parallel}}\right)\frac{B}{B'}\right)^2}. \quad (5.10)$$

Thus, if the PDF is isotropic, $T_{\perp} = T_{\parallel}$, then $P_{\perp}' = P_{\perp}$ for all B , while if $T_{\perp} \neq T_{\parallel}$ then P_{\perp}' varies from P_{\perp} at B to $P' = \left(\frac{T_{\parallel}}{T_{\perp}}\right)^2 P_{\perp}$ when $B' \rightarrow \infty$. The rate of change of P_{\perp}' with B'

is then

$$\frac{1}{P_{\perp}} \frac{\partial P_{\perp}'}{\partial B'} = \frac{2 \left(1 - \frac{T_{\perp}}{T_{\parallel}}\right) \frac{B}{B'^2}}{\left(\frac{T_{\perp}}{T_{\parallel}} + \left(1 - \frac{T_{\perp}}{T_{\parallel}}\right) \frac{B}{B'}\right)^3},$$

so that at the observation point where $P_{\perp}' = P_{\perp}$ and $B' = B$ we have

$$\frac{1}{P_{\perp}} \frac{\partial P_{\perp}}{\partial B} = 2 \left(1 - \frac{T_{\perp}}{T_{\parallel}}\right) \frac{1}{B}, \quad (5.11)$$

which is positive if $T_{\parallel} > T_{\perp}$ (P_{\perp} increases with B), and negative if $T_{\perp} > T_{\parallel}$ (P_{\perp} decreases with B), and zero if $T_{\parallel} = T_{\perp}$ (isotropic case).

The rate of change of P_{\perp} with distance S along a field line is given by

$$\frac{\partial P_{\perp}}{\partial S} = \hat{\mathbf{b}} \cdot \nabla P_{\perp} = b_r \frac{\partial P_{\perp}}{\partial r} + \frac{b_{\theta}}{r} \frac{\partial P_{\perp}}{\partial \theta} = \frac{\partial P_{\perp}}{\partial B} \frac{\partial B}{\partial S} = 2 \left(1 - \frac{T_{\perp}}{T_{\parallel}}\right) \frac{P_{\perp}}{B} \frac{\partial B}{\partial S}.$$

We thus have

$$\frac{b_{\theta}}{r} \frac{\partial P_{\perp}}{\partial \theta} = -b_r \frac{\partial P_{\perp}}{\partial r} + 2 \left(1 - \frac{T_{\perp}}{T_{\parallel}}\right) \frac{P_{\perp}}{B} \frac{\partial B}{\partial S}. \quad (5.12)$$

Substituting into equation (5.9) we thus have

$$j_{\perp \phi P} = \frac{1}{B} \left[-b_{\theta} \frac{\partial P_{\perp}}{\partial r} + \frac{b_r}{r} \frac{r}{b_{\theta}} \left(-b_r \frac{\partial P_{\perp}}{\partial r} + 2 \left(1 - \frac{T_{\perp}}{T_{\parallel}}\right) \frac{P_{\perp}}{B} \frac{\partial B}{\partial S} \right) \right],$$

which gives

$$j_{\perp \phi P} = -\frac{(b_r^2 + b_{\theta}^2)}{b_{\theta} B} \frac{\partial P_{\perp}}{\partial r} + \frac{2 b_r}{B b_{\theta}} \left(1 - \frac{T_{\perp}}{T_{\parallel}}\right) \frac{P_{\perp}}{B} \frac{\partial B}{\partial S}. \quad (5.13)$$

We note that since $b_r^2 + b_{\theta}^2 + b_{\phi}^2 = 1$ we can also write $b_r^2 + b_{\theta}^2 = 1 - b_{\phi}^2$ (which will generally be close to 1). The first term in equation (5.13) does not depend explicitly on the anisotropy, while the second term does, and goes to zero for $T_{\perp} = T_{\parallel}$ (i.e. isotropic pressure).

Now $\frac{\partial B}{\partial S}$ relates principally to the variation of the field strength north-south along the near-equatorial field lines and is again not directly measured. However, the anisotropy is significantly large only in the inner part of the system (as will be discussed in later chapters), where we can take a quasi-dipolar field as a first approximation, and estimate $\frac{\partial B}{\partial S}$ in terms of the measured radial field. For a dipole field we have $\frac{\partial B}{\partial S} \approx -\frac{9B}{r}\lambda$ and

$$B_r \approx 2\lambda B \text{ where } \lambda \text{ is the latitude away from the equator, so we can write } \frac{\partial B}{\partial S} \approx -\frac{9}{2} \frac{B_r}{r}.$$

Therefore, the term proportional to the anisotropy in equation (5.13) (i.e. the second term) is estimated to be

$$\delta j_{\perp\phi P} = \frac{2b_r}{Bb_\theta} \left(1 - \frac{T_\perp}{T_\parallel}\right) \frac{P_\perp}{B} \frac{\partial B}{\partial S} = -\frac{b_r}{Bb_\theta} \left(1 - \frac{T_\perp}{T_\parallel}\right) \frac{P_\perp}{B} \left(9 \frac{B_r}{r}\right)$$

Substituting $b_r = \frac{B_r}{B}$, $b_\theta = \frac{B_\theta}{B}$ and re-arranging gives

$$\delta j_{\perp\phi P} = 9 \left(\frac{T_\perp}{T_\parallel} - 1\right) \left(\frac{B_r}{B}\right)^2 \frac{P_\perp}{rB_\theta}.$$

We can show experimentally that this term is approximately a few percent of the first term in equation (5.13) and therefore neglect it, to arrive at

$$j_{\perp\phi P} \approx -\frac{(1-b_\phi^2)}{b_\theta B} \frac{\partial P_\perp}{\partial r} = -\frac{(1-b_\phi^2)}{B_\theta} \frac{\partial P_\perp}{\partial r}. \quad (5.14)$$

5.5 Pressure anisotropy current density

From equation (5.4) the pressure anisotropy current density is

$$\mathbf{j}_{\perp A} = \left(\frac{P_\parallel - P_\perp}{B}\right) \hat{\mathbf{b}} \wedge \left(\hat{\mathbf{b}} \cdot \nabla \hat{\mathbf{b}}\right). \quad (5.15)$$

The vector $(\hat{\mathbf{b}} \cdot \nabla) \hat{\mathbf{b}}$ describes the rate of change of unit vector $\hat{\mathbf{b}}$ along $\hat{\mathbf{b}}$ (i.e. along the field vector), or in other words, the curvature of the field lines.

If S is the distance along a field line then $(\hat{\mathbf{b}} \cdot \nabla) \equiv \frac{\partial}{\partial S}$ so $(\hat{\mathbf{b}} \cdot \nabla) \hat{\mathbf{b}} = \frac{\partial \hat{\mathbf{b}}}{\partial S}$. If we consider a small displacement (dS) along a field line, then the local radius of curvature R is given by $d\psi = \frac{dS}{R}$, where $d\psi = |\Delta \hat{\mathbf{b}}|$ (see Figure 5.1 below).

So, $\frac{1}{R} = \frac{d\psi}{dS} = \frac{|\Delta \hat{\mathbf{b}}|}{dS}$. But $\Delta \hat{\mathbf{b}} = \frac{\partial \hat{\mathbf{b}}}{\partial S} dS$ so $\frac{1}{R} = \left| \frac{\partial \hat{\mathbf{b}}}{\partial S} \right| = |(\hat{\mathbf{b}} \cdot \nabla) \hat{\mathbf{b}}|$.

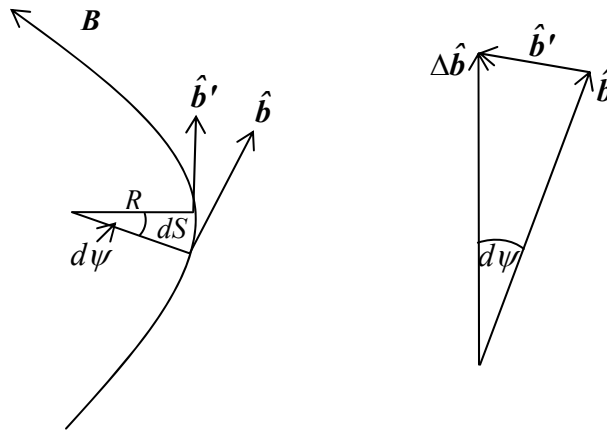


Figure 5.1. Local radius of curvature geometry.

The direction of $\Delta \hat{\mathbf{b}}$ points to the centre of the instantaneous circle tangent to the field line so $(\hat{\mathbf{b}} \cdot \nabla) \hat{\mathbf{b}} = \frac{\hat{\mathbf{R}}}{R}$, where R is the radius of curvature of the field lines at a point, and $\hat{\mathbf{R}}$ is the unit vector perpendicular to \mathbf{B} that points to the centre of the circle (see Figure 5.2 below).

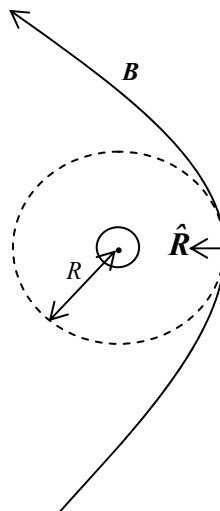


Figure 5.2. Relation of R and $\hat{\mathbf{R}}$ to the instantaneous circle tangent to the field line.

We thus have

$$\mathbf{j}_{\perp A} = \frac{(P_{\parallel} - P_{\perp})}{RB} \hat{\mathbf{b}} \wedge \hat{\mathbf{R}} . \quad (5.16)$$

We do not directly measure R or $\hat{\mathbf{R}}$, but noting again that the pressure anisotropy is only significant in the inner part of the system, we again estimate these quantities using a quasi-dipolar field. For a general field vector \mathbf{a} we have $(\mathbf{a} \cdot \nabla) \mathbf{a} = |\mathbf{a}| \nabla |\mathbf{a}| - \mathbf{a} \wedge \text{curl} \mathbf{a}$, so if $\mathbf{a} = \hat{\mathbf{b}}$ such that $\nabla |\hat{\mathbf{b}}| = 0$ since $|\hat{\mathbf{b}}| = 1$, a constant, then we have $(\hat{\mathbf{b}} \cdot \nabla) \hat{\mathbf{b}} = -\hat{\mathbf{b}} \wedge \text{curl} \hat{\mathbf{b}}$. Assuming a dipolar field we also have $\hat{\mathbf{b}} = (b_r(r, \theta), b_{\theta}(r, \theta), 0)$ i.e. $\frac{\partial}{\partial \varphi} \equiv 0$ and $B_{\varphi} \equiv 0$. In spherical polar coordinates we then have

$$(\hat{\mathbf{b}} \cdot \nabla) \hat{\mathbf{b}} = -\hat{\mathbf{b}} \wedge \text{curl} \hat{\mathbf{b}} = -\hat{\mathbf{b}} \wedge \frac{1}{r} \left(\frac{\partial}{\partial r} (r b_{\theta}) - \frac{\partial b_r}{\partial \theta} \right) \hat{\boldsymbol{\phi}} ,$$

where

$$\hat{\mathbf{b}} \wedge \hat{\boldsymbol{\phi}} = \begin{bmatrix} \hat{\mathbf{r}} & \hat{\boldsymbol{\theta}} & \hat{\boldsymbol{\phi}} \\ b_r & b_{\theta} & 0 \\ 0 & 0 & 1 \end{bmatrix} = (b_{\theta} \hat{\mathbf{r}} - b_r \hat{\boldsymbol{\theta}}) .$$

Thus,

$$(\hat{\mathbf{b}} \cdot \nabla) \hat{\mathbf{b}} = \frac{1}{r} \left(\frac{\partial}{\partial r} (r b_{\theta}) - \frac{\partial b_r}{\partial \theta} \right) (-b_{\theta} \hat{\mathbf{r}} + b_r \hat{\boldsymbol{\theta}}) . \quad (5.17)$$

So we have $\frac{1}{R} = \frac{1}{r} \left(\frac{\partial}{\partial r} (r b_{\theta}) - \frac{\partial b_r}{\partial \theta} \right)$ and $\hat{\mathbf{R}} = (-b_{\theta} \hat{\mathbf{r}} + b_r \hat{\boldsymbol{\theta}})$, which is a unit vector such

that $\hat{\mathbf{b}} \wedge \hat{\mathbf{R}} = \begin{bmatrix} \hat{\mathbf{r}} & \hat{\boldsymbol{\theta}} & \hat{\boldsymbol{\phi}} \\ b_r & b_{\theta} & 0 \\ -b_{\theta} & b_r & 0 \end{bmatrix} = (b_r^2 + b_{\theta}^2) \hat{\boldsymbol{\phi}} = \hat{\boldsymbol{\phi}}$ since $b_r^2 + b_{\theta}^2 = 1$.

Thus, the pressure anisotropy current density is azimuthal in this approximation and is given by

$$j_{\perp \varphi A} = \frac{(P_{\parallel} - P_{\perp})}{RB} \quad \text{where} \quad \frac{1}{R} = \frac{1}{r} \left(\frac{\partial}{\partial r} (r b_{\theta}) - \frac{\partial b_r}{\partial \theta} \right) . \quad (5.18)$$

In spherical polar coordinates the B_r and B_θ components of a dipole field are

$$B_r = 2B_0 \left(\frac{R_S}{r} \right)^3 \cos \theta \quad \text{and} \quad B_\theta = B_0 \left(\frac{R_S}{r} \right)^3 \sin \theta$$

where B_0 is the equatorial field ($\theta = 90^\circ$) on the surface $r = R_S$, so that

$$B = (B_r^2 + B_\theta^2)^{1/2} = B_0 \left(\frac{R_S}{r} \right)^3 (4\cos^2 \theta + \sin^2 \theta)^{1/2} = B_0 \left(\frac{R_S}{r} \right)^3 (1 + 3\cos^2 \theta)^{1/2}$$

This gives
$$b_r = \frac{B_r}{B} = \frac{2\cos \theta}{(1 + 3\cos^2 \theta)^{1/2}} \quad \text{and} \quad b_\theta = \frac{B_\theta}{B} = \frac{\sin \theta}{(1 + 3\cos^2 \theta)^{1/2}}$$

So, since b_θ does not depend on r , only θ , we have

$$\frac{1}{R} = \frac{1}{r} \left(b_\theta - \frac{\partial b_r}{\partial \theta} \right)$$

Working through the derivative we have

$$\frac{\partial b_r}{\partial \theta} = - \frac{2\sin \theta}{(3\cos^2 \theta + 1)^{3/2}}$$

and we note that near the equator ($\theta = 90^\circ$) we have $\sin \theta = 1$, $\cos \theta = 0$, so we have

$b_\theta \approx 1$, and $\frac{\partial b_r}{\partial \theta} \approx -2$, so the variation of b_r with θ is the biggest effect.

So $\frac{1}{R} = \frac{1}{r} \left(b_\theta - \frac{\partial b_r}{\partial \theta} \right)$ becomes
$$\frac{1}{R} = \frac{1}{r} \left(\frac{\sin \theta}{(1 + 3\cos^2 \theta)^{1/2}} + \frac{2\sin \theta}{(1 + 3\cos^2 \theta)^{3/2}} \right).$$

Thus we have
$$\frac{1}{R} = \frac{3\sin \theta}{r} \frac{(1 + \cos^2 \theta)}{(1 + 3\cos^2 \theta)^{3/2}}. \quad (5.19)$$

This function (for a given r) peaks on the equator ($\theta = 90^\circ$), and decreases away from the equator to zero at the poles, but not rapidly. So, within a few degrees of the equator

($\sim 10 - 20^\circ$) we can set $\theta \approx 90^\circ$ in equation (5.19) to find $\frac{1}{R} \approx \frac{3}{r}$, i.e. the radius of

curvature, $R \approx \frac{r}{3}$. Thus, we have

$$j_{\perp\phi} \approx \frac{3(P_{\parallel} - P_{\perp})}{rB} \quad (5.20)$$

where r is the radial distance and B is the field strength. The pressure anisotropy current density will increase as the field becomes more curved (i.e. the “3” in the numerator will increase). In general equation (5.20) therefore represents a lower limit.

5.6 Azimuthal current density

Collecting all the terms together we obtain the following expression for the azimuthal current density

$$j_{\perp\phi} = \frac{\rho_m V_{\phi}^2}{Br \sin\theta} (b_{\theta} \sin\theta - b_r \cos\theta) - \frac{(1 - b_{\phi}^2)}{B_{\theta}} \frac{\partial P_{\perp}}{\partial r} + \frac{3(P_{\parallel} - P_{\perp})}{rB} \quad (5.21)$$

where $\frac{\mathbf{B}}{B} = (b_r, b_{\theta}, b_{\phi})$, i.e. $b_r = \frac{B_r}{B}$, $b_{\theta} = \frac{B_{\theta}}{B}$, $b_{\phi} = \frac{B_{\phi}}{B}$.

For near-equatorial data $\theta \approx 90^\circ$ and equation (5.21) can therefore be simplified to

$$j_{\perp\phi} \approx \frac{1}{B} \left[\frac{\rho_m V_{\phi}^2 b_{\theta}}{r} - (1 - b_{\phi}^2) \left(\frac{1}{b_{\theta}} \frac{\partial P_{\perp}}{\partial r} + \frac{(P_{\perp} - P_{\parallel})}{R} \right) \right]. \quad (5.22)$$

Chapter 6

Nature of the ring current in Saturn's dayside magnetosphere

6.1 – Introduction

As discussed in Section 2.8, determination of the physical origins of Saturn's ring current, i.e., the actual combination of currents associated with the inertia of the near-corotating plasma and hot particle effects, has proved to be considerably elusive. The present chapter addresses the issue of the nature of Saturn's ring current by examining plasma parameter profiles obtained by Cassini on individual passes through the region, and comparing the azimuthal current density profiles derived from these with those obtained from current disk modelling of the magnetic field perturbations from each pass. Data from more than twenty passes have been studied, and are exemplified in this chapter by a detailed discussion of two consecutive passes through the dayside ring current, on Revs 15 and 16 in September and October 2005 (the results from the extended data study of all twenty passes are presented in Chapter 7). These passes are closely equatorial, with latitudes that deviate from zero by at most 0.3° in the region of interest, and are distinguished amongst the near-equatorial Cassini orbits by providing the maximum radial coverage to date, between ~ 3 and $\sim 20 R_S$. The passes thus span the radial range from the Enceladus plasma torus in the inner region to the vicinity of the dayside magnetopause. Otherwise, analysis of the magnetic field data by *Bunce et al.* [2007] indicates that the ring current conditions on these passes are not unusual.

In the next section we re-visit the expression for the azimuthal component of the field-perpendicular current density derived in Chapter 5, and the assumptions on which this is based. Section 6.3 then details the data sets used and how they were combined with empirical models to obtain the azimuthal current density profiles. The results are presented in Section 6.4, and the chapter concludes with a summary and discussion in Section 6.5.

6.2 – Plasma current density

In Chapter 5 we derived the following expression for the current density perpendicular to the magnetic field \mathbf{B} flowing in a magnetised plasma, equation (5.4):

$$j_{\perp} = \frac{\mathbf{B}}{B^2} \wedge \left[\rho_m \frac{d\mathbf{V}}{dt} + \nabla P_{\perp} + (P_{\parallel} - P_{\perp}) \left(\hat{\mathbf{b}} \cdot \nabla \right) \hat{\mathbf{b}} \right],$$

where ρ_m is the plasma mass density, \mathbf{V} the bulk speed, $\hat{\mathbf{b}} = \mathbf{B}/B$ the unit vector along the field, and P_{\parallel} and P_{\perp} are the field-parallel and perpendicular plasma pressures, respectively. The first term on the right side is the inertia current, the second the pressure gradient current, and the third the pressure anisotropy current. The latter term goes to zero in the limit of isotropic pressure, $P_{\parallel} = P_{\perp} = P$.

For practical application to the Cassini plasma data used in this study and the study presented in Chapter 7, this expression was then simplified using suitable approximations. Briefly, we assume approximate local axi-symmetry about the planet's spin and magnetic axis (i.e. $\partial/\partial\varphi \equiv 0$), and that the observations are made exactly on the planet's spin equator (a very good approximation), such that the plasma parameter and field variations observed on a particular equatorial spacecraft pass are taken to relate primarily to radial rather than to local time (LT) effects. We expect that these assumptions should be well satisfied in the inner part of the system dominated by warm (~ 10 eV - 1 keV) plasma and the planetary field, but may be more questionable at larger distances where variable structured hot (tens of keV) plasma becomes important as observed in energetic neutral atom images [e.g., *Krimigis et al.*, 2007; *Mitchell et al.*, 2009b], and the field has local time dependency associated with the day-night asymmetry. Even so, the principal gradients will still generally be those in the meridian, thus justifying axial symmetry as an appropriate approximation for initial study. We also note that the overall validity of this approximation can be checked a posteriori from the results. We assume that the plasma velocity is purely azimuthal about the co-aligned spin and magnetic axes, with speed V_{φ} . However, we make no further assumption about the direction of the magnetic field, such that in general we

take $\hat{\mathbf{b}} = (b_r, b_\theta, b_\phi)$. While clearly the principal field component in the equatorial region will generally be the co-latitudinal component, such that $b_\theta \approx 1$, significant, but not dominant, radial and azimuthal fields may also occur in the outer part of the system (beyond $\sim 12 R_S$). Persistent radial fields are due to the northward displacement of the magnetic equator from the spin equator due to solar wind forcing effects under the southern summer conditions prevailing [Arridge *et al.*, 2008b], while azimuthal fields may be produced by field sweepback effects in the presence of sub-corotating flow. With these assumptions, equation (5.4) then yielded the following expression for the azimuthal component of the field-perpendicular current density, equation (5.22):

$$j_{\perp\phi} \approx \frac{1}{B} \left[\frac{\rho_m V_\phi^2 b_\theta}{r} - (1 - b_\phi^2) \left(\frac{1}{b_\theta} \frac{\partial P_\perp}{\partial r} + \frac{(P_\perp - P_\parallel)}{R} \right) \right],$$

where r is radial distance from the spin/magnetic axis, and R is the local radius of curvature of the field lines. Equation (5.22) neglects a small term in the pressure gradient current that contains the pressure anisotropy and the square of the radial field, and additional small terms in the pressure anisotropy current that contain the azimuthal field and its spatial derivatives. Of the quantities in equation (5.22), only the field radius of curvature R in the pressure anisotropy current cannot be directly determined from near-equatorial data. However, the pressure anisotropies of main concern here are the strong $P_\perp > P_\parallel$ anisotropies in the warm ion population in the inner part of the system, within $\sim 10 R_S$, as discussed in Section 6.3. Inside such distances the field does not generally depart strongly from a near-dipolar field [Bunce *et al.*, 2008; Arridge *et al.*, 2008a], for which $R = r/3$. Here we will therefore use this value as a simple approximation in equation (5.22), recognising that as the field becomes increasingly extended in the outer region by the plasma currents, the radius of curvature of the equatorial field will be reduced, and the pressure anisotropy currents correspondingly enhanced compared with those calculated here.

In addition to the plasma currents considered here, we note that *Wahlund et al.* [2009] have recently suggested that negatively-charged ice grains associated with the E-ring, moving in the inner magnetosphere in near-Kepler orbits, may also produce a

significant westward azimuthal current. If so, the current would flow in a narrowly-confined equatorial ring at a radial distance of $\sim 4 R_S$ where the grain density sharply maximises (e.g., *Kurth et al.* [2006]), close to the orbit of the moon Enceladus, which is the source of the ice grains. Here we do not consider the physics of this suggestion, but will comment further below on the empirical basis of the nature of the magnetic field perturbations observed.

6.3 – Plasma parameter profiles

As indicated in Section 6.1, the data examined here were obtained on consecutive inbound Cassini orbits, Revs 15 and 16. Figure 6.1 shows the spacecraft trajectory in the planet's equatorial x - y plane with the Sun at the top. The coordinate system employed is such that z points along the planet's spin axis, the x points towards the Sun, and y points towards dusk, completing the right-handed system. The trajectories of Revs 15 and 16 are closely similar, both being represented by the black line, where the solid and dashed portions represent the inbound and outbound parts of the orbits respectively. Only the data from the inbound passes are examined here, the more complicated situation on the nightside being reserved for future study. The coloured circles show day boundaries for Revs 15 (red) and 16 (blue), which are marked with similarly colour-coded 'day of year' (2005) numbers. The red and blue dashed lines show model magnetopause positions for Revs 15 and 16 respectively, computed using the *Arridge et al.* [2006] model fitted to the inner-most magnetopause crossing observed on the pass.

Given the assumptions discussed in Section 6.2, all the parameters in equation (5.22) can in principle be determined, allowing estimates to be made of the local azimuthal current density on individual passes through the ring current, such as those shown in Figure 6.1. In practice, however, not all parameters are routinely available, particularly those of the warm ion population, due to instrument field-of-view restrictions that are dependent on the orientation of the three-axis stabilised spacecraft. Where required, therefore, available data have been augmented with empirical models derived from particular data sets, as described below. In addition to data from the magnetic field instrument [*Dougherty et al.*, 2004], employed here at 1 min resolution, the data sets routinely available which are employed in this study are as follows.

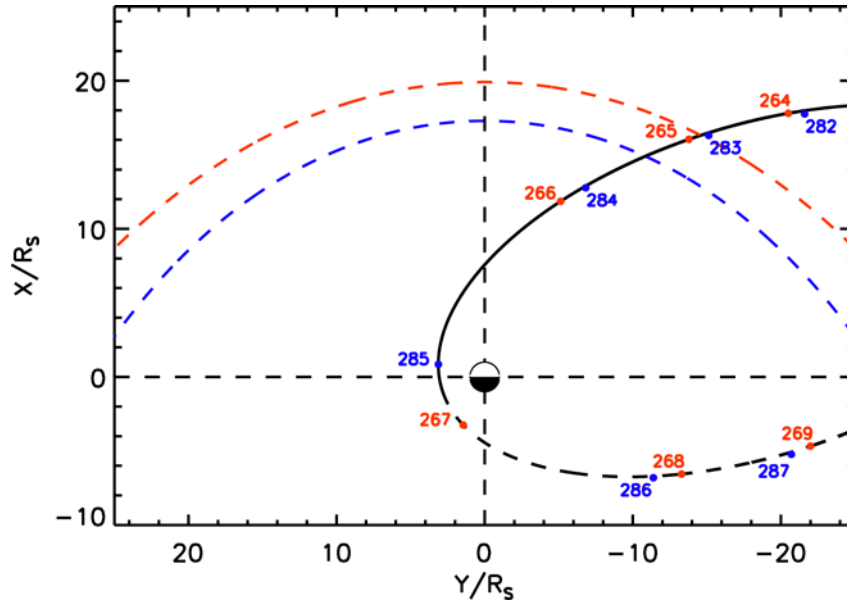


Figure 6.1. Cassini trajectory for Revs 15 and 16 shown in the planet's equatorial (x - y) plane, with noon at the top and dusk to the left. The trajectories of both Revs are represented by the thick black line where the solid and dashed sections represent the inbound and outbound parts of the orbits respectively. The coloured circles indicate day boundaries for Rev 15 (red) and Rev 16 (blue), which are marked with similarly colour-coded 'day of year' (2005) numbers. The red and blue dashed lines show model magnetopause positions for Revs 15 and 16 respectively, computed using the *Arridge et al.* [2006] model fitted to the last inbound magnetopause crossing.

(a) Density and pressure data at 5 min resolution for hot (>3 keV) protons (H^+) and water group ions (W^+) combined, derived from MIMI/CHEMS and LEMMS data by integration over the energy range from 3 keV to >200 keV, the water group ion spectrum being extrapolated to 3 keV from minimum measured energies of 9 keV [Krimigis *et al.*, 2004; Sergis *et al.*, 2007, 2009]. Pressure anisotropies are not presently available, but are not believed to be large [Sergis *et al.*, 2009], such that the hot ion pressure is taken to be isotropic at all radial distances as in previous related works.

(b) Density and pressure data at 1 min resolution for cold ($T_e \sim 1-10$ eV) and warm ($T_e \sim 100$ eV-1 keV) electrons combined, obtained from CAPS/ELS data by integration over the energy band from 0.6 eV to 26 keV [Young *et al.*, 2004; Lewis *et al.*, 2008; Schippers *et al.*, 2008]. The pressure is again taken to be isotropic. Valid parameters can only be derived in lower plasma density regions where the spacecraft potential is positive, typically beyond radial distances of $\sim 10-12 R_S$, the data then being corrected for the determined positive spacecraft potential with elimination of measured spacecraft photoelectrons. In inner regions of higher plasma density where the spacecraft potential becomes a few volts negative, the cold electron population is not fully measured. In these regions we instead use the CAPS/ELS data to compute the partial density and pressure of electrons with energy >20 eV. Electrons with these energies are not strongly affected by the spacecraft potential, such that the partial densities and pressure >20 eV provide valid information on the warmer electron population.

(c) Total electron density measurements at 8-16 second resolution obtained from measurements of the upper hybrid resonance frequency by the RPWS instrument [Gurnett *et al.*, 2004; Persoon *et al.*, 2009]. These data are generally available between periapsis and radial distances of $\sim 8-10 R_S$.

The methodology adopted is illustrated in Figure 6.2, where we show radial profiles of plasma density (upper panels) and pressure (lower panels) for the inbound passes of Revs 15 (left) and 16 (right), spanning ~ 3 to $20 R_S$. The vertical dashed lines at a radial distance of $18.8 R_S$ in the plots for Rev 16 show the last inbound magnetopause crossing, such that we do not consider data beyond that point. We first construct a radial profile of the total electron number density by combining RPWS data (yellow) in the inner region with CAPS/ELS data (blue) in the outer region where the spacecraft potential is positive. Similarly coloured solid lines join values averaged over $0.25 R_S$ intervals. A small data gap of $\sim 1-2 R_S$ generally remains between the RPWS

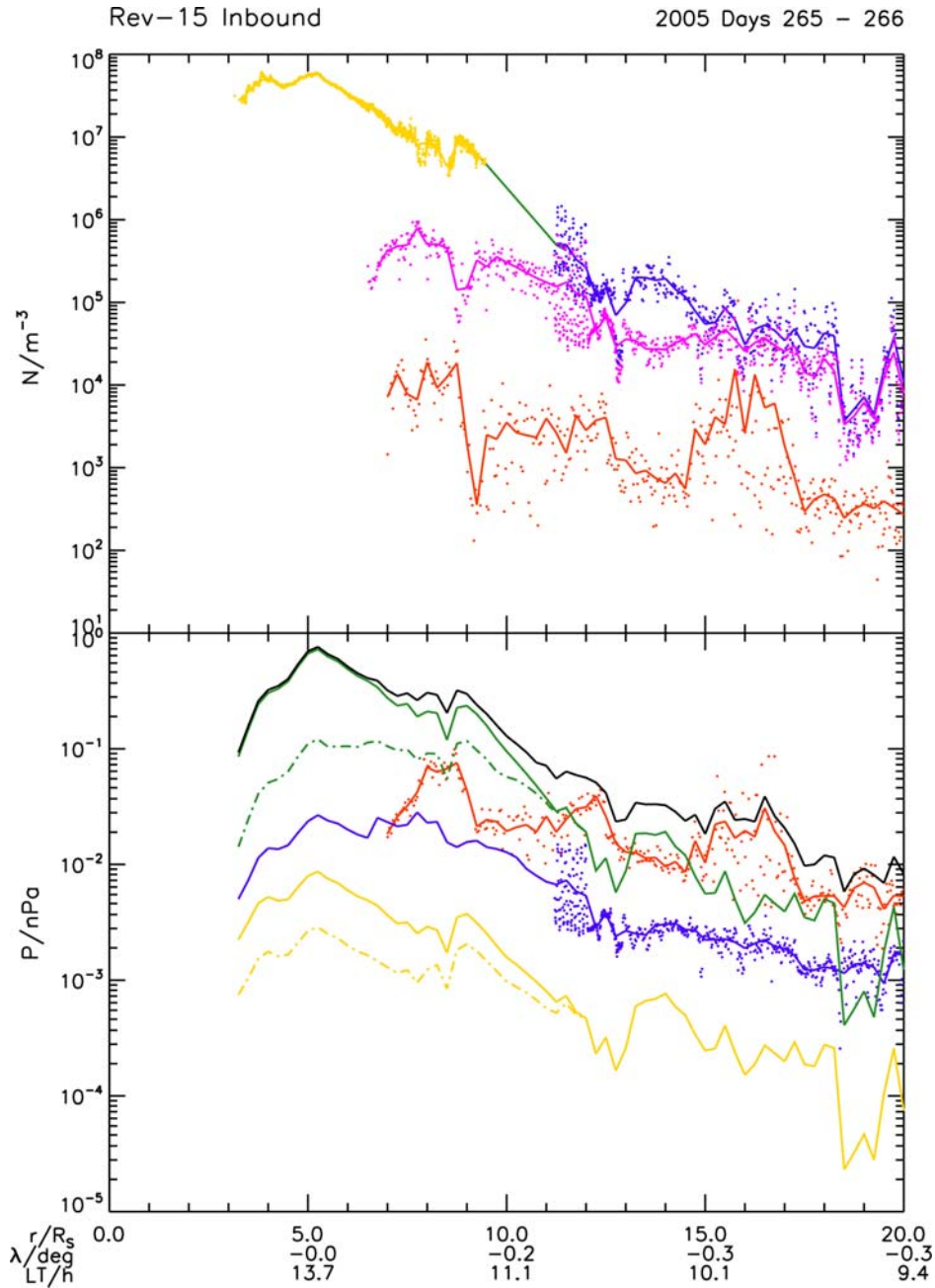


Figure 6.2a. Profiles of particle density and pressure for Rev 15 over the radial range from ~ 3 to $20 R_S$. The top panel of the plot shows the radial profile of the electron density (m^{-3}). The yellow, green and blue data show the total number density. The magenta data show the partial density of warm (>20 eV) electrons, while the red data show the hot (>3 keV) ion density. The lower panel in each plot shows the related radial profiles of the plasma pressure (nPa). The red data show the hot (>3 keV) ion pressure, while the blue data show the electron pressure. The green and yellow solid lines show the perpendicular pressure of the warm water group ions and protons respectively, while the similarly-colored dot-dashed lines show the parallel pressures of these populations. The total perpendicular pressure is shown by the solid black line. Spacecraft radial distance (R_S) is shown at the bottom of the plot, together with the latitude (degrees) and local time (hours).

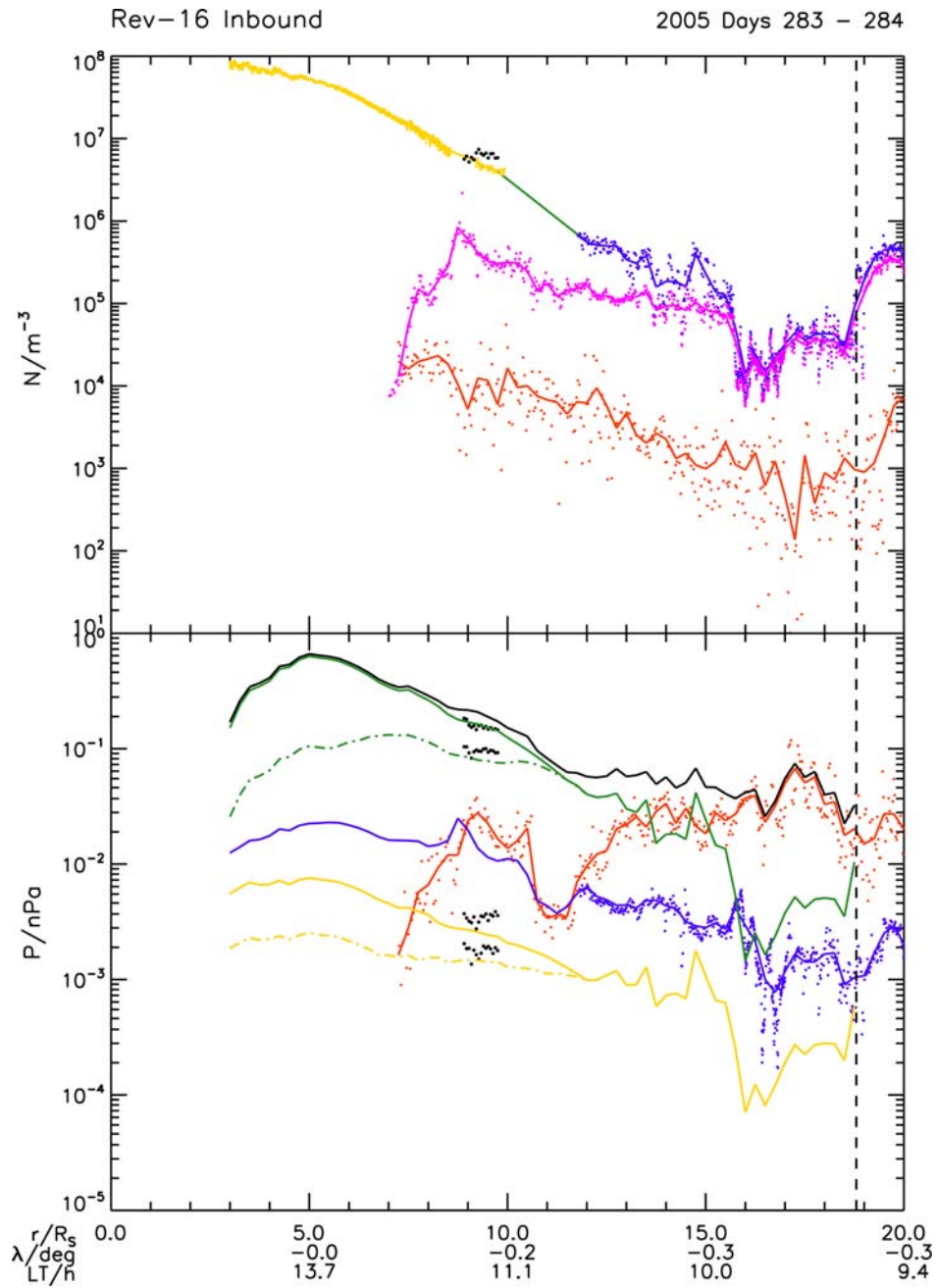


Figure 6.2b. As for Figure 6.2a except for Rev 16. The vertical black dashed line at a radial distance of $18.8 R_S$ shows the last inbound magnetopause crossing and the black points in the panels for Rev 16 show a small number of warm ion density and pressure values derived from CAPS/IMS data by *Wilson et al.* [2008].

and CAPS/ELS density data, centred near $\sim 10 R_S$, which we close by log-linear interpolation shown by the green line.

The magenta data in the upper panels show the partial density of >20 eV electrons as described above, extending into the inner region where the spacecraft potential becomes negative, but truncated and set to zero in the innermost region (where the density is much less than the total) due to contamination of the CAPS/ELS data by penetrating radiation belt particles. The difference in density between these values and the total electron density is taken to be the density of the cold ($T_e \sim 1-10$ eV) electrons. By charge neutrality, the total electron density shown in the upper panels of Figure 6.2 is also the total ion density (the charge density of charged ice grains generally being negligible), assuming the ions are predominantly singly-charged. The red data in the upper panels show the hot (>3 keV) water group ion plus proton density obtained by integration of the MIMI data, such that the difference between these values and the total density then represents the density of the warm (<3 keV) ions. The hot ion values are also truncated and set to zero in the inner region (where they are also much less than the total) for reasons similar to the electron data. It can be seen that except for some regions in the outer magnetosphere, the hot ions represent $\sim 1\%$ or less of the total ion density, such that the vast majority of the ions belong to the warm population. The black points at radial distances of $\sim 9-10 R_S$ in the density panel for Rev 16 show a small number of warm ion density values derived from CAPS/IMS data on this pass by *Wilson et al.* [2008]. It can be seen that these values agree very well with the concurrent RPWS density data. No such determinations are available for Rev 15 due to a lack of suitable spacecraft orientation.

The mass density of the plasma, ρ_m , required for the inertia current, is then obtained by applying a model ratio $R_i = (n_{w^+}/n_{H^+})$ of warm water group ions (mass 17 AMU) and protons (mass 1 AMU) to the total density data. This model is shown in panel (a) of Figure 6.3 (which shows all the empirical model profiles employed here), obtained from the overall analyses of CAPS/IMS data presented by *Wilson et al.* [2008] and *McAndrews et al.* [2009]. The value of R_i decreases from ~ 15 at $\sim 5 R_S$, to ~ 5 at $\sim 10 R_S$, and to ~ 1.5 at $\sim 20 R_S$, and is in agreement with the few individual values derived for Rev 16 by *Wilson et al.* [2008], shown by the red points in the plot. The

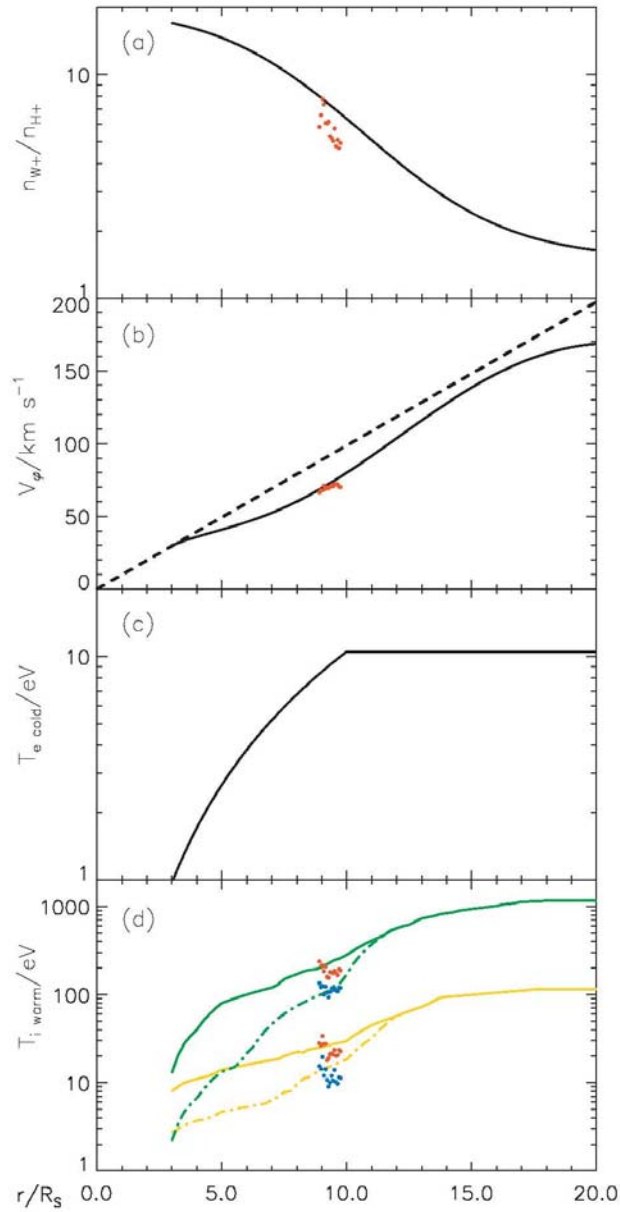


Figure 6.3. Plots of empirical model plasma parameter profiles employed to estimate the quantities required to derive the plasma currents. The continuous lines in the figure show models of (a) the number density ratio of warm water group ions and protons, (b) the azimuthal velocity of the plasma (the dashed line corresponds to rigid corotation with the planet), (c) the cold electron temperature model, and (d) the field-perpendicular (solid lines) and field-parallel (dot-dashed lines) temperatures of warm water group ions (green) and protons (yellow).

moderately sub-corotational azimuthal velocity of the plasma, V_ϕ , required for the inertia current has been taken from the empirical model employed by *Achilleos et al.* [2010a], based on the overall results of *Wilson et al.* [2008] and *Kane et al.* [2008]. This model is shown in panel (b) of Figure 6.3, where the dashed straight line shows rigid corotation for comparison. The model is again in good agreement with the Rev 16 data derived by *Wilson et al.* [2008] shown by the red points. These values are then combined with magnetic data to derive the inertia current density in equation (5.22).

We now turn to the pressure profiles shown in the lower panels Figure 6.2. The red data show the hot (>3 keV) ion pressure for water group ions and protons combined, derived from MIMI data, which make a small contribution to the total pressure inside $\sim 8 R_S$ but dominate the total pressure beyond $\sim 15 R_S$. The blue data show the electron pressure, determined by direct integration in the outer region where the spacecraft potential is positive, and by combining the >20 eV partial electron pressure with an estimate of the cold electron pressure in the inner region where the spacecraft potential is negative. The cold electron pressure has been determined by combining the difference between the >20 eV and total electron densities shown in the upper panels, with the cold electron temperature model of *Persoon et al.* [2009], shown in panel (c) of Figure 6.3. In this model the cold electron temperature increases from ~ 1 eV at $\sim 3 R_S$ to ~ 10 eV at $\sim 10 R_S$, where we note that we have slightly extrapolated the original model of *Persoon et al.* [2009] from an inner limit of $3.5 R_S$ to cover the whole range to $3 R_S$ considered here. Beyond $10 R_S$ the cold electron temperature is taken to remain constant at ~ 10 eV on the basis of the results presented by *Schippers et al.* [2008]. The 20 eV cut-off in the warm electron integrations was thus chosen to approximately interface with these values without a significant gap or overlap. The total electron pressure in Figure 6.2 is seen to peak at $\sim 5-7 R_S$ where the cold electrons dominate, and falls gradually with increasing distance in the outer region where the warm electrons dominate. Overall, the electron pressure throughout is $\sim 10\%$ or less of the total perpendicular pressure (shown by the solid black line).

The green and yellow solid lines in the lower panels of Figure 6.2 then show the perpendicular pressures of the warm water group ions and protons respectively. These have been determined by combining the warm ion number densities estimated as above with the perpendicular ion temperature models shown by the corresponding green and

yellow solid lines in panel (d) of Figure 6.3. The temperature profiles have been obtained from smoothed CAPS/IMS data derived by *Wilson et al.* [2008] and *McAndrews et al.* [2009] for radial distances beyond $\sim 5.5 R_S$, which have been augmented in the inner region ($\sim 3-5 R_S$) with Voyager data modelled by *Richardson* [1995] that interface well with the Cassini data. The temperatures increase with radial distance, lying typically in the range $\sim 10-100$ eV for protons and ~ 100 eV to 1 keV for water group ions, thus again approximately interfacing with the hot (>3 keV) ion data without a significant gap or overlap. The small number of perpendicular temperatures determined on Rev 16 by *Wilson et al.* [2008] (red data in Figure 6.3) again agree very well with the overall temperature model, such that the corresponding perpendicular pressures (black data in the lower panel of Figure 6.2) also agree very well with the overall estimates.

Our results show that while the warm proton pressure (yellow) is negligible throughout, being $\sim 1\%$ of the total, the warm water group ion perpendicular pressure (green) dominates in the inner region, peaking at ~ 1 nPa at $\sim 5-6 R_S$. Its value then falls to become comparable to the hot ion pressure (red) in the range $\sim 12-15 R_S$, before becoming smaller than the latter beyond $\sim 15 R_S$, in agreement with the previous results of *Sergis et al.* [2010]. The total perpendicular pressure profile, obtained by summing the contributions of the various populations is then shown by the black solid line, from which the pressure gradient current density in equation (5.22) is derived in Section 6.4. It peaks with the warm water group ions in the inner region, and falls gradually in the outer region in a manner determined principally by the combined behaviour of the hot and warm ions.

A significant feature of the warm ion populations is that their distributions are strongly anisotropic in the inner region with $P_{\perp} > P_{\parallel}$, as shown by both Voyager and Cassini ion data [*Richardson and Sittler*, 1990; *Richardson*, 1995; *Wilson et al.*, 2008], though approaching isotropy beyond $\sim 12 R_S$. The parallel pressures of these populations are shown by the dot-dashed green and yellow lines in the lower panels of Figure 6.2, again obtained by combining the warm ion density profiles for water group ions and protons with the parallel temperature model shown by the corresponding dot-dashed green and yellow lines in panel (d) of Figure 6.3. These model temperatures

have been determined in the same way as for the perpendicular temperature models described above. The parallel temperature values derived for Rev 16 by *Wilson et al.* [2008] are shown by the blue data in panel (d) of Figure 6.3, corresponding to the parallel pressure values shown by the black data in the lower panel of Figure 6.2. The pressure anisotropies of these populations are those employed here to determine the pressure anisotropy current density in equation (5.22). As mentioned above, pressure anisotropy profiles of the hot ions and the electrons are not presently available, being generally difficult to determine due to variably incomplete pitch angle coverage. However, examination of hot ion distributions observed during spacecraft roll manoeuvres in the central ring current region on Revs 15 and 16 indicate the presence of distributions that differ from isotropy only by a few tens of percent, while electrons beyond $\sim 10 R_S$ exhibit field-aligned distributions with pressure ratios $P_{\parallel}/P_{\perp} \sim 2$ or less. As indicated in Section 6.4 below, the pressure anisotropy currents produced by these populations will generally be more than an order of magnitude less than the current sources included here. The warm ions are thus expected to produce the most important anisotropy effects within the ring current, with pressure ratios $(P_{\perp}/P_{\parallel}) \approx 5$ for the dominant water group ions in the inner region.

6.4 – Current density profiles

Given the data shown in Figure 6.2, we can now compute the current density profile from equation (5.22), and compare it to that deduced from CAN disk modelling of the observed magnetic field perturbations. Results are shown in Figure 6.4 for (a) Rev 15 and (b) Rev 16. The top panels show the CAN model fits (grey dashed lines) to the colatitudinal component of the magnetic data (blue), from which the ‘Cassini SOI’ internal field model has been subtracted [*Dougherty et al.*, 2005]. The residual field results principally from the ring current, and shows strong negative values of ~ 10 to 15 nT in the inner region ($< 8 R_S$), reversing to weaker positive values in the outer region ($> 15 R_S$). The methodology employed to obtain the CAN model fits follows the best-fit process of *Bunce et al.* [2007], except that here we have used a current sheet half-thickness of $1.5 R_S$, instead of $2.5 R_S$ in the former study, following the results presented in Chapter 4 concerning the thickness of the current sheet in the dayside sector. The remaining three fit parameters (the inner and outer radii, and current

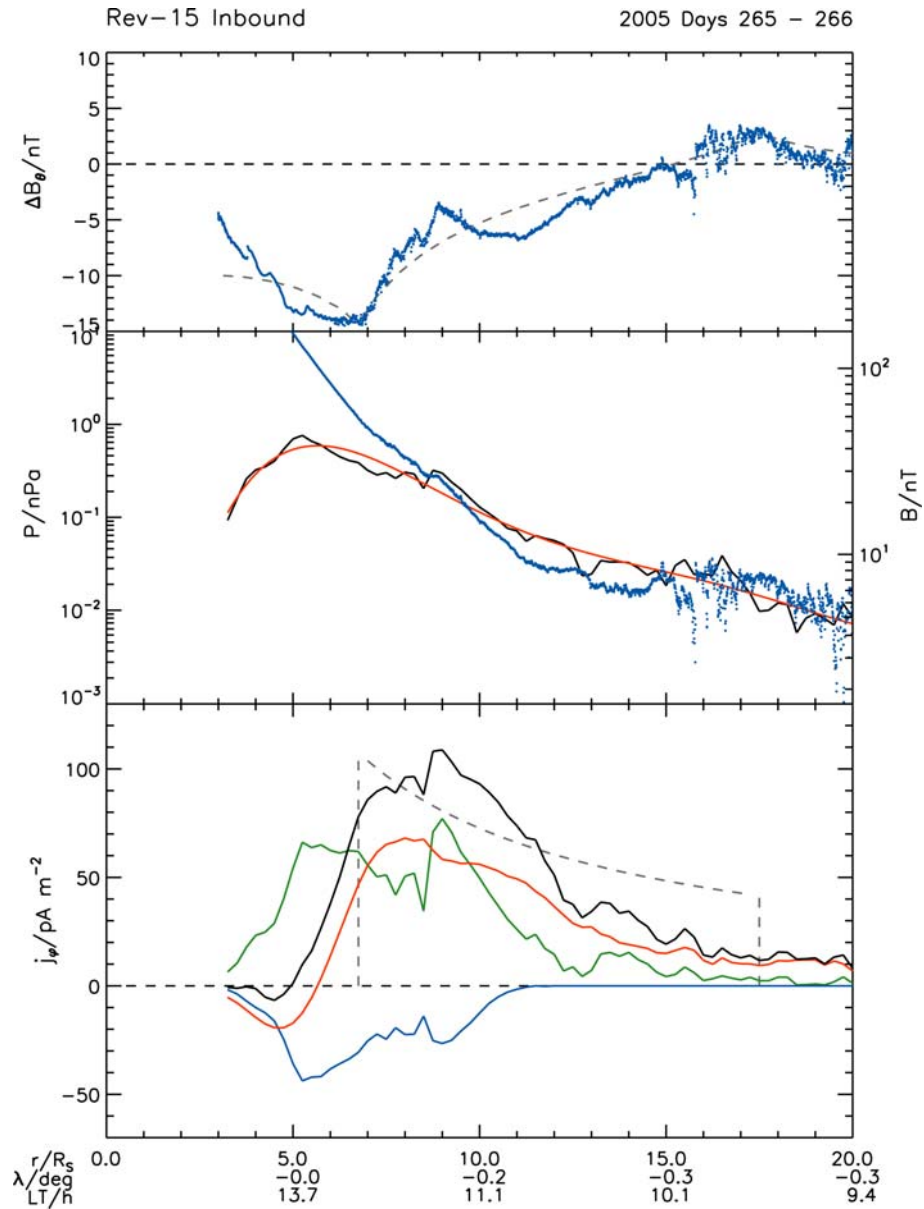


Figure 6.4a. Radial profiles of the magnetic field, pressure, and current density for Rev 15. The top panel of shows the co-latitude component of the magnetic field (nT) from which the ‘Cassini SOI’ model of the internal field has been subtracted (blue). The CAN model fit to these data is shown by the grey dashed line. The second panel shows the total perpendicular plasma pressure (black), a fifth order polynomial fit to this data (red), and the magnetic pressure (blue). A magnetic field strength scale is also shown on the right side of the panel. Current density profiles are shown in the third panel. The green line shows the inertia current density, the red line the pressure gradient current density, the blue line the anisotropy current density, and the black line the total current density. The grey dashed line shows the equatorial current density profile obtained from the CAN modelling of the magnetic field on these passes.

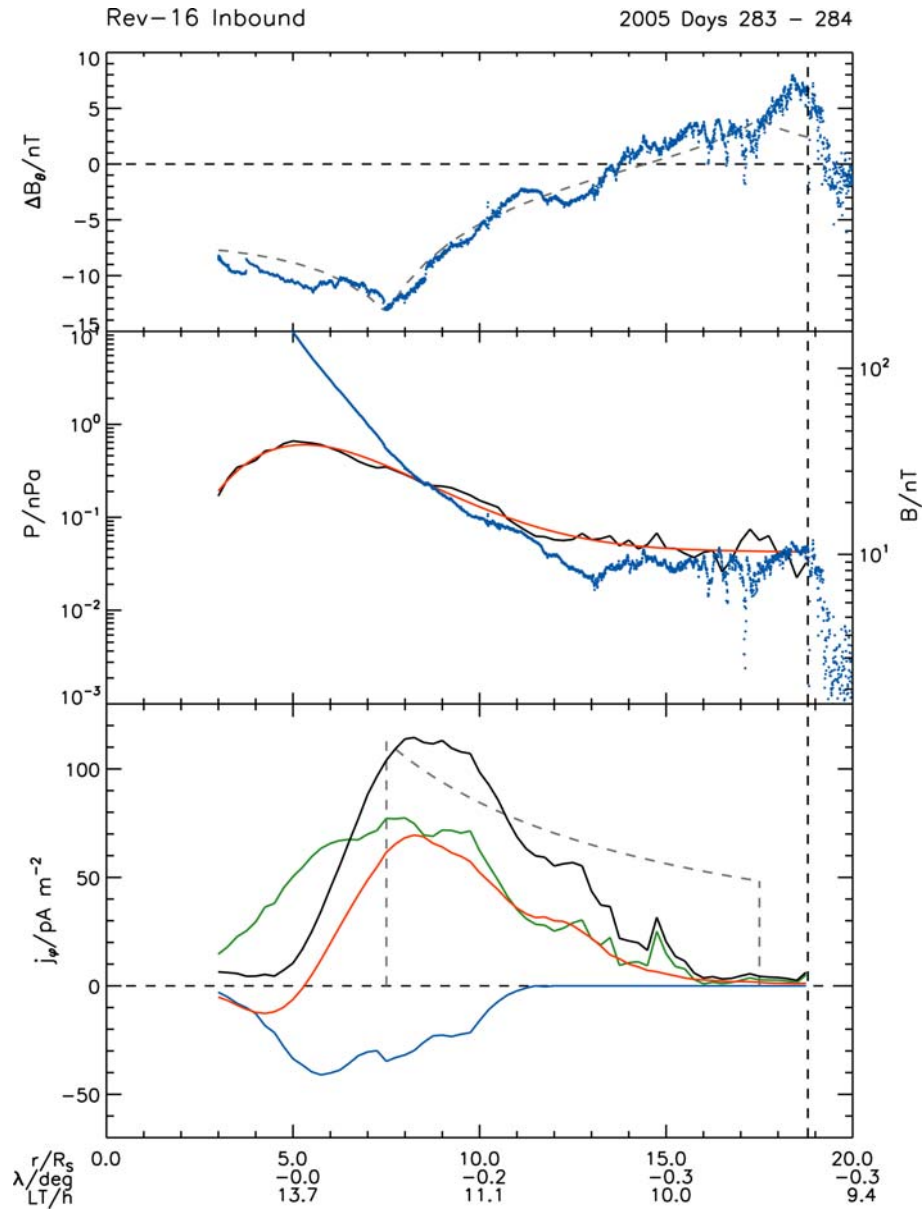


Figure 6.4b. As for Figure 6.4a except for Rev 16.

parameter) are determined by visual inspection of the data combined with consideration of the RMS deviation of the data points from the model. For Rev 15 we have inner and outer radii of 6.75 and 17.5 R_S , and a current density parameter, $\mu_0 I_0 = 55.0$ nT (the current density within the current disk being given by $j_\phi = I_0/\rho$ where ρ is the perpendicular distance from the magnetic/spin axis), while for Rev 16 these parameters are 7.5 and 17.5 R_S , and 64.0 nT. The resulting fits to the data are seen to be reasonably good in both cases, with RMS deviations of 2.07 and 2.10 nT for Revs 15 and 16 respectively. The implied equatorial current density profile is shown by the grey dashed line in the bottom panel, for comparison with the estimated plasma current density profiles.

We note in passing at this point that there is no evidence in these (or other) magnetic field data for significant currents associated with charged E-ring grains as suggested by *Wahlund et al.* [2009]. As mentioned in Section 6.2, these would produce an equatorial ring of eastward (positive azimuthal) current at a radial distance near $\sim 4 R_S$ where the grain density sharply maximises, which will produce negative perturbations in the co-latitudinal field inside this distance, reversing sharply to positive perturbations outside this distance. Clearly no such perturbations are observed in the upper panels of Figure 6.4, at least within the ~ 1 nT level of general field fluctuations. Biot-Savart considerations then show that the upper limit to such a current is ~ 0.4 MA, which may be compared with the total plasma ring current of ~ 8 MA implied by the CAN modelling of the observed field perturbations for both Revs 15 and 16 above.

The middle panels in Figure 6.4 then show comparisons between the total perpendicular plasma pressure (black), obtained from the lower panels of Figure 6.2, with the magnetic pressure (blue), such that their ratio gives the local plasma β value. It can be seen that β is small in the inner region, but increases to unity at $\sim 8-9 R_S$ where the field and plasma pressures are near-equal, while $\beta > 1$ conditions are maintained throughout the outer magnetosphere, as found previously by *Sergis et al.* [2010]. The fifth order polynomial fits to the perpendicular pressure profiles (red) are used to determine the pressure gradient current in equation (5.22). The polynomial profile is seen to provide a good overall fit to the pressure data in each case, while smoothing over small-scale structure in the data.

Current density profiles resulting from each term in equation (5.22) are shown in the bottom panels of Figure 6.4, where the green line shows the inertia current density, the red line the pressure gradient current density, and the blue line the pressure anisotropy current density. The black line shows the sum of these three, for comparison with the CAN model profile shown by the grey dashed line. It can be seen that the pressure gradient current is small and negative in the innermost region where the pressure increases with radius, passes through zero at $\sim 5-6 R_S$ where the total perpendicular pressure peaks (solid black line in the middle panel), peaks at $\sim 7-8 R_S$ near the inner edge of the CAN model profile, and then falls with distance in the outer magnetosphere, more quickly for Rev 16 than Rev 15, due to the weaker radial gradient in the former pressure profile than in the latter. By contrast, the inertia current, which is positive throughout, rises rapidly from small values in the innermost region at $\sim 3 R_S$, to values much larger than that of the pressure gradient current in the inner region out to $\sim 7 R_S$, as found by *Sergis et al.* [2010]. It then peaks around $\sim 7-9 R_S$ before falling again in the outer region. The outer values are similar on the two passes, being comparable with the smaller outer pressure gradient currents on Rev 16, while being lower than the higher pressure gradient currents on Rev 15.

The blue lines in the lower panels of Figure 6.4 show the pressure anisotropy current densities for the two passes determined from the warm ion populations, which are negative and of significant magnitude throughout the inner region due to the $P_{\perp} > P_{\parallel}$ conditions prevailing. It can be seen that in the innermost region between ~ 4 and $\sim 7 R_S$ these currents are approximately equal and opposite to the inertia currents, such that the pressure anisotropy current strongly modifies the current profile in the inner region. Beyond $\sim 7 R_S$, however, these currents gradually decline to smaller values as the warm ion pressures approach isotropy, and are zero within our estimates beyond $\sim 12 R_S$ where pressures are isotropic. Due to the approximate cancellation between the inertia current and the pressure anisotropy current in the inner region ($< 6 R_S$), the total current curve shown by the black line in the lower panels of Figure 6.4 more nearly follows the pressure gradient current in this region. As the pressure anisotropy current declines in strength in the region beyond ($> 7 R_S$), however, the total current increases, following a similar profile to the pressure gradient current, but with values which are a factor of

~ 1.5 greater than the latter in the case of Rev 15, increasing to ~ 2 times greater for Rev 16.

With regard to the pressure anisotropy currents of hot ions and electrons in the central and outer ring current region, neglected here, we note that estimates based on equation (5.22) show that the hot ion departures from isotropy of a few tens of percent indicated in Section 6.3 will produce pressure anisotropy currents of typically $\sim 2 \text{ pA m}^{-2}$, smaller by more than an order of magnitude than the currents estimated here. Similarly, while electron pressure anisotropies $P_{\parallel}/P_{\perp} \sim 2$ in the outer region may typically be somewhat larger, the estimated pressure anisotropy currents remain at similar low values because the electron pressures are typically $\sim 10\%$ of the ion pressures. Inclusion of these effects, whilst desirable in future work, is thus unlikely to change our overall conclusions.

Comparing with the CAN model profiles, we observe significant correspondences, with both currents peaking at similar values of $\sim 100 \text{ pA m}^{-2}$. The peak values deduced from the plasma data occur at radial distances of $\sim 8\text{-}9 R_S$, just outside the $\sim 7 R_S$ inner edges of the best-fit disk models, with values decreasing rapidly at smaller radial distances. Beyond the peak, however, the current deduced from the plasma data decreases more rapidly with increasing radial distance than is assumed in the disk model, as previously noted by *Sergis et al.* [2010].

6.5 – Summary and Discussion

Following the recent discussion by *Sergis et al.* [2010] of average conditions within Saturn's central ring current region ($6\text{-}15 R_S$) deduced from plasma data obtained by the Cassini spacecraft, here we have presented a first complementary discussion of the ring current densities over the radial range ~ 3 to $\sim 20 R_S$ on two individual near-equatorial dayside passes. Magnetic field and plasma data from twenty additional passes have been studied with similar results (see Chapter 7). Here we have also compared the results with those obtained for the same passes from modelling the observed magnetic perturbations using the *Connerney et al.* [1983] current disk model, following the methodology of *Bunce et al.* [2007]. We have firstly shown that although the inertia

current density associated with warm water group ions is the largest individual current component inside radial distances of $\sim 6 R_S$, the eastward current due to this component is strongly reduced in this region by the oppositely-directed westward current due to the strong $P_\perp > P_\parallel$ pressure anisotropy of these ions, such that these currents approximately cancel inside this distance. The total current density in the inner region then more nearly follows the pressure gradient current density, rising quite sharply from near-zero values near $\sim 6 R_S$, and peaking at $\sim 8 R_S$.

We suggest that the physical origin of this near-cancellation effect results from the nature of the warm water ion source, which is believed to be due to charge exchange-related ion pick-up from the Enceladus-related torus of water group neutral particles that orbit Saturn [e.g., *Tokar et al.*, 2008]. Ion pick-up from a cold neutral source which is orbiting with a Keplerian speed V_K , significantly less than the near-corotation speed of the plasma V_ϕ , produces a strong pressure anisotropy with $P_\perp > P_\parallel$, for which it is easy to show that the inertia and pressure anisotropy currents are approximately equal and opposite in a quasi-dipolar field. Putting $R \approx r/3$ into equation (5.22) for a quasi-dipolar field and neglecting factors close to unity, the magnitude of the ratio of the pressure anisotropy current density $j_{\perp\phi A}$ to the inertia current density $j_{\perp\phi I}$ is

$$\left| \frac{j_{\perp\phi A}}{j_{\perp\phi I}} \right| \approx \frac{3(P_\perp - P_\parallel)}{\rho_m V_\phi^2} . \quad (6.1)$$

Ion pick-up under the above circumstances results in the formation of a ring-distribution in velocity space in the plasma bulk flow frame, the ring being located at the field-perpendicular difference speed $(V_\phi - V_K)$ for all ion components, with near-zero speed parallel to the field lines. For such distributions we have $P_\perp \approx \rho_m (V_\phi - V_K)^2 / 2 \gg P_\parallel$, such that equation (6.1) gives $|j_{\perp\phi A} / j_{\perp\phi I}| \approx 3(1 - f)^2 / 2$, where $f = (V_K / V_\phi)$. The two current densities will thus generally be of comparable magnitude, but opposite in direction. For example, in the cold plasma torus at a radial distance of $\sim 5 R_S$ the Kepler speed of the neutrals is $\sim 11 \text{ km s}^{-1}$, compared with our empirically-based model plasma

speed (at ~85% of rigid corotation) of $\sim 41 \text{ km s}^{-1}$. We then have $f \approx 0.27$ and $|j_{\perp\phi A}/j_{\perp\phi I}| \approx 0.8$, comparable with our results in the inner region shown in Figure 6.4. The ratio of these currents computed from the results shown in Figure 6.4 rises from values of ~ 0.3 at a radial distance of $\sim 3 R_S$ to peak at ~ 0.7 at $\sim 5.5 R_S$, then falling to near zero at $\sim 11 R_S$ where the warm ions become near-isotropic.

The cancellation effect is thus reduced at larger distances where the water group ions become scattered towards isotropy, such that beyond $\sim 6 R_S$ the growing positive difference between the inertia and pressure anisotropy currents significantly augments the pressure gradient current. Overall, the equatorial radial profile of the eastward current density is similar in shape to that produced by the pressure gradient current alone, but augmented in strength by factors of ~ 1.5 - 2.0 . In the two examples investigated here, which exhibit magnetic field perturbations that are entirely typical of the Cassini data set as a whole [Bunce *et al.* 2007], the total azimuthal current density rises from small values near $\sim 6 R_S$, peaks at $\sim 100 \text{ pA m}^{-2}$ near $\sim 8 R_S$, and then falls more slowly with radial distance in the outer magnetosphere, reducing to values below $\sim 25 \text{ pA m}^{-2}$ at distances beyond $\sim 15 R_S$, up to the $20 R_S$ limit of our study. Estimates of the pressure anisotropy currents of the hot ions and plasma electrons in the central and outer ring current, not included here, are more than an order of magnitude below such values. The similarity of the results obtained on the two passes, on nearly identical trajectories but separated in time by ~ 18 days, again suggests that the results reflect typical conditions within Saturn’s dayside magnetosphere. This conclusion is tested by the analysis of a larger data set, the results of which are presented in Chapter 7. Comparison with the results of current disk modelling of the magnetic field perturbations on these passes shows good agreement with the gross features, particularly with the locations and magnitude of the peak current density. However, the currents derived from the plasma data are found to fall more rapidly with distance beyond the peak than the $1/r$ dependence assumed in the model.

Finally, no evidence is found for a current ring at a radial distance of $\sim 4 R_S$ associated with the charged Kepler-rotating ice grains associated with the E-ring, as suggested by Wahlund *et al.* [2009]. The magnetic data suggest an upper limit on such a current of $\sim 0.4 \text{ MA}$, compared with $\sim 8 \text{ MA}$ in the outer plasma-produced ring current.

Chapter 7

Local time dependency and temporal variability of Saturn's ring current

7.1 – Introduction

The study presented in Chapter 6 used plasma parameter and magnetic field profiles to derive the current contributions on two individual Cassini passes through the dayside magnetosphere spanning the radial range from ~ 3 to $20 R_S$. In this chapter we employ the same pass-by-pass methodology as detailed in Chapter 6, but extend the data set to a wider range of orbits to explore both local time (LT) and pass-to-pass temporal variations in Saturn's ring current. Specifically, we consider magnetic field and plasma particle data from both the inbound and outbound passes of eleven near-equatorial Cassini orbits that span the radial range ~ 3 to $20 R_S$, together with a wide range of LTs. The LT dependence and temporal variability of the ring current is investigated by deriving azimuthal current density profiles from the magnetic field and plasma data for each pass, which are then compared and combined to consider the mean current profiles and the range of variation about the mean.

In the next section we provide details of the data sets employed in this study, together with an outline of the essential features of the analysis methodology. As indicated above, the methodology largely follows that detailed in Chapter 6, to which we thus refer for further details (specifically Sections 6.2 and 6.3). The results are presented in Section 7.3, and the chapter concludes with a summary and discussion in Section 7.4.

7.2 – Data Set and Methodology

7.2.1 - Data Coverage

The data examined in this chapter were obtained during 11 Cassini periapsis passes on revolutions (Revs) 15-25, spanning September 2005 to July 2006, thus yielding 22

traversals of Saturn's ring current. These passes were all closely equatorial, the spacecraft being located within half a degree of latitude of Saturn's equatorial plane throughout. Figure 7.1 shows the relevant segments of the trajectories plotted in the planet's equatorial X - Y plane, with the Sun at the top. The coordinate system employed is such that Z points along the planet's spin (and magnetic) axis, the X points towards the Sun, and Y points toward dusk, completing the right-handed system. All 11 trajectories are shown labelled by the Rev number, with inbound and outbound segments being coloured blue and red, respectively, inside the radial range of $20 R_S$ examined here, while being shown black outside this range. The trajectory for Rev 20, data from which are employed in Section 7.2.2 to exemplify the methodology, is shown by the solid line, with black circles plotted at the beginning of each day of year (DOY) of 2006 as marked. The trajectories of other Revs are shown by dashed lines. We note that the results presented in Chapter 6 were derived using data from the inbound passes of Revs 15 and 16, spanning the dayside sector from pre-noon to dusk, which also form part of the data set employed here.

The black dot-dashed lines in the upper part of Figure 7.1 show for reference the *Kanani et al.* [2010] model magnetopause positions for solar wind dynamic pressures of 0.01 and 0.1 nPa, spanning the usual range at Saturn. It can be seen that the data segments inside $20 R_S$ should generally lie within the magnetosphere on the dayside, unless unusually high solar wind dynamic pressure conditions prevail. All dayside data have thus been screened to exclude magnetosheath intervals. Overall, it can be seen from Figure 7.1 that good radial coverage is obtained at all LTs from the post-dusk to the pre-noon sector. However, radial coverage is limited to the inner part of the system, within $\sim 9 R_S$, in the noon to dusk sector.

7.2.2 - Plasma Properties and Data Sources

We now consider how the Cassini data have been employed to determine the azimuthal current density from equation (5.22). The main particle populations in Saturn's magnetosphere that contribute to the density and pressures in this equation are the warm (few tens to few hundreds of eV) and hot (few keV and above) water ions and protons [e.g., *Krimigis et al.*, 2007; *Wilson et al.*, 2008; *McAndrews et al.*, 2009; *Mitchell et al.*, 2009b], together with cold (few eV) and warm (few hundred eV to a few keV) electrons

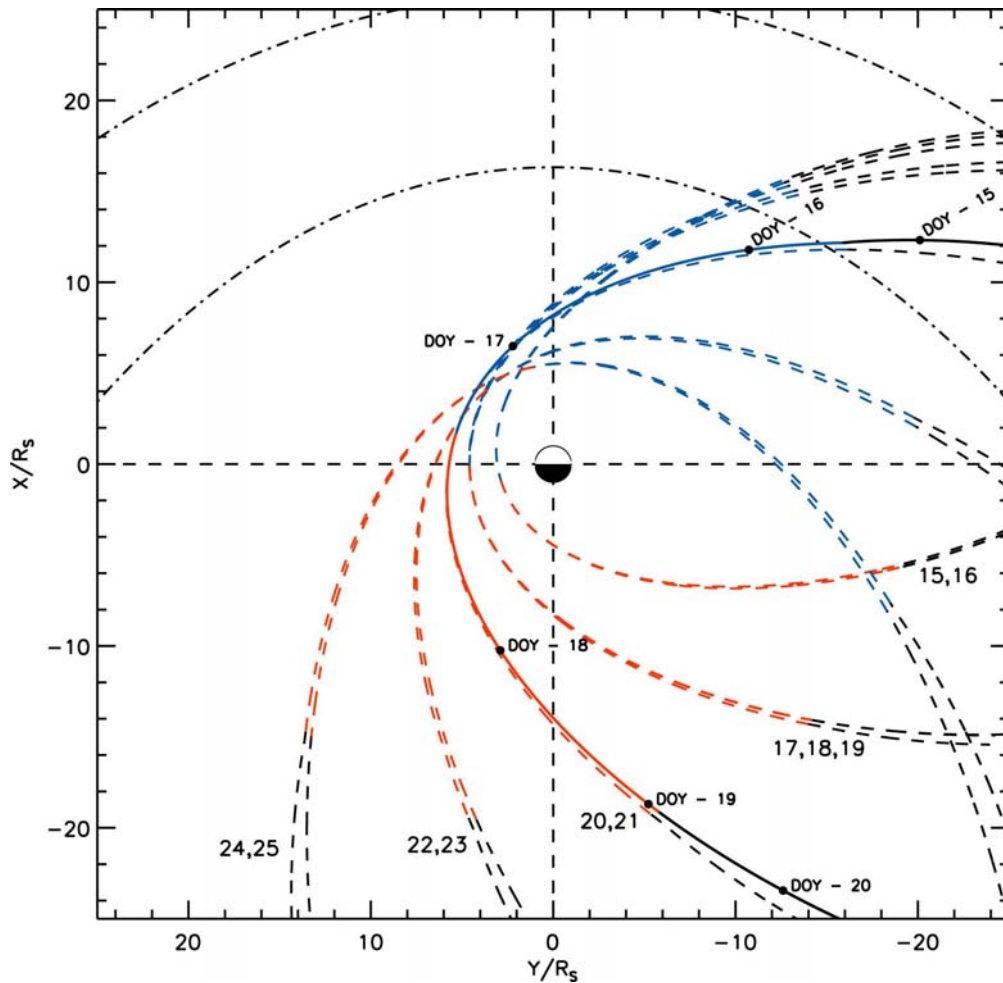


Figure 7.1. Near-equatorial Cassini periapsis-pass trajectories for Revs 15-25 plotted in Saturn's equatorial X - Y plane, with noon at the top and dusk to the left. Inbound and outbound segments within radial distances of $20 R_S$ are shown blue and red, respectively, while being shown black beyond that distance. The trajectory for Rev 20, whose data are shown in Figure 7.3, is indicated by the solid line, with black circles being plotted at the beginning of each day, marked with day of year (DOY) numbers of 2006. The trajectories of other Revs are similarly shown by the dashed lines. The black dot-dashed lines in the upper part of the figure show the *Kanani et al.* [2010] model magnetopause positions for solar wind dynamic pressures of 0.01 (outer line) and 0.1 nPa (inner line), spanning the usual range at Saturn.

[e.g., *Lewis et al.*, 2008; *Schippers et al.*, 2008]. The warm ions and cold electrons originate in the Enceladus torus and are dominant in the inner part of the system, while the hot ions and warm electrons become more important further out. Given the bulk parameter profiles of these populations, all of the terms in equation (5.22) can be determined on individual passes through the ring current, thus making it possible to estimate the local azimuthal current density. However, as previously mentioned in Chapter 6, not all parameters are routinely available, particularly those of the warm ion population due to instrument field-of-view restrictions, such that it is necessary to augment available data with empirical models.

The routinely available Cassini data sets employed in this study are described in Chapter 6. The empirical models required to convert these data into mass density and pressure profiles are similar to those shown in Figure 6.3, however, here we employ an updated velocity model (described below) such that an updated version of the models employed is shown in Figure 7.2. From top to bottom these are (a) the water ion to proton number density ratio of the warm ion population, (b) the warm ion temperatures for water ions (green) and protons (yellow), both perpendicular (solid lines) and parallel (dot-dashed lines) to the magnetic field, (c) the temperature of the cold electrons, and (d) the azimuthal bulk velocity of the plasma, where the dashed line shows rigid corotation. These are all shown as profiles versus equatorial radial distance over the range 3 to 20 R_S . The warm ion parameters are based on the Cassini CAPS/IMS measurements of *Wilson et al.* [2008] and *McAndrews et al.* [2009], augmented in the innermost region by Voyager results presented by *Richardson* [1995]. The cold electron temperatures are based on the model of *Persoon et al.* [2009], derived over the radial range between 3.5 and 10 R_S from RPWS and CAPS/ELS data. Here we slightly extrapolate the model inwards to 3 R_S , shown by the dashed line in Figure 7.2c, while taking a constant value beyond 10 R_S as suggested by the CAPS/ELS measurements of *Schippers et al.* [2008]. The velocity model follows the CAPS/IMS results of *Wilson et al.* [2010] inside 10 R_S (this being updated from the model employed in Chapter 6 and the model of *Achilleos et al.* [2010a] beyond, the latter being based on the MIMI/INCA results of *Kane et al.* [2008] in that regime. It can be seen in panel (b) that the warm ion temperatures only differ significantly from isotropy inside of $\sim 12 R_S$, but are strongly anisotropic in the inner region. In panel (d) it can be seen that the plasma azimuthal

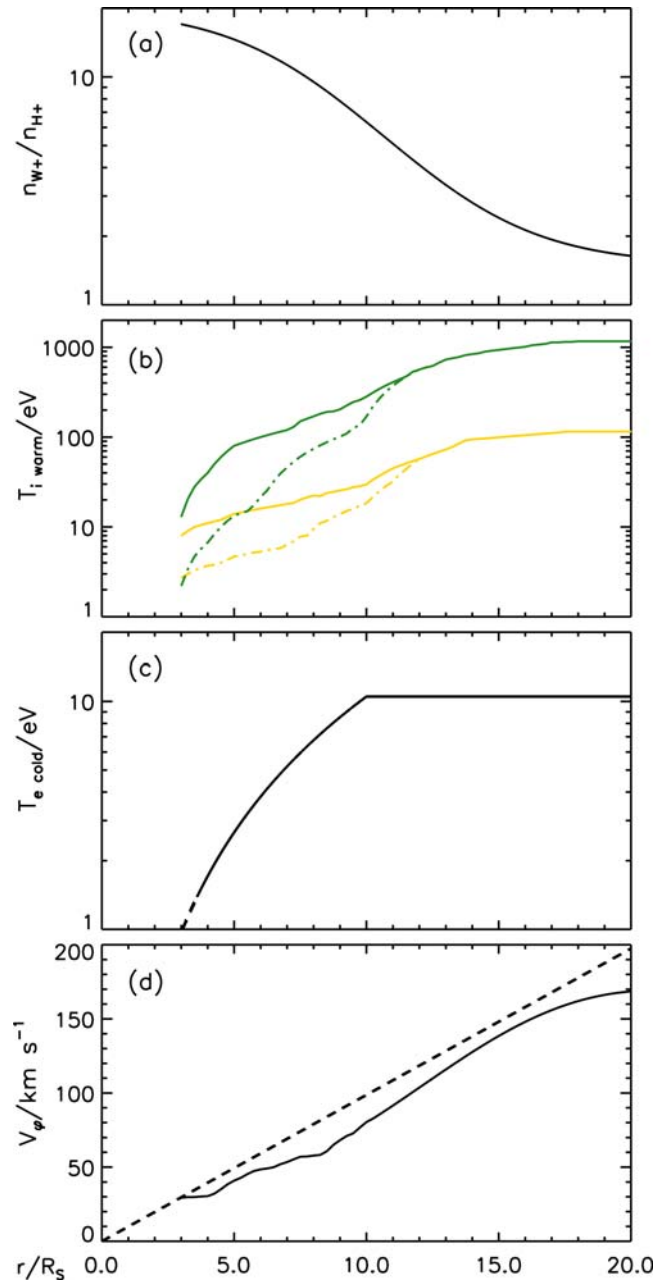


Figure 7.2. Plots of empirical model plasma parameter profiles that are combined with pass-to-pass Cassini data to derive plasma current density profiles. These show (a) the ratio of the number density of warm water group ions to protons, (b) the field-perpendicular (solid lines) and field-parallel (dot-dashed lines) temperatures of warm water group ions (green) and protons (yellow), (c) the temperature of the cold electrons, and (d) the azimuthal velocity of the plasma (solid line) compared with rigid corotation (dashed line). The source information on which these profiles are based is given in Section 7.2.2.

velocity remains modestly lower than rigid corotation throughout the region investigated here.

7.2.3 - Plasma Parameter Profiles

The detailed methodology adopted is illustrated in Figure 7.3, where in Figures 7.3a and 7.3b we show results for the inbound and outbound passes of Rev 20, respectively. These passes span radial distances between periapsis at $\sim 5.5 R_S$ and $20 R_S$, and LTs between 8.5 and 16.8 h on the inbound pass and 16.8 and 1.1 h on the outbound pass (Figure 7.1). The first panels of these figures show total electron number density profiles obtained from RPWS data (yellow) and CAPS/ELS (blue), together with the partial densities of ≥ 20 eV electrons from CAPS/ELS (magenta) and hot water ions and protons combined from MIMI (red). Similarly coloured solid lines join values averaged over $0.25 R_S$ intervals. As indicated above, the total electron density values have a few- R_S gap between the RPWS data in the inner region and the CAPS/ELS data in the outer region, which we close by a log-linear interpolation shown by the green line to form an overall total electron density profile spanning the full radial range. The difference between the total density values and those of the ≥ 20 eV electrons is taken to represent the density of the cold electrons, a reasonable assumption since the cold electron temperatures are generally several eV (Figure 7.2c), such that their velocity distribution interfaces with that of the ≥ 20 eV electrons without a major energy gap or overlap. Similarly the difference between the total density values and those of the hot ions is taken to represent the density of the warm ion population, assuming the ions are principally singly-charged. This is again a reasonable procedure since the warm ion parameters employed here (shown in Figure 7.2) were derived by *Wilson et al.* [2008] from convecting bi-Maxwellian fits to CAPS/IMS data that primarily characterise the ion population with energies up to a few keV, while the MIMI hot ion distributions employed extend in energy above ~ 3 keV. Thus there is again no major energy gap or overlap. It can then be seen from Figure 7.3 that the warm ions dominate the ion number density by at least an order of magnitude at all radial distances.

The second panels in Figures 7.3a and 7.3b show the pressure profiles. The perpendicular (solid) and parallel (dot-dashed) pressures of warm water ions (green) and

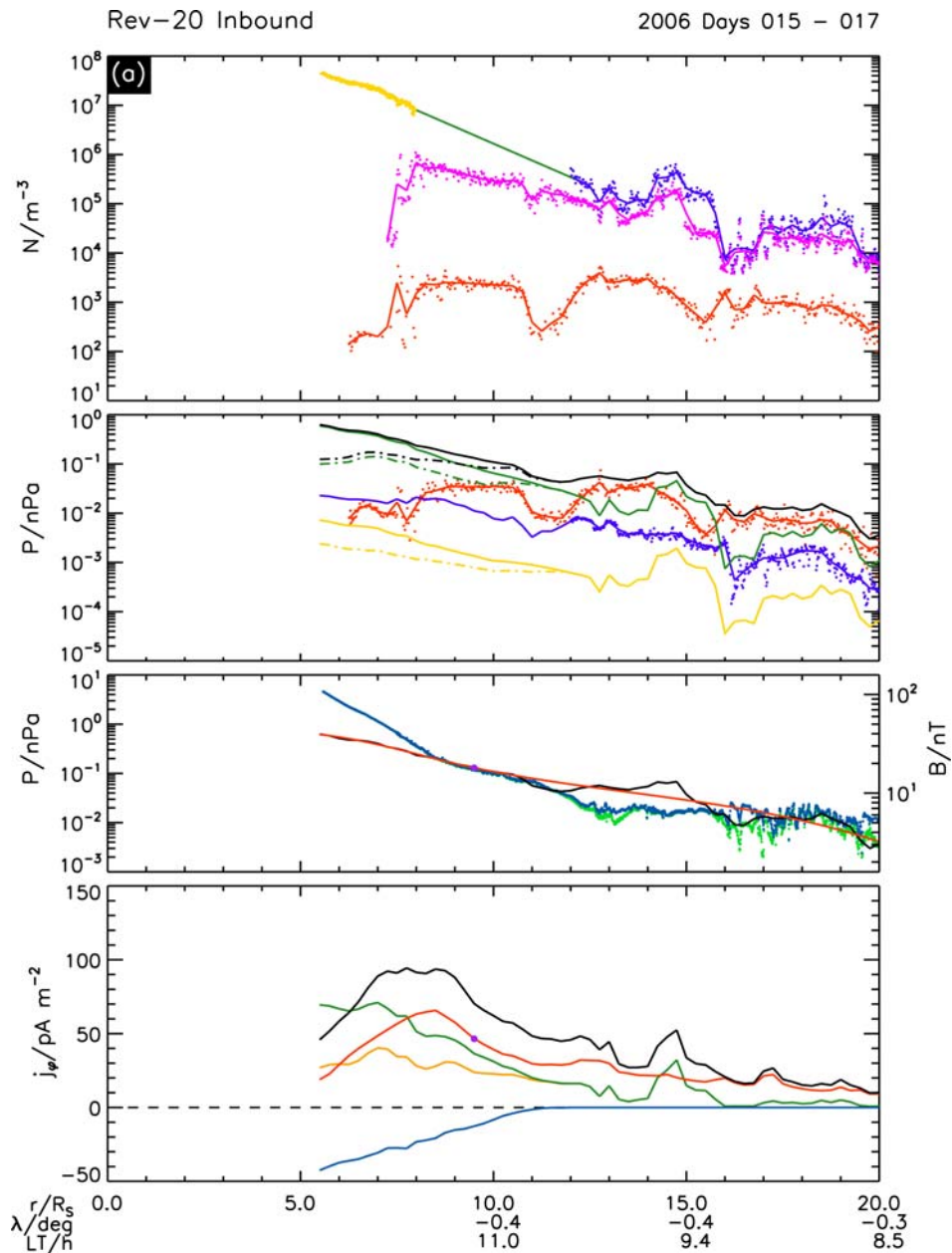


Figure 7.3a. Radial profiles of particle and field parameters for the inbound pass of Rev 20. The top panel shows the particle density (m^{-3}), while the second panel shows related radial profiles of the plasma pressure (nPa), as shown in Figure 6.2. The third panel shows the total perpendicular plasma pressure (black line), a combination of fifth order (inner) and third order (outer) polynomial fits to this data (red, with a purple dot indicating where these fits join), the total magnetic pressure (blue), and the pressure of the co-latitude component of the magnetic field (green). A magnetic field strength scale (nT) is also shown on the right side of the panel. The fourth panel shows the inertia current density (green), the pressure anisotropy current density (blue), their sum (orange), the perpendicular pressure gradient current density (red), and the total current density (black). At the bottom of the plot we also give the latitude (degrees) and LT (hours) of the spacecraft at various radial distances on the pass concerned.

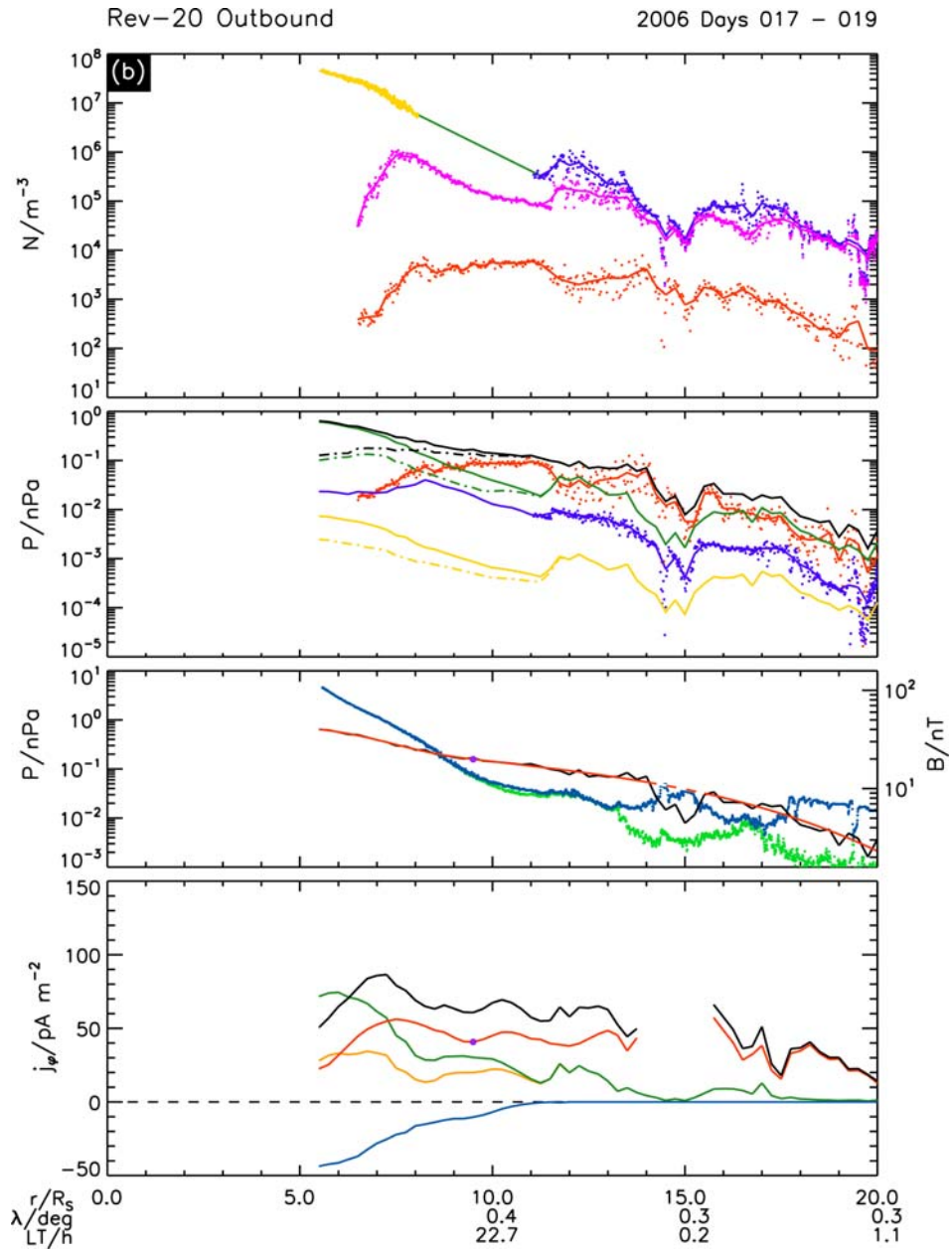


Figure 7.3b. As for Figure 7.3a, except for the outbound pass of Rev 20. In the third panel, perpendicular pressure values (black line) are omitted from the outer polynomial fit (red line) where the spacecraft appears temporarily to have exited the hot central plasma sheet (dashed portion of the red line). Current values in the fourth panel are omitted in this interval.

protons (yellow) are obtained by combining the total warm ion density profile derived from the data in the upper panels with the models of the water ion to proton density ratio and the warm ion temperatures in Figures 7.2a and 7.2b. Of these two, the warm water ion pressure dominates the warm proton pressure over the whole range by more than an order of magnitude. The warm water ion pressure also dominates the combined hot ion pressure obtained by direct integration of MIMI data (red) inside $\sim 10 R_S$, while the latter pressure becomes comparable with and larger than the warm ion pressure at larger distances. The total electron pressure (blue) is obtained by direct integration of corrected CAPS/ELS data in the outer region where the spacecraft potential is positive, while in the inner region it is obtained by combining the partial pressure of ≥ 20 eV electrons (not shown) with the pressure of the cold electrons, obtained in turn by combining the cold electron number density derived from the data in the upper panels with the cold electron temperature model shown in Figure 7.2c. The ≥ 20 eV electron pressure typically dominates outside $\sim 7 R_S$, while the cold electron pressure dominates inside these distances where the ≥ 20 eV electron densities become strongly reduced. The total perpendicular (solid) and parallel (dot-dashed) pressure profiles are shown by the black lines, obtained by summing the pressures of the warm ions (green and yellow lines), the hot ions (red), and the electrons (blue).

7.2.4 - Current Density Profiles

The plasma parameter profiles are then employed to derive the values of the various current density terms in equation (5.22), shown in the bottom panels of Figure 7.3. The inertia current requires the mass density ρ_m of the plasma, dominated throughout by the warm ions, determined by combining the total number density with the water ion (mass 17 AMU) to proton (mass 1 AMU) number density ratio in Figure 7.2a. This is then combined with the azimuthal velocity model shown in Figure 7.2d and magnetic field parameters, of which the total field strength B is shown in the third panels of Figures 7.3a and 7.3b (blue data). A field strength scale is shown on the right-hand side of this panel, which also shows the co-latitudinal component of the field, B_θ (green), for use in later discussion. The inertia current density so determined is then shown by the green curve in the fourth panels of Figures 7.3a and 7.3b. It peaks in the innermost

region sampled at values of $\sim 70 \text{ pA m}^{-2}$, and falls quite rapidly outside $\sim 7 R_S$ both inbound and outbound to values of $\sim 10 \text{ pA m}^{-2}$ and below at distances beyond $\sim 13 R_S$.

Similarly, the pressure anisotropy current density in equation (5.22) is determined from the difference between the perpendicular and parallel pressures, which thus involves only the warm ion population in this formulation, combined with magnetic field parameters and the $R \approx r/3$ approximation. This is shown in the fourth panels of Figures 7.3a and 7.3b (blue), where, due to the $P_{\perp} > P_{\parallel}$ conditions prevailing, this current has large negative (westward-directed) values of $\sim -45 \text{ pA m}^{-2}$ in the innermost region, rising rapidly towards zero at and beyond $12 R_S$ where the distributions become near-isotropic. The pressure anisotropy current thus cancels a significant fraction of the inertia current in the inner region, a finding which in Chapter 6 we argued to be a direct consequence of the ion pick-up process from Enceladus-related neutrals in this region. The combination of the two currents inside $12 R_S$ is shown in the fourth panels (orange), which peaks near $\sim 7 R_S$ at $\sim 35 \text{ pA m}^{-2}$, half the peak inertia current value, and falls more gradually to smaller values beyond.

While the inertia and pressure anisotropy current densities depend only on individual values of plasma and field parameters as modelled or measured, the pressure gradient current density must be determined from the variation of the perpendicular pressure along the spacecraft track, assumed to be due principally to radial rather than to LT variations. This is done by least-squares fitting polynomial functions to the total perpendicular pressure data (black), as shown in the third panels of Figures 7.3a and 7.3b. Also shown are the combination of fifth order (inner) and third order (outer) polynomial fits to this data (red, with a purple dot indicating where these fits join, ensuring that the pressure and its gradient are continuous at the join). Some pressure data have been omitted from the fit on the outbound pass, indicated by the dashed-line portion of the red curve, where the spacecraft appears temporarily to have left the hot central plasma sheet region. It can be seen that these polynomials provide good overall fits to the pressure data while smoothing over the small-scale variability. We also note that comparison of the perpendicular plasma pressure (black) and magnetic field pressure (blue) in the third panels of Figures 7.3a and 7.3b relates directly to the local

plasma β value (the perpendicular pressure divided by the magnetic pressure). It can be seen that β is small but increasing with radial distance in the inner region reaching $\beta \approx 1$ at $\sim 8-9 R_S$, while $\beta \geq 1$ conditions generally prevail throughout the outer equatorial magnetosphere, as found previously by *Sergis et al.* [2010].

The perpendicular pressure gradient current density derived using the polynomial fits combined with magnetic field parameters is shown in the fourth panels of Figures 7.3a and 7.3b (red). Values are omitted in regions where the fitted curves are not representative of the pressure data (shown dashed in panel three), under which condition the fitted profile cannot appropriately be combined with the simultaneously observed field data. It can be seen that the current increases from values of $\sim 20 \text{ pA m}^{-2}$ in the inner region to peak at $\sim 65 \text{ pA m}^{-2}$ at $\sim 8.5 R_S$ and $\sim 55 \text{ pA m}^{-2}$ at $\sim 7.5 R_S$ for the inbound and outbound data respectively, before falling again in the outer region, more quickly on the inbound (dayside) pass than on the outbound (nightside) pass. Comparison with the combined inertia-pressure anisotropy current (orange then green lines) shows that the two components are comparable in the innermost region at $\sim 6 R_S$, while the inertia-pressure anisotropy current then falls to roughly half the pressure gradient current at radial distances ~ 8 to $\sim 13 R_S$, and to even smaller fractions beyond. The total current density, shown in the fourth panels (black), thus has a profile similar to that of the pressure gradient current, but elevated by overall factors of ~ 1.5 in agreement with the results presented in Chapter 6 based on Revs 15 and 16 inbound data, the factor being somewhat larger than this in the innermost region, and somewhat smaller in the outermost region.

With regard to the significance of the current densities determined in Figure 7.3, and on other passes, we note that due to the near-equatorial nature of the spacecraft trajectory, the currents determined will generally correspond to the central equatorial current layer where the current density will generally maximise with respect to latitude. North-south displacements of the spacecraft from the equatorial plane are typically $\sim 0.1 R_S$ or less throughout, small compared with the current layer half-thickness of $\sim 1.5 R_S$ determined in Chapter 4. Beyond radial distances of $\sim 10 R_S$, however, we note that previous studies have shown that the current sheet centre becomes increasingly

displaced northward of the planet’s equatorial plane due to the action of the solar wind flow during the southern summer conditions that prevailed throughout the study interval [Chapter 4 of this thesis and *Arridge et al.*, 2008b]. Estimates of this effect based on the modelling results of *Arridge et al.* [2008b] suggest that the displacement of the current sheet centre northward of the spacecraft may increase typically to $\sim 1 R_S$ at the $20 R_S$ outer radial limit considered here. However, with a half-thickness of $\sim 1.5 R_S$ this still implies that the spacecraft will lie within the main part of the equatorial current layer at such distances. Consequently, our results should provide representative values of the ring current density over the full radial range considered here.

7.2.5 - Comparison with Field Modelling Results

In Figure 7.4 we show a comparison of these total current density profiles with those obtained from CAN model fits to the magnetic field data, where in Figures 7.4a and 7.4b we show results for the inbound and outbound passes of Rev 20, respectively. The top panels of these figures show the CAN model fits (grey dashed lines) to the co-latitudinal component of the magnetic field (blue dots), from which the Cassini Saturn Orbit Insertion (SOI) internal field model of *Dougherty et al.* [2005] has been subtracted. The residual field results principally from the ring current, and has strong negative values inwards of $\sim 10 R_S$, increasing to small positive values for the dayside inbound pass and weaker negative values for the nightside outbound pass in the outer region ($> 15 R_S$). This minor day-night asymmetry is an effect due mainly to magnetopause and tail currents flowing at larger distances. Significant field variations are also present associated with the global field oscillations near the planetary period [e.g., *Andrews et al.*, 2008, 2010], which we attempt to ‘average through’ in the fitting.

The methodology employed to obtain the CAN model fits is described in *Bunce et al.* [2007], except that here we use a current sheet half-thickness of $1.5 R_S$ following the results presented in Chapter 4. The remaining three ring current model parameters (as described in Section 2.8) for the inbound pass are inner and outer radii of 7 and $23 R_S$, and a current parameter $\mu_0 I_0 = 50$ nT, while for the outbound pass these parameters are 7 and $16.75 R_S$, and 50 nT. In addition we also use a simple representation of the day-night asymmetry effect of the more distant currents to improve the fits, given by a co-

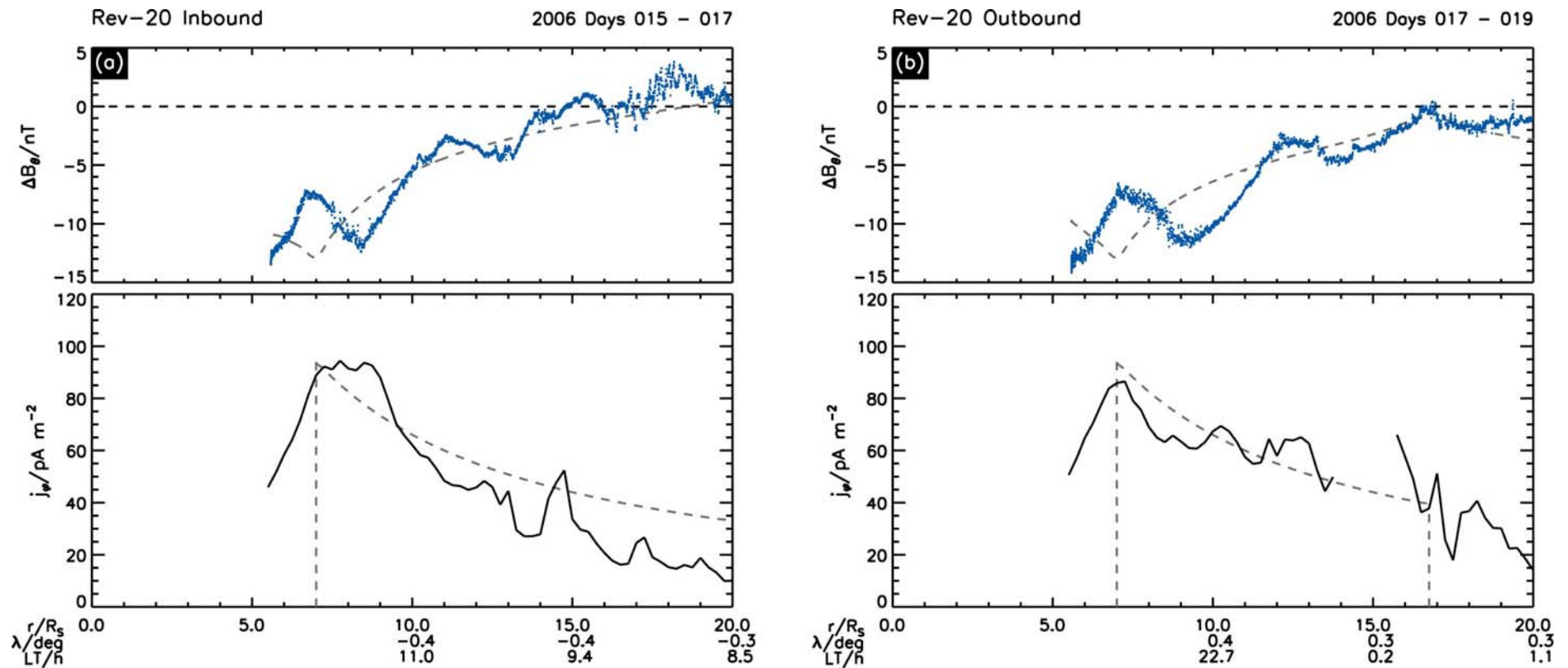


Figure 7.4. Radial profiles of the magnetic field and current density for Rev 20 (a) inbound and (b) outbound. The top panel of each plot shows the co-latitude component of the magnetic field (nT) from which the ‘Cassini SOI’ model of the internal field has been subtracted (blue). The CAN model fit to these data is shown by the grey dashed line, the parameters of which are given in the text. The bottom panel shows the total current density derived from the plasma data (black solid line) as shown in the lower panels of Figures 7.3a and 7.3b, together with the current density profile corresponding to the CAN model fit shown in the upper panel (grey dashed line).

latitudinal field that varies linearly with the X coordinate (see *Bunce et al.* [2007]) from -1.0 nT at $X = 20 R_S$ to $+4.0$ nT at $X = -20 R_S$. The resulting fits to the data are seen to be good for both passes, with RMS deviations of 1.9 and 2.1 nT for the inbound and outbound passes respectively, compared with peak perturbations in excess of ~ 10 nT.

The CAN model azimuthal current density profiles are then shown by the grey dashed lines in the bottom panels of Figures 7.4a and 7.4b, while the solid black lines show the total current density obtained from the plasma data in the bottom panels of Figures 7.3a and 7.3b, respectively. Comparison of these two empirical estimates shows good agreement between their gross features, thus showing that the current density deduced from the plasma data, combined with a full layer width of $\sim 3 R_S$, is compatible with the perturbations observed in the equatorial magnetic field. In particular, the peak current densities deduced from the plasma data on the inbound and outbound passes have values of ~ 95 pA m⁻² at $\sim 8 R_S$ and ~ 85 pA m⁻² at $\sim 7 R_S$, respectively, compared with ~ 95 pA m⁻² at $\sim 7 R_S$ for the inbound and outbound CAN models. However, for the inbound pass, the current density deduced from the plasma data then decreases more rapidly with increasing radial distance than the $1/\rho$ dependence assumed in the CAN model, as previously noted by *Sergis et al.* [2010]. This is not the case for the outbound pass, however, where the current deduced from the plasma data decreases at a slower rate with radius than on the inbound pass, more comparable with that of the CAN model profile.

7.3 - Results

Having thus described the analysis of the data from one Rev in detail, we now survey and compare the results obtained from all 22 ring current passes.

7.3.1 - Local Time Dependence

We begin by providing an overview of the dependence on LT of the principal plasma and field parameters and the resulting current density components. These are shown in

Figures 7.5-7.7, where we have divided values calculated at $0.25 R_S$ radial resolution into four LT quadrants, corresponding to midnight to dawn, dawn to noon, and so on, and have determined mean profiles versus radial distance. With this choice, radial coverage is good in all quadrants except noon to dusk, where data are available only in the inner region to distances of $\sim 9 R_S$.

In Figure 7.5 we show radial profiles of the plasma and field parameters, where the blue lines correspond to 0-6 h LT, orange to 6-12 h, red to 12-18 h, and green to 18-24 h. Green and blue thus correspond to the nightside, and orange and red to the dayside. The grey shaded regions on each profile indicate the associated standard errors of the mean (shown individually in Figure 7.9). Panel (a) of Figure 7.5 first shows the number of available passes that contribute to each mean plasma parameter value. Panel (b) shows profiles of the total number density, while panel (c) shows the total perpendicular (solid lines) and parallel (dot-dashed lines) plasma pressures summed over the contributions of warm ions, hot ions, and electrons. Panel (d) then shows profiles of the main co-latitudinal component of the magnetic field that appears in the numerator of the inertia current and the denominator of the pressure gradient current. In Figure 7.6 we show the individual contributions to the plasma pressure, where in separate panels for each quadrant we show radial profiles of the perpendicular (solid) and parallel (dot-dashed) pressures of the warm ions (water group plus protons, green), hot ions (water group plus protons, red), and electrons (blue).

If we first consider the total number density profiles shown in panel (b) of Figure 7.5, dominated by the warm ion population throughout, it can be seen that the mean densities are essentially independent of LT in the inner region between ~ 5 and $\sim 9 R_S$. Increasing variability between the quadrants is evident at larger distances, but typically only by factors of ~ 2 , and without a clear systematic dependency on LT. Indications can be seen of a day-night asymmetry in the dusk sector in the innermost region between ~ 3 and $\sim 5 R_S$, with modestly larger densities on the nightside than on the dayside. While this result is based on data from only two passes (Revs 15 and 16), the effect is present in both these data sets.

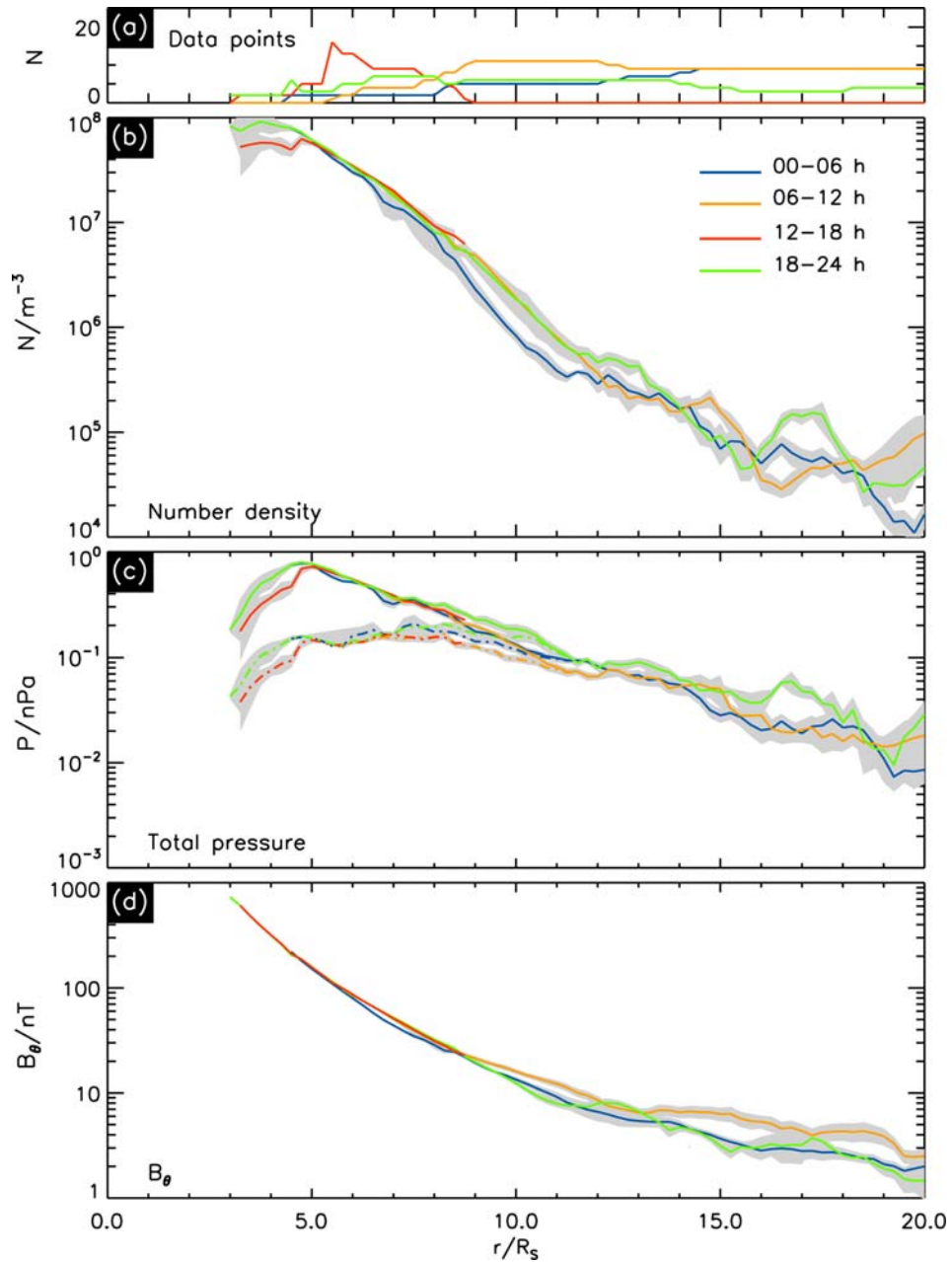


Figure 7.5. Radial profiles of mean plasma and magnetic field parameters separated into four LT quadrants, namely midnight to dawn (blue), dawn to noon (orange), noon to dusk (red), and dusk to midnight (green). The solid coloured lines show the mean values in each quadrant of the $0.25 R_S$ radial resolution data obtained from each pass, while the grey shaded region represents the associated standard error of the mean for each profile (shown individually for each quadrant in Figure 7.9). The panels of the figure show (a) the number of available data points (passes) for the plasma parameter profiles, (b) the mean total number density, (c) the mean total plasma pressures perpendicular (solid lines) and parallel (dot-dashed lines) to the field, and (d) the mean co-latitude component of the magnetic field.

Turning now to the pressure data, we first note that since the warm ion pressures are derived in our formulation by combining the warm ion density with the temperature model shown in Figure 7.2b, these profiles, shown separately for the perpendicular pressure in Figure 7.6, also show little systematic variation with LT. The mean electron pressures in Figure 7.6 similarly show a lack of systematic LT effects, though these provide only modest contributions ($\sim 10\%$ or less) to the total pressure throughout. The mean hot ion pressures in Figure 7.6, on the other hand, become important in the outer region, typically rising to exceed the mean warm ion pressures by factors of ~ 2 beyond $\sim 10\text{-}12 R_S$. In this outer regime they again display only modest LT dependencies of factors of ~ 2 , however, with a tendency for somewhat higher mean pressures and densities in the dusk to midnight sector. The hot ion pressures and densities are considerably more variable in the inner region inside $\sim 9 R_S$, but here they generally provide only small contributions to total values. As a consequence of these behaviours, the mean total plasma pressure values in panel (c) of Figure 7.5 also show a marked lack of dependency on LT, particularly between ~ 5 and $\sim 9 R_S$, though with a tendency for the perpendicular pressure in the dusk to midnight sector (green) to be marginally higher than those in other quadrants outside this range.

Panel (d) of Figure 7.5 shows that the strength of the co-latitudinal field also has a modest LT dependence, with values beyond $\sim 9 R_S$ becoming increasingly larger on the dayside (at least in the dawn to noon sector) than on the nightside, reaching almost factors of ~ 2 at $\sim 15 R_S$ and beyond. A similar effect is not seen in the total field strength in the outer magnetosphere, however, which again shows little dependency on LT (not shown). From equation (5.22) we note that this field effect will enhance the pressure gradient current in the outer region on the nightside compared with the dayside for given pressure gradients. It will also enhance the inertia current on the dayside compared with the nightside for given centrifugal ‘forces’, but as already noted in relation to Figure 7.3 this component is generally less important than the pressure gradient current in the outer region.

Corresponding radial profiles of the mean current density similarly divided into LT quadrants is shown in Figure 7.7, in a similar format to Figure 7.5. In panel (a) we

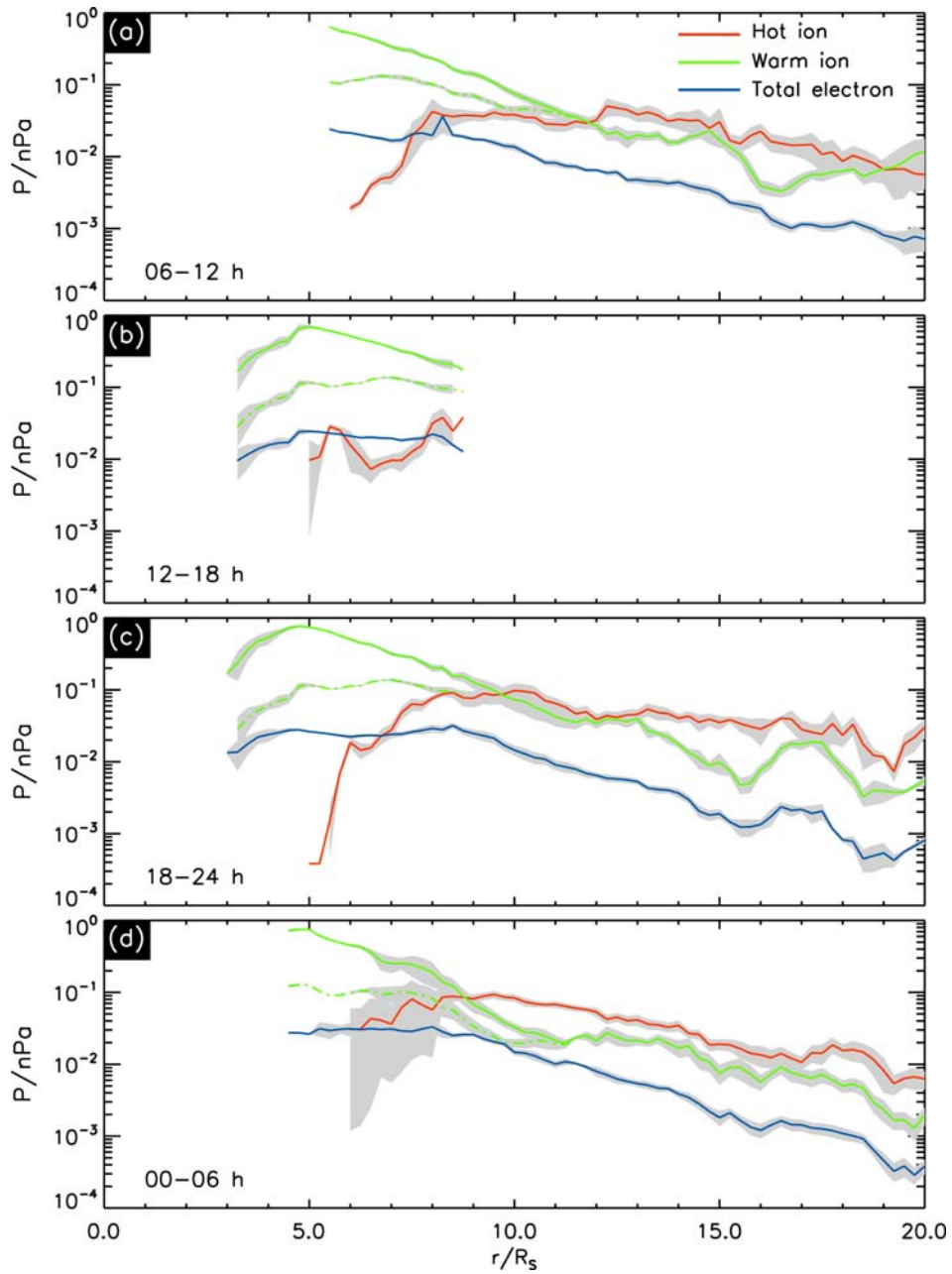


Figure 7.6. Radial profiles of the mean perpendicular (solid) and parallel (dot-dashed) pressures of warm ions (water group plus protons, green), hot ions (water group plus protons, red), and electrons (blue), divided into LT quadrants corresponding to (a) dawn to noon, (b) noon to dusk, (c) dusk to midnight, and (d) midnight to dawn.

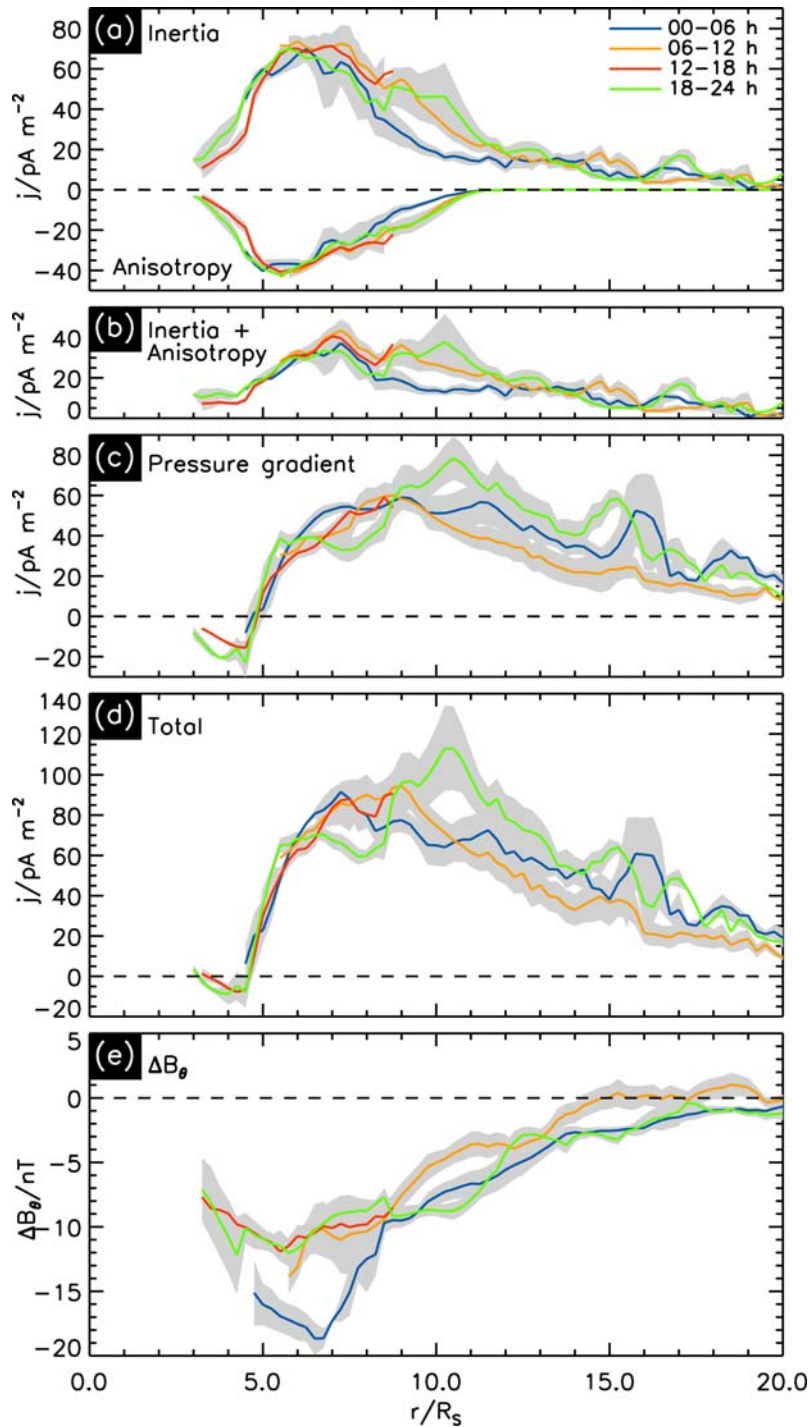


Figure 7.7. Radial profiles of the mean current density components and magnetic field separated into four LT quadrants, in the same format as Figure 7.5. The panels of the figure show (a) the mean inertia (upper) and pressure anisotropy (lower) current densities, (b) their sum, (c) the mean perpendicular pressure gradient current density, (d) the mean total current density, and (e) the mean co-latitude component of the perturbation magnetic field (nT), from which the ‘Cassini SOI’ model of the internal field has been subtracted.

show the mean inertia and pressure anisotropy current densities, panel (b) shows their sum, while panel (c) shows the mean perpendicular pressure gradient current density. Panel (d) shows the mean total current density. Panel (e) then shows the mean co-latitudinal component of the magnetic field with the ‘Cassini SOI’ internal field subtracted, principally showing the magnetic effect of the ring current.

As may be anticipated from the discussion of Figure 7.5, it can be seen that the inertia and pressure anisotropy currents in panel (a) both have very similar profiles in all four LT quadrants, particularly in the inner region to radial distances of $\sim 9 R_S$. The inertia current rises from small values of $\sim 15 \text{ pA m}^{-2}$ at $\sim 3 R_S$, peaks at $\sim 70 \text{ pA m}^{-2}$ at $\sim 6 R_S$, and then falls with radial distance to values of $\sim 10 \text{ pA m}^{-2}$ by $\sim 15 R_S$. The pressure anisotropy current similarly increases in magnitude from small values at $\sim 3 R_S$ to a negative peak $\sim -40 \text{ pA m}^{-2}$ near $\sim 5.5 R_S$, approximately half the peak inertia current value, and then decreases in magnitude back towards zero at and beyond $\sim 12 R_S$ where the pressure becomes near-isotropic. The combined inertia-pressure anisotropy current shown in panel (b) thus peaks at $\sim 35\text{-}40 \text{ pA m}^{-2}$ at $\sim 7 R_S$, and falls gradually to smaller values in the outer regions, where the nightside current (blue and green) appears somewhat more variable than the dayside current (orange).

Considering the pressure gradient current in panel (c), we similarly see that the profiles are all quite similar in the inner region to $\sim 9 R_S$, but are more variable in the outer region beyond. The current is small and negative in the innermost region where the perpendicular pressure rises with radial distance, passes through zero at $\sim 5 R_S$ where the pressure maximises, and peaks at $\sim 60 \text{ pA m}^{-2}$ at $\sim 8.5\text{-}9.0 R_S$ for the LT quadrants from midnight to dusk via dawn and noon (blue, orange, and red lines). In the dusk to midnight sector (green), however, the mean current initially peaks at smaller $\sim 40 \text{ pA m}^{-2}$ values at $\sim 6.5 R_S$, before increasing further with radial distance, reaching $\sim 80 \text{ pA m}^{-2}$ at $\sim 10.5 R_S$. Beyond these distances the pressure gradient current then decreases in the outer region, with all profiles reaching $\sim 10\text{-}20 \text{ pA m}^{-2}$ by $\sim 20 R_S$. Overall, the strongest pressure gradient current in the outer region beyond the peaks is found in the dusk to midnight sector, declining in the midnight to dawn sector, and further in the dawn to noon sector. These differences reflect the similar behaviour of

the perpendicular pressure gradient in these sectors, overall differences being factors of ~ 2 or less, combined with the effect of the day-night asymmetry in the co-latitudinal field strength shown in the lower panel of Figure 7.5. Comparison of the profiles of the pressure gradient current with the combined inertia-pressure anisotropy current shows that these currents are comparable at radial distances between ~ 5 and $7 R_S$, beyond which the inertia-pressure anisotropy current falls to roughly half the pressure gradient current at distances ~ 8 to $\sim 14 R_S$, and to smaller fractions in the outermost regions. The mean total current density profiles shown in panel (d) of Figure 7.7 are thus similar to those of the pressure gradient current, but are elevated in value relative to the latter by factors of ~ 1.5 - 2.0 .

Overall these results show that within the limits of the data coverage, the mean current density in Saturn's ring current does not vary greatly with LT, though being modestly larger on the nightside than on the dayside, particularly in the dusk sector, in the region beyond $\sim 10 R_S$. The magnetic perturbations relative to the planetary field observed in the equatorial magnetosphere correspondingly also show relatively little LT variation, as seen in panel (e) of Figure 7.7, though again being somewhat larger on the nightside than on the dayside in conformity with the above discussion.

These principal features are found to be true not only of the mean values shown in Figure 7.7, but also on individual Revs that traverse the dayside sector on the inbound pass and the nightside sector on the outbound pass, separated in time typically by only ~ 2 days. This is illustrated in Figure 7.8, which shows results for Revs 16 and 20 in Figures 7.8a and 7.8b, respectively. We note that the inbound pass of Rev 16 was previously discussed in detail in Chapter 6, while the detailed data for Rev 20 are shown in Figure 7.3. The trajectories of both passes are shown in Figure 7.1. The current density profiles derived from the inbound (dayside) and outbound (nightside) passes of these Revs are shown by the blue and red lines respectively, in a similar format to Figure 7.7. Thus the top panels show the inertia and pressure anisotropy current densities, the second panels their sum, the third panels show the pressure gradient current density, while the fourth panels show the total current density. The fifth panels then show the residual co-latitudinal field.

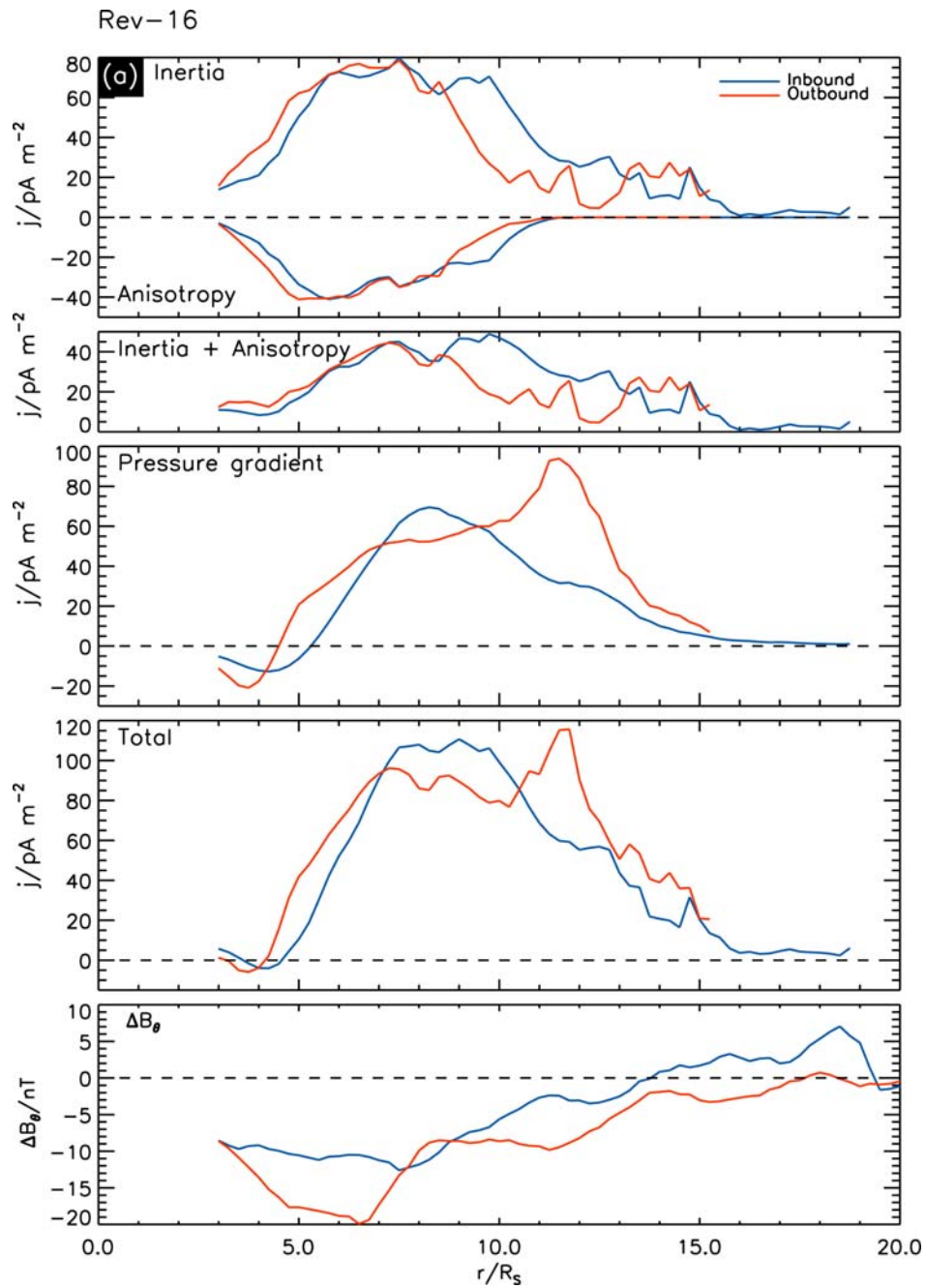


Figure 7.8a. Comparison of current density profiles on the inbound (dayside) and outbound (nightside) passes of Rev 16, in a similar format to Figure 7.7. The inbound and outbound passes are represented by the blue and red lines respectively. The top panel of shows the inertia and pressure anisotropy current densities, while the second panel shows their sum. The third panel shows the pressure gradient current density, while the fourth panel shows the total current density. The fifth panel shows the residual co-latitude component of the magnetic field.

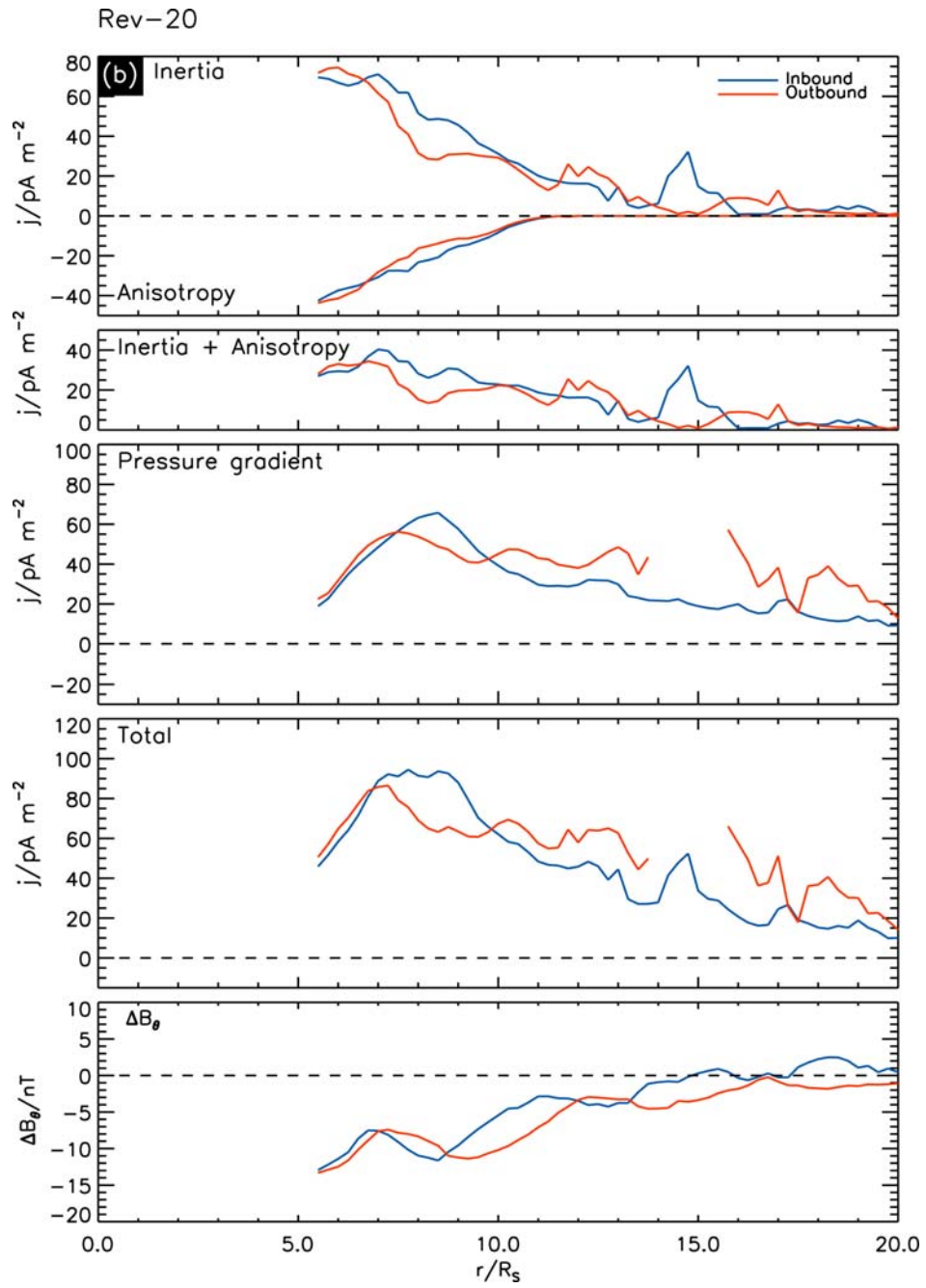


Figure 7.8b. As for Figure 7.8a, except for Rev 20.

In these cases the inbound and outbound current density profiles are similar to each other in the inner region to $\sim 7-8 R_S$ where the current rises to peak values of $\sim 100 \text{ pA m}^{-2}$, though showing a tendency for the rise to occur at slightly smaller radii on the outbound (nightside) pass than on the inbound (dayside) pass particularly for Rev 16. This reflects the related day-night asymmetry in the density of the warm ion population in the innermost region noted above in the discussion of Figure 7.5. The peak currents on both Revs are then sustained over a somewhat larger radial range on the dayside than on the nightside, before the dayside values fall more rapidly to drop below the nightside values in the outer region beyond $\sim 10 R_S$, an effect that results mainly from the pressure gradient current.

7.3.2 - Pass-to-Pass Temporal Variability

In Figures 7.9 and 7.10 we now examine in more detail the pass-to-pass temporal variability in the data that were used to construct the mean radial profiles for each LT quadrant in Figures 7.5-7.7. In each figure separate plots are shown for each LT quadrant, specifically for (a) noon to dusk, (b) dawn to noon, (c) dusk to midnight, and (d) midnight to dawn. The solid black line in each data panel shows the mean value of the parameter concerned, with the grey shaded region indicating the associated standard error, as in Figures 7.5-7.7, while the individual $0.25 R_S$ data values used to construct the plots are shown by dots, colour-coded for each Rev as shown in panel (a) of each figure. Figure 7.9 shows from top to bottom the total plasma number density, the perpendicular pressures of the warm ions (water group plus protons), hot ions, and electrons (note the change in range in the latter panel), the total perpendicular pressure, and the co-latitude field strength. Figure 7.10, similar to Figure 7.7, shows from the top the inertia and pressure anisotropy current densities, their sum, the perpendicular pressure gradient current density, and the total current density.

It can firstly be seen from these figures that there is no strong pass-to-pass variability in the total density, plasma pressure, or current density values in the inner region extending outwards towards the usual peak in the current density profile at $\sim 9 R_S$. This is particularly evident in the noon to dusk sector shown in panels (a) of

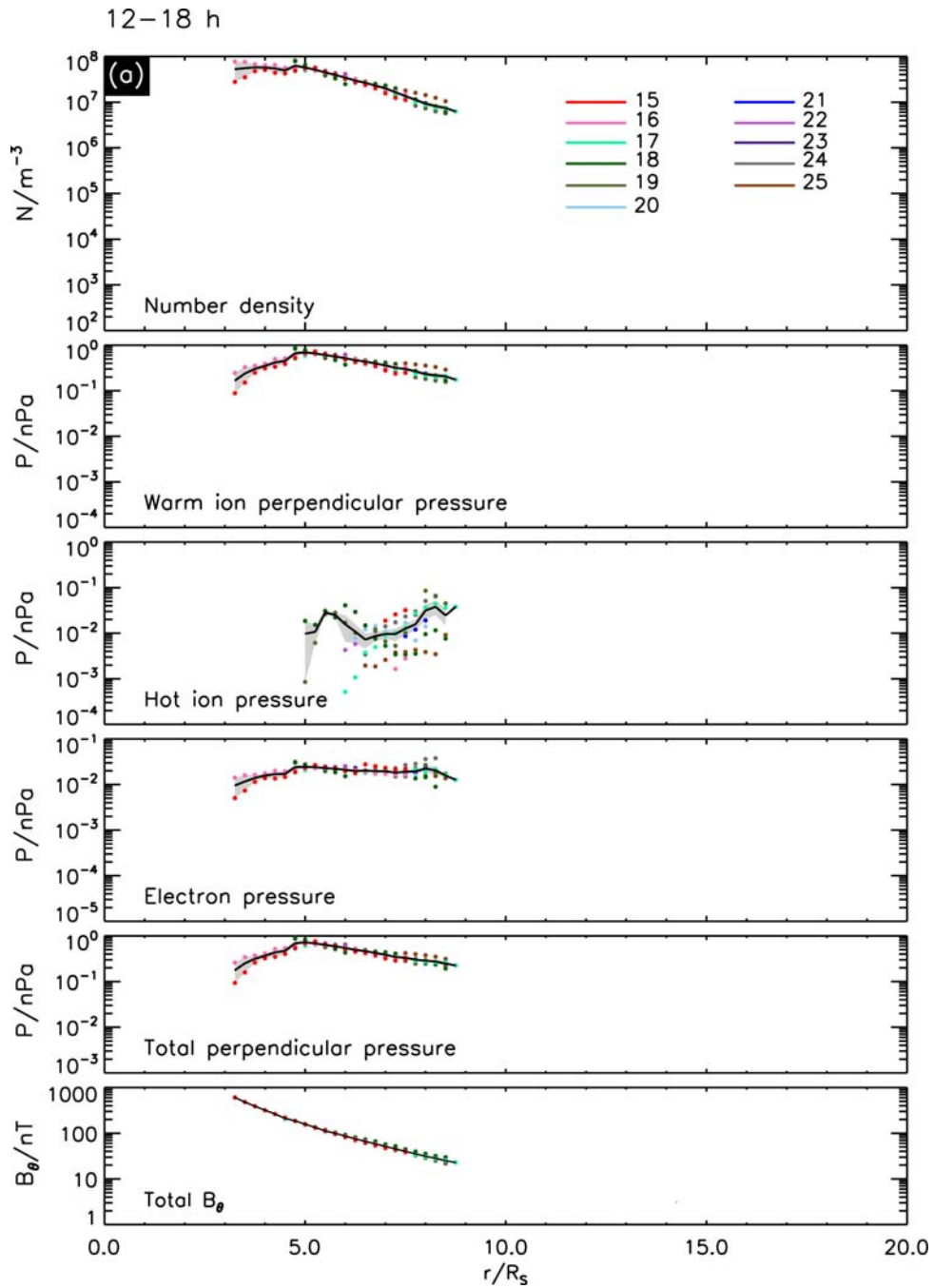


Figure 7.9a. Plots showing each individual $0.25 R_S$ radial resolution data point that contributes to the mean plasma and field profiles in Figure 7.5, specifically for the noon to dusk sector. The data values from each Rev are colour-coded as shown in the top panel. The black lines and grey shaded regions show the mean values and their standard error, as in Figure 7.5. From top to bottom the panels show the total number density, the perpendicular pressures of the warm ions (water group plus protons), the hot ions, and the electrons, the total perpendicular pressure, and the co-latitude field strength.

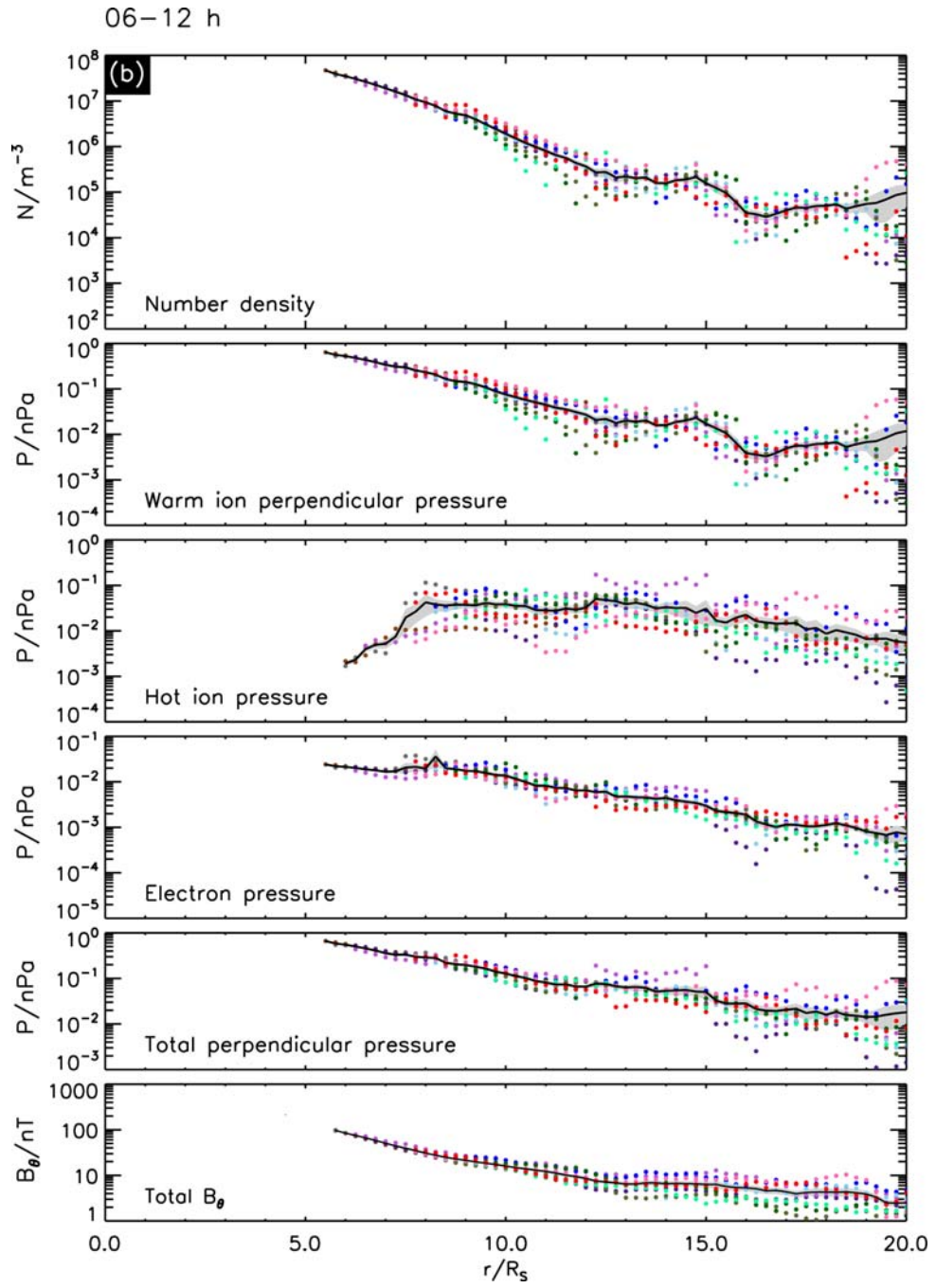


Figure 7.9b. As for Figure 7.9a, except for the dawn to noon sector.

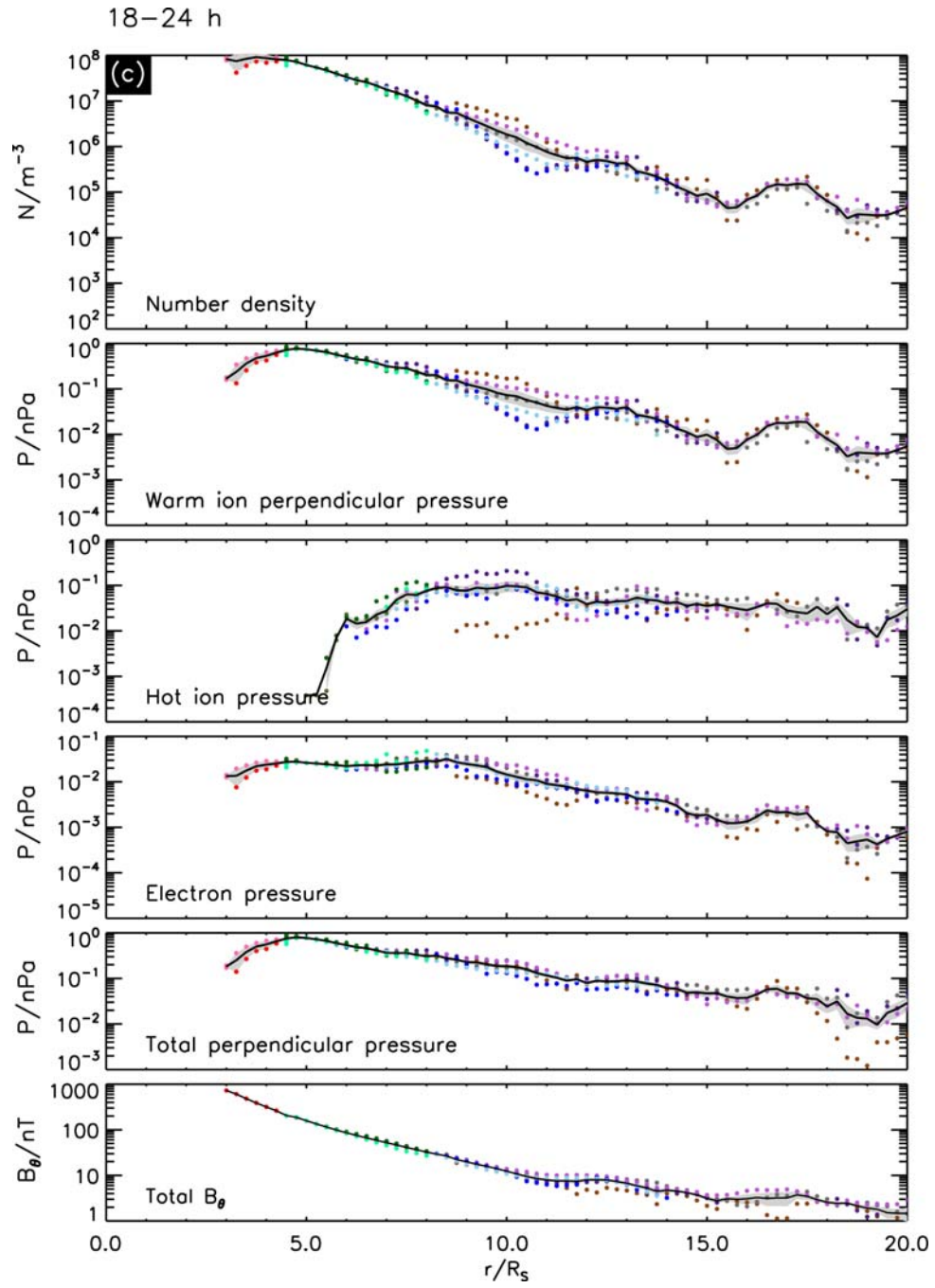


Figure 7.9c. As for Figure 7.9a, except for the dusk to midnight sector.

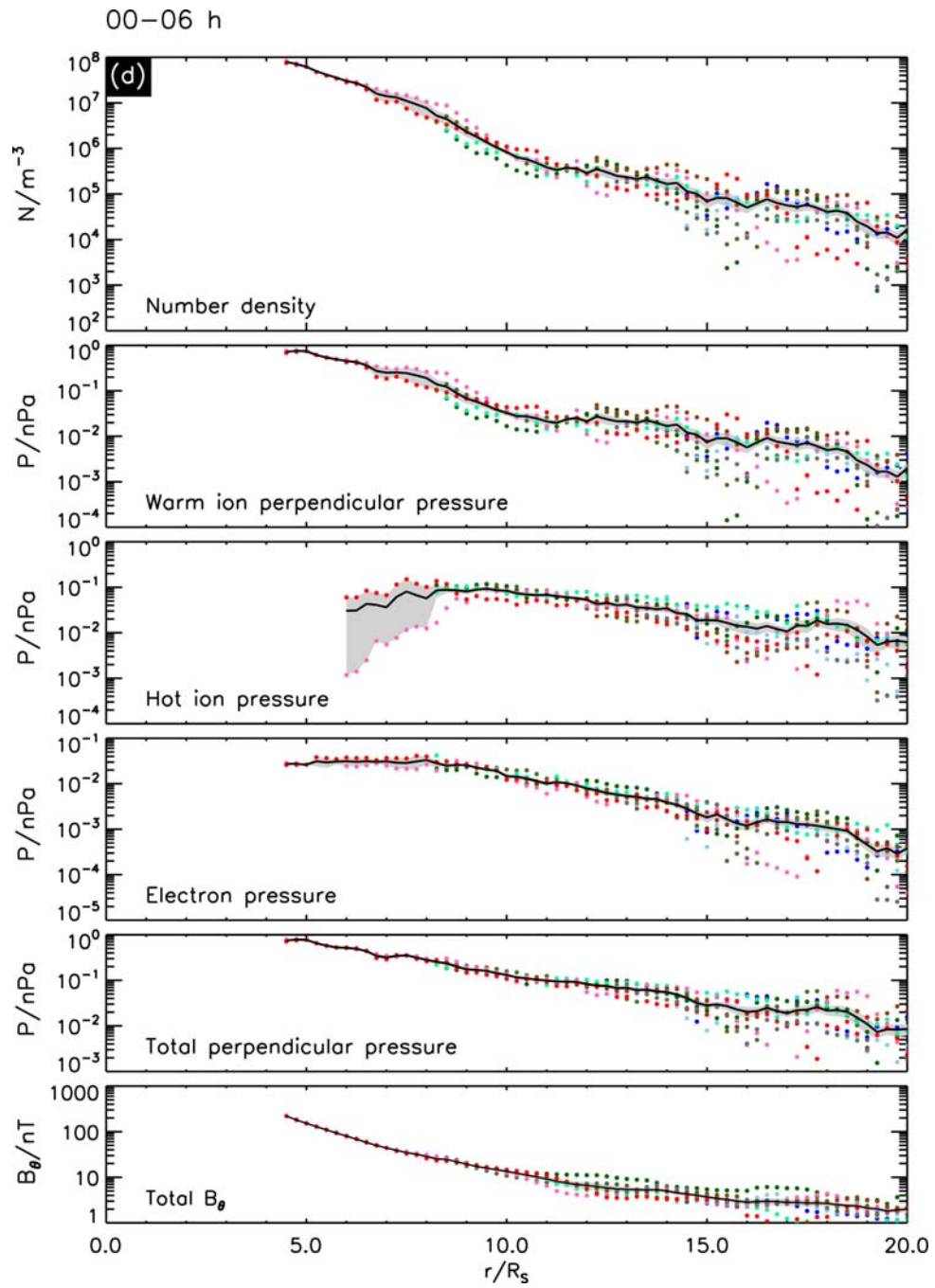


Figure 7.9d. As for Figure 7.9a, except for the midnight to dawn sector.

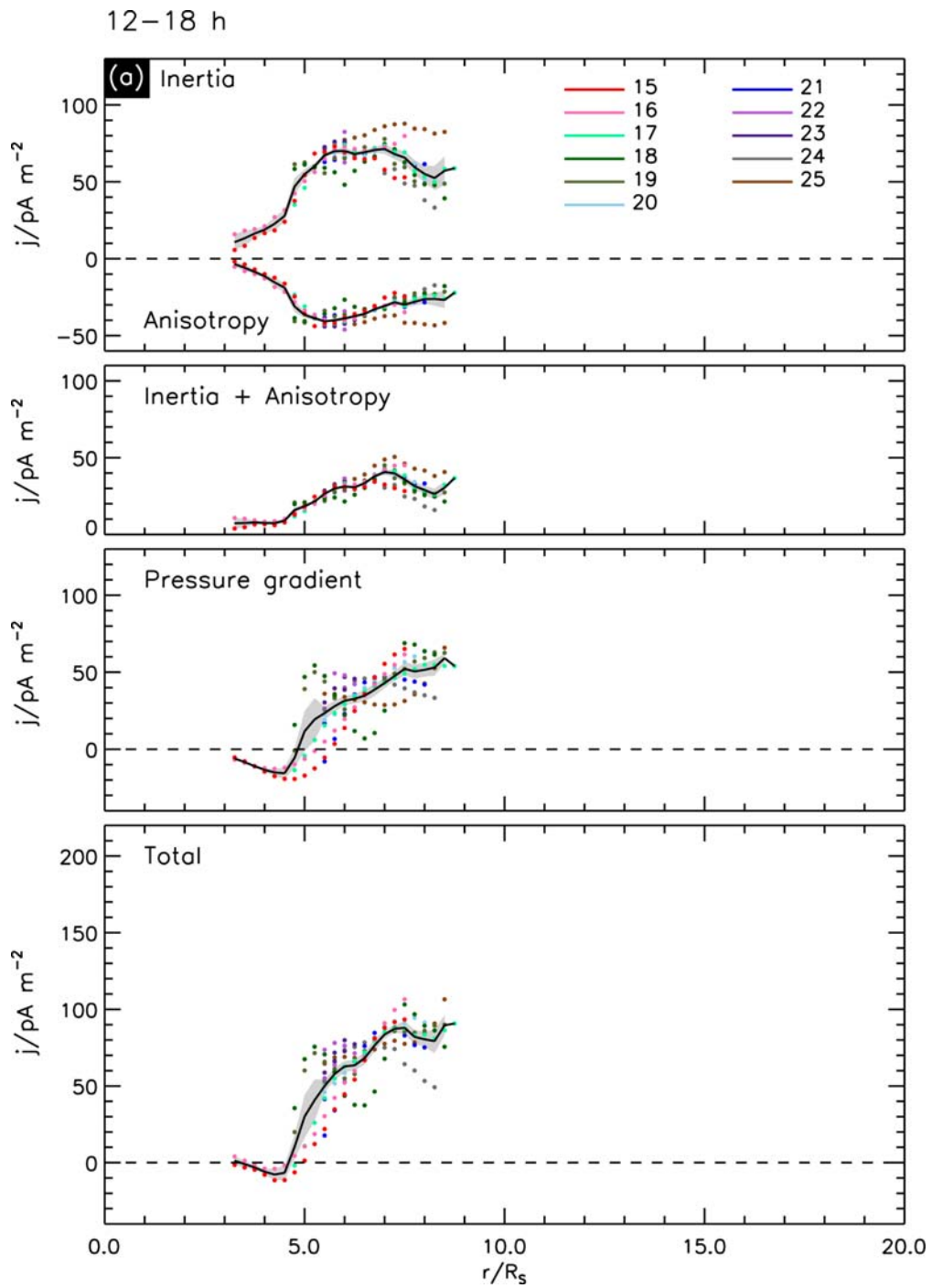


Figure 7.10a. Plot showing radial profiles of the current density components in the same format as Figure 7.9 specifically for the noon to dusk sector. From top to bottom the panels show the inertia and pressure anisotropy current densities, their sum, the pressure gradient current density, and the total current density.

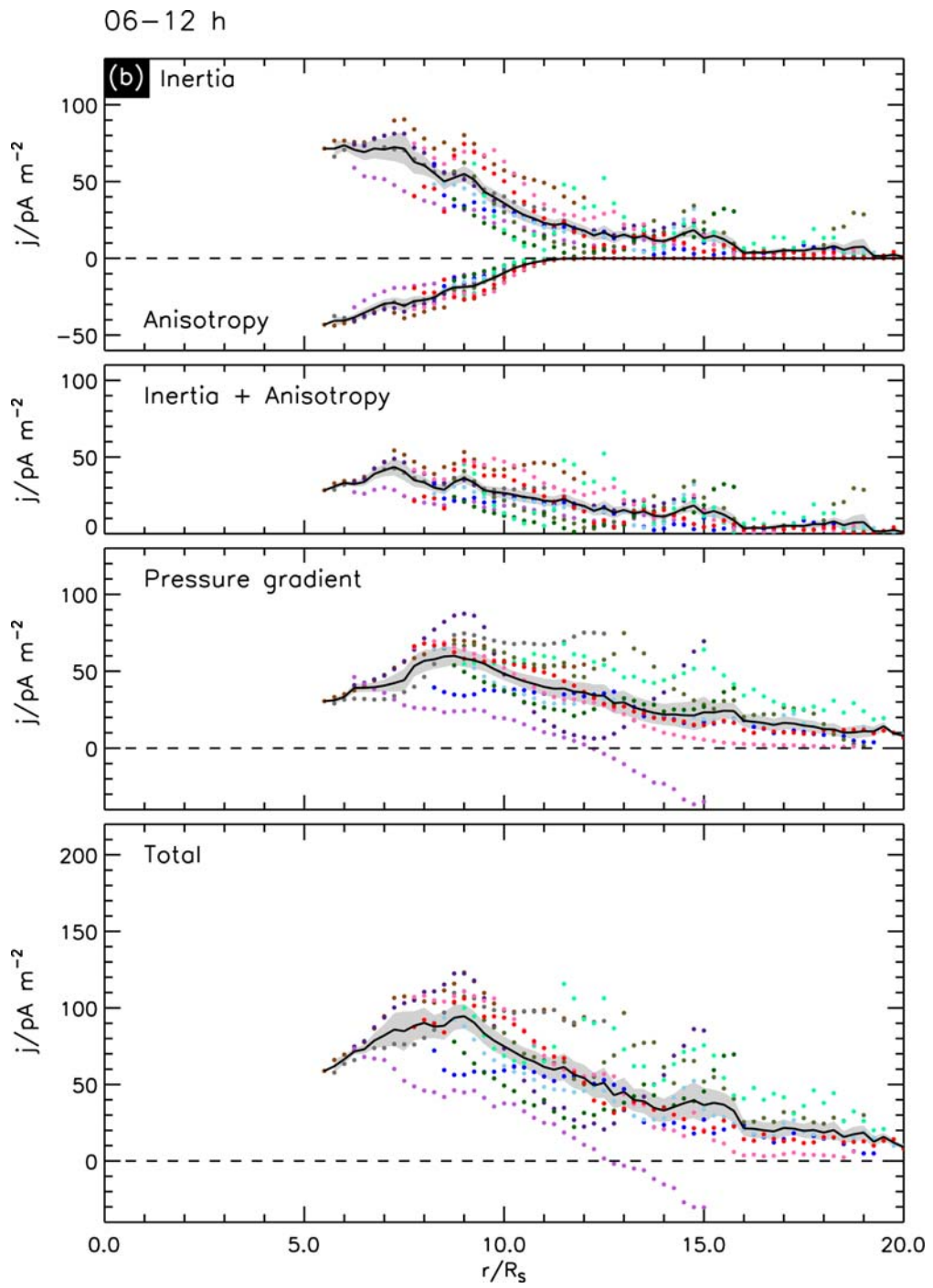


Figure 7.10b. As for Figure 7.10a, except for the dawn to noon sector.

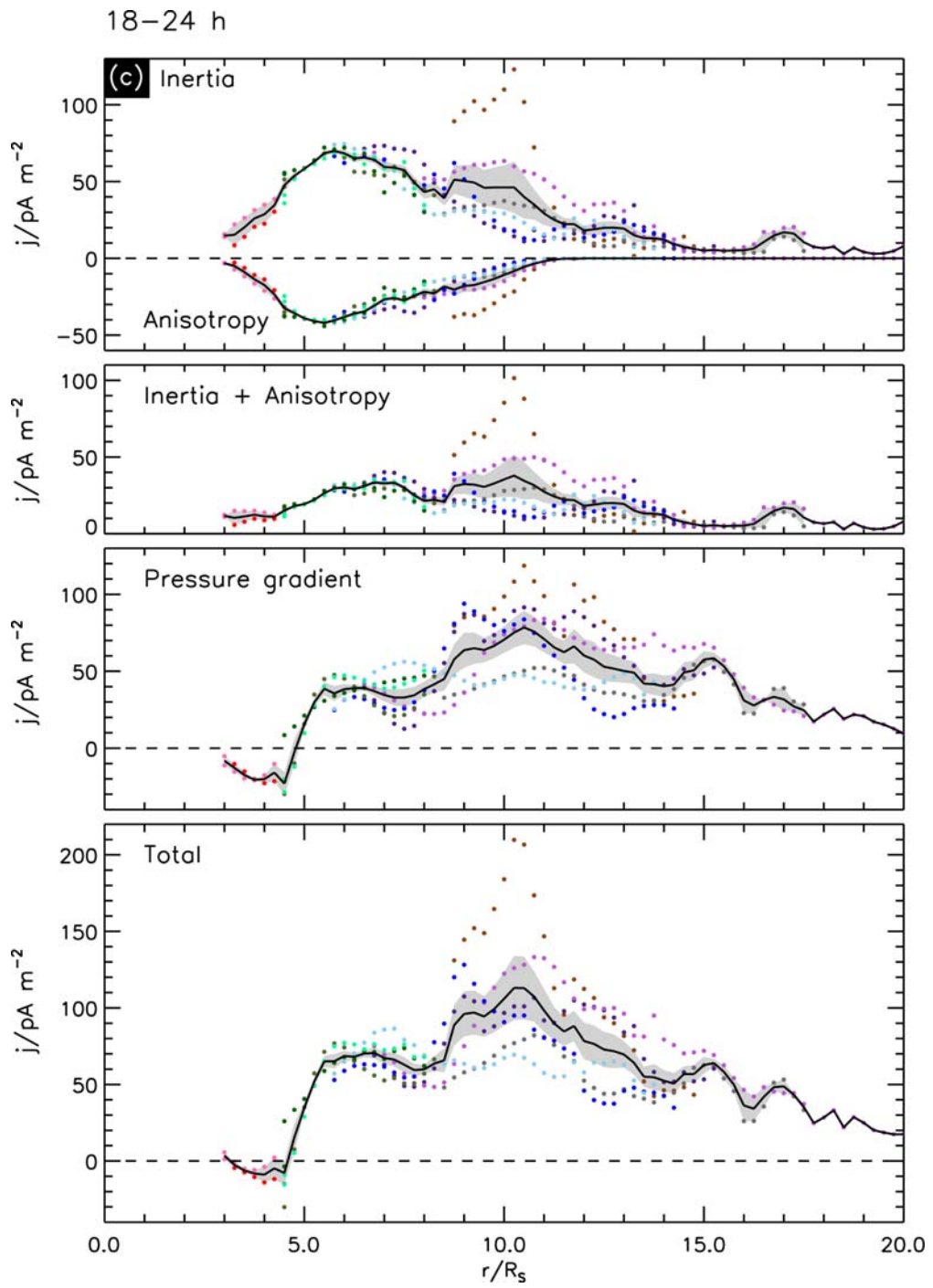


Figure 7.10c. As for Figure 7.10a, except for the dusk to midnight sector.

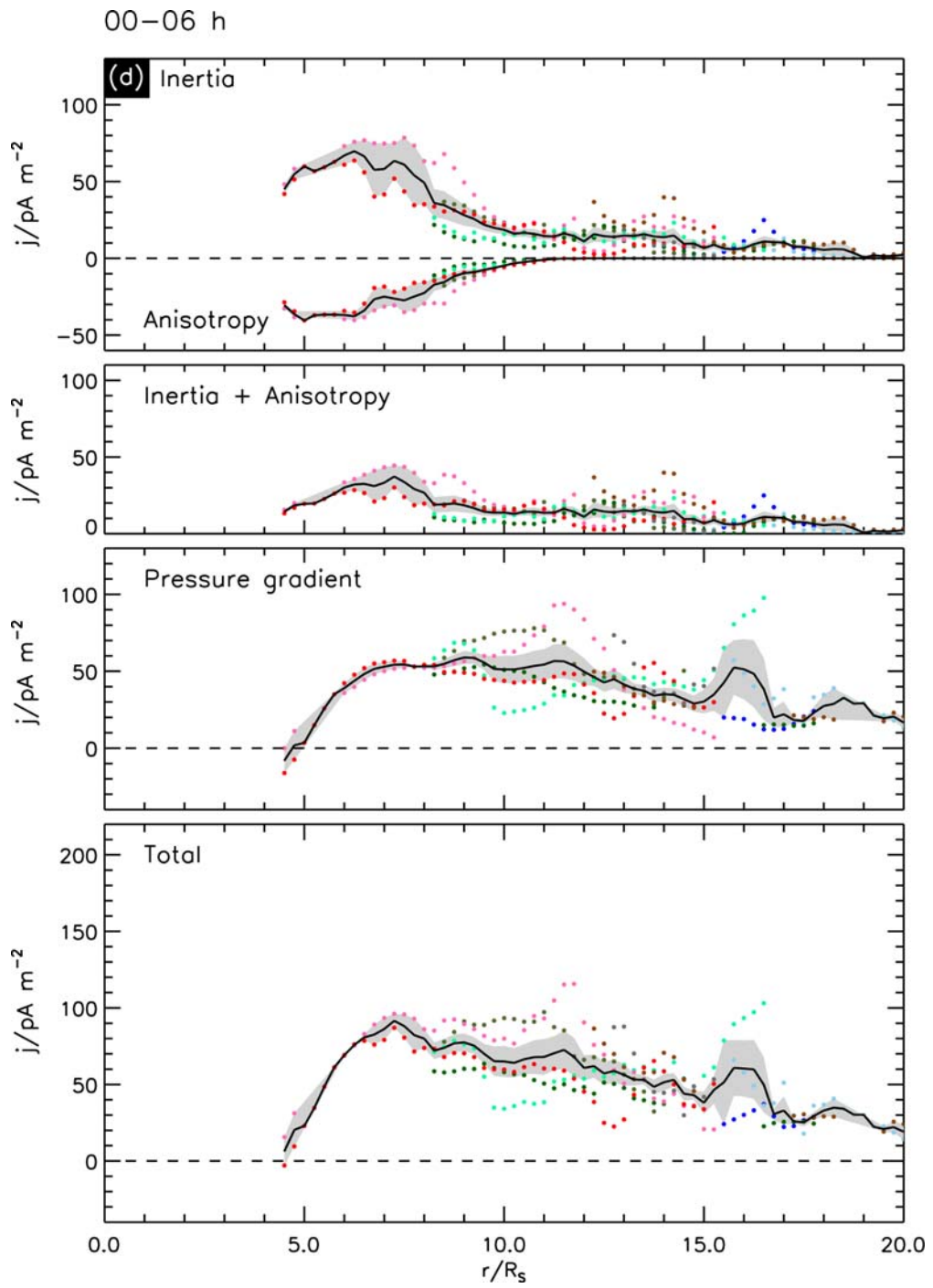


Figure 7.10d. As for Figure 7.10a, except for the midnight to dawn sector.

both figures, where all eleven Revs contribute data. Correspondingly, the current density data generally lie within $\sim\pm 10\text{-}15\text{ pA m}^{-2}$ of the mean values in this region, compared for example with peak values of $\sim 90\text{ pA m}^{-2}$. There is thus no evidence of major variability in the dominant warm ion population in this region over the ~ 10 -month interval of this study. Beyond these distances, however, the pass-to-pass variations generally grow in magnitude in all quadrants for which data exists, both in the plasma parameters and the current components. This is particularly notable in the dawn to noon sector shown in panel (b) of both figures, where the scatter in the data beyond $\sim 9 R_S$, especially in the hot ion pressure, results in scatter in the current densities rising to $\sim\pm 20\text{ pA m}^{-2}$, compared for example with typical current density values in this region of $\sim 50\text{ pA m}^{-2}$. In addition, large pass-to-pass variations in the current density are evident in the dusk to midnight sector shown in panel (c) of Figure 7.10, specifically at central radial ranges between ~ 8.5 and $\sim 11.5 R_S$. While some profiles show rather steadily-declining current densities with radial distance in this region, exemplified by Rev 20 outbound shown in Figures 7.3b and 7.6b (pale blue dots in Figures 7.9 and 7.10), others show a significant secondary peak in this region, in one case (Rev 25) reaching estimated total current densities of $\sim 200\text{ pA m}^{-2}$ (brown dots) resulting from enhancements in both the inertia and pressure-gradient currents in this region.

In Figure 7.11 we present individual examples illustrating the variability of the current on the dayside. Specifically we show results for the inbound passes of Revs 17, 18, and 19 (dots with shades of green in Figures 7.9 and 7.10), which share essentially the same trajectories as each other separated in time by ~ 28 days, spanning the pre-noon sector in the outer region beyond $\sim 9 R_S$, and the noon to dusk sector inwards to periapsis at $\sim 4.5 R_S$ (Figure 7.1). In Figures 7.11a-c we show plasma, field, and current profiles for each pass in the same format as Figure 7.3, while in Figure 7.11d the current and field profiles from each pass are compared in a similar format to Figure 7.8, but where the red, green, and blue lines correspond to Revs 17, 18, and 19, respectively.

It can be seen from Figure 7.11d that the currents are similar to each other in the inner region up to the peak values at around $8\text{-}9 R_S$, but differ more markedly in the

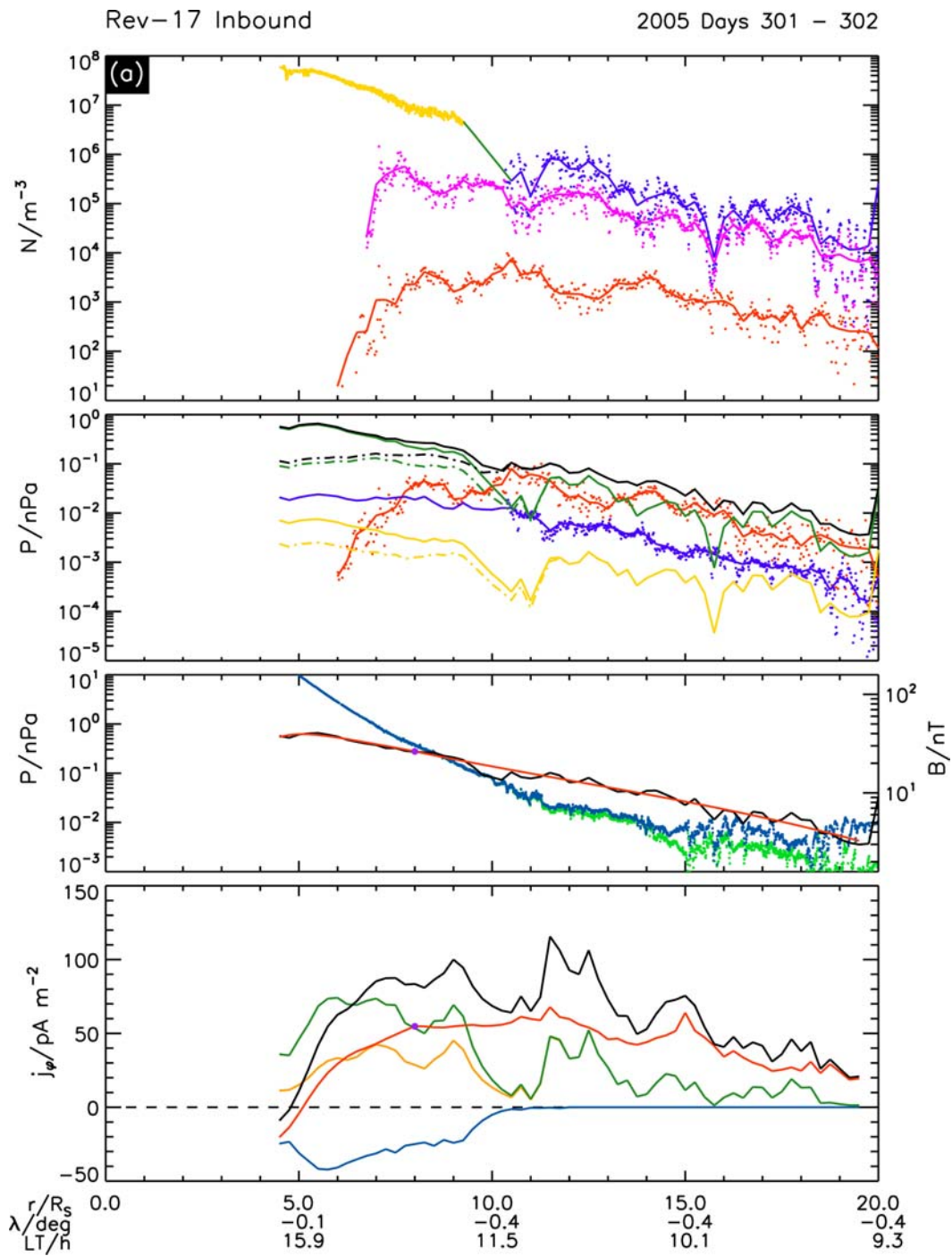


Figure 7.11a. Radial profiles of particle and field parameters for the inbound pass of Rev 17, in the same format as Figure 7.3.

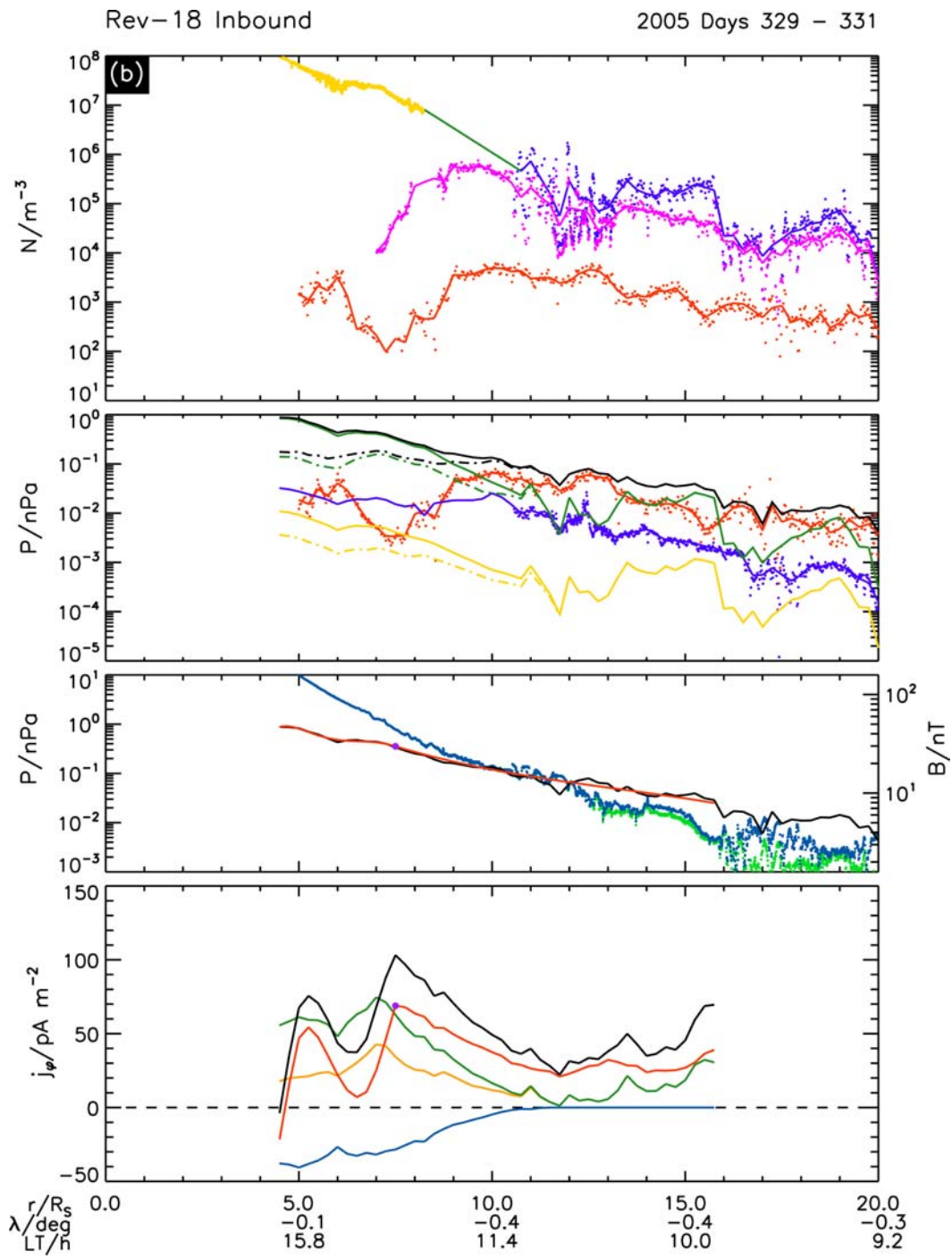


Figure 7.11b. As for Figure 7.11a, except for the inbound pass of Rev 18.

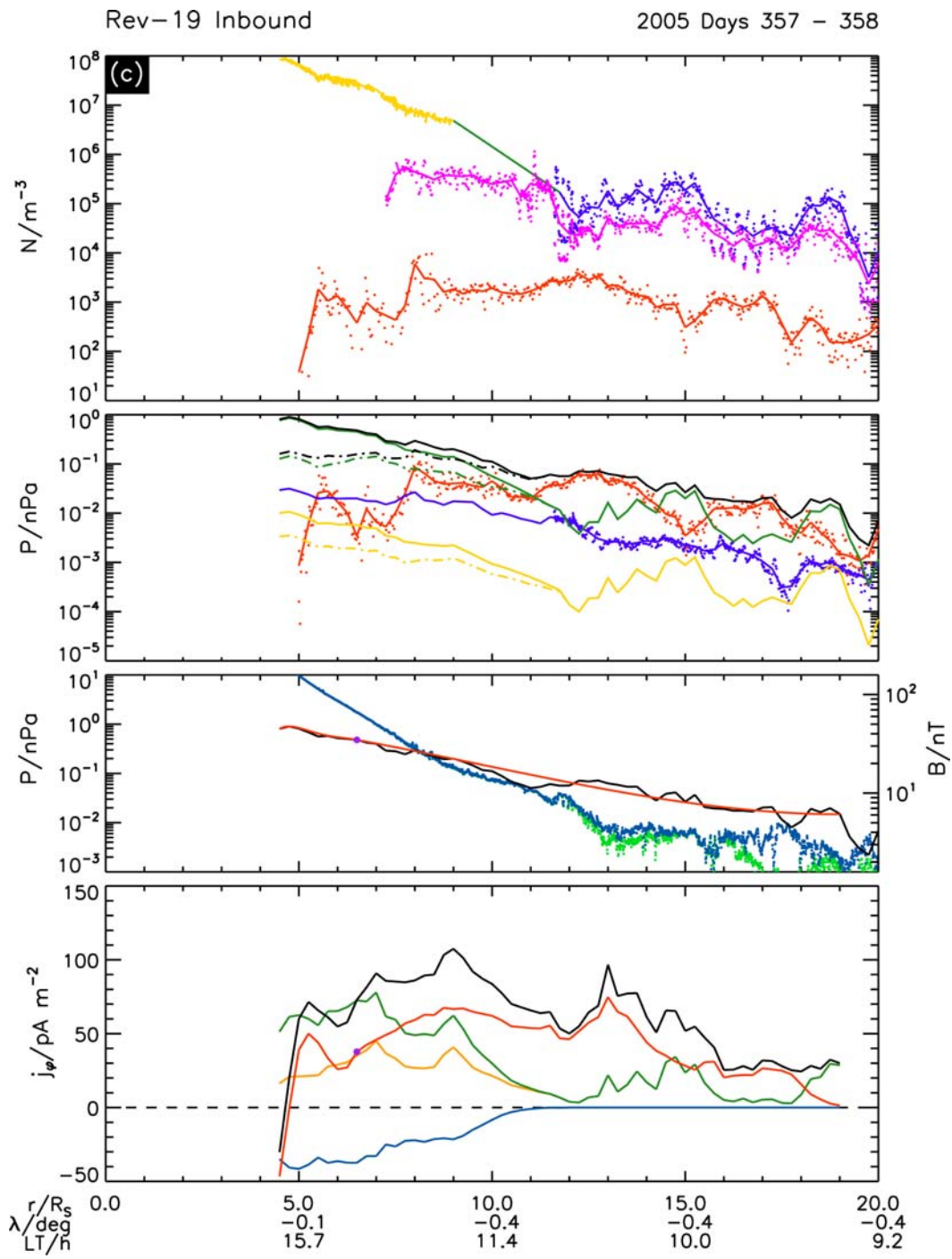


Figure 7.11c. As for Figure 7.11a, except for the inbound pass of Rev 19.

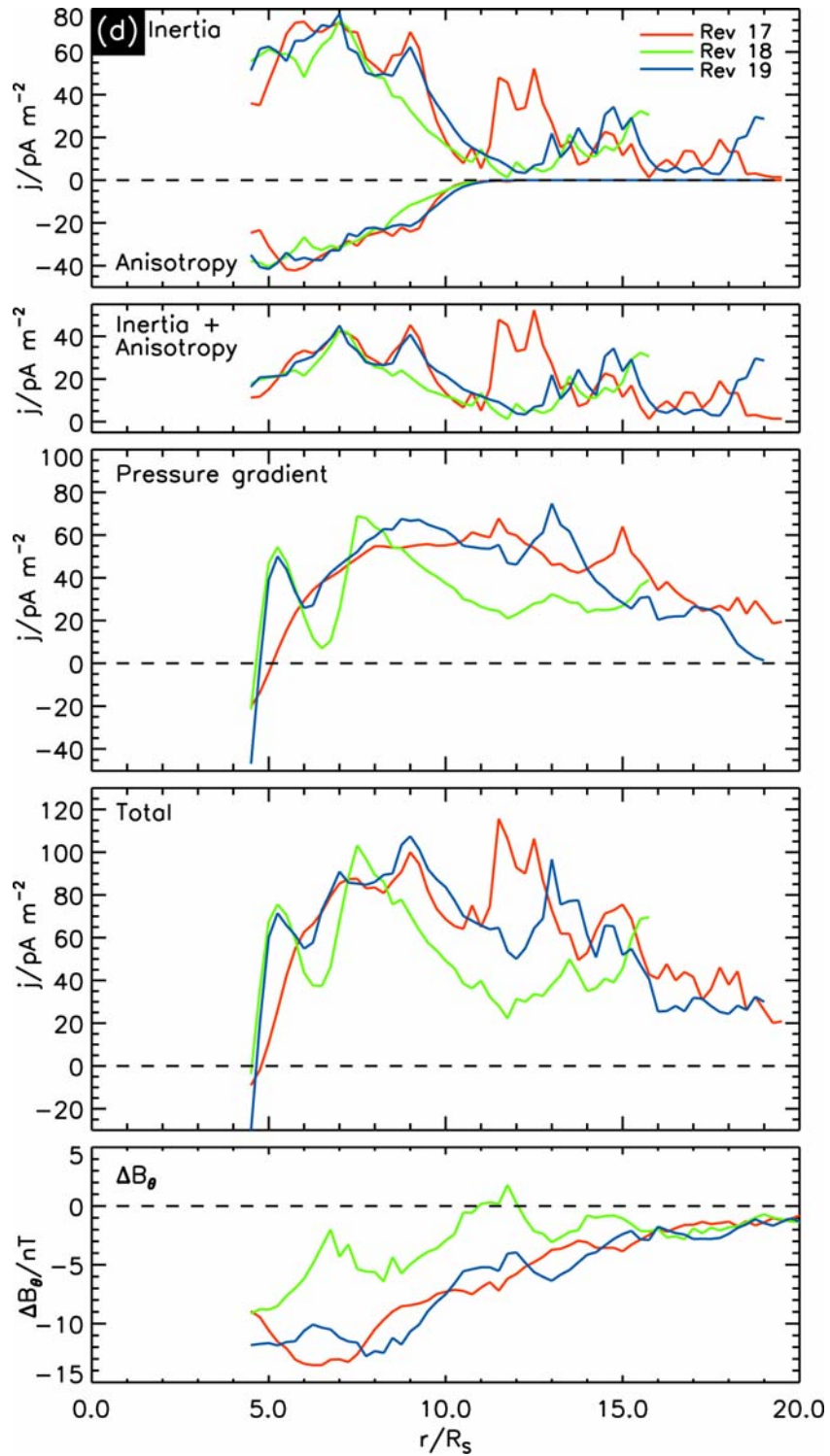


Figure 7.11d. Current density and magnetic field profiles versus radial distance for the inbound passes of Revs 17 (red), 18 (green) and 19 (blue). The format is similar to Figure 7.8.

dawn-side outer region. Most notably, while the currents in the outer region are very similar to each other on Revs 17 and 19 (red and blue lines), the current on Rev 18 (green) is weaker by a factor of up to ~ 2 , due principally to a significant reduction in the perpendicular pressure gradient current. Examination of the plasma parameters in Figures 7.11a-c shows, however, that this is not principally due to changes in the perpendicular pressure profiles, but rather to the presence of a stronger co-latitude field in the case of Rev 18 than for Revs 17 and 19. The fifth panel of Figure 7.11d shows that the negative perturbation fields for Revs 17 and 19 are very similar (as are the current profiles), while that for Rev 18 is significantly smaller in magnitude (consistent with smaller currents), meaning that the total equatorial B_θ field is stronger in that case, as can be seen in Figures 7.11a-c. A likely possibility is that this effect results from differing upstream solar wind conditions during these passes such that the magnetosphere was more compressed during Rev 18 than on Revs 17 and 19. These observations may then relate to the results of *Bunce et al.* [2007] based on CAN modelling of the magnetic field perturbations, who found weaker currents for more compressed magnetospheres. Figure 7.11 also illustrates a further difference in the current profiles between these Revs, in the presence on Rev 17 of a major secondary peak in the current density in the radial range from ~ 11 to $\sim 13 R_S$. This originates from the inertia current term, and is due to a relatively localised peak in the plasma number density seen in Figure 7.11a.

Plots illustrating the appearance of secondary current maxima near $\sim 10 R_S$ in the pre-midnight sector are shown in Figure 7.12. In Figure 7.12a we show plasma, field, and current profiles for Rev 21 outbound which exhibits such a peak (dark blue dots in Figures 7.9 and 7.10), which we compare with the corresponding profiles for Rev 20 outbound shown in Figure 7.3b which does not (light blue dots in Figures 7.9 and 7.10). From Figure 7.1 we note that these Revs again share essentially the same trajectory separated in time by ~ 39 days, outbound in the dusk to pre-midnight sector, crossing the meridian into the post-midnight sector at $\sim 14 R_S$. The current and field profiles from these Revs are compared in Figure 7.12b in the same format as Figures 7.8 and 7.11d. The principal difference again involves the pressure gradient current, but unlike the dayside example in Figure 7.11, this is not now due to differences in the equatorial field strength as seen from the fifth panel of Figure 7.12b, but rather to differences in the

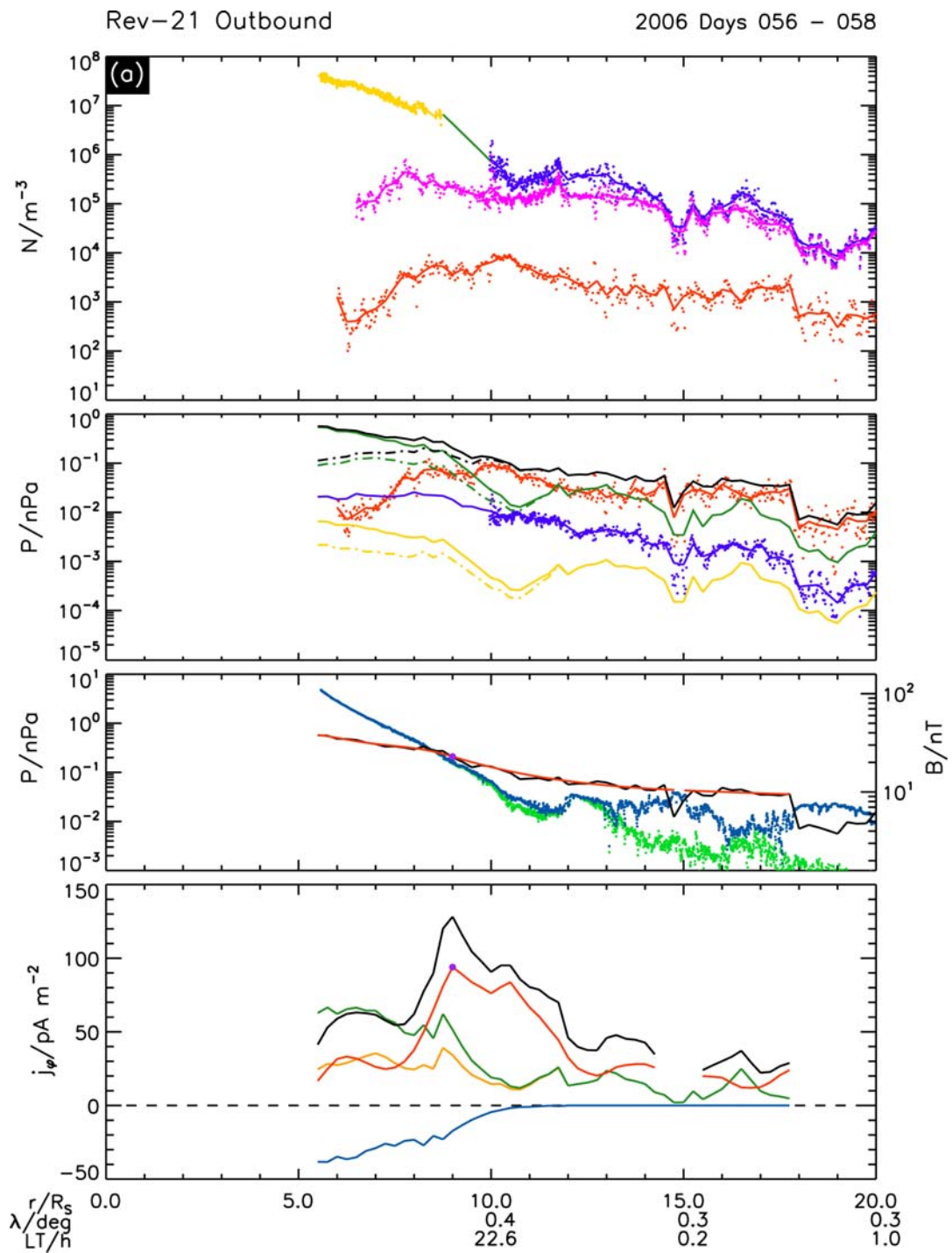


Figure 7.12a. Radial profiles of particle and field parameters for the inbound pass of Rev 21, in the same format as Figure 7.3.

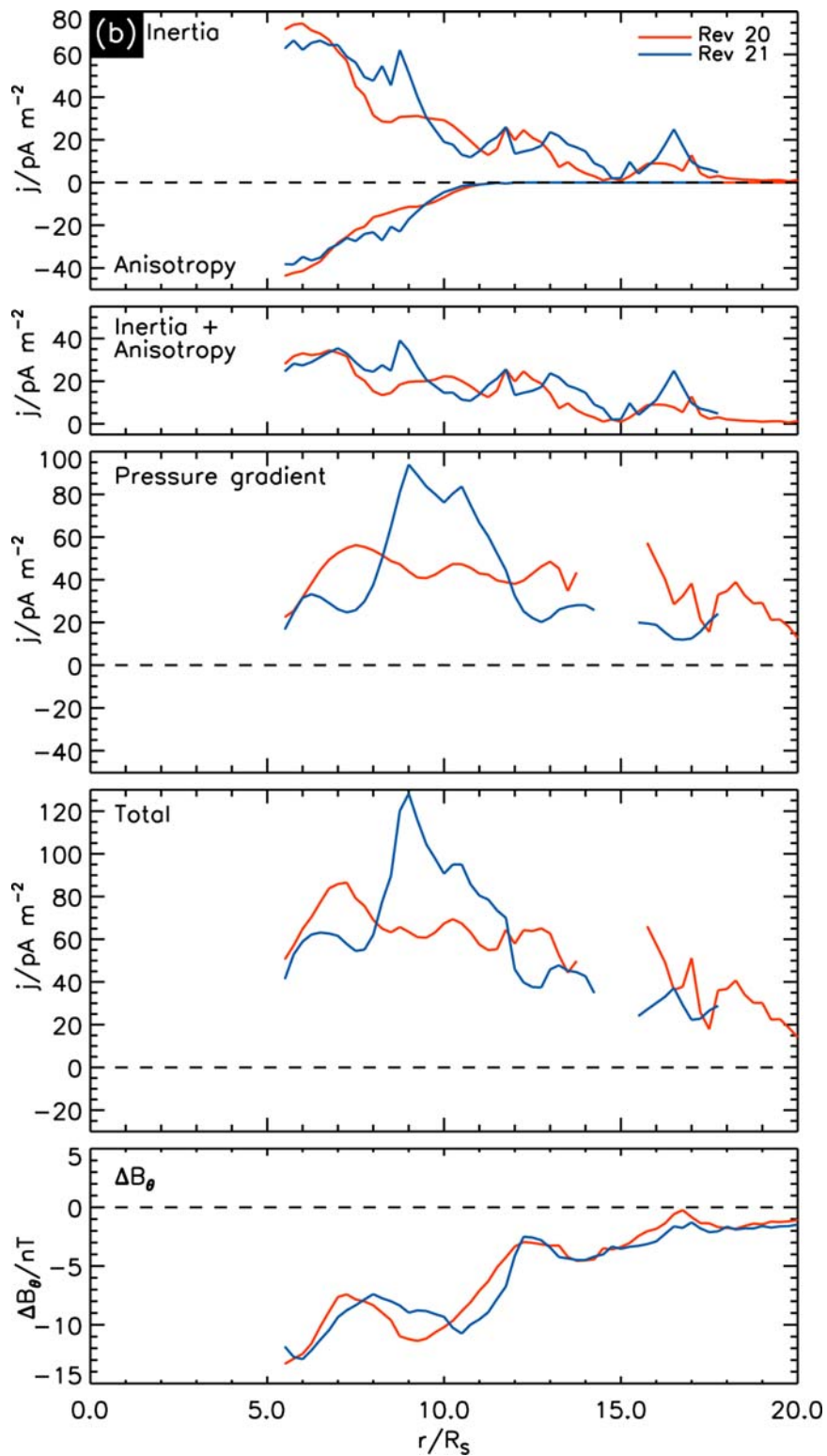


Figure 7.12b. Current density and magnetic field profiles versus radial distance for the outbound passes of Revs 20 (red) and 21 (blue). The format is the same as Figures 7.8 and 7.11d.

radial profile of the perpendicular pressure. Comparison of these profiles in the third panels of Figures 7.3b and 7.12a shows that the pressure profile is somewhat flatter in the inner region to distances of $\sim 8 R_S$ for Rev 21 than for Rev 20, leading to smaller pressure gradient currents in the former case than in the latter in this region. However, the pressure profile for Rev 21 then dips more rapidly to smaller values than for Rev 20 beyond $\sim 10 R_S$, leading to a corresponding peak in the pressure gradient current in the former case, located between ~ 8 and $\sim 12 R_S$. Similar effects are also seen on the outbound passes of Revs 22, 23, and 25, all of which span the dusk to midnight sector (Figure 7.1), while the current profile for Rev 24 appears more similar to Rev 20.

7.3.3 - Overall Mean Profiles

Although we have focused above on the LT dependence and temporal variability that occur in the plasma and field parameters in Saturn's ring current region, and in the consequent current densities, it should nevertheless be emphasised that these variations are overall modest in nature, typically factors of ~ 2 or less, such that discussion of overall properties is meaningful. In Figure 7.13 we thus show overall mean profiles of the plasma and field parameters obtained by averaging the data from all 22 near-equatorial passes examined here, irrespective of LT, while in Figure 7.14 we similarly show the current density components. The mean values in each panel are shown by the solid lines, while the grey shaded regions again indicate the associated standard error of the mean. Specifically, in Figure 7.13 panel (a) shows the number of data points contributing to each $0.25 R_S$ radial interval, panel (b) shows the total number density (blue), and the partial densities of the warm (≥ 20 eV) electrons (magenta) and the hot ions (red), panel (c) shows the perpendicular (solid) and parallel (dot-dashed) pressures of the warm ions (water group plus protons, green), hot ions (water group plus protons, red), and electrons (blue), while panel (d) shows the total perpendicular (solid) and parallel (dot-dashed) pressures. Figure 7.14 similarly shows the mean values of the current components in the same format as Figure 7.7, where the dashed lines in the panels (d) and (e) also show a mean CAN model profile as will be discussed further below.

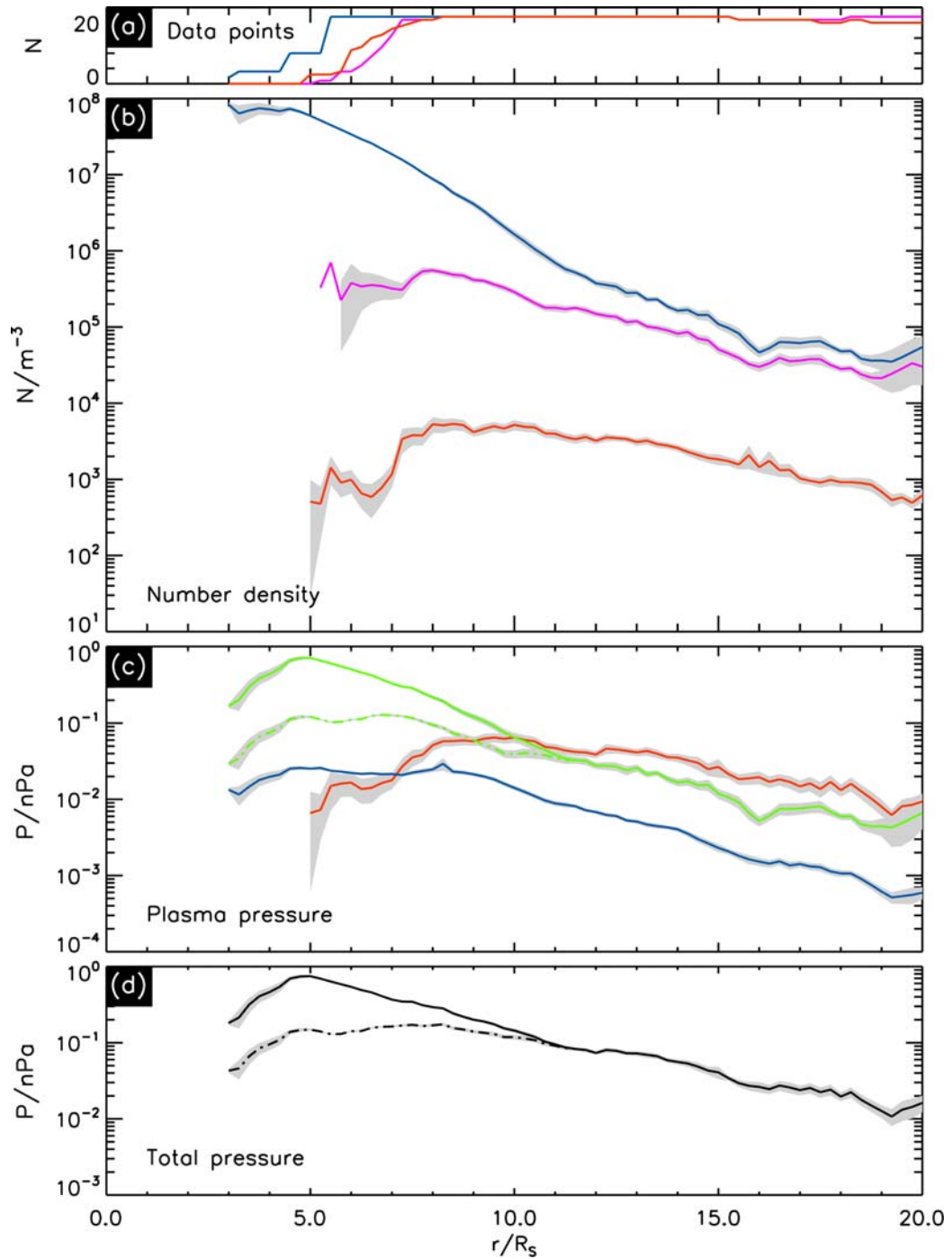


Figure 7.13. Overall mean radial profiles of plasma and magnetic field parameters for all LTs combined. The mean values are shown by the solid and dot-dashed lines, while the grey shaded regions indicate the associated standard error of the mean. The panels show (a) the number of data points contributing to each $0.25 R_S$ radial interval, (b) the number densities of hot ions (red), warm (≥ 20 eV) electrons (magenta), and the total number density (blue), (c) the perpendicular (solid) and parallel (dot-dashed) pressures of the warm ions (water group plus protons, green), hot ions (red), and electrons (blue), and (d) the total perpendicular (solid) and parallel (dot-dashed) pressures.

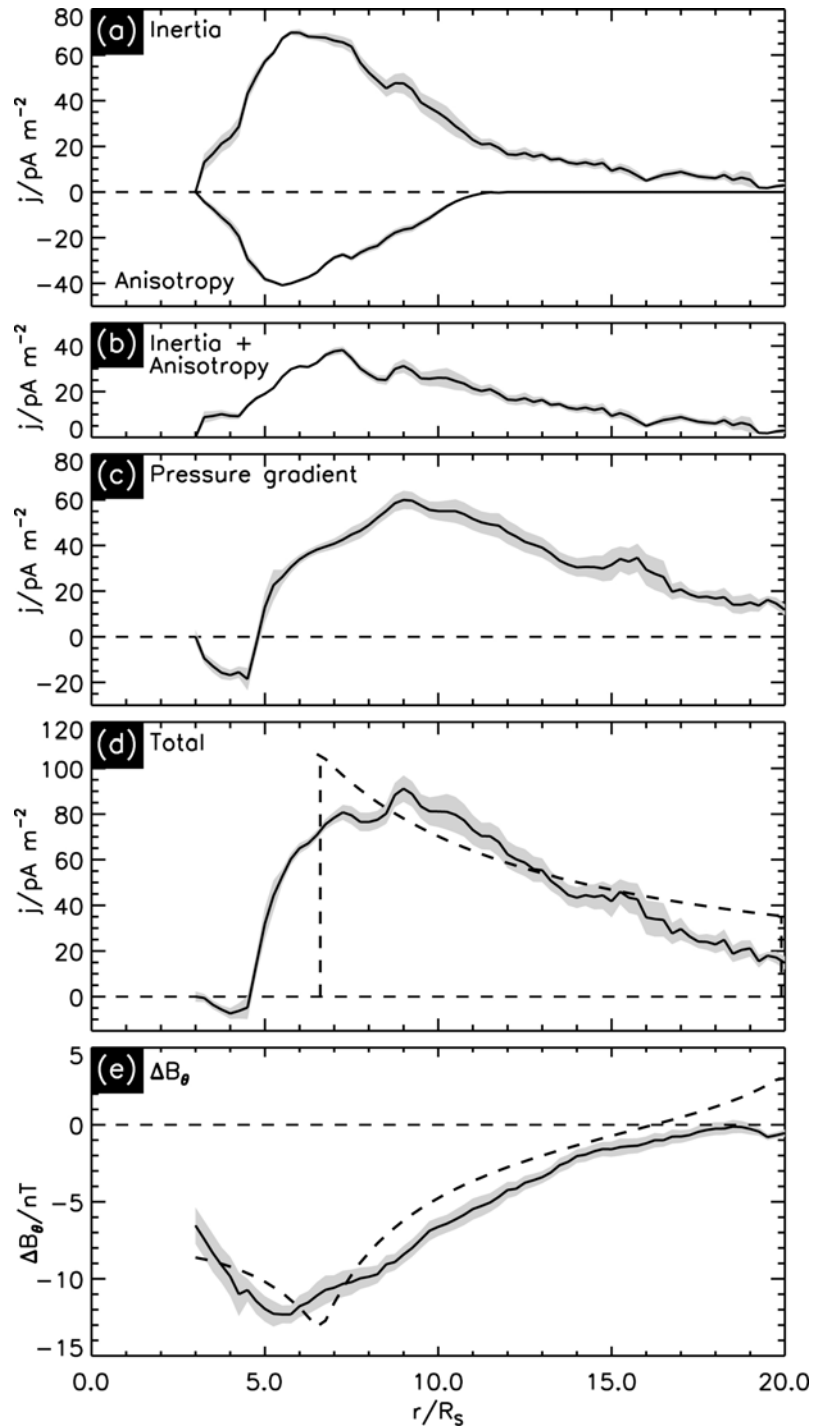


Figure 7.14. Overall mean current density and magnetic field profiles shown in a similar format to Figure 7.7. The overall mean parameter values are shown by the black solid lines, while the grey shaded regions indicate the associated standard error of the mean. The dashed black lines in panels (d) and (e) correspond to a representative CAN model obtained by averaging the model parameters determined from individual fits to the field data from each pass.

It can again be seen from Figure 7.13 that the warm ions dominate the plasma density throughout, and hence the inertia current density. In our formulation they are also the only contributor to the pressure anisotropy current density. The warm ions also dominate the plasma pressure to distances of $\sim 10 R_S$, while the pressure of the hot ions typically exceeds that of the warm ions by factors of ~ 2 at distances beyond $\sim 12 R_S$. Thus the pressure gradient current is also determined mainly by the properties of the warm ions in the inner region to $\sim 10 R_S$, encompassing the rapid rise in this current component with radius and the usual region of peak values, while the hot ions are the more important component by factors of ~ 2 in the outer region beyond $\sim 12 R_S$ where the pressure gradient current more slowly declines.

Turning now to Figure 7.14, it can be seen that the mean inertia current increases from small values in the inner region to peak at $\sim 70 \text{ pA m}^{-2}$ at $\sim 6 R_S$, before decreasing with radial distance to values of $\sim 10 \text{ pA m}^{-2}$ by $\sim 15 R_S$. The pressure anisotropy current peaks in magnitude at $\sim 40 \text{ pA m}^{-2}$ at $\sim 5.5 R_S$, and declines toward zero at and beyond $\sim 12 R_S$ where the pressure becomes isotropic. The combined inertia-pressure anisotropy current thus increases from small positive values to peak at $\sim 40 \text{ pA m}^{-2}$ at $\sim 7 R_S$, approximately half the peak inertia current, and then gradually decreases with increasing radial distance. The pressure gradient current has negative values of $\sim 15 \text{ pA m}^{-2}$ inside of $\sim 5 R_S$ where the perpendicular pressure increases with radius, then increases rapidly to peak at $\sim 60 \text{ pA m}^{-2}$ at $\sim 9 R_S$, before decreasing slowly with increasing radial distance to values of $\sim 15 \text{ pA m}^{-2}$ by $\sim 20 R_S$. The total current follows a similar profile to the pressure gradient current, but is augmented in strength by the combined inertia-pressure anisotropy current by factors of ~ 2 in the inner region, and by lesser factors at larger distances. The current has small negative values in the innermost region, crosses through zero at $\sim 4.5 R_S$, and continues to increase to its peak at $\sim 90 \text{ pA m}^{-2}$ at $\sim 9 R_S$ after which it falls off with increasing radial distance at a similar rate to that of the pressure gradient current. These results are overall very comparable to the mean values obtained by *Sergis et al.* [2010] in the central radial range $6\text{-}15 R_S$ which they investigated, although our estimates of the mean pressure gradient current are somewhat elevated in the inner region to $\sim 10 R_S$, and are somewhat reduced beyond.

The mean CAN model profiles shown in panels (d) and (e) of Figure 7.14 have been derived simply by averaging the model parameters obtained from the fits to the field perturbations for each individual pass. Along with a current sheet half-thickness of $1.5 R_S$, the mean inner and outer radii are 6.6 and $19.9 R_S$, respectively, while the mean current density parameter is $\mu_0 I_0 = 53.2 \text{ nT}$. The dashed-line profiles shown in panels (d) and (e) of Figure 7.14 then simply represent results for a CAN model employing these mean parameter values. No additional fields representing the effect of more distant magnetopause and tail currents are now included, since these data generally cover a wide range of LTs at a given radial distance. Nevertheless, the model fit to the mean perturbation fields shown in the sixth panel is seen to be reasonably good, with a RMS deviation of 1.6 nT compared with peak negative values of $\sim -12 \text{ nT}$. Comparison of the mean total current density profile derived from the plasma data with the mean CAN model profile also shows reasonable agreement of the gross features. Specifically we note similar peak current densities of $\sim 100 \text{ pA m}^{-2}$ located at comparable radial distances of $\sim 7-9 R_S$, with rapid rises of the current inside those distances, and more gradual falls beyond. However, the model current profile with its assumed sharp inner cut-off clearly cannot account for the details of the rise in current with radius in the inner region, while beyond the peak the mean current density falls off somewhat more rapidly with distance than the model does.

7.4 - Summary and Discussion

In this chapter we have derived radial profiles of the azimuthal current density in Saturn's ring current region between distances of ~ 3 and $20 R_S$, using plasma bulk parameter and magnetic field data obtained from the inbound and outbound passes of eleven consecutive closely-equatorial Cassini orbits that span a 10-month interval from September 2005 to July 2006. These current densities are expected to be representative of the central part of the equatorial ring current layer over the full radial range, though the spacecraft may typically be located towards its southern boundary at the largest radial distances due to the northward displacement of the current layer under the southern summer conditions prevailing. LT coverage of the equatorial region is generally good, though not including the noon to dusk sector at radial distances beyond $\sim 9 R_S$. Within this limitation, however, the data set allows exploration of both the LT

dependence and pass-to-pass temporal variability of the plasma, field, and current density within the above radial range, thus expanding significantly on the study presented in Chapter 6 based on two passes through the dayside sector, and the study of averaged conditions by *Sergis et al.* [2010].

Our principal finding is that the plasma parameters, azimuthal current, and perturbation field in the above region generally show only modest variations in both LT and from pass-to-pass over the interval of the study. This is particularly true of the inner region up to the usual peak in current density at radial distances near $\sim 9 R_S$, though modest variability is present in the outer region beyond. This finding thus provides significant justification for our main analysis assumption of approximate local axi-symmetry, such that parameter variations observed on given spacecraft passes are attributed primarily to radial rather than to LT effects. The total azimuthal current density derived on this basis is then found to rise rapidly from near-zero values inside $\sim 5 R_S$ to peak at $\sim 90 \text{ pA m}^{-2}$ at $\sim 9 R_S$, and then falls more slowly with increasing radial distance to values below $\sim 20 \text{ pA m}^{-2}$ at the $20 R_S$ outer limit of our study. Comparison with the current profiles obtained from CAN modelling of the magnetic perturbations, assuming the current layer has a full thickness of $3 R_S$, based on the results of Chapter 4, shows good agreement between their gross features, though the details of the radial profiles differ somewhat as may be expected. The gross agreement shows, however, that the current density deduced from the plasma data is overall compatible with the simultaneous perturbations observed in the magnetic field data, though further work is required to examine their mutual consistency at a more detailed level.

Of the components that form the total current, the most important overall is found to be the perpendicular pressure gradient current. In the inner region the inertia current dominates, but is significantly cancelled by the oppositely-directed pressure anisotropy current. The combined inertia-pressure anisotropy current is thus reduced to comparability with the pressure gradient current at radial distances $\sim 5\text{-}7 R_S$ inside the current peak, while falling to roughly half the latter values at larger distances. These findings are in agreement with the initial results presented in Chapter 6 where we argue that the significant reduction of the inertia current by the pressure anisotropy current in

the inner region follows directly from the nature of the source of the dominant warm water plasma in this region. These plasma particles originate from ionisation of Kepler-orbiting neutrals in the Enceladus gas torus, which are then ‘picked up’ by the significantly faster flow of the near-corotating plasma. This process results in the pick-up ion population being strongly peaked perpendicular to the field in velocity space, with a consequent dominant perpendicular pressure giving rise to the pressure anisotropy current that is directly related to the near-corotational plasma flow speed that also gives rise to the inertia current. Estimates show that these current components should then be comparable in magnitude and opposite in direction, as found here in the inner region.

With regard to the plasma populations that principally determine the currents, we note that the warm ion plasma that originates in the Enceladus torus in the inner magnetosphere dominates both the inertia and the pressure anisotropy currents throughout, together with the pressure gradient current to radial distances of $\sim 10 R_S$. The properties of this population thus govern the rapid growth in the current with radius in the inner part of the system, extending to the region just beyond the usual peak in the total current density at $\sim 9 R_S$. Inside this region the warm plasma parameters and related current densities are found to be relatively unvarying with LT and from pass-to-pass, typically within factors of less than ~ 2 . At larger distances the hot (≥ 3 keV) ion pressure becomes more important, typically exceeding the pressure of the warm ions by factors of ~ 2 at radial distances beyond $\sim 12 R_S$. This corresponds to the region where the total current density, of which the pressure gradient current is the most important component, falls more slowly with increasing distance. In this region both warm and hot plasma parameters and resulting current densities vary more strongly with LT and from pass-to-pass, but again typically only within factors of ~ 2 -3. The overall relative invariance of the plasma parameters and currents is correspondingly reflected in the relatively modest variations in the magnetic perturbations in the inner magnetosphere noted previously by *Bunce et al.* [2007] and *Leisner et al.* [2007].

This overall relatively steady picture contrasts significantly with related conditions at Earth, where the ring current within the quasi-dipolar magnetosphere changes by

significant factors over time both in magnitude and radial extent [e.g., *Lui et al.*, 1987; *De Michelis et al.*, 1997]. The equivalent perturbation field in the inner region, monitored, e.g., as the D_{ST} index by equatorial magnetic observatories, consequently also changes by significant factors over time, from typical quiet-time values of ~ 10 nT to storm-time values up to a few hundred nT. Similar to Saturn, the terrestrial ring current results mainly from the perpendicular pressure gradient current, but the dominant plasma population involved in the latter case is the dynamically variable hot magnetospheric plasma which is injected into the inner magnetosphere from the nightside during magnetically disturbed intervals. No equivalent to Saturn's relatively unvarying warm plasma population is present in this case, the Earth's plasmasphere (of ionospheric origin) producing only negligible magnetic effects. Nightside plasma injection dynamics appear also to occur periodically at Saturn, at least involving ions with energies of a few tens of keV and above [e.g., *Krimigis et al.*, 2007; *Mitchell et al.*, 2009b], but this activity clearly does not usually perturb the equatorial plasma bulk parameters and resulting currents beyond the extent reported here. While the hot ion parameters are evidently highly variable in the inner part of the system, inside $\sim 9 R_S$, they usually make only a small contribution to the total current in this regime.

Of the LT variations that are observed at Saturn, the most significant occur in the outer region beyond $\sim 10 R_S$, where the mean azimuthal current density is strongest in the dusk to midnight sector, and declines gradually in the midnight to dawn, and dawn to noon sectors (data being unavailable in the noon to dusk sector in this region). This effect is due to corresponding LT variations in the perpendicular pressure gradient of the plasma, overall differences generally being less than factors of ~ 2 , combined with co-latitudinal fields that are weaker on the nightside than on the dayside by factors of a comparable order. Corresponding differences are found in the dayside (inbound) and nightside (outbound) current density profiles on individual spacecraft Revs separated by minimum intervals of ~ 2 days, suggesting that this asymmetry is a consistent feature.

Pass-to-pass variability is also present in the outer region, even on spacecraft trajectories that are essentially identical, but now separated in time by ~ 30 -40 days. An example has been presented in which the current density in the outer dayside region,

specifically the dominant perpendicular pressure gradient current, varies by a factor of ~ 2 between successive passes, in this case due mainly to changes in the equatorial field strength rather than in the pressure profile. It seems likely that this effect is due to variations in the upstream solar wind conditions leading to compressions and expansions of the dayside magnetosphere, connected to those found by *Bunce et al.* [2007] from CAN modelling of the magnetic field perturbations. Investigation of the dependency of the current profiles on external conditions remains a topic for future work. The appearance of a significant second peak in the current density, centred near $\sim 10 R_S$, is also found to be a common but not invariable feature in the pre-midnight sector. These current peaks again mainly involve the perpendicular pressure gradient current, sometimes the inertia current too, but are now found to be due to somewhat subtle variations in the radial pressure profile.

We finally note that the properties of the ring current beyond $\sim 9 R_S$ in the noon to dusk sector remains to be investigated. This region was not covered by the set of eleven near-equatorial Cassini orbits examined here, but has now been sampled during subsequent near-equatorial phases of the Cassini mission. Investigation of these data also represents a further topic for future work.

Chapter 8

Summary and Future Work

8.1 - Introduction

In this thesis we have employed plasma and magnetic field data from the Cassini spacecraft in order to better understand Saturn's ring current region. In Chapter 1 we gave a brief introduction to solar-planetary physics, followed by a detailed description of the Saturnian system in Chapter 2. The Cassini orbiter and the instruments employed to obtain the data presented in this thesis were described in Chapter 3. Three science studies were presented in Chapters 4, 6, and 7, while a derivation of the azimuthal current density in terms of plasma parameters was presented in Chapter 5.

8.2 – Summary

In Chapter 4 we investigated magnetic field and plasma electron data from six north-south Cassini orbits to determine the half-thickness and offset of the current layer. Three of these passes took place in the post-noon sector and three in the post-midnight sector, each at radial distances of ~ 9 , ~ 12 , and $\sim 15 R_S$, corresponding to the inner, middle, and outer regions of the ring current. The data used therefore allowed for the first time an essentially direct study of the equatorial current sheet thickness, its offset from the equator, and an initial examination of its relation to the distribution of plasma about the equatorial plane. Previous to this study, determinations of the half-thickness of Saturn's ring current had been obtained from Pioneer-11 and Voyager magnetic field data yielding values for the half-thickness of between ~ 1.5 and $\sim 3 R_S$. However, these were overall values due to the oblique nature of the fly-by trajectories.

In this study the dayside data indicated the presence of an equatorial current disk with a near constant half-thickness of $\sim 1.5 R_S$. In the inner region the current layer is centred near the planet's equatorial plane, but is displaced by $\sim 0.6 R_S$ north of the equatorial plane in the outer region. On application of the *Arridge et al.* [2008b] warped current sheet model this displacement was found to be in good agreement with a model with a hinging distance of $\sim 20 R_S$. A comparison of the magnetic field data with

simultaneously measured electron spectrograms indicated that the current layer is located within a significantly broader layer of hot plasma, with the main current layer located in the region containing the most intense fluxes of low-energy (~ 10 eV) electrons. More variable conditions were found on the nightside. In the inner region a thin equatorial current layer of half-thickness $\sim 0.5 R_S$ was found embedded at the centre of a much broader layer of current and plasma, as was found on the dayside. The half-thickness then increases to $\sim 2.5 R_S$ for the central pass, before falling strongly to $\sim 0.4 R_S$ for the outer pass. This suggests that the thicker ring current observed in the central region thins rapidly to smaller values on moving towards the tail plasma sheet, though the possibility of significant temporal variations cannot be ruled out. The outer nightside data also provided evidence of a northward displacement of the current layer from the equatorial plane.

Physically, the existence of Saturn's ring current is due to a combination of plasma currents resulting from the spatial gradient of the perpendicular plasma pressure, the anisotropy of the plasma pressures parallel and perpendicular to the field lines in the presence of field line curvature, and the inertia of the flowing (near-corotating) plasma.

In Chapter 5 we derived the general expression for the field-perpendicular current density in terms of the plasma bulk parameters and then modified the expression to suit the particular circumstances required for the studies presented in Chapters 6 and 7 of this thesis.

In Chapter 6 we employed magnetic field and plasma particle data from two near-equatorial Cassini passes (Revs 15 and 16) spanning the radial range between ~ 3 and $\sim 20 R_S$, to investigate the nature of the ring current in Saturn's dayside magnetosphere. We examined plasma parameters obtained by Cassini for each pass and compared the azimuthal current density profiles derived from these to those obtained from current disk modelling of the magnetic field perturbations from each pass.

We first showed that the westward current associated with the $P_{\perp} > P_{\parallel}$ pressure anisotropy of the warm water group ions is important inside $\sim 10 R_S$, cancelling a significant fraction of the oppositely directed, and otherwise dominant, inertia current

inside $\sim 6 R_S$. As the water group ions become scattered towards isotropy at larger radial distances, this cancellation effect is reduced. The overall total current density profile was then found to be similar to that produced by the pressure gradient current, but augmented in strength by factors of ~ 1.5 - 2.0 by the difference between the inertia and pressure anisotropy currents. The total azimuthal current density was found to rise from small values near $\sim 6 R_S$, peak at $\sim 100 \text{ pA m}^{-2}$ near $\sim 8 R_S$, and then reduce to values below $\sim 25 \text{ pA m}^{-2}$ at distances beyond $\sim 15 R_S$, up to the $20 R_S$ limit of our study.

Comparison of the current density profiles deduced from plasma data with those obtained from current disk modelling of the magnetic field perturbations showed good agreement with the gross features, particularly with the locations and magnitudes of the peak current densities. However, beyond the peak the currents derived from the plasma data were found to fall more rapidly with radial distance than the $1/r$ dependence assumed in the model.

In Chapter 7 we expanded significantly on the initial results presented in Chapter 6 by exploring both the local time (LT) dependency and temporal variability of Saturn's ring current. We used plasma and magnetic field data from eleven near-equatorial Cassini orbits spanning a 10-month interval and a wide range of local times to derive radial profiles of the azimuthal current density between ~ 3 and $\sim 20 R_S$ in Saturn's equatorial magnetosphere. These were then compared and combined to consider the mean current profiles and the range of variation about the mean.

Our principal finding was that within this region the plasma parameters, azimuthal current, and related magnetic perturbation fields are generally found to exhibit only modest variations with local time and from pass-to-pass over the interval of this study. This is particularly true of the inner region up to the usual peak in current density at radial distances near $\sim 9 R_S$, though modest variability is present in the outer region beyond. The total azimuthal current density rises rapidly from near-zero values inside $\sim 5 R_S$ to peak at $\sim 90 \text{ pA m}^{-2}$ at $\sim 9 R_S$, and then falls more gradually to below $\sim 20 \text{ pA m}^{-2}$ at $20 R_S$.

Of the components that form the total current, the perpendicular pressure gradient current was found to be the most important since the otherwise dominant inertia current is significantly cancelled in the inner region by the oppositely directed pressure anisotropy current. This behaviour is in agreement with the initial results presented in Chapter 6 and principally reflects the properties of the warm water plasma originating from the Enceladus torus. This warm water plasma dominates both the inertia and pressure anisotropy currents throughout, together with the pressure gradient current to distances of $\sim 10 R_S$. Inside this distance the warm plasma parameters and related current densities are found to be relatively unvarying with LT and from pass-to-pass, typically within factors of less than ~ 2 . Increased variability is present at larger distances where the pressure of the hot (>3 keV) magnetospheric plasma plays the more important role. In these outer regions both the warm and hot plasma parameters and the resulting current densities vary more strongly with LT and from pass-to-pass, but again typically only within factors of ~ 2 -3.

The dominant pressure gradient current and hence the mean azimuthal current density are found to be strongest in the dusk to midnight sector, and decline modestly in the midnight to dawn, and dawn to noon sectors. Variations were also observed in the dayside (inbound) and nightside (outbound) current density profiles on individual Revs separated by a minimum of ~ 2 days, which suggested that this asymmetry is a consistent feature. Pass-to-pass temporal variability by factors of ~ 2 -3 is also present in the outer regions, particularly in the dawn to noon sector, most likely due to variations in the upstream solar wind conditions. A significant second peak in the current density, centred near $\sim 10 R_S$, was also found to be a common but not invariable feature in the pre-midnight sector. These peaks are mainly evident in the perpendicular pressure gradient current and are attributed to somewhat subtle variations in the radial pressure profile.

As in the study presented in Chapter 6, a comparison of the current density profiles deduced from plasma data with those obtained from CAN modelling of the magnetic field perturbations shows good agreement between their gross features. Although this gross agreement shows that the current density deduced from the plasma data is overall compatible with the simultaneous magnetic field perturbations observed, further work is required to examine their mutual consistency at a more detailed level.

The studies in this thesis have provided significant impetus to future studies of the ring current region on Saturn's magnetosphere, and its relationship to the complex plasma populations contained within, some of which are described below.

8.3 – Future Work

There are several possible extensions to the studies presented in this thesis. The first of these is to extend the study into the thickness of Saturn's ring current presented in Chapter 4 by analysing a larger data set. Since undertaking this initial study, the Cassini spacecraft has completed many other high inclination passes through the ring current region. The data from these passes could be utilised to characterise the thickness of the ring current as a function of radial distance and to search for any potential local time dependence of both the thickness and offset of the current layer.

The studies into the local time dependence and temporal variability of Saturn's ring current (Chapters 6 and 7) could be extended to include data from more recent equatorial passes and to investigate of the dependency of the azimuthal current profiles on external conditions (i.e. upstream solar wind conditions). This would determine whether the compressions and expansions of the dayside magnetosphere cause the pass-to-pass variability observed in the outer ring current region. The eleven near-equatorial Cassini orbits examined in Chapter 7 did not provide data from the noon to dusk sector of the ring current over all radial distances (data was only available out to $\sim 9 R_S$). This region has now been sampled during subsequent near-equatorial phases of the Cassini mission and so investigation of these data also represents a further topic for future work.

The magnetic field modelling method employed for the studies presented in this thesis is based on the work of *Bunce et al.* [2007] who studied 17 equatorial Cassini passes covering the dawn sector. A complementary study could be undertaken which employs the same methodology as *Bunce et al.* [2007] but uses data from Cassini passes covering the dusk sector (which were unavailable at the time of the *Bunce et al.* [2007] study). This work would give further insight into any dawn-dusk asymmetries present in the ring current region.

As was noted in Chapters 6 and 7, the CAN model does not always accurately describe the magnetic field data (particularly at the inner and outer edges of the ring current region) and thus has scope for refinement. An alternative model has recently been published by *Achilleos et al.* [2010a, b] and it would be interesting to re-run the analysis conducted in this thesis with this model to see how the two models compare to each other and the magnetic field data.

There is still much to be learned about the Saturnian system. The Cassini spacecraft will remain in orbit around Saturn until 2017, continuing to provide data so that many of the unanswered questions about this unique system may be answered.

References

- Achilleos, N., C. Bertucci, C.T. Russell, G.B. Hospodarsky, A.M. Rymer, C.S. Arridge, M.E. Burton, M.K. Dougherty, S. Hendricks, E.J. Smith, B.T. Tsurtani (2006), Orientation, location and velocity of Saturn's bow shock: Initial results from the Cassini spacecraft, *J. Geophys. Res.*, *111*, A03201, doi:10.1029/2005JA011297.
- Achilleos, N., P. Guio, and C.S. Arridge (2010a), A model of force balance in Saturn's magnetodisc, *Mon. Not. R. Astron. Soc.*, *401*, 2349-2371.
- Achilleos, N., P. Guio, C. S. Arridge, N. Sergis, R. J. Wilson, M. F. Thomsen, and A. J. Coates (2010b), Influence of hot plasma pressure on the global structure of Saturn's magnetodisk, *Geophys. Res. Lett.*, *37*, L20201, doi:10.1029/2010GL045159.
- Acuña, M.H., and N.F. Ness (1980), The magnetic field of Saturn: Pioneer 11 observations, *Science*, *207*, 444.
- Alexeev, I.I., and Y.I. Feldstein (2001), Modeling of geomagnetic field during magnetic storms and comparison with observations, *J. Atmos. Sol.-Terr. Phys.*, *63*, 431-440.
- Alexeev, I.I., and E.S. Belenkaya (2005), Modelling of the Jovian magnetosphere, *Ann. Geophys.*, *23*, 809-826.
- Alexeev, I.I., V.V. Kalegaev, E.S. Belenkaya, S.Y. Bobronikov, E.J. Bunce, S.W.H. Cowley, and J.D. Nichols (2006), A global magnetic model of Saturn's magnetosphere and a comparison with Cassini SOI data, *Geophys. Res. Lett.*, *33*, L08101, doi:10.1029/2006GL025896.
- Anderson, J.D., and G. Schubert (2007), Saturn's gravitational field, internal rotation, and interior structure, *Science*, *317*, 1384-1387.

André, N., et al. (2008), Identification of Saturn's magnetospheric regions and associated plasma processes: Synopsis of Cassini observations during orbit insertion, *Rev. Geophys.*, *46*, RG4008, doi:10.1029/2007RG000238.

Andrews, D. J., E. J. Bunce, S. W. H. Cowley, M. K. Dougherty, G. Provan, and D. J. Southwood (2008), Planetary period oscillations in Saturn's magnetosphere: Phase relation of equatorial magnetic field oscillations and Saturn kilometric radiation modulation, *J. Geophys. Res.*, *113*, A09205, doi:10.1029/2007JA012937.

Andrews, D. J., S. W. H. Cowley, M. K. Dougherty, and G. Provan (2010), Magnetic field oscillations near the planetary period in Saturn's equatorial magnetosphere: Variation of amplitude and phase with radial distance and local time, *J. Geophys. Res.*, *115*, A04212, doi:10.1029/2009JA014729.

Arridge, C.S., N. Achilleos, M.K. Dougherty, K.K. Khurana, and C.T. Russell (2006), Modeling the size and shape of Saturn's magnetopause with variable dynamic pressure, *J. Geophys. Res.*, *111*, A11227, doi:10.1029/2005JA011574.

Arridge, C.S., C.T. Russell, K.K. Khurana, N. Achilleos, N. André, A.M. Rymer, M.K. Dougherty, and A.J. Coates (2007), Mass of Saturn's magnetodisc: Cassini observations, *Geophys. Res. Lett.*, *34*, L09108, doi:10.1029/2006GL028921.

Arridge, C.S., C.T. Russell, K.K. Khurana, N. Achilleos, S.W.H. Cowley, M.K. Dougherty, D.J. Southwood, and E.J. Bunce (2008a), Saturn's magnetodisc current sheet, *J. Geophys. Res.*, *113*, A04214, doi:10.1029/2007JA012540.

Arridge, C.S., K.K. Khurana, C.T. Russell, D.J. Southwood, N. Achilleos, M.K. Dougherty, A.J. Coates, and H.K. Leinweber (2008b), Warping of Saturn's magnetospheric and magnetotail current sheets, *J. Geophys. Res.*, *113*, A08217, doi:10.1029/2007JA012963.

Baumjohann, W., and R.A. Treumann (1997), Convection and substorms, in *Basic Space Plasma Physics*, Imperial College Press, p. 77

Broadfoot, A.L., B.R. Sandel, D.E. Shemansky, J.B. Holberg, G.R. Smith, D.F. Strobel, J.C. McConnell, S. Kumar, D.M. Hunten, S.K. Atreya, T.M. Donahue, H.W. Moos, J.L. Bertaux, J.E. Blamont, R.B. Pumphrey and S. Linick (1981), Extreme Ultraviolet Observations from Voyager 1 Encounter with Saturn, *Science*, *212*, 206-211.

Brandt, P.C., K.K. Khurana, D.G. Mitchell, N. Sergis, K. Dialynas, J.F. Carbary, E.C. Roelof, C.P. Paranicas, S.M. Krimigis, and B.H. Mauk (2010), Saturn's periodic magnetic field perturbations caused by a rotating partial ring current, *Geophys. Res. Lett.*, *37*, L22103, doi:10.1029/2010GL045285.

Bunce, E.J., and S.W.H. Cowley (2003), A note on the ring current in Saturn's magnetosphere: Comparison of magnetic data obtained during the Pioneer-11 and Voyager-1 and -2 fly-bys, *Ann. Geophys.*, *21*, 661-669.

Bunce, E.J., S.W.H. Cowley, I.I. Alexeev, C.S. Arridge, M.K. Dougherty, J.D. Nichols, and C.T. Russell (2007), Cassini observations of the variation of Saturn's ring current parameters with system size, *J. Geophys. Res.*, *112*, A10202, doi:10.1029/2007JA012275.

Bunce, E.J., C.S. Arridge, S.W.H. Cowley, and M.K. Dougherty (2008), Magnetic field structure of Saturn's dayside magnetosphere and its mapping to the ionosphere: Results from ring current modeling, *J. Geophys. Res.*, *113*, A02207, doi:10.1029/2007JA012538.

Burton, M.E., B. Buratti, D.L. Matson, and J.-P. Lebreton (2001), The Cassini/Hugens Venus and Earth flybys: An overview of operations and results, *J. Geophys. Res.*, *106*, A12, doi:10.1029/2001JA900088.

Burton, M.E., M.K. Dougherty, and C.T. Russell (2009), Model of Saturn's internal planetary field based on Cassini observations, *Planetary and Space Science*, *57*, 1706–1713.

Burton, M. E., M.K. Dougherty, and C.T. Russell (2010), Saturn's internal planetary magnetic field, *Geophys. Res. Lett.*, *37*, L24105, doi:10.1029/2010GL045148.

Carbary, J.F., D.G. Mitchell, S.M. Krimigis, D.C. Hamilton, and N. Krupp (2007), Charged particle periodicities in Saturn's outer magnetosphere, *J. Geophys. Res.*, *112*, A06246, doi:10.1029/2007JA012351.

Carbary, J.F., D.G. Mitchell, P. Brandt, C. Paranicas, and S.M. Krimigis (2008a), ENA periodicities at Saturn, *Geophys. Res. Lett.*, *35*, L07102, doi:10.1029/2008GL033230.

Carbary, J.F., D.G. Mitchell, P. Brandt, E.C. Roelof, and S.M. Krimigis (2008b), Statistical morphology of ENA emissions at Saturn, *J. Geophys. Res.*, *113*, A05210, doi:10.1029/2007JA012873.

Carbary, J.F., D.G. Mitchell, C. Paranicas, E.C. Roelof, and S.M. Krimigis (2008c), Direct observation of warping in the plasma sheet of Saturn, *Geophys. Res. Lett.*, *35*, L24201, doi:10.1029/2008GL035970.

Carbary, J.F., N. Achilleos, C.S. Arridge, K.K. Khurana, and M.K. Dougherty (2010), Global configuration of Saturn's magnetic field derived from observations, *Geophys. Res. Lett.*, *37*, L21806, doi:10.1029/2010GL044622.

Caudal, G. (1986), A self-consistent model of Jupiter's magnetodisc including the effects of centrifugal force and pressure, *J. Geophys. Res.*, *91*, 4201-4221.

Chen, Y., and T.W. Hill (2008), Statistical analysis of injection/dispersion events in Saturn's inner magnetosphere, *J. Geophys. Res.*, *113*, A07215, doi:10.1029/2008JA013166.

Clarke, J.T., J.-C. Gérard, D. Grodent, S. Wannawichian, J. Gustin, J. Connerney, F. Crary, M. Dougherty, W. Kurth, S.W.H. Cowley, E. J. Bunce, T. Hill, and J. Kim (2005), Morphological differences between Saturn's ultraviolet aurorae and those of Earth and Jupiter, *Nature*, *433*, 717-719.

Clarke, J. T., et al. (2009), Response of Jupiter's and Saturn's auroral activity to the solar wind, *J. Geophys. Res.*, *114*, A05210, doi:10.1029/2008JA013694.

Clarke, K. E., N. André, D.J. Andrews, A.J. Coates, S.W.H. Cowley, M.K. Dougherty, G.R. Lewis, H.J. McAndrews, J.D. Nichols, T.R. Robinson, and D.M. Wright (2006), Cassini observations of planetary-period oscillations of Saturn's magnetopause, *Geophys. Res. Lett.*, *33*, L23104, doi:10.1029/2006GL027821.

Clarke, K.E., D.J. Andrews, A.J. Coates, S.W.H. Cowley, and A. Masters (2010), Magnetospheric period oscillations of Saturn's bow shock, *J. Geophys. Res.*, *115*, A05202, doi:10.1029/2009JA015164.

Connerney, J.E.P., M.H. Acuña, and N.F. Ness (1981a), Modeling the Jovian current sheet and inner magnetosphere, *J. Geophys. Res.*, *86*, 8370-8384.

Connerney, J.E.P., M.H. Acuña, and N.F. Ness (1981b), Saturn's ring current and inner magnetosphere, *Nature*, *292*, 724-726.

Connerney, J.E.P., N.F. Ness and M.H. Acuña (1982), Zonal harmonic model of Saturn's magnetic field from Voyager 1 and 2 observations, *Nature*, *298*, doi:10.1038/298044a0.

Connerney, J.E.P., M.H. Acuña, and N.F. Ness (1983), Currents in Saturn's magnetosphere, *J. Geophys. Res.*, *88*, 8779-8789.

Cowley, S.W.H., E.J. Bunce, and J.M. O'Rourke (2004), A simple quantitative model of plasma flows and currents in Saturn's polar ionosphere, *J. Geophys. Res.*, *109*, A05212, doi:10.1029/2003JA010375.

Cowley, S.W.H., D.M. Wright, E.J. Bunce, A.C. Carter, M.K. Dougherty, G. Giampieri, J.D. Nichols, and T.R. Robinson (2006), Cassini observations of planetary-period magnetic field oscillations in Saturn's magnetosphere: Doppler shifts and phase motion, *Geophys. Res. Lett.*, *33*, L07104, doi:10.1029/2005GL025522.

Crary, F.J., J.T. Clarke, M.K. Dougherty, P.G. Hanlon, K.C. Hansen, J.T. Steinberg, B.L. Barraclough, A.J. Coates, J.-C. Gérard, D. Grodent, W.S. Kurth, D.G. Mitchell,

A.M. Rymer, and D.T. Young (2005) , Solar wind dynamic pressure and electric field as the main factors controlling Saturn's aurorae, *Nature*, 433, 720-722.

Davis, L., Jr., and E.J. Smith (1990), A model of Saturn's magnetic field based on all available data, *J. Geophys. Res.*, 95(A9), 15,257–15,261, doi:10.1029/JA095iA09p15257.

De Michelis, P., I.A. Daglis, and G. Consolini (1997), Average terrestrial ring current derived from AMPTE/CCE-CHEM measurements, *J. Geophys. Res.*, 102, 14103-14111.

Dougherty, M.K., et al. (2004), The Cassini Magnetic Field Investigation, *Space Sci. Rev.*, 114, 331-383.

Dougherty, M.K., et al. (2005), Cassini magnetometer observations during Saturn orbit insertion, *Science*, 307, 1266-1270.

Galopeau, P.H.M., and A. Lecacheux (2000), Variations of Saturn's radio rotation period measured at kilometre wavelengths, *J. Geophys. Res.*, 106, 13,089-13,101.

Giampieri, G., and M.K. Dougherty (2004), Modelling of the ring current in Saturn's magnetosphere, *Ann. Geophys.*, 22, 653-659.

Giampieri, G., M.K. Dougherty, E.J. Smith, and C.T. Russell (2006), A regular period for Saturn's magnetic field that may track its internal rotation, *Nature*, 441, doi:10.1038/nature04750

Gosling, J.T., and V.J. Pizzo (1999), Formation and evolution of corotating interaction regions and their three dimensional structure, *Space Sci. Rev.*, 89, 21-52.

Grodent, D., J.-C. Gérard, S.W.H. Cowley, E.J. Bunce, and J.T. Clarke (2005), Variable morphology of Saturn's southern ultraviolet aurora, *J. Geophys. Res.*, 110, A07215, doi:10.1029/2004JA010983.

Grodent, D., A. Radioti, B. Bonfond, and J.-C. Gérard (2010), On the origin of Saturn's outer auroral emission, *J. Geophys. Res.*, *115*, A08219, doi:10.1029/2009JA014901.

Gurnett D.A., et al. (2004), The Cassini Radio and Plasma Wave Investigation, *Space Sci. Rev.*, *114*, 395-463.

Gurnett D.A., et al. (2005), Radio and Plasma Wave observations at Saturn from Cassini's approach and first orbit, *Science*, *307*, 1255-1259, doi: 10.1126/science.1105356.

Gurnett D.A., A.M. Persoon, W.S. Kurth, J.B. Groene, T.F. Averkamp, M.K. Dougherty, and D.J. Southwood (2007), The variable rotation period of the inner region of Saturn's plasma disk, *Science*, *316*, 442-445, doi: 10.1126/science.1138562.

Gurnett, D. A., A. Lecacheux, W.S. Kurth, A.M. Persoon, J.B. Groene, L. Lamy, P. Zarka, and J.F. Carbary (2009), Discovery of a north-south asymmetry in Saturn's radio rotation period, *Geophys. Res. Lett.*, *36*, L16102, doi:10.1029/2009GL039621.

Hill, T.W., A.M. Rymer, J.L. Burch, F.J. Crary, D.T. Young, M.F. Thomsen, D. Delapp, N. André, A.J. Coates, and G.R. Lewis (2005), Evidence for rotationally driven plasma transport in Saturn's magnetosphere, *Geophys. Res. Lett.*, *32*, L14S10, doi:10.1029/2005GL022620.

Hughes, W.J. (1995), The magnetopause, magnetotail and magnetic reconnection, in *Introduction to Space Physics*, edited by M.G. Kivelson and C.T. Russell, Cambridge Univ. Press, UK, p229, 243.

Hundhausen, A.J. (1995), The solar wind, in *Introduction to Space Physics*, edited by M.G. Kivelson and C.T. Russell, Cambridge Univ. Press, UK, p92-93, 108.

Jurac, S., M.A. McGrath, R.E. Johnson, J.D. Richardson, V.M. Vasyliunas, and A. Eviatar (2002) Saturn: Search for a missing water source, *Geophys. Res. Lett.*, *29*(24), 2172, doi:10.1029/2002G L015855.

Jurac, S., and J.D. Richardson (2005), A self-consistent model of plasma and neutrals at Saturn: Neutral cloud morphology, *J. Geophys. Res.*, *110*, A09220, doi:10.1029/2004JA010635.

Kanani, S.J., C.S. Arridge, G.H. Jones, A.N. Fazakerley, H.J. McAndrews, N. Sergis, S.M. Krimigis, M.K. Dougherty, A.J. Coates, D.T. Young, K.C. Hansen, and N. Krupp (2010), A new form of Saturn's magnetopause using a dynamic pressure balance model, based on in situ, multi-instrument Cassini measurements, *J. Geophys. Res.*, *115*, A06207, doi:10.1029/2009JA014262.

Kane M., D.G. Mitchell, J.F. Carbary, S.M. Krimigis, and F.J. Crary (2008), Plasma convection in Saturn's outer magnetosphere determined from ions detected by the Cassini INCA experiment, *Geophys. Res. Lett.*, *35*, L04102, doi:10.1029/2007GL032342.

Krimigis, S.M., J. F. Carbary, E.P. Keath, T.P. Armstrong, L.J. Lanzerotti, and G. Gloeckler (1983), General characteristics of hot plasma and energetic particles in the Saturnian magnetosphere: Results from the Voyager spacecraft, *J. Geophys. Res.*, *88*, 8871–8892.

Krimigis, S.M., et al. (2004), Magnetospheric Imaging Instrument (MIMI) on the Cassini Mission to Saturn/Titan, *Space Sci. Rev.*, *114*, 233-329.

Krimigis, S.M., et al. (2005), Dynamics of Saturn's magnetosphere from MIMI during Cassini's orbital insertion, *Science*, *307*, 1270-1273.

Krimigis, S.M., N. Sergis, D.G. Mitchell, D.C. Hamilton, and N. Krupp (2007), A dynamic, rotating ring current around Saturn, *Nature*, *450*, doi.:10.1038/nature06425, 1050-1053.

Kurth, W.S., T.F. Averkamp, D.A. Gurnett, and Z. Wang (2006), Cassini RPWS observations of dust in Saturn's E ring, *Planetary and Space Science*, *54*, 988-998.

Kurth, W.S., A. Lecacheux, T.F. Averkamp, J.B. Groene, and D.A. Gurnett (2007), A Saturnian longitude system based on a variable kilometric radiation period, *Geophys. Res. Lett.*, *34*, L02201, doi:10.1029/2006GL028336.

Kurth, W.S., T.F. Averkamp, D.A. Gurnett, J.B. Groene, and A. Lecacheux (2008), An update to a Saturnian longitude system based on kilometric radio emissions, *J. Geophys. Res.*, *113*, A05222, doi:10.1029/2007JA012861.

Lebreton J.-P., and D.L. Matson (2002), The Huygens probe: Science, payload and mission overview, *Space Sci. Rev.*, *104*, 59-100.

Leisner, J.S., C.T. Russell, K.K. Khurana, and M.K. Dougherty (2007), Measuring the stress state of the Saturnian magnetosphere, *Geophys. Res. Lett.*, *34*, L12103, doi:10.1029/2006GL028921.

Lewis, G.R., N. André, C.S. Arridge, A.J. Coates, L.K. Gilbert, D.R. Linder, and A.M. Rymer (2008), Derivation of density and temperature from the Cassini-Huygens CAPS electron spectrometer, *Planetary and Space Science*, *56*, 901-912.

Lui, A.T.Y., R.W. McEntire, and S.M. Krimigis (1987), Evolution of the ring current during two geomagnetic storms, *J. Geophys. Res.*, *92*, 7459-7470.

Masters, A., N. Achilleos, M.K. Dougherty, J.A. Slavin, G.B. Hospodarsky, C.S. Arridge, and A.J. Coates (2008), An empirical model of Saturn's bow shock: Cassini observations of shock location and shape, *J. Geophys. Res.*, *113*, A10210, doi:10.1029/2008JA013276.

Mauk, B.H., and S.M. Krimigis (1985), Particle and field stress balance within a planetary magnetosphere, *J. Geophys. Res.*, *90*, 8253-8264.

McAndrews H.J., M.F. Thomsen, C.S. Arridge, C.M. Jackman, R.J. Wilson, M.G. Henderson, R.L. Tokar, K.K. Khurana, E.C. Sittler, A.J. Coates, and M.K. Dougherty, (2009), Plasma in Saturn's nightside magnetosphere and the implications for global circulation, *Planet. Space Sci.*, *57*, 1714-1722.

McNutt, R.L., Jr. (1983), Force balance in the magnetospheres of Jupiter and Saturn, *Adv. Space Res.*, *3*, 55-58.

McNutt, R.L., Jr. (1984), Force balance in outer planet magnetospheres, *Physics of Space Plasmas, Proc. 1982-4 MIT Symposia, SPI Conf. Proc. & Reprint Ser.*, vol. 5, edited by J. Belcher et al., Scientific Publishers, Cambridge, Mass., p. 179-210.

Mitchell, D.G., S.M. Krimigis, C. Paranicas, P.C. Brandt, J.F. Carbary, E.C. Roelof, W.S. Kurth, D.A. Gurnett, J.T. Clarke, J.D. Nichols, J.-C. Gérard, D.C. Grodent, M.K. Dougherty, and W.R. Pryor (2009a), Recurrent energization of plasma in the midnight-to-dawn quadrant of Saturn's magnetosphere, and its relationship to auroral UV and radio emissions, *Planet. Space Sci.*, *57*, 1732-1742.

Mitchell, D.G., J.F. Carbary, S.W.H. Cowley, T.W. Hill, and P. Zarka (2009b), The dynamics of Saturn's magnetosphere, in *Saturn from Cassini-Huygens*, edited by M.K. Dougherty, L.W. Esposito, and S.M. Krimigis, Springer, UK, p.273.

Ness, N.F. (1970), Magnetometers for space research, *Space Sci. Rev.*, *11*, 459-554.

Ness, N.F., M.H. Acuña, R.P. Lepping, J.E.P. Connerney, K.W. Behannon, L.F. Burlaga, and F. Neubauer (1981), Magnetic field studies by Voyager 1: Preliminary results at Saturn, *Science*, *212*, 211-217.

Ness, N.F., M.H. Acuña, K.W. Behannon, L.F. Burlaga, J.E.P. Connerney, R.P. Lepping, and F. Neubauer (1982), Magnetic field studies by Voyager 2: Preliminary results at Saturn, *Science*, *215*, 558-563.

Nichols, J.D., J.T. Clarke, S.W.H. Cowley, J. Duval, A.J. Farmer, J.-C. Gérard, D. Grodent, and S. Wannawichian (2008), Oscillation of Saturn's southern auroral oval, *J. Geophys. Res.*, *113*, A11205, doi:10.1029/2008JA013444.

Nichols, J.D., et al. (2009), Saturn's equinoctial auroras, *Geophys. Res. Lett.*, *36*, L24102, doi:10.1029/2009GL041491.

Nichols, J.D., S.W.H. Cowley, and L. Lamy (2010), Dawn-dusk oscillation of Saturn's conjugate auroral ovals, *Geophys. Res. Lett.*, *37*, L24102, doi:10.1029/2010GL045818.

Paranicas, C.P., B.H. Mauk, and S.M. Krimigis (1991), Pressure anisotropy and radial stress balance in the Jovian neutral sheet, *J. Geophys. Res.*, *96*, 21135-21140.

Peredo, M., J.A. Slavin, E. Mazur, and S.A. Curtis (1995), Three-dimensional position and shape of the bowshock and their variation with Alfvénic, sonic and magnetosonic Mach numbers and interplanetary magnetic field orientation, *J. Geophys. Res.*, *100*, A5, 7907-7916.

Persoon A.M., D.A. Gurnett, W.S. Kurth, G.B. Hospodarsky, J.B. Groene, P. Canu, and M.K. Dougherty (2005), Equatorial electron density measurements in Saturn's inner magnetosphere, *Geophys. Res. Lett.*, *32*, L23105, doi:10.1029/2005GL024294.

Persoon A.M., D.A. Gurnett, O. Santolik, W.S. Kurth, J.B. Faden, J.B. Groene, G.R. Lewis, A.J. Coates, R.J. Wilson, R.L. Tokar, J.-E. Wahlund, and M. Moncuquet (2009), A diffusive equilibrium model for the plasma density in Saturn's magnetosphere, *J. Geophys. Res.*, *114*, A04211, doi:10.1029/2008JA013912.

Pontius, D.H., Jr., and T.W. Hill (2006), Enceladus: A significant plasma source for Saturn's magnetosphere, *J. Geophys. Res.*, *111*, A09214, doi:10.1029/2006JA011674.

Porco, C.C., et al. (2006), Cassini observes the active South pole of Enceladus, *Science*, *311*, doi: 10.1126/science.1123013.

Priest, E.R. (1995), The Sun and its magnetohydrodynamics, in *Introduction to Space Physics*, edited by M.G. Kivelson and C.T. Russell, Cambridge Univ. Press, UK, p58, 61.

Richardson, J.D., and E.C. Sittler, Jr. (1990), A plasma density model for Saturn based on Voyager observations, *J. Geophys. Res.*, *95*, 12019-12031.

Richardson, J.D. (1995), An extended plasma model for Saturn, *Geophys. Res. Lett.*, *22*, 1177-1180.

Russell, C.T., and R.J. Walker (1995), The magnetospheres of the outer planets, in *Introduction to Space Physics*, edited by M.G. Kivelson and C.T. Russell, Cambridge Univ. Press, UK, p.509.

Rymer, A.M., A.J. Coates, K. Svenes, G.A. Abel, D.R. Linder, B. Narheim, M. Thomsen, and D.T. Young (2001), Cassini plasma spectrometer electron spectrometer measurements during the Earth swing-by on August 18, 1999, *J. Geophys. Res.*, *106*, A12, doi:10.1029/2001JA90087.

Rymer, A.M., et al. (2009), Cassini evidence for rapid interchange transport at Saturn, *Planet. Space Sci.*, *57*, 1779-1784.

Saur, J., N. Schilling, F.M. Neubauer, D.F. Strobel, S. Simon, M.K. Dougherty, and C.T. Russell (2008), Evidence for temporal variability of Enceladus' gas jets: Modeling of Cassini observations, *Geophys. Res. Lett.*, *35*, L20105, doi:10.1029/2008GL035811.

Schippers, P., M. Blanc, N. André, I. Dandouras, G.R. Lewis, L.K. Gilbert, A.M. Persoon, N. Krupp, D.A. Gurnett, A.J. Coates, S.M. Krimigis, D.T. Young, and M.K. Dougherty (2008), Multi-instrument analysis of electron populations in Saturn's magnetosphere, *J. Geophys. Res.*, *113*, A07208, doi:10.1029/2008JA013098.

Sergis, N., S.M. Krimigis, D.G. Mitchell, D.C. Hamilton, N. Krupp, B.H. Mauk, E.C. Roelof, and M. Dougherty (2007), Ring current at Saturn: Energetic particle pressure in Saturn's equatorial magnetosphere measured with Cassini/MIMI, *Geophys. Res. Lett.*, *34*, L09102, doi:10.1029/2006GL029223.

Sergis, N., S.M. Krimigis, D.G. Mitchell, D.C. Hamilton, N. Krupp, B.H. Mauk, E.C. Roelof, and M.K. Dougherty (2009), Energetic particle pressure in Saturn's magnetosphere measured with the Magnetospheric Imaging Instrument on Cassini, *J. Geophys. Res.*, *114*, A02214, doi: 10.1029/2008JA013774.

Sergis, N., S.M. Krimigis, E.C. Roelof, C.S. Arridge, A.M. Rymer, D.G. Mitchell, D.C. Hamilton, N. Krupp, M.F. Thomsen, M.K. Dougherty, A.J. Coates, and D.T. Young (2010), Particle pressure, inertial force and ring current density profiles in the magnetosphere of Saturn, based on Cassini measurements, *Geophys. Res. Lett.*, *37*, L02102, doi:10.1029/2009GL041920.

Sibeck, D.G., R.E. Lopez, and E.C. Roelof (1991), Solar wind control of the magnetopause shape, location, and motion, *J. Geophys. Res.*, *96*, A4, 5489-5495.

Sitnov, M.I., M. Swisdak, P.N. Guzdar, and A. Runov (2006), Structure and dynamics of a new class of thin current sheets, *J. Geophys. Res.*, *111*, A08204, doi: 10.1029/2005JA011517.

Sittler, E.C., Jr., K.W. Ogilvie, and J.D. Scudder (1983), Survey of low-energy plasma electrons in Saturn's magnetosphere: Voyagers 1 and 2, *J. Geophys. Res.*, *88*, 8847-8870.

Smith, E.J., L. Davis, Jr., D.E. Jones, P.J. Coleman, Jr., D.S. Colburn, P. Dyal, and C.P. Sonett (1980), Saturn's magnetosphere and its interaction with the solar wind, *J. Geophys. Res.*, *85*, 5655-5674.

Thomsen, M.F., D.B. Reisenfeld, D.M. Delapp, R.L. Tokar, D.T. Young, F.J. Crary, E.C. Sittler, M.A. McGraw, and J.D. Williams (2010), Survey of ion plasma parameters in Saturn's magnetosphere, *J. Geophys. Res.*, *115*, A10220, doi:10.1029/2010JA015267.

Tokar, R.L., et al. (2006), The interaction of the atmosphere of Enceladus with Saturn's plasma, *Science*, *311*, 1409-1412, doi: 10.1126/science.1121061.

Tokar, R.L., R.J. Wilson, R.E. Johnson, M.G. Henderson, M.F. Thomsen, M.M. Cowee, E.C. Sittler, Jr., D.T. Young, F.J. Crary, H.J. McAndrews, and H.T. Smith (2008), Cassini detection of water-group pick-up ions in the Enceladus torus, *Geophys. Res. Lett.*, *35*, L14202, doi:10.1029/2008GL034749.

Trauger, J.T., J.T. Clarke, G.E. Ballester, R.W. Evans, C.J. Burrows, D. Crisp, J.S. Gallagher III, R.E. Griffiths, J.J. Hester, J.G. Hoessel, J.A. Holtzman, J.E. Krist, J.R. Mould, R. Sahai, P.A. Scowen, K.R. Stapelfeldt, and A.M. Watson (1998), Saturn's hydrogen aurora: Wide field and planetary camera 2 imaging from the Hubble Space Telescope, *J. Geophys. Res.*, *103*, E9, 20237-20244.

Wahlund, J.-E., M. André, A.I.E. Eriksson, M. Lundberg, M.W. Morooka, M. Shafiq, T.F. Averkamp, D.A. Gurnett, G.B. Hospodarsky, W.S. Kurth, K.S. Jacobsen, A. Pedersen, W. Farrell, S. Ratynskaia, and N. Piskunov (2009), Detection of dusty plasma near the E-ring of Saturn, *Planetary and Space Science*, *57*, 1795-1806.

Wilson, R.J., R.L. Tokar, M.G. Henderson, T.W. Hill, M.F. Thomsen, and D.H. Pontius Jr. (2008), Cassini plasma spectrometer thermal ion measurements in Saturn's inner magnetosphere, *J. Geophys. Res.*, *113*, A12218, doi:10.1029/2008JA013486.

Wilson, R.J., R.L. Tokar, and M.G. Henderson (2009), Thermal ion flow in Saturn's inner magnetosphere measured by the Cassini plasma spectrometer: A signature of the Enceladus torus? *Geophys. Res. Lett.*, *36*, L23104, doi:10.1029/2009GL040225.

Wolf, R.A. (1983), The quasi-static (slow-flow) region of the magnetosphere, in *Solar-Terrestrial Physics*, edited by R.L. Carovillano and J.M. Forbes, D. Reidel Publ. Co., Dordrecht, Holland, p. 303-369.

Wu, C.S., and L.C. Lee (1979), A theory of the terrestrial kilometric radiation, *The Astrophysical Journal*, *230*, 621-626.

Young, D.T., et al. (2004), Cassini Plasma Spectrometer Investigation, *Space Sci. Rev.*, *114*, 1-112.

Young, D.T., et al. (2005), Composition and dynamics of plasma in Saturn's magnetosphere, *Science*, *307*, 1262-1266.

Zarka, P., L. Lamy, B. Cecconi, R. Prangé, and H.O. Rucker (2007), Modulation of Saturn's radio clock by solar wind speed, *Nature*, 450, 265-267, doi:10.1038/nature06237.

Zieger, B., and K.C. Hansen (2008), Statistical validation of a solar wind propagation model from 1 to 10 AU, *J. Geophys. Res.*, 113, A08107, doi: 10.1029/2008JA013046.